The variability and dynamics of the Antarctic Circumpolar Current south of Africa using proxy techniques

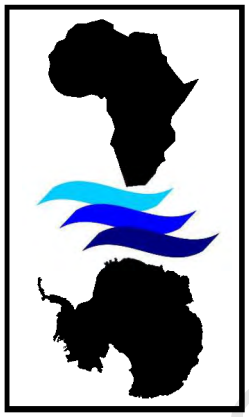

Sebastiaan Swart

Ph.D. Thesis in Physical Oceanography

January 2009

université de bretagne occidentale

Laboratoire de Physique des Océans

Supervisors

Dr Isabelle J. Ansorge
Department of Oceanography, University of Cape Town, Rondebosch, South Africa

Prof Sabrina Speich
Laboratoire de Physique des Océans, IFREMER, Université de Bretagne Occidentale, Brest, France

Prof Johann R. E. Lutjeharms
Department of Oceanography, University of Cape Town, Rondebosch, South Africa

Thesis abstract

The general circulation of the Southern Ocean is dominated by the eastward flowing Antarctic Circumpolar Current (ACC). This is a continuous feature linking the three major ocean basins and thus forms a vital link in the transport of heat and salt on a global scale. These exchanges provide a vital mechanism for the global thermohaline circulation (THC), which regulates the Earth's climate. In the high latitudes, where conditions are hostile, routine hydrographic observations are scarce resulting in a poor understanding of the physical and dynamic processes controlling the variability of the ACC and its influence on the THC.

The GoodHope program launched in early 2004 aimed to establish an intensive monitoring platform that would provide detailed information on the physical structure and volume flux of water masses south of Africa. Sustained observations along the GoodHope cruise track provide the means to monitor the vertical structure and variability of the ACC and its associated fronts south of Africa. Such intense monitoring has been under way in the Drake Passage and south of Australia since the 1970s. A major objective of this thesis is to provide sound estimates of ACC transport and variability using both *in situ* measurements and remote sensing techniques. These estimates are crucial in understanding the role the ACC plays in the global thermohaline circulation (THC) and how the region south of Africa acts as a major conveyor of heat and salt to the higher latitudes. Baroclinic transports of the ACC, relative to 2500 dbar, are calculated from altimetry data alone. These transports agree with simultaneous observed estimates (rms difference in net transport is 5.2 Sv). These observations suggest that sea level anomalies largely reflect baroclinic transport variations above 2500 dbar. The transports contribution per ACC front shows that the SAF is responsible for the highest variability signals (>50%) even though its net transport contribution to the ACC was less (9%) than the APF.

Furthermore, direct measurements of heat and salt content in the Southern Ocean are based on the few synoptic transects, the majority of which are restricted in the austral summer. To overcome the poor temporal and spatial resolution of measurements in the south African sector of the Southern Ocean, this thesis makes use of the gravest empirical mode (GEM) method and applies this technique to weekly composites of satellite altimetry data. The GEM method makes use of all available hydrographic casts from the south-east Atlantic Ocean and projects the data into a baroclinic stream function space parameterised by pressure and dynamic height. The GEM fields were shown to compare closely with independent *in situ* observations of the water column, capturing more than 97% of the total temperature and density variance in the ACC domain. The GEM-derived heat and salt content estimates attempt to determine the variability signals of the ACC due to external influences, such as topographical obstacles and oceanic features originating from subtropical regions.

The exploitation of such proxy methods is useful in improving our understanding of the subsurface properties of the Southern Ocean and more importantly the influences temporal changes in the system have on the structure and transport of the ACC. With time, these methods will be refined with the input of new observations, thereby enhancing their ability to determine the dynamic nature of the ACC and its impact on the Earth's system.

Acknowledgements

I never really know where to start with this part, so lets start with a small joke: why is the beach sand wet? Because the sea weed...

I was lucky enough to have three supervisors who were there to shed light on my study path. Dr Isabelle Ansorge was the first to really introduce me to the science of oceanography in the Southern Ocean. Her enthusiasm and new angles on science have been continually uplifting. She has also exposed me to a great deal of opportunities during my PhD. Isabelle, thank you for your unwavering support and belief. I was also very fortunate to be introduced to a scientist and supervisor like Prof Sabrina Speich. She immediately took me under her wing in France and taught me a great deal about ocean sciences that I would never have learnt back home. She has also become a friend and she will remain an important role model in my life. I thank her for all the opportunities she has given me in France, a place that I hold close to my heart now. Then, to Prof Johann Lutjeharms, who has always been available when advice was needed. Thank you for keeping an eye on my work, for your guidance and 'het levens kleine lessen'. Thank you to Helen King, who provided support on the administrative and financial side of things.

To my friends, particularly Ross, Björn, Neil Swartskaap, Neil H., Mykl, Jen and Sharky. Thanks so much for your friendship and constant opportunity to laugh at life (and me sometimes). It's been a mad fun time. Natalie (aka. Burly) deserves special mention for listening and helping me with numerous work obstacles, and for great lunches. Then to Scott and Lid, who were always there during the final dark three months of my PhD, cooking me dinners and keeping me company.

Et pour la troupe Française: merci á tous pour votre amitié et votre hospitalité. Je remercie particulièrement Vincent et Beci, Marie et Matthieu et Jeff. Sans u, Brest ne se sentirait pas comme ma résidence secondaire. Je veux à un jour une phase à Brest pendant quelque temps de sorte que je puisse finir par vous connaître tout mieux. DTC !

Then there is my family who has always supported and shown interest in what I do. My mom has really taught me the value of education and has never once held back in supporting me with my studies. My brother, Jeroen, has been a solid base in my life and has always been full of good advice. In particular, I would like to thank Kate. She has been so patient. She has always been there for me, even when there were over 12 000 km separating us. In the final month of my study she fended off many distractions so that I could focus, which proved to be really valuable. Those not mentioned here have been duly mentioned in the acknowledgements at the end of the three Papers within this thesis.

Lastly, some thoughts about the project and my experiences. I have been very proud to be part of the GoodHope project, which aims to achieve so much in ocean sciences. I believe its positive name has played an important part in its success and its acceleration onto the world's scientific stage has been impressive. So much has been achieved in only five years. To all the GoodHopers who toiled to retrieve data from the Southern Ocean, enkosi kakhulu. Some of the best times of my life have been at sea in the past five years. I find the Southern Ocean and Antarctica a remarkable, unforgiving and unbelievably beautiful place to work, and I will never forget its magic.

Preface

This thesis is presented as a synthesis and collection of papers for the degree of Doctor of Philosophy (Ph.D.) in Physical Oceanography at the Department of Oceanography, University of Cape Town, South Africa. The completion of this work would not have been made possible without extensive collaboration at the Laboratoire de Physique des Océans, IFREMER, Université de Bretagne Occidentale, Brest, France.

This work has been funded by the following institutions:

1. The South African National Antarctic Program (SANAP) under the auspices of the National Research Foundation (NRF), Department of Science and Technology, South Africa.
2. The Postgraduate Funding Office at the University of Cape Town, South Africa.
3. INSU-CNRS through the French Program National d'Etude de la Dynamique de Climat (PNEDC) for travel grants and expenses.

This thesis is presented in four parts. First, the introduction outlines the oceanic nature of the region of interest while a literature review describes the work previously completed and identifies the knowledge gaps. It also includes the research objectives of this study and a short description of the work accomplished. In the second part, the three papers published and submitted to scientific journals present the results of the thesis. This is followed by a conclusion to the study and work that could be accomplished in the future. The final part is the Appendix, which displays material not included in the scientific papers as well as electronic material, such as animations. The three papers are as follows:

Paper I

Transport and variability of the Antarctic Circumpolar Current south of Africa.

S. Swart, S. Speich, I. J. Ansorge, G. J. Goni, S. Gladyshev, J. R. E. Lutjeharms. J. Geophys. Res. 2008.

Paper II

An altimetry-based Gravest Empirical Mode south of Africa. Part 1: Development and validation.

S. Swart, S. Speich, I. J. Ansorge, J. R. E. Lutjeharms. J. Geophys. Res. 2009.

Paper III

An altimetry-based Gravest Empirical Mode south of Africa. Part 2: Dynamic nature of the ACC fronts.

S. Swart and S. Speich. J. Geophys. Res., 2009.

Contents

Chapter 1

Introduction

1.1 Thesis introduction

The Southern Ocean plays a unique role in coupling the ocean to the atmosphere and cryosphere. Southern Ocean dynamics are dominated by the substantial zonal flow associated with the Antarctic Circumpolar Current (ACC), which is the only current that links all three ocean basins (Figure 1.1). The ACC is, by far, the largest conduit for the exchange of heat and salts between the tropics and the higher latitudes as well as between the Atlantic, Indian and Pacific Oceans. These exchanges provide a vital mechanism by which the efficacy of the global thermohaline circulation (THC) is permitted, which in turn regulates the global climate system (*Gordon*, 1986; *Rintoul*, 1991; *Sloyan and Rintoul*, 2001; *Speich et al.*, 2001; *Rintoul*, 2007). The interaction between the atmosphere, ocean and cryosphere in the Southern Ocean result in the genesis of a number of water masses which ventilate the deeper layers through their advection and thus playing an important role in the THC.

In spite of its global importance, suitable Southern Ocean observations are severely limited. Its vast size and harsh environmental conditions make the task of obtaining observations extremely challenging. This hampers our ability to better understand this integral branch of the THC as well as provide data to accurately test ocean numerical models. Since the 1970s, more extensive surveys have taken place in Drake Passage and south of Australia. This has greatly improved estimates of the ACC transports and its dynamic variability for these regions only. However, these 'snapshot' surveys are not able to define the higher order temporal and spatial variability of the ACC's flow. The recent seeding of profiling floats in the world ocean is, for the first time, greatly improving the spatial coverage of hydrographic profiles in the Southern Ocean but this data is only available from approximately 2002, onwards.

The oceanic domain south of Africa represents the least understood chokepoint of the Southern Ocean. Only a hand full of hydrographic surveys have taken place (see Section 2 for details) south of Africa and therefore our knowledge of the influence of this region on the ACC is severely limited. The vast distance between Africa and Antarctica (approximately 4000 km) and lack of scientific data make the task of monitoring this region very difficult. Furthermore, the south-east Atlantic Ocean is recognised as one of the most dynamic and variable ocean domains in the world due to the interaction between the ACC and the Agulhas Current (Figure 1.2).

The GoodHope project launched in early 2004 (*Ansorge et al.*, 2004; *Speich and Arhan*, 2007) aims to establish an intensive monitoring program that will provide detailed information on the varying physical structure and

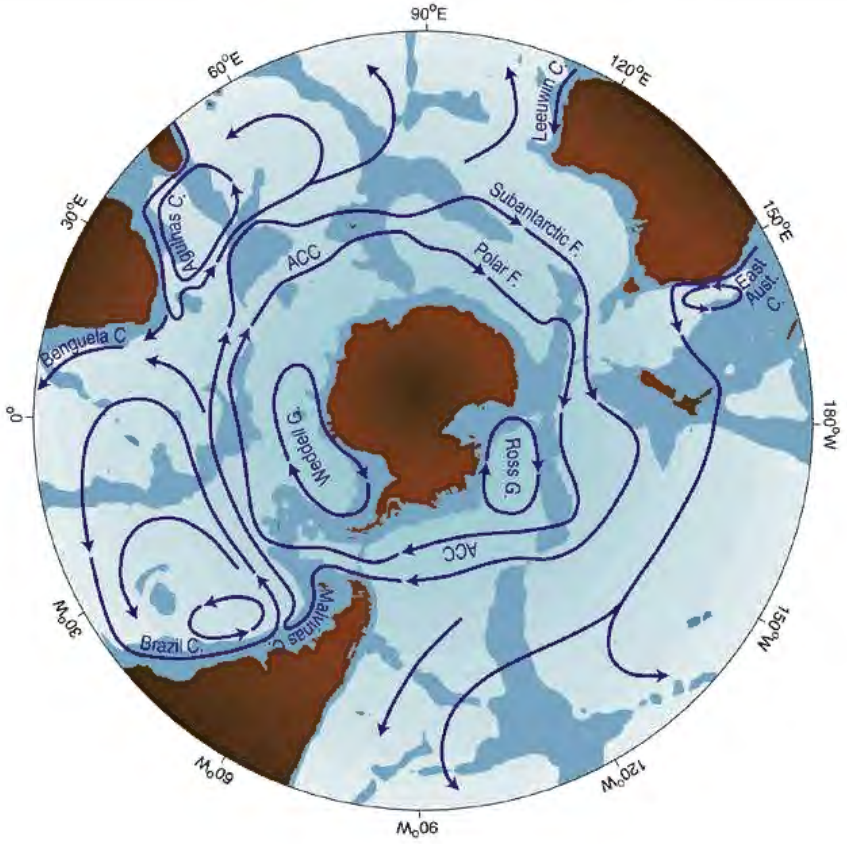

Figure 1.1: Schematic of the major currents in the southern hemisphere oceans south of 20°S (from *Rintoul et al.*, 2001). The Subantarctic Front and Polar Front represent the two main cores of the ACC. Depths shallower that 3500 m are shaded.

volume flux of ACC water masses south of Africa. A key component of GoodHope was the implementation of a high density, expendable bathythermograph (XBT) repeat line between Cape Town and Antarctica (AX25) which runs largely along the TP-JASON 1 altimeter ground-track. This serves for ground truthing altimetry-derived sea-height anomaly data. Furthermore, the southern fraction of GoodHope (south of 50°S) has already been sampled for several years by moorings of the German WECCON project. To the north, the monitoring line overlaps with the USA ASTTEX programme, thus linking the Southern Ocean data set with that of the one collected in the Benguela region. Sustained observations along the GoodHope line (Figure 1.3) provide the means to monitor the vertical structure and variability of the ACC and its associated fronts. This repeat hydrographic line provides the ideal platform to test the hypothesis that a variety of subsurface hydrographic information is closely related to the sea-surface-height signal. Previous studies have already provided some evidence that shows this to be true in the Southern Ocean. The objective of this thesis is to establish the methodology in which proxy methods can be exploited to improve our understanding of the ACC in this region. Until recently, transport studies have relied mostly on sparse observations, which have been limited to the summer months. This thesis aims to integrate both observations and altimetry derived products and in doing so understand the influence dynamic variability has on the structure of the ACC, as a desktop study.

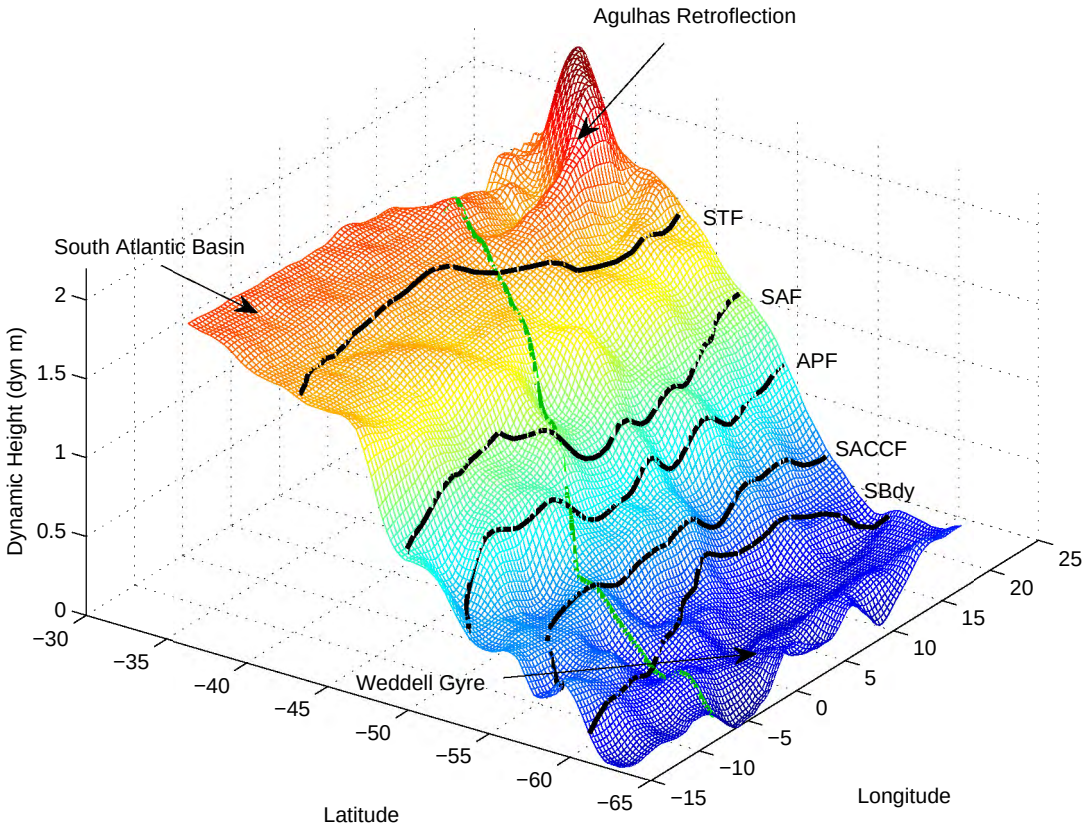

Figure 1.2: The 16-year mean dynamic height distribution (in dyn m) for the south-eastern sector of the Atlantic Ocean. Traces of the ACC fronts, by *Orsi et al.* (1995) have been overlaid. The solid green curve represents the GoodHope cruise track. The color shading is directly related to the dynamic height represented on the left figure axis.

1.2 Literature review

1.2.1 Oceanic regimes between Africa and Antarctica

The African sector of the Southern Ocean constitutes the one of the most variable of the world's ocean. South of Africa three oceanic regimes dominate the hydrography: circulation associated with the south-west Indian subtropical gyre to the north, a circumpolar current, and the largest subpolar gyre found in the extreme south. For this study, the focus is on these three systems in the south-east Atlantic realm between Africa and Antarctica.

1.2.1.1 Agulhas Current System

The strongest western boundary current, the Agulhas Current, lies along the south-eastern edge of the African continental shelf and encompasses the southern-most cell of the South-west Indian Ocean Gyre (*Lutjeharms*, 2006). The current's strength and dynamic behavior compare with that of the Gulf Stream and Kuroshio Current with volume transports estimated at ∼73 Sv (*Beal and Bryden*, 1999).

The Agulhas Current leaves the continental shelf in the region of 36°S, where the lateral dimensions of the flow

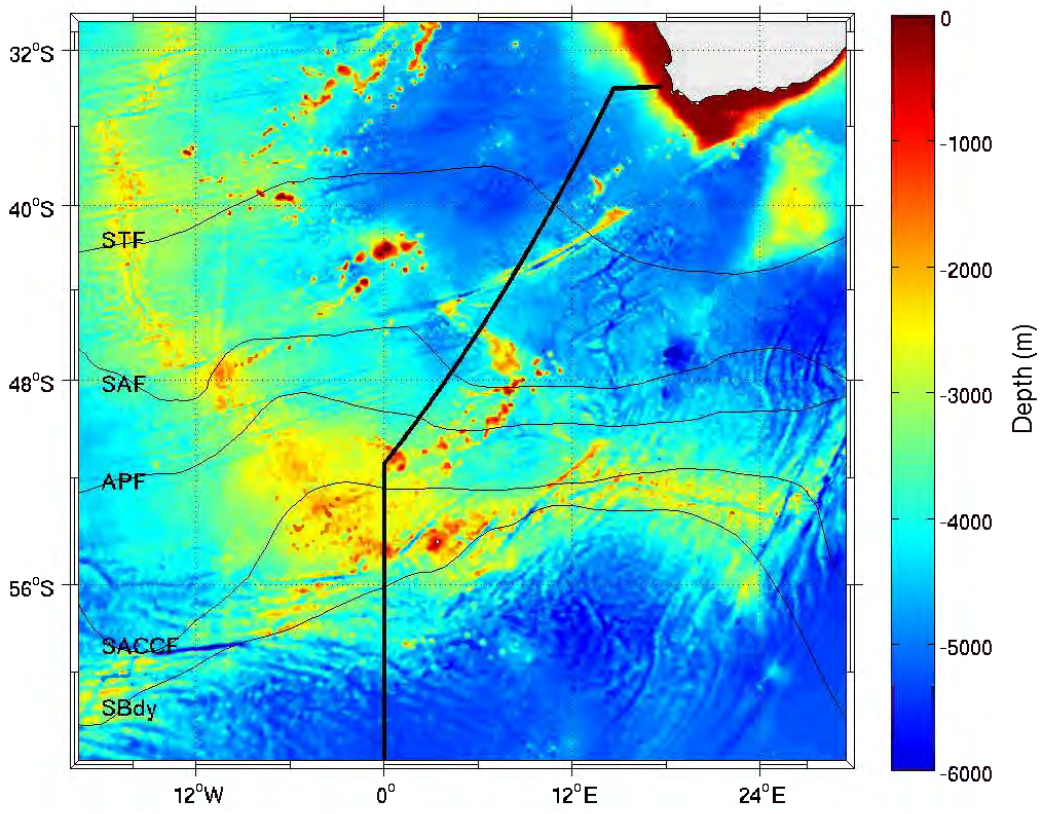

Figure 1.3: Bathymetric map for the region south of Africa depicting the mean ACC frontal positions, as defined by *Orsi et al.* (1995): STF (Subtropical Front), SAF (Subantarctic Front), APF (Antarctic Polar Front), SACCF (southern ACC front), SBdy (southern boundary of the ACC). The solid black line represents the repeat cruise track of the GoodHope CTD and XBT sections.

increase (*Lutjeharms et al.*, 2003). Its westward termination is marked with a region of extreme mesoscale variability (*Lutjeharms*, 2006) in the form of eddy shedding that is associated with the current retroflecting back towards the east as the Agulhas Return Current (Figure 1.4; *Gordon*, 1985; *Lutjeharms and Ballegooyen*, 1988; *Duncombe-Rae*, 1991; *Lutjeharms*, 1996; *Boebel et al.*, 2003). The Agulhas Retroflection produces an intermittent stream of Agulhas Rings (*Lutjeharms and Gordon*, 1987; *Lutjeharms*, 1996; *de Ruijter et al.*, 1999), which are occluded from the Agulhas Retroflection and propagate in generally a north-westerly direction (Figure 1.4; *Schouten et al.*, 2000). The shedding frequency of these Agulhas Rings is believed to be strongly influenced by Natal Pulses (*van Leeuwen et al.*, 2000) and the propagation of shear edge features along the edge of the Agulhas Bank (*de Ruijter et al.*, 1999). This leakage of warm, salty Indian Ocean water into the Atlantic Ocean has attracted considerable attention recently due to the idea that it is an important mechanism, which influences the strength and stability of the THC in the Atlantic Ocean (*Gordon*, 1985, 1987; *Weijer et al.*, 1999). Observations, by *Boebel et al.* (2003), have shown that a highly energetic field of anticyclonic rings and cyclonic eddies in the southern half of the Cape Basin interact extensively with each other and provide the vehicles for substantial heat and salt anomalies to propagate across the Atlantic, thus providing the mechanism for Indo-Atlantic interocean exchange.

Recent studies (*Swart et al.*, 2008; *Gladyshev et al.*, 2008; G. Dencausse, pers. comm.) have shown that

occasionally an Agulhas Ring detaches from the Agulhas Retroflection and propagates in a west to south-west direction. These features have been observed well into the Subantarctic Zone (SAZ) and may directly influence the stability and continuity of the Subtropical Front (STF) and therefore the most northerly domain of the ACC in this region (*Belkin and Gordon*, 1996; *Boebel et al.*, 2003).

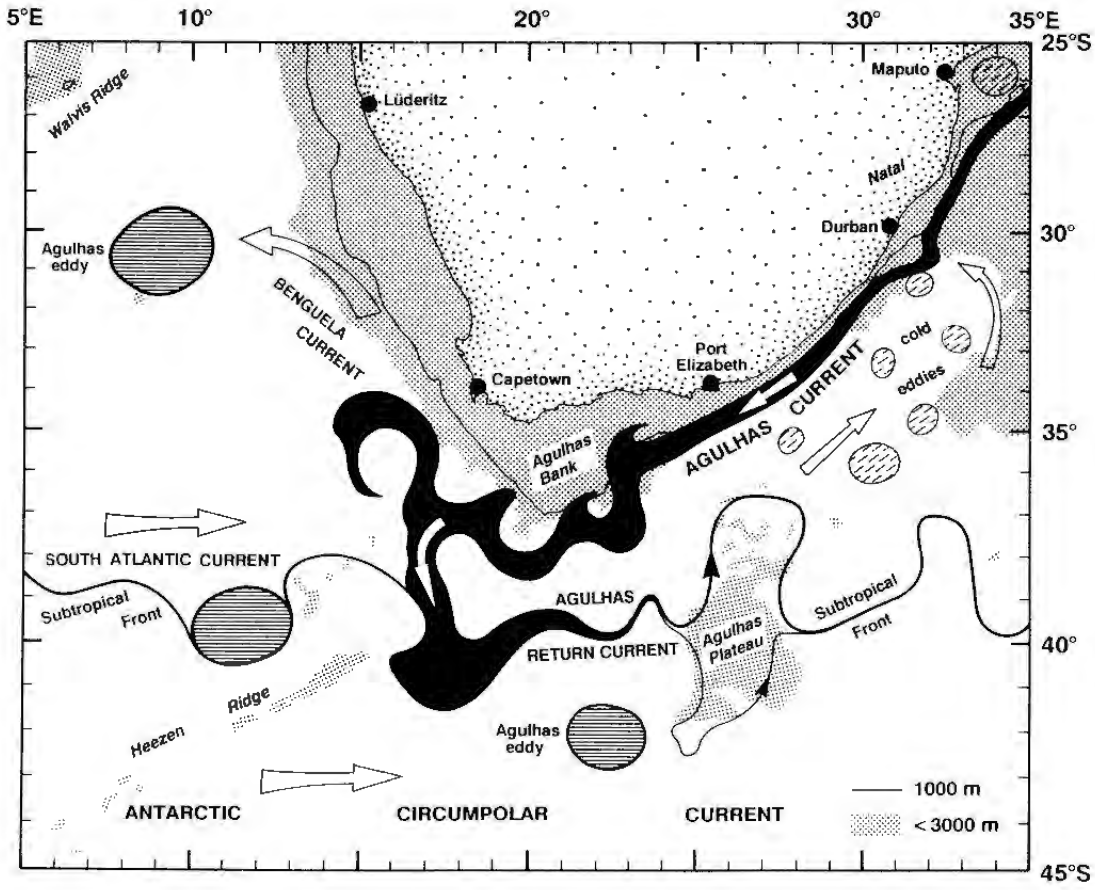

Figure 1.4: Agulhas Current and Agulhas Retroflection (south of Africa) and associated currents and eddies (from *Peterson and Stramma*, 1991).

1.2.1.2 Antarctic Circumpolar Current

The Southern Ocean represents the meeting point for many diverse water masses that circulate around the Antarctic continent via the ACC. This endless circumpolar flow is aided by the world's strongest westward winds, found between 45-55°S (*Trenberth et al.*, 1990). The distribution of land masses in the southern hemisphere allow the ACC to maintain a global link that connects all major oceans. This allows for inter-ocean exchanges in water masses, which carry heat and salt anomalies between the major ocean basins of the world. For this reason, the ACC plays a major role in regulating mean global climate through changes in heat supplied by the deep ocean that may influence the atmosphere directly or through changes in the cryosphere. The ACC is generally conceded to be driven primarily by surface wind stress, however, the coupling and relevant importance of thermohaline driving has likely been underestimated as the primary driving force (*Olbers et al.*, 2004; *Olbers and Visbeck*, 2005; *Olbers and*

Lettmann, 2007; A. C. Naveira-Garabato, pers. comm.).

The ACC is particularly famous for its zonal jet structure and that it contains bands where similar thermohaline properties are found. Meridional gradients in surface and subsurface properties separate water masses of different physical and chemical properties. These frontal boundaries were first described in detail by *Deacon* (1937) and *Mackintosh* (1946).

Fronts of the Antarctic Circumpolar Current The ACC fronts are identified as narrow bands of sharp horizontal density gradients (due to stark changes in temperature and salinity), which often extend from the surface to the ocean bottom. They are particularly conspicuous in the upper layer of the ocean, where they separate different water masses of the Southern Ocean. Antarctic Intermediate Water and Circumpolar Deep Water (further south) dominate the intermediate layers of the ACC. This often conceals the presence of the front below the upper layer (*Whitworth and Nowlin*, 1987).

Frontal positions are not marked by a specific spatial point but a narrow zone across which sharp changes in water properties occur. However, for practical purposes we have to identify the central position of the front using axial property values. This may be achieved by using surface or subsurface criteria or a combination of both. Determining frontal locations using surface criteria shows the highest meridional variability. This is likely due to the atmospheric connection with the near surface layer such as through seasonal warming and wind induced upper level mixing. The use of subsurface criteria to define the front locations has shown to be more stable and subsequently has been used by authors such as *Orsi et al.* (1995), *Belkin and Gordon* (1996) and *Park et al.* (2001).

The evolution of satellite oceanography, more recently, has allowed one to study the fronts using sea surface temperature (SST) and sea surface height (SSH). The majority of the fronts, south of Africa, have distinguishable surface temperature signatures (*Belkin and Gordon*, 1996), which means satellite SST data with high spatial and temporal resolution can be used to study them. *Kostianoy et al.* (2004) have investigated the structure and both spatial and temporal variability of the position and intensity of the main fronts in the Southern Indian Ocean using weekly SST at a relatively high resolution (1/6°) for the period of 1997-1999. From this data it was shown that SST gradient maps were effective at determining the pattern of all the fronts and frontal zones over the whole basin simultaneously. In recent studies (*Sokolov and Rintoul*, 2007a) the position of the fronts have been accurately mapped using information of the SSH gradient from altimeter data. This is extremely useful because the spatial boundaries of the ACC can be separated over long time series in order to better understand the hydrographic dynamics of the fronts and frontal exchange mechanisms.

Overall frontal locations and their latitudinal changes at larger scales appear to be strongly constrained by bottom topography. Variability in the front's position tends to increase over flat bottom topography and therefore indicates that local bathymetry plays an important role in the stability of the fronts (*Moore et al.*, 1997; *Moore et al.*, 1999).

The ACC is bounded to the north by the Subtropical Front (STF). Polewards, we find the Subantarctic Front (SAF), Antarctic Polar Front (APF), southern Antarctic Circumpolar Current front (SACCF) and finally the Southern Boundary (SBdy), which marks the southern terminus of the ACC and the beginning of the Weddell Gyre circulation. The main ACC fronts for the region south of Africa are shown in Figure 2 and 3. These front positions have been determined using subsurface expressions and have been defined by *Orsi et al.* (1995).

Water masses The hydrographic sections, to date completed in the south Atlantic, have crossed water masses within three main ocean zones: the Subtropical, Subantarctic and Polar Zones. Throughout these zones one

encounters seven key water masses where generally speaking the least dense water masses are found at the northern end and most dense at the southern end.

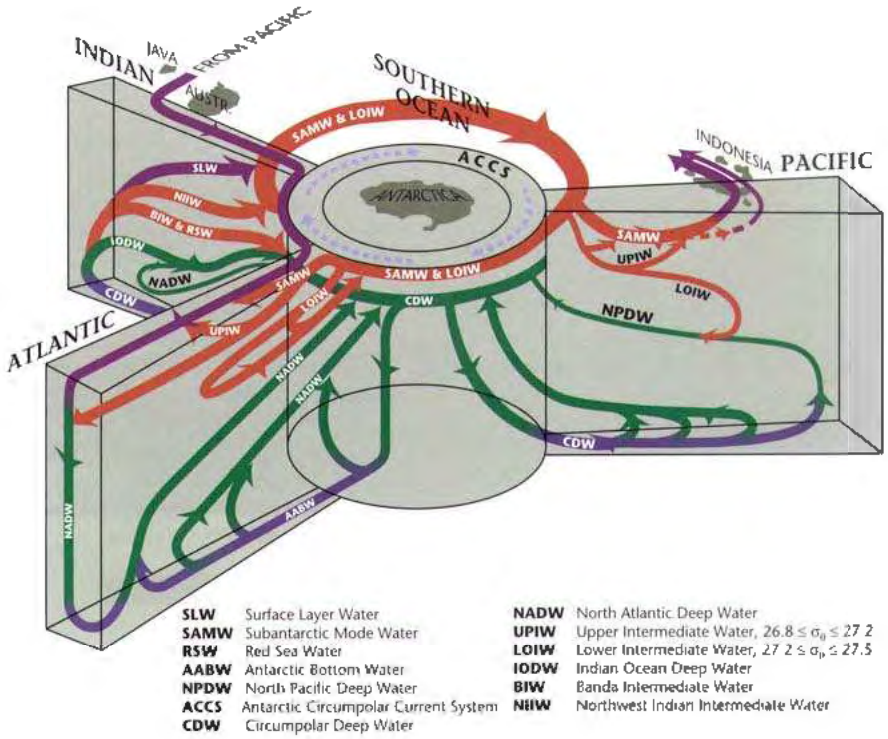

Figure 1.5: A section through the ACC at each major ocean basin region showing the expected water masses and their links with the THC (from *Schmitz*, 1996). The THC link of the seven water masses, discussed in this Section, can be identified in this schematic.

Subtropical Surface Water Warm, salty Subtropical Surface Water (STSW) is located north of the STF. The layer of STSW generally deepens in areas where the Indian Subtropical Gyre is centered. Therefore, the vertical extent of STSW varies from section to section depending where a particular Atlantic hydrographic section cut the Agulhas Retroflection or came into contact with waters coupled to Agulhas Rings. STSW has a wide range of thermohaline characteristics and is defined as lying along the temperature-salinity line 15°C, 35.50 to 24°C, 34.60 (*Darbyshire*, 1963).

Subantarctic Surface Water Immediately south of the STF and extending to the SAF we find Subantarctic Surface Water (SASW), which extends above the salinity minimum of the Antarctic Intermediate Water at approximately 150 m. Due to its presence in the northern ACC, it is influenced by the properties of the adjacent subtropical gyres as well as air-sea exchanges along its circumpolar course (*Whitworth and Nowlin*, 1987).

Subantarctic Mode Water Subantarctic Mode Water (SAMW) forms a homogeneous layer below the SASW and above Antarctic Intermediate Water between the depths of approximately 100-500 m. Similarly to Subtropical Mode Water (*Worthington*, 1972; *Warren*, 1972), the basic mechanism responsible for the formation of SAMW is

vertical convective overturning at the end of winter. In the Subantarctic Zone, cooling in the autumn and winter months erases the seasonal thermocline, which allows deep convection to approximately 500 m. With the onset of spring, warming in the surface layers isolates the thermostad at depth and creates an overlying thermocline, which will once again be erased in the subsequent winter (*McCartney*, 1977). *McCartney* (1977) mentions that SAMW contributes substantial volumetric modes to the central water masses, indicating SAMW to be the renewal agent of high oxygen parts of the main thermocline water of the subtropical gyres in the southern hemisphere.

Antarctic Surface Water Between the Antarctic Polar Front and the Antarctic continent, the upper 200 m contain waters, which are cold, fresh and high in oxygen and nutrients when compared to adjacent SASW. This water mass is known as Antarctic Surface Water (AASW). In summer, this water mass is most easily distinguishable by an intense temperature minimum at about 200 m that marks the base of the winter mixed layer (*Whitworth and Nowlin*, 1987) and has been commonly referred to as Winter Water (*Mosby*, 1934; *Park et al.*, 1998). An increase in salinity (from about 33.8 to 34.6) is experienced between summer and winter due to the discharge of brine with the formation of sea ice (*Legeais*, 2005).

Antarctic Intermediate Water Fresh, highly oxygenated water at the Subantarctic Front is characteristic of Antarctic Intermediate Water (AAIW). This water mass sinks towards the north between potential densities of 27.1 and 27.2 $kg.m^{-3}$ (*Whitworth and Nowlin*, 1987) and reaches a depth of about 1000 m at mid-latitudes (*Piola and Georgi*, 1982). AAIW is characterised by a salinity minimum at intermediate depths (*Deacon*, 1933, 1937; *Wust*, 1935). At the Greenwich Meridian, *Whitworth and Nowlin* (1987) found that the salinity minimum surfaces abruptly at the Subantarctic Front, and no subsurface minimum is found within the Antarctic Polar Frontal Zone (APZ). Initially, two opposing theories for the formation of AAIW were given. One attributed AAIW to wind-driven convergence (*Sverdrup*, 1940) while the other attributed it to thermohaline-driven circulation (*Wust*, 1935; *Deacon*, 1933; 1937). Today it can be accepted that in addition to sea-air interactions, cross frontal mixing is necessary to determine the characteristics of AAIW north of the Antarctic Polar Front (*Gordon et al.*, 1977).

Circumpolar Deep Water Circumpolar Deep Water (CDW) is the most volumous water mass in the Southern Ocean. It is necessary to distinguish CDW between its upper and lower layers based on properties acquired from different source regions (*Gordon*, 1967). In the southwest Atlantic, North Atlantic Deep Water (NADW) penetrates the ACC splitting the CDW into two parts. Upper CDW (UCDW) is characterised by an oxygen minimum and nutrient maxima whose source regions are in the Indian and Pacific oceans (*Callahan*, 1972) while Lower CDW (LCDW) has a salinity maximum and nutrient minima due to its interaction with NADW (*Whitworth and Nowlin*, 1987).

Antarctic Bottom Water The formation of Antarctic Bottom Water (AABW) takes place in explicit locations around the Antarctic shelf. At these locations CDW, entrained southward from the ACC, comes into contact with very cold and dense shelf waters. Interactions between these two water masses produces convective plumes that descend along the continental slope and replenish the AABW layer offshore (*Naveira-Garabato et al.*, 2002). AABW can be distinguished by very low temperatures and salinities ($<0.5°C$ and 34.75, respectively) and high dissolved oxygen (>5 $ml.l^{-1}$) (*Read and Pollard*, 1993).

1.2.1.3 Weddell Gyre

Directly south of the ACC system we find the Weddell Gyre, which constitutes the largest cyclonic circulation of the subpolar regimes in the Southern Ocean. The Weddell Gyre extends well beyond the geographic boundaries of the Weddell Sea. The elongated cyclonic circulation, whose axis trends from southwest to northeast, is bounded to the west by the Antarctic Peninsula and to the south by the Antarctic Continent. Its northern limit is found south of the South Scotia Ridge in the west and south of the Mid-Ocean Ridge system farther east (*Whitworth and Nowlin*, 1987) where the northern boundary of the Weddell Gyre corresponds to the southern boundary of the ACC (*Klatt et al.*, 2005). The alternating atmospheric pressure systems over the ocean and the Antarctic continent give rise to strong wind systems, which largely drive the Weddell Gyre's circulation (*Gordon et al.*, 1981), however, thermohaline forcing and topography also contribute to the structure of the gyre (*Olbers and Wubber*, 1991). Recent estimates show the absolute transport of the Weddell Gyre to be 45 $\pm$7 Sv (*Klatt et al.*, 2005). The Weddell Gyre plays an important role through the entrainment and transport of heat and salt from the ACC to the Antarctic Continental shelves, where deep and bottom waters are produced (*Orsi et al.*, 1993). For this reason it is the most important source of AABW (*Deacon and Moorey*, 1975), which escapes the gyre's circulation and spreads northward into the major ocean basins thereby maintaining the ocean heat and freshwater balances.

Antarctic surface waters, CDW and Weddell Sea Deep and Bottom Waters (WSDW and WSBW) dominate the water masses in the Weddell Gyre. Warm, saline CDW is the only major water mass advected into the Weddell Gyre from a northern source while the other water masses are formed locally (*Orsi et al.*, 1993).

1.2.2 ACC Transports

It has been a major goal to determine the volume transport of the ACC for many Southern Ocean oceanographers since the first estimates were produced in the early 1930's. Knowledge of the net flow of this current can be essential in improving our understanding of inter-ocean exchange processes and the role it plays in the THC. In addition, volume transport estimates of the ACC have frequently and will continue to be used as inputs to or validation of circulation models. Realistic estimates of the transport and its variability can be of significant value as an assessment of the ability of models to account for pertinent dynamics.

Transport estimates have also been a point of contention with the development of varied methods and the selection of different referencing schemes. In doing so estimates through the Drake Passage, as an example, have ranged from more than 200 Sv eastward, to flow in the opposite direction as listed by *Peterson and Stramma* (1991). Much of this disparity may also come from using the equivalent barotropic assumption and in adjusting geostrophic shears to direct measurements in a variable current system (*Peterson and Stramma*, 1991).

Initial studies were concentrated in the Drake Passage where natural continental boundaries to the ACC simplify the computation of the total volume transport. Here, direct measurements using current meter arrays have been used while elsewhere it has been necessary to rely on geostrophic principles to attain transport estimates and hence solely the baroclinic component of the transport field. Using 16 summer sections, *Whitworth* (1980) observed the baroclinic volume transport to average about 80 Sv relative to 2500 dbar and *Nowlin and Clifford* (1982) obtained a range of between 86 and 88 Sv relative to 2500 m. Relative to 3000 dbar 12 independent estimates range from 75 to 110 Sv with an average of 93 Sv while relative to the bottom, four estimates average 109 Sv (as summarised by *Peterson and Stramma*, 1991). Furthermore, *Whitworth and Peterson* (1985) used multi-year records of bottom pressure at each side of Drake Passage to estimate variations in volume transport over longer time intervals. Their four year time series produced a mean transport of 123 Sv in the upper 2500 m. Their study showed that transport

fluctuations of nearly half the mean value can occur over a period as short as two weeks. *Peterson and Stramma* (1991) suggest that a much longer time series is needed to better understand the transport fluctuations occurring over seasonal and extra-seasonal time scales. A recent review of the baroclinic transport above 3000 m at the western and eastern ends of Drake Passage shows that the transport has been steady between 1975 and 2000 with an average value of 107.3 ± 10.4 Sv (*Cunningham et al.*, 2003). The zonal separation of the two sections has introduced some uncertainty into the transport estimates, the main reason being that there is potential for upper ocean flow passing the western Drake Passage to be lost to the South Atlantic, between South America and Burdwood Bank, before it crosses the eastern Drake Passage. A study by *Cunningham et al.* (2003) using six WOCE sections (SR1b) between 1993 and 2000 render a section-integrated baroclinic transport of 136.7 ± 7.8 Sv relative to the deepest common level. This estimate is a few Sverdrups more than the net transport measured by the ISOS (International Southern Ocean Study) array of 133.8 ± 11.2 Sv (*Whitworth and Peterson*, 1985). In addition, it was shown by *Cunningham et al.* (2003) that this transport occurred predominantly at three fronts. The vast majority of the transport was carried by the APF (57.5 ± 5.7 Sv) and the SAF (53 ± 10 Sv) while the SACCF carried the remaining volume (9.3 ± 2.4 Sv). Intermittently, the APF and SAF merged to carry a total transport in the order of 110 Sv. Lowered Acoustic Doppler Current Profiler (LADCP) measurements were also exploited to yield transport estimates. In three years the total net transport was estimated to range from 95 to 184 Sv. However, this range does not appear to be consistent with the range of transports from the ISOS array of 95 to 149 Sv (*Cunningham et al.*, 2003).

Other than at Drake Passage, volume transport estimates are influenced by other flow regimes that border the ACC to the north and south. Transport studies have been infrequent south of Africa and those that have occurred have taken place primarily in the Atlantic sector of the ACC. Relative to the deepest observations, *Jacobs and Georgi* (1977) and *Georgi and Toole* (1982) arrived at 129 and 140 Sv eastward for the ACC, respectively. Further west, *Whitworth and Nowlin* (1987) used a section along the Greenwich Meridian to produce a higher estimate of 162 Sv. The SAF and APF were found to produce the greatest volume transports between stations pairs. This transport value is at the highest range of transports estimated in Drake Passage. The measured increase in transport between the Drake Passage and the Greenwich Meridian is believed to be caused by the injection of NADW in the Atlantic (*Gordon*, 1986). *Gordon* (1986) implies that 5 Sv of NADW upwells in the Atlantic and that 15 Sv is exported to the Indian and Pacific Oceans by the ACC assuming that NADW has a production rate of 20 Sv. This means that the ACC transport at the Greenwich Meridian should be about 15 Sv greater than at Drake Passage. Following this, *Gordon et al.* (1992) produced a new hypothesis by stating that 14 Sv of upper and intermediate water from the South Atlantic sector of the Southern Ocean continues into the Indian sector and recirculates in the Southwest Indian Gyre. This was confirmed through the results presented by *Read and Pollard* (1993) where AAIW from the South Atlantic, identified by its lower salinity was found in the southern part of the Subantarctic Zone in the Indian sector between 45°S and 48°S. In addition, *Read and Pollard* (1993) state that there must be some addition of NADW to the CDW because of its higher salinity.

More recently, in a study farther east (30°E) *Park et al.* (2001), estimated the bottom referenced net baroclinic transport across the entire Civa-2 section (including the Agulhas Current and Weddell Gyre domains) to be 175 Sv eastward, for which the ACC regime accounted for 157 Sv. These estimates fall well above previous estimates from the Conrad cruises (*Jacobs and Georgi*, 1977) and the expected range of the total ACC transport (baroclinic plus barotropic) through Drake Passage (*Nowlin and Klinck*, 1986). Furthermore, the APF region accounted for ∼70% of the transport in the ACC regime during the 1996 Civa-2 cruise, probably due to the APF's confluence with a meandering branch of the SAF. This highlights the significant role the fronts play in the transport of the ACC.

Apart from transport studies completed subsequent to the repeats of WOCE section SR3 south of Australia, the most extensive estimates in the Australia sector have come from studies completed in the last decade (*Rintoul and Sokolov*, 2001; *Rintoul et al.*, 2002). The mean baroclinic transport above and relative to 2500 m from six CTD repeats of the WOCE SR3 section is estimated at 107 Sv (*Rintoul and Sokolov*, 2001) while the mean based on 31 summer XBT sections is 109 Sv (*Rintoul et al.*, 2002). When the mean transport inshore of 2500 m at the southern end is added, and the fact that transport above 2500 m is a nearly constant fraction of the total baroclinic transport across SR3 (66%), the corresponding top-to-bottom transport is calculated as 147 ± 10 Sv (*Rintoul and Sokolov*, 2001), which is about 13 Sv larger than that of Drake Passage. The higher transports south of Australia are expected to balance the Indonesian Throughflow (*Rintoul and Sokolov*, 2001).

1.2.3 Baroclinic and barotropic components of the ACC

The total current in the ocean can be represented by the combination of two components: baroclinic and barotropic. If the isopycnals are inclined between two stations, a pressure gradient exists and is compensated by the Coriolis force. Geostrophic flow appears perpendicular to the Coriolis force and thus along the slope. If one integrates the flow along a vertical profile, one obtains the baroclinic component of the transport. This means that the geostrophic equation gives us information about the baroclinic component of the flow but informs us nothing about the barotropic component. The barotropic situation is one in which the density depends on depth only and therefore the isopycnal surfaces are parallel to the isobars. The surface height anomaly over the ocean can therefore be written:

$$\eta = \eta_{bc} + \eta_{bt} \tag{1.1}$$

where the baroclinic contribution defined as

$$\eta_{bc} = \frac{1}{\rho_0} \int_{-H}^{0} \rho'(z) dz \tag{1.2}$$

and the contribution of the barotropic field is given as:

$$\eta_{bt} = \frac{1}{g\rho_0} P_b. \tag{1.3}$$

In the above, η is the surface height anomaly, $H(x)$ is the water depth, ρ' is the density anomaly relative to a constant reference density ρ_0, and P_b is the bottom pressure anomaly (*Gill and Niiler*, 1973).

With the acquisition of information regarding the space and time scales of current variability (see *Nowlin and Klinck*, 1986), it was believed that while most of the ACC transport is in the baroclinic field, the transport fluctuations are mainly barotropic and the baroclinic component of variability is comparatively small (*Whitworth and Peterson*, 1985). This was shown previously by *Reid and Nowlin* (1971) who revealed that the internal pressure field is relatively steady and that the various hydrographic sections yield similar transports when treated with the same approach. This meant that measuring pressure differences alone could provide a good estimate of transport variability. One would expect that the variability of the transport to be found in the barotropic field due to the fact that meridional density changes would remain relatively constant over short to medium length scales and that the volatility in the current would come from varying wind fields, which could potentially alter over shorter temporal scales.

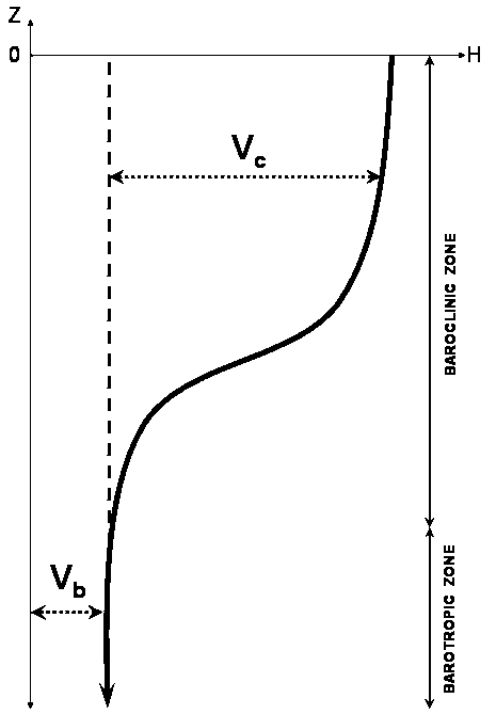

Figure 1.6: Horizontal speed as a combination of barotropic (Vb) and baroclinic (Vc) components of the geostrophic velocity (adapted from *Pond and Pickard*, 1983).

Peterson (1988) analysed the spectral composition of the baroclinic and barotropic components of transport variability at Drake Passage measured by moored instruments. Important components arising from the lunar fortnightly and monthly tides and baroclinic activity at the northern side of the passage were found in the transport variability occurring over subseasonal time scales, these being processes that are independent of wind. The time series of dynamic height from either side of the passage (even though only a year long apiece) confirmed the fact that most of the variability over seasonal time scales is barotropic. Furthermore, a nonlinear analytical model presented by *Clarke* (1982) also simulates the seasonal transport fluctuations as barotropic.

Contrary to the above mentioned results, *Cunningham et al.* (2003) bring to bear evidence to show that the baroclinic variability makes a substantial contribution to the net variability in the ACC. The baroclinic transport relative to and above 2500 m, made by *Whitworth* (1983), has a mean transport of 87 ± 5.5 Sv and the absolute transport above 2500 m for the same period is 125 ± 9.9 Sv (*Whitworth and Peterson*, 1985). This denotes that although the barotropic transport variability contributes most to the net transport variability of 9.9 Sv, the baroclinic transport variability of 5.5 Sv is a significant fraction of the total variability (*Cunningham et al.*, 2003). *Whitworth and Peterson* (1985) found that a linear fit between net transport and cross passage pressure difference in Drake Passage had a correlation coefficient of 0.8 and explained 65% of the variance in net transport. However, the baroclinic transport between 2500 and 500 m had a year long mean of 77 ± 5.3 Sv and a range of 29 Sv. The modeled transport residuals had a standard deviation of 5.9 Sv and a range of 39 Sv and are coherent with the model residuals. This means that using cross pressure differences to calculate transport variability underestimates

the actual variability as they do not account for any significant baroclinic variability. Therefore, *Cunningham et al.* (2003) conclude that the baroclinic variability is an important contribution to the total variability. The uncertainty in transport variability could be largely solved by the provision of longer transport time series resolved at improved spatial and temporal resolutions.

1.3 Objectives and motivation

From the previous section it is evident that hydrographic surveys and moored instrumentation are adequate at measuring the transport and physical structure of major currents around the globe, including the ACC. However, these measurements occur at temporal frequencies, which neither resolve the higher order variability of the system nor allow for proper statistical decomposition of the true variability signal. The uncertainty in both transport and thermohaline variability could be solved by providing a longer time series of data over improved spatial scales. This remains a major focus of ocean sciences in the Southern Ocean. Thus, the objectives of this thesis are strongly aimed at improving the hydrographic temporal sampling resolution by incorporating satellite altimetry data, which in this case, is provided at weekly time steps.

The core objective of this thesis is to observe and understand the variability and dynamics of the ACC using proxy methods. The GoodHope monitoring program provides the ideal platform from which to test this concept. A key component of the GoodHope project is the implementation of a high-density, expendable bathythermograph (XBT) repeat line between Cape Town and Antarctica (AX25), largely along the TP-JASON 1 altimeter ground-track. The temporal and spatial coverage of XBT deployments in the Southern Ocean is considerably higher than CTD profiles, which require more time to complete. However, these XBT profiles only provide one with direct information of the ocean thermal structure to approximately 800 m. The primary aim of this study is to derive proxy relationships, which exploit the available information of the upper thermal structure of the ACC, from XBT data, to estimate the dynamic height and baroclinic transport of the ACC relative to deeper levels (2500 dbar). These empirical relationships form the base from which to test the idea that baroclinic transport estimates of the ACC can be made from altimetry data alone. This contributes to a major goal of the GoodHope program, which is to provide sound estimates of the ACC transport and variability using both *in situ* and remote sensing techniques.

The principles set up by estimating baroclinic transports from altimetry data are extended to the subsurface thermohaline structure of the ACC for the first time. This method, in essence, yields a 16-year time series of temperature and salinity fields along the GoodHope line. These fields can then be used to improve our understanding of the ocean dynamics in the south-eastern Atlantic sector of the Southern Ocean. Direct measurements of heat and salt content in the Southern Ocean have been based on synoptic hydrographic transects, the majority of which are completed in austral summer only. The fields of temperature and salinity deduced from altimetry data are, therefore, used to estimate the variability of heat and salt content in the ACC along the GoodHope line at improved temporal scales. These estimates are then used to determine the dynamic nature of the ACC fronts and the role they play in governing the larger scale variability of the ACC and its links with the broader modes of variability.

In summary, this thesis contains three papers which contribute to the core objectives by:

1. Developing empirical relationships which are used to estimate the baroclinic transport, relative to 2500 dbar, from satellite altimetry data alone.

2. Exploiting the relationships between the surface dynamic height and the subsurface thermohaline structure of the ACC to estimate weekly fields of temperature and salinity from satellite altimetry data alone.

3. Using the data output from the above methods to estimate the heat and salt content of the ACC and their associated variability in relation to frontal dynamics.

1.4 Description of the Papers

The thesis contains three papers which address the key objectives described overleaf. The first two papers specifically focus on exploiting proxy methods to derive new information on the hydrographic structure of the ACC south of Africa, while the final paper explicitly makes use of the data output from the second paper to describe the dynamics of the ACC and associated fronts.

Paper I:

Transport and variability of the Antarctic Circumpolar Current south of Africa

A study by *Legeais et al.* (2005) use proxy methods to derive baroclinic transport estimates of the ACC south of Africa. In the first paper, these proxy relationships are extended to include measurements of dynamic height referenced to a level of no motion (2500 dbar). All available XBT data from the south-east Atlantic Ocean is gathered and used to estimate the dynamic height and baroclinic transport across the ACC extent. This allows one to analyse a much greater quantity of hydrographic sections south of Africa. This available data is then used to improve our description of the upper ocean thermal structure and frontal variability south of Africa and extend the amount of dynamic height and transport data in order to test further proxy methods.

By exploiting dynamic height as a parameter, one is able to incorporate satellite altimetry data to extend the spatial and temporal scales of the empirical relation output and therefore extend the time series of baroclinic transport estimates for the ACC. This yields a 16-year time series of weekly spaced baroclinic transport estimates of the ACC along a fixed geographic track. The altimetry data is also used to accurately define the latitudinal limits of each ACC frontal zone. We then decompose the time series of baroclinic transports for each frontal zone so that the contribution and variability of each zone can be assessed individually. Lastly, the transports are separated into latitudinal bins which reveal the meridional extent and standard deviation of the transports in each frontal domain. This study, therefore, demonstrates that baroclinic transports can be accurately computed using altimetry data alone.

Paper II:

An altimetry-based Gravest Empirical Mode south of Africa. Part 1: Development and validation

The exploitation of proxy methods is continued from Paper I by expanding on the hypothesis that the subsurface structure of the ACC is closely related to the surface dynamic height signal. The proxy methods are extended to include the subsurface thermohaline parameters in the ACC at all pressures to 2500 dbar. All available hydrographic profiles from the south-eastern Atlantic are projected into baroclinic stream function space parameterised by pressure and dynamic height. This produces a two-dimensional Gravest Empirical Mode (GEM) that captures more than 97% of the total temperature and density variance in the ACC. The GEM-produced thermohaline fields are then compared with independent *in situ* observations in order to test their accuracy.

Altimetry data is combined with the GEM (AGEM) to allow us to produce weekly fields of temperature and salinity, which give us much needed insight into the time-varying subsurface structure of the ACC. These fields are validated against independent *in situ* observations. The positions of the ACC fronts are followed in time

using altimetry data. These locations correspond to both observed and GEM-based positions. As a final test, we derive baroclinic transports from the AGEM thermohaline fields and compare them to CTD-based estimates. The two methods are separated into latitudinal bins and are shown to compare favourably. Finally, a time-averaged meridional distribution of the zonal velocities with depth, deduced from the AGEM fields, is presented. The core velocity jets are identified across the span of the ACC and co-located with the mean positions of the ACC fronts derived from altimetry.

Paper III:

An altimetry-based Gravest Empirical Mode south of Africa. Part 2: Dynamic nature of the ACC fronts

Paper III expressly uses the data produced by combining altimetry with the GEM in Paper II to estimate the heat and salt content along the meridional extent of the ACC south of Africa. This is undertaken to improve our understanding of the basin-scale dynamics of the ACC fronts in the south-eastern Atlantic sector of the Southern Ocean. The heat and salt content is first represented in Hovmöller diagrams to explain the varying meridional behavior in time between different regions of the ACC. The heat and salt content is then integrated with depth and in specific front limits and frontal zones in order to quantify the observed variability over the 16-year time series.

This Paper makes explicit use of altimetry products to assist explaining the AGEM-observed variability. One of the most striking observations is the intrusion of Agulhas Rings into the SAZ, bringing marked increases in heat and salt content into the ACC. Using these products, we are able to track and quantify the frequency and intensity of these features and analyse their subsurface behavior over a 16-year period. The study focuses on one major Agulhas Ring event to illustrate the impact features of this kind may have on the ACC hydrographic structure. A large portion of the remaining variability found south of the SAZ can be explained using the potential vorticity equation and the distribution of the local topography. Continuous wavelet analysis is applied to the time series of heat and salt content to explain the distinct orders of variability. In the final parts of the study, we attempt to relate the dominant atmospheric modes of variability with the observed heat and salt content.

Chapter 2

Paper I: Transport and variability of the Antarctic Circumpolar Current south of Africa

This chapter is based on the work published as:
Swart, S., S. Speich, I. J. Ansorge, G. J. Goni, S. Gladyshev and J. R. E. Lutjeharms (2008), Transport and variability of the Antarctic Circumpolar Current south of Africa, *J. Geophys. Res.*, **113**, C09014, doi:10.1029/2007JC004223.

Abstract

Data from five CTD and 18 XBT sections are used to estimate the baroclinic transport (referenced to 2500 dbar) of the ACC south of Africa. Surface dynamic height is derived from XBT data, by establishing an empirical relationship between vertically-integrated temperature and surface dynamic height calculated from CTD data. This temperature-derived dynamic height data compares closely with dynamic heights calculated from CTD data (average RMS difference = 0.05 dyn m). A second empirical relationship between surface dynamic height and cumulative baroclinic transport is defined, allowing us to study a more extensive time series of baroclinic transport derived from upper ocean temperature sections. From 18 XBT transects of the ACC, the average baroclinic transport, relative to 2500 dbar, is estimated at 90 ± 2.4 Sv. This estimate is comparable to baroclinic transport values calculated from CTD data. We then extend the baroclinic transport time-series by applying an empirical relationship between dynamic height and cumulative baroclinic transport, to weekly maps of absolute dynamic topography derived from satellite altimetry, between October, 14, 1992 and May, 23, 2007. The estimated mean baroclinic transport of the ACC, obtained this way, is 84.7 ± 3.0 Sv. These transports agree well with simultaneous *in situ* estimates (RMS difference in net transport = 5.2 Sv). This suggests that sea level anomalies largely reflect baroclinic transport changes above 2500 dbar.

2.1 Introduction

The Antarctic Circumpolar Current (ACC) flows, uninterrupted, around Antarctica. It is the primary means by which water, heat and salt are transported between the Atlantic, Indian and Pacific Oceans. These exchanges provide a vital mechanism for the global Meridional Overturning Circulation (MOC), which regulates the global climate system (*Gordon*, 1986; *Rintoul*, 1991; *Sloyan and Rintoul*, 2001; *Speich et al.*, 2001; *Speich and Arhan*, 2007). The spatial and temporal coverage of hydrographic measurements in the Southern Ocean remain severely limited by the logistic difficulty of sampling in this remote and harsh environment. This results in a poor understanding of the physical and dynamical processes that control the variability of the ACC and its influence on the MOC. The ACC is largely influenced by the oceanographic regimes that extend beyond its northern and southern borders. This is particularly true south of Africa where the ACC flows alongside the Agulhas Current system to the north. This system is regarded as one of the strongest western boundary currents in the world. Agulhas Rings, shed by the Agulhas Retroflection, are the primary means driving exchanges of water between the Indian and Atlantic Oceans (*Byrne et al.*, 2006). This leakage plays an important role on the MOC (*Gordon*, 1985; *Gordon*, 1986; *Weijer et al.*, 1999; *Speich and Arhan*, 2007). The influence of the Agulhas Retroflection and associated ring shedding largely determines the latitudinal extent of the Subtropical Front south of Africa (*Belkin and Gordon*, 1996; G. Dencausse, personal communication), and, therefore, the northern limit of the ACC (Figure 2.1). South of the ACC, in this same sector of the Southern Ocean, the Weddell Gyre constitutes the largest cyclonic circulation regime in the Southern Ocean. The Weddell Gyre transfers heat and salt from the ACC to the Antarctic Continental shelves, where deep and bottom waters are formed (*Orsi et al.*, 1993).

The GoodHope project launched in early 2004 (www.ifremer.fr/lpo/speich/GOODHOPE.htm; *Ansorge et al.*, 2004; *Speich and Arhan*, 2007) aims to establish an intensive monitoring programme that will provide detailed information on the varying physical structure and volume flux of water masses and of the associated mass, heat and fresh-water fluxes between the Atlantic and Indian sector of the Southern Ocean. Sustained observations along the GoodHope cruise track provide the means to monitor the vertical thermal and salinity structure and variability of the ACC and its associated fronts. More extensive monitoring has been underway, since the 1970s, in Drake Passage (*Sprintall et al.*, 1997), and in the Australian and the New Zealand 'chokepoints' (*Rintoul et al.*, 1997; *Budillon and Rintoul*, 2003). The deployment of XBTs by research and merchant vessels that supply the Antarctic bases provides an economical and rapid means to collect ocean temperature data. Nevertheless, these data need to be complimented by full depth CTD casts, current observations through Acoustic Doppler Current Profilers, current meter moorings or pressure inverted echo sounder (PIES) arrays in order to robustly constrain the structure and variability of mass, heat and fresh-water transports through the widest 'chokepoint' of the Southern Ocean (approximately 4000 km between Africa and Antarctica). This vast distance and lack of scientific data in this remote region make the task of monitoring the Southern Ocean south of Africa very challenging.

A major objective of the GoodHope programme is to provide sound estimates of ACC transport and its variability. Previous ACC transport estimates in the region of the Greenwich Meridian came from *Whitworth and Nowlin* (1987) and *Legeais et al.* (2005). Using CTD casts from the AJAX expedition, *Whitworth and Nowlin* (1987) estimated the baroclinic transport, relative to the bottom of the ACC, to be 162 Sv. From three CTD sections occupied near the Greenwich Meridian the baroclinic transports were averaged to 144.6 Sv, relative to the bottom, and 88.9 Sv, relative to 2500 dbar (*Legeais et al.*, 2005). *Legeais et al.* (2005), following *Rintoul et al.* (2002), used a proxy method based on an empirical relationship between upper ocean temperatures and the potential energy anomaly to derive the baroclinic transport of the ACC from 14 XBT sections near the Greenwich Meridian. The

Table 2.1: Summary of the CTD sections used in this study

Section	Date	Ship	Institute	Chief Scientist
AJAX	Jan. 1984	R/V Knorr	Texas A&M U.	T. Whitworth
A21	Jan.-Mar. 1990	R/V Polarstern	U. Bremen	W. Roether
A12	May-Aug. 1992	R/V Meteor	A.W.I.	P. Lemke
SR2	Jan.-Feb. 1993	M/V SA Agulhas	U. Cape Town	M. I. Lucas
GH2	Nov. 2004	R/V Vavilov	Shirshov	S. Gladyshev
GH4	Oct. 2005	R/V Vavilov	Shirshov	S. Gladyshev

mean of these baroclinic transport estimates is 97.5 Sv, relative to 2500 dbar, and range from 87.5 Sv to 109.6 Sv.

In this study, we establish empirical relationships whereby dynamic height and baroclinic transport of the ACC can be determined from the upper ocean mean temperature alone. These relationships allow us to apply remotely sensed sea surface height (SSH) data to the proxy techniques, thereby enhancing the spatial and temporal sampling resolutions. One of the direct outcomes of this method allows us to monitor the upper ocean ACC thermal structure and its variability through the variability of the ACC fronts and SSH. These estimates are crucial in understanding the changes in the density field and its associated mass, heat and fresh-water transports. Our proxy methods prove to be robust by comparing our results to previous classical estimates and are very useful in an ocean region where observations remain scarce. Indeed, our understanding of how the ACC transport varies, even at seasonal scales, is still largely incomplete. As the ACC is the major component of the global ocean circulation, it is especially important to evaluate the internal variability of this large flow system and to identify interannual and long term changes in its transports, as they are intimately related to the interocean exchange of mass, heat and fresh-water. The combination of *in situ* and remotely sensed data offers a powerful means to provide the first quantitative insight on the ACC transport variability.

The data used in this study are presented in Section 2.2. Section 2.3 describes the upper thermal structure and frontal variability between Africa and Antarctica primarily using XBT data. Detailed procedures and results, related to the proxy methods used to derive dynamic height data from the upper ocean mean temperature alone, are explained in Section 2.4. In Section 2.5, we use the available hydrographic dynamic height data in the study region to derive baroclinic transport estimates of the ACC south of Africa and then analyse the meridional distribution of these transports in Section 2.6. In Section 2.7, transport estimates from satellite altimetry are discussed and compared to the CTD and XBT estimates. A time series of baroclinic transports, derived from satellite altimetry for the whole ACC and for each ACC front, is considered in Section 2.8. A summary completes the paper, where we go over the main points of the study and give some perspectives on further exploitation of the proxy methods we have presented here.

2.2 Data

2.2.1 Conductivity-Temperature-Depth

We use data from six CTD sections completed in the South-East Atlantic between November 1983 and October 2005. The sections provide a good coverage of the seasonal variability expected in the South-East Atlantic region because they are occupied during all seasons (Table 2.1). While the first four of these data sets come from historical observations (from 1984 to 1993), the last two of them consist of the first two repeats of the GoodHope transect

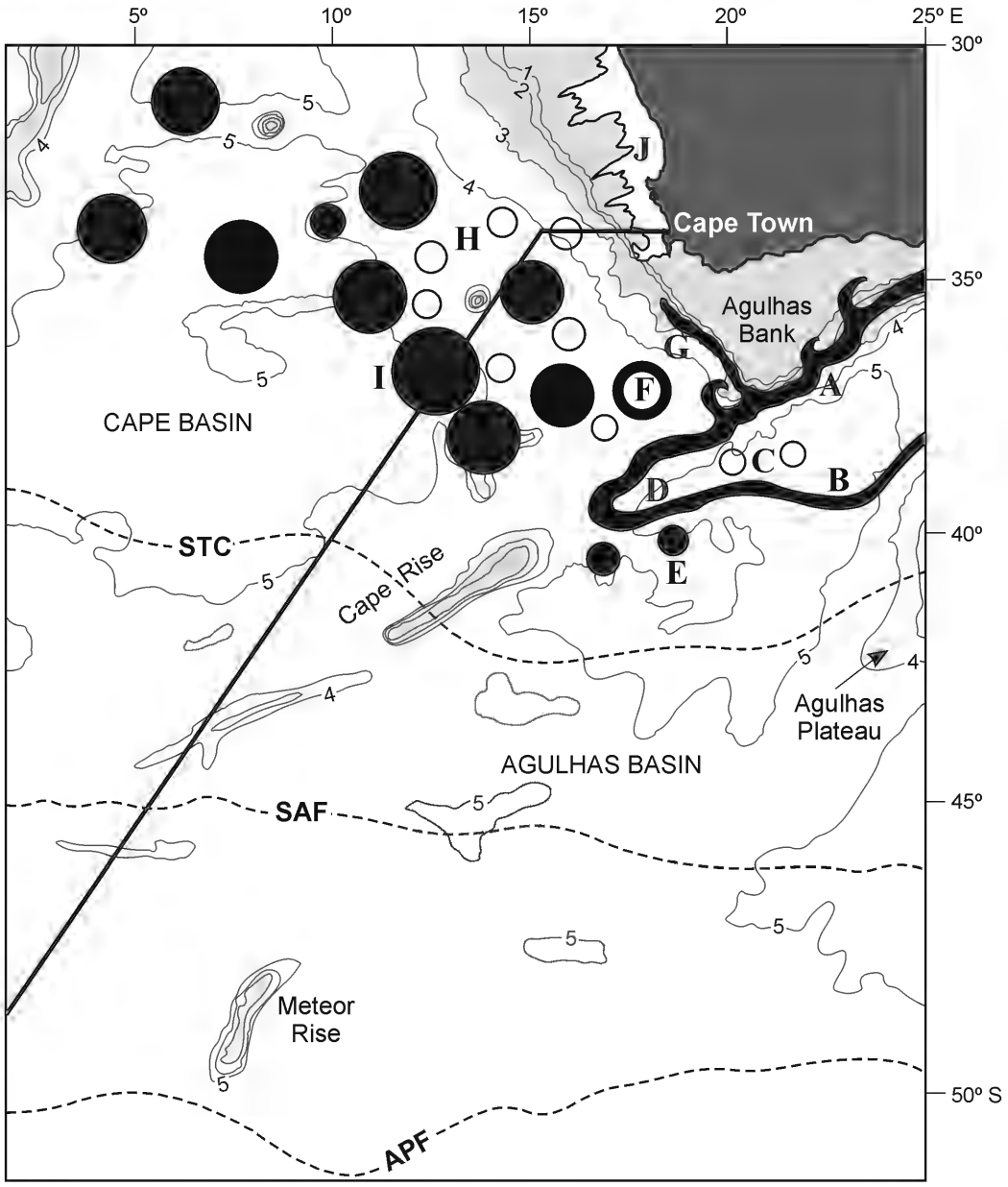

Figure 2.1: A conceptual diagram of the southern Agulhas Current system. Agulhas Rings (I) and filaments (G) are shed at the Agulhas Retroflection (D) and are carried equatorward by the Benguela Current (H). The Agulhas Current retroflects forming an eastward flow (B) to the north of the Subtropical Convergence (STC; otherwise known as the Subtropical Front). The GoodHope transect (solid line) crosses the southern domains of the Benguela upwelling regime (J). The STC, SAF and APF denote the mean locations of the Subtropical Convergence, Subantarctic and Antarctic Polar fronts, respectively. Bathymetry contours are in km and depths less than 3000 m are shaded.

completed by the Shirshov Institute of Oceanology, aboard the RV Akademik Sergey Vavilov (*Gladyshev et al.*, 2008). The two CTD occupations along the GoodHope line allow us to improve the accuracy of the baroclinic transport estimates from those already made by *Legeais et al.* (2005). This is because the two GoodHope cruises are occupied over the same cruise track (in different years) and the water column was sampled with a relatively high spatial resolution (each station is separated by approximately 45 km). In total, we use data from 276 CTD casts (of which 232 stations lie within the ACC domain), which connect Cape Town to Antarctica primarily following a ground track of the satellite altimeters (track no. 133 of Topex-Poseidon initially, followed by Jason1) till the Greenwich Meridian from where the GoodHope transect continues south to the Antarctic continent (Figure 2.2). The AJAX and A21 transects have the coarsest spatial resolution, where stations are spaced approximately 100 km apart as opposed to a 75 and 88 km spacing between stations occupied by the A12 and SR2-WOCE sections, respectively. The first GoodHope CTD section has a mean spacing of 43 km, while the mean station spacing for the second GoodHope CTD section is 56 km. In most cases, tighter station spacing is found over regions of dynamic or steep bottom topography. The closer spacing between the GoodHope CTD casts allow us to include 'snapshots' of the mesoscale structure of the flow along the whole GoodHope transect (the characteristic length scale of eddies and meanders is greater than 100 km in diameter). Details concerning the CTD calibration, station positions, bottle analysis, problems encountered, and sampling carried out on each cruise can be found in a series of technical reports and papers (*SIO*, 1985; *Roether et al.*, 1990; *Lemke*, 1992; *Gladyshev et al.*, 2008).

2.2.2 Expendable Bathythermograph (XBT)

The XBT data, in part, originates from 13 sections completed close to the Greenwich Meridian (Figure 2.3), between 1989 and 2006, as part of German and Russian research cruises and one ferry service completed by the University of Cape Town. Apart from the August 1989 transect, sampling took place during summer months, between November and March. In addition to this, five repeat high-density XBT sections have been completed since February 2004 along the GoodHope cruise track, as part of the GoodHope and the AOML Atlantic high-density XBT programs. The ocean structure is extremely well resolved by using XBTs deployed at high resolution. This proves to be particularly important when studying the dynamics and variability of the ACC as its flow is composed of discrete and intense narrow jet-like structures (*Sokolov and Rintoul*, 2007a; 2007b).

During the GoodHope transects, XBTs were deployed to measure the upper ocean temperature at intervals of 25 km, increasing the frequency to 15 km over the frontal regions of the ACC. Most deployments reached a maximum working depth of the Sippican Deep Blue XBT, which is in the order of 780 m. The GoodHope and Alfred Wegner Institute (AWI) XBT transects are sampled with a vertical resolution of 2 dbar, while the section completed by the Arctic and Antarctic Russian Institute (AARI) has a vertical resolution of 1 dbar. The 4000 km transect between Africa and Antarctica was on average completed within two weeks, with each section providing a roughly synoptic picture of the upper thermal layer in this sector of the Southern Ocean.

Extensive quality control procedures have been applied to the XBT data by AOML/NOAA in the United States. Adjacent temperature profiles were compared with each other and to the Levitus climatology (*Levitus*, 1982) in the region. Profiles were declared bad and discarded if they did not reach a minimum depth of 400 dbar. When feasible and if the temperature data recovered well, 'spikes' in the profile were removed and edited. For more details on AOML quality control procedures, refer to *Bailey et al.* (1994) and *Daneshzadeh et al.* (1994).

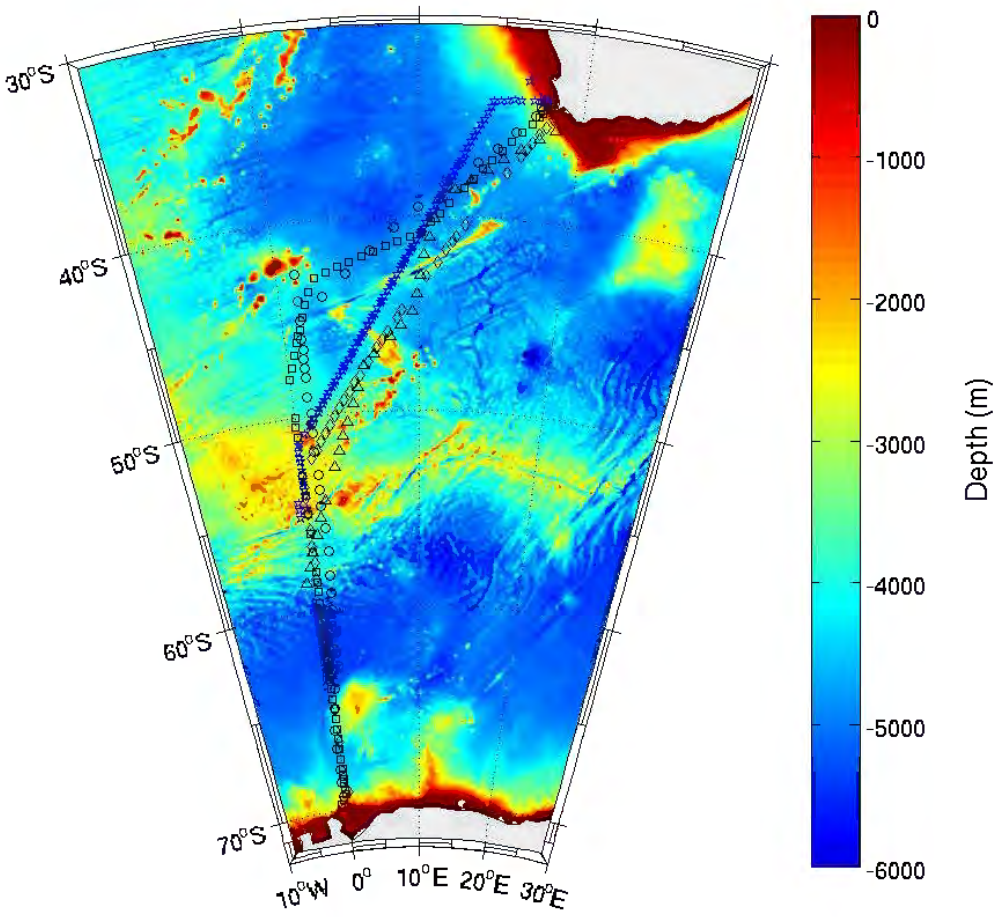

Figure 2.2: Locations of the six CTD sections used in this study (Table 2.1). The AJAX section (circles), A21 section (triangles), A12 section (squares), SR2 (diamonds), GoodHope 1 and 2 (stars). The section tracks have been overlaid on bathymetry (in meters).

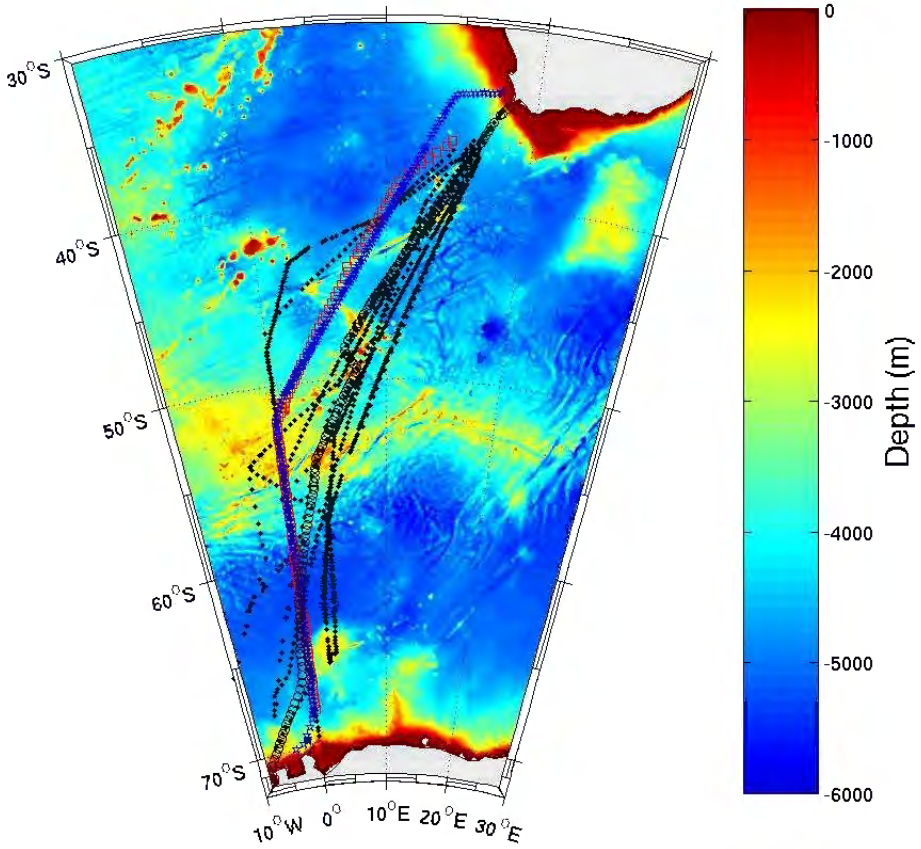

Figure 2.3: Locations of the XBT stations used in this study. GoodHope repeat section (stars), AARI section (squares), AWI sections (dots) and the AA-CT section (circles). The section tracks have been overlaid on bathymetry (in meters).

2.2.3 Satellite altimetry data

2.2.3.1 Sea level anomaly

Satellite altimetry measurements of SSH are used to estimate baroclinic transport. The 'Maps of Sea Level Anomaly (MSLA)' product from CLS/AVISO, a weekly SSH anomaly map on a 1/3° Mercator grid that incorporates T/P, Jason-1, ERS-1/2 and Envisat altimeters, was used in this study. Because the ACC is characterized by fine scale structures and variability we choose to use the "up to date" data processing that makes use of all the satellite data available for each period. The satellite data, for this time series, are not homogeneous in number but for long periods they provide an improved resolution and data accuracy compared with the classical "referenced" data set. These multi-mission gridded SSHs are referenced to a seven year (1993-1999) mean. For details on mapping methods and error corrections applied to these fields, refer to *le Traon et al.* (1998), *le Traon and Ogor* (1998) and *Ducet et al.* (2000).

2.2.3.2 Absolute dynamic topography

The 'Maps of Absolute Dynamic Topography (MADT)' product from CLS/AVISO has the same temporal and spatial resolution described in the sea level anomaly section. The MADT is the sum of the sea level anomaly data and a mean dynamic topography (Rio05 – Combined Mean Dynamic Topography (CMDT); *Rio and Hernandez*, 2004). The CMDT is a combined product using *in situ* measurements (hydrographic and surface drifter data), altimetry data and the EIGEN-GRACE 03S geoid. The CMDT is computed over a seven year period (1993-1999).

2.3 Upper ocean thermal structure and frontal variability south of Africa

South of Africa, the ACC flows between the South Atlantic and South Indian subtropical domains in the north and the eastern part of the Weddell Gyre in the south. The criteria and classical position of the following fronts observed in this region: the Subtropical Front (STF), the Subantarctic Front (SAF), the Antarctic Polar Front (APF), the southern ACC front (sACCf) and the southern boundary of the ACC (SBdy) are listed in Table 2.2. A time sequence of six XBT sections (five repeat GoodHope occupations and an Antarctica - Cape Town section) between 2004 and 2006 (Figure 2.4), depicts the temporal and latitudinal variability of the upper ocean temperature structure in the Atlantic sector south of Africa.

Significant thermal variability is produced in the form of mesoscale structures: eddies, meanders and narrow, intense horizontal temperature gradients corresponding to the jet-like structure of the ACC (e.g., *Sokolov and Rintoul*, 2007a). An almost continual presence of eddies are found in the northern domain of the GoodHope section (located between 34-39°S). These features are spawned at the Agulhas Current Retroflection, where large Agulhas Rings detach from the Agulhas Current and spin into the Atlantic Ocean (*Duncombe-Rae*, 1991; *Lutjeharms*, 1996; *de Ruijter et al.*, 1999). SSH and RAFOS float data illustrate this region as a 'cauldron' of turbulent mesoscale activity, which may directly influence the stability and continuity of the STF south of Africa (*Belkin and Gordon*, 1996; *Boebel et al.*, 2003). For this reason we question the use of the STF as a northern delimiter of the ACC in Section 2.7.

A weekly time series of the MADT data shows that Agulhas Rings propagate towards the south-west and cross the GoodHope transect, between 39-42°S, on approximately 1-2 occasions per year. Agulhas rings further

Table 2.2: Temperature criteria used to locate the ACC fronts, reproduced from *Orsi et al.* (1995)[a].

Front	Temperature criteria	Classical position (°S)
STF	$10°C < \theta_{100m} < 12°C$	39.9
SAF	$\theta >$ 4-5°C at 400 m, farther north	47.6
APF	$\theta < 2°C$ along θ_{min} at z < 200 m, farther south	49.6
sACCf	$\theta < 0°C$ along θ_{min} at z < 150 m, farther south	52.4
SBdy	Southern limit of vertical maximum of $\theta > 1.5°C$, (∼200m)	56.1

[a]STF is the Subtropical Front, SAF the Subantarctic Front, APF the Antarctic Polar Front, sACCf the southern ACC front, SBdy the southern boundary of the ACC and θ is potential temperature. The classical positions of the ACC fronts, along the GoodHope transect, as determined by *Orsi et al.* (1995), are given.

complicate the process of defining the STF because they transfer subtropical water signatures into the ACC realm. Furthermore their anticyclonic rotation result in large transport reversals in the ACC (*Richardson*, 2007; *Gladyshev et al.*, 2008; refer also to Section 2.6). We identify these features using MADT data and back-track their trajectories to confirm their point of origin is within the Agulhas Current Retroflection (Figure 2.5). The centre of an Agulhas Ring is marked by a black circle on Figure 2.5. During October, 19, 2005, the feature can be seen propagating, in a west-southwest direction. By December, 7, 2005, the western limit of the feature has crossed the GoodHope transect (dashed line), at approximately 40.5°S. The fifth GoodHope XBT transect (Figure 2.4e) crosses the same feature on December, 5, 2005. Only the western edge of the ring is encountered. As a result of the ring being only clipped during the December 2005 transect, the thermal signal of the XBT data appears to be less dominant than the January 2005 transect, which bisected a larger proportion of a ring at ˜42°S (Figure 2.4c). In addition, an Agulhas Ring is located in the Subantarctic Zone (SAZ), in the December 2005 section (Figure 2.4e). The temperature sections, where these features are located, reveal a warming of the waters to ∼700 m, with surface temperatures ranging from 19.0°C (January 2005) to 15.5°C during the December 2005 occupation. The Agulhas Ring, seen in January 2005 causes a strong subsurface meridional temperature gradient between <8°C to >13°C over a distance of <60 km. The diameter of the warm core eddy, defined by the maximum horizontal temperature gradient ($\Delta T/\Delta x$) at 200 m, is approximately 170 km. Even though this constitutes a strong warm anomaly, for this region, it does not seem to affect the latitude of the SAF at 44.22°S, but rather it strengthens the temperature gradient across the front. In contrast, due to the absence of warm or cold mesoscale features in the remaining sections, the horizontal temperature gradient, between 41-44°S, decreased at a steady rate, without large temperature fluctuations.

The latitude of the ACC fronts for the six XBT transects[1] are shown in Figure 2.6 (during three of the GoodHope transects the SBdy was not reached so we do not include it in our present discussion). The XBT-inferred positions of the ACC fronts are generally found slightly south of the traces by *Orsi et al.* (1995). The only discrepancy comes from the path of the SAF, where *Orsi et al.* (1995) show the front to steer south (˜47.6°S) of Meteor Rise, located at approximately 47°S, 7°E. The XBT and CTD sections, described in this study, which cross Meteor Rise, show that the SAF is, on all occasions, located to the north of this rise in bathymetry.

The sequence of frontal latitudes (Figure 2.6) reveals a southward shift in both the SAF and APF, at least during the spring and summer months. Between 2004 - 2006, the SAF moved 1.16° (130 km) southward while the APF shifted 2.65° (294 km). For the last three sections (between October 2005 and February 2006) some of the southward signal could be induced by seasonal warming of the upper thermal layer between spring and the late

[1]The February 2006 section does not follow the GoodHope cruise track and, therefore, some spatial differences occur. However, variability in the altimeter SSH field is small (<3 cm) for the latitudinal bands of the SAF and APF (between February 2004-2006). This reveals that no significant change in the XBT-derived frontal positions results from the distance between the two sections.

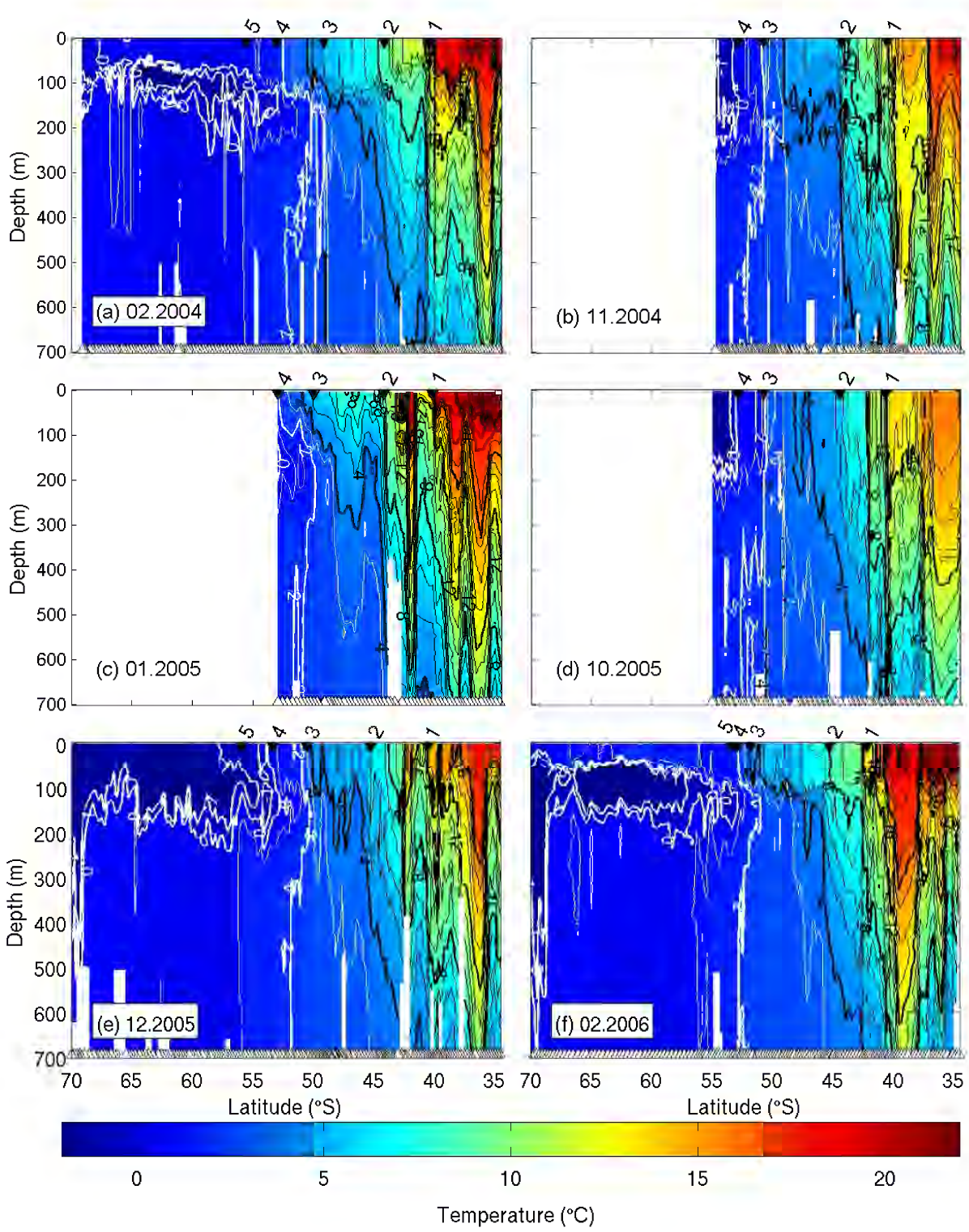

Figure 2.4: Temperature sections for the following transects: (a) GoodHope 1: February 2004, (b) GoodHope 2: November 2004, (c) GoodHope 3: January 2005, (d) GoodHope 4: October 2005, (e) GoodHope 5: December 2005, (f) Antarctica-Cape Town (AA-CT): February 2006. The black arrows show the latitudes of the ACC fronts (from north to south: STF (1), SAF (2), APF (3), sACCf (4), SBdy (5)). Triangles, along the bottom x-axis, indicate station positions. Note that the figures have equal axes of depth and latitude.

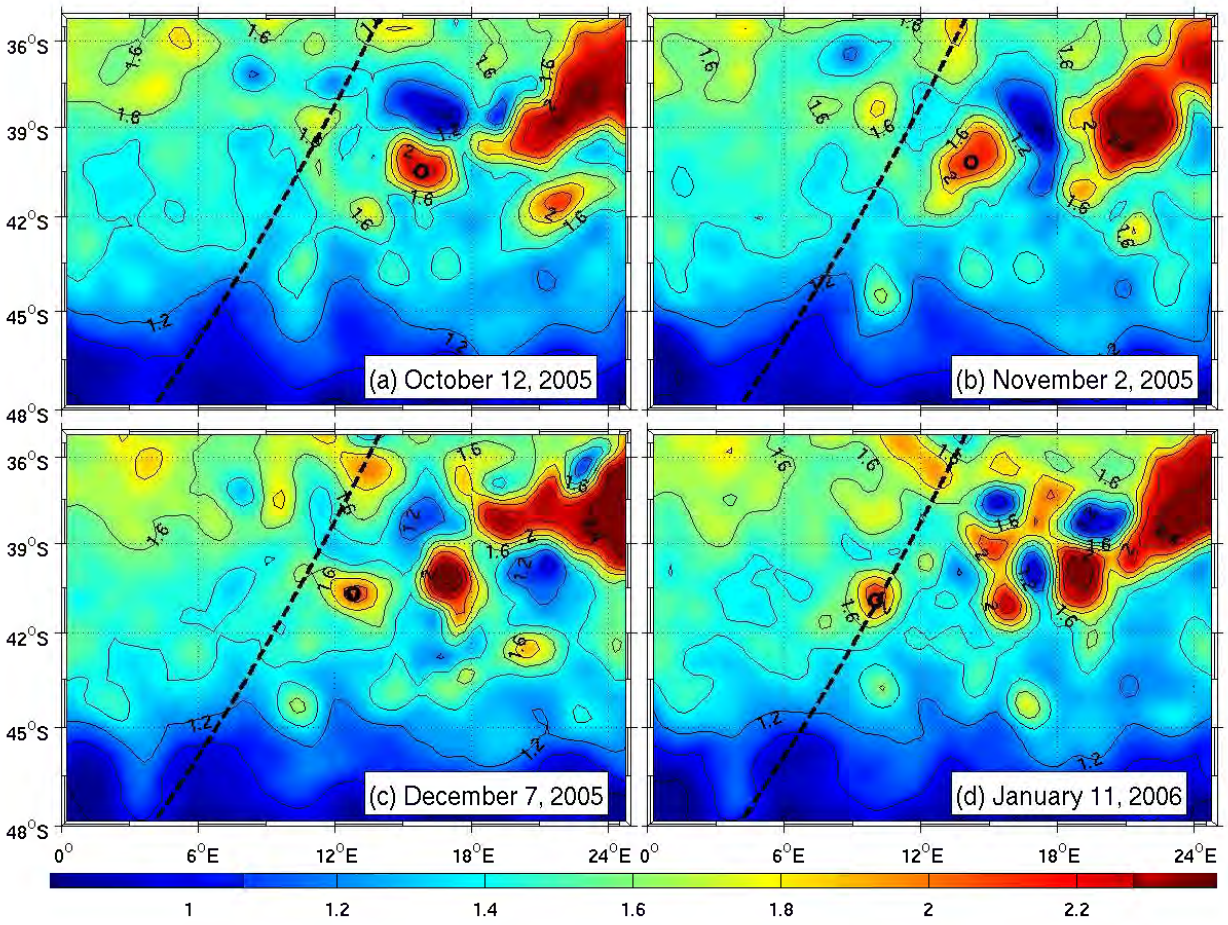

Figure 2.5: The MADT data (in dyn m) for the region located near the GoodHope cruise track between October 12, 2005 and January, 11, 2006. The propagation of an Agulhas Ring, marked with a black circle near its core, crosses the GoodHope cruise track (dashed line), at approximately 40°S.

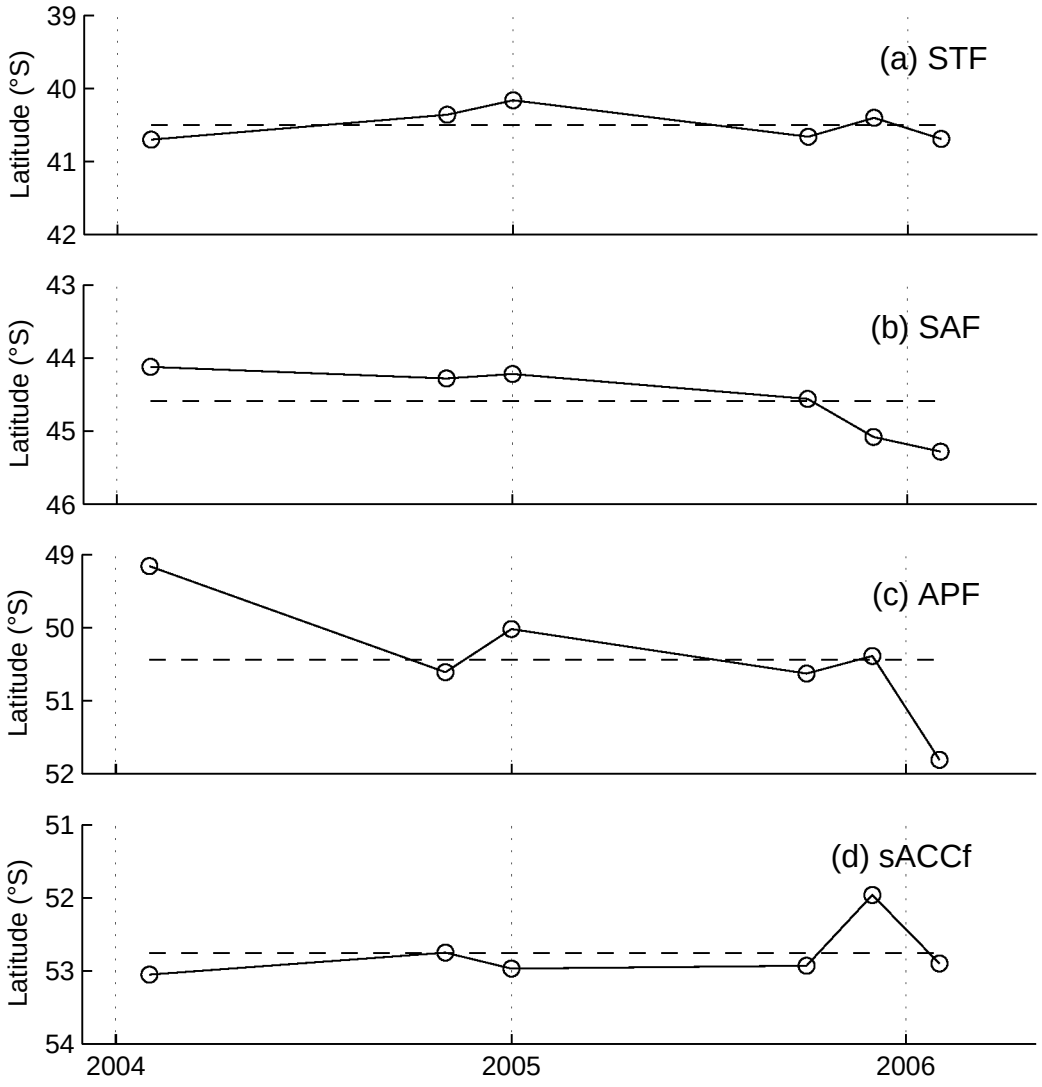

Figure 2.6: Latitudes of the (a) STF, (b) SAF, (c) APF, (d) sACCf for the Africa to Antarctica transects completed between 2004-2006. The dashed line depicts the mean frontal position for six transects.

summer months. This is suggested by the temperature anomaly sections for each of the XBT realizations (Figure 2.7). The three sections, between October 2005 and February 2006, shows that the temperature anomaly, in the upper 150-200 m layer, adjusts from <-1°C to >1°C. Taking the latitudes of the SAF and APF for two February months (2004 and 2006), a southward movement in these two fronts is evident and corresponds to a warmer upper ocean state. The comparison is only made over two years, so it is likely that this large southward shift in the fronts is part of the short-term variability experienced in the region. In order to understand how much of this southward movement forms part of long-term southward trend, we will need a greater ensemble of data. Nonetheless, it is important to note that *Gille* (2002) has analysed temperature data from Lagrangian floating platforms to show that the Southern Ocean, and in particular the ACC, has warmed by 0.17°C since the 1950s. A possible explanation is the 50 km southward shift in the ACC. More recently, *Cai* (2006) has shown a trend in the positive wind stress curl (1978 and onward from NCEP/NCAR reanalysis), induced by Antarctic ozone depletion. This trend drives an intensifying, southward shifting of the Southern Ocean super-gyre circulation (*Speich et al.*, 2002; 2007). It is suggested that the trend in winds and related ocean circulation leads to a greater influx of warm water to the south in all three oceans, and contributes to an increased rate of warming in the polar region. This may explain the southward shift in the ACC fronts as observed over a short period here, and over a longer period, as observed by *Gille* (2002).

2.4 Dynamic heights from XBT data

Rintoul et al. (1997) have shown that a tight correlation exists between the average upper ocean temperature and dynamic height south of Australia. This suggests that, across the ACC, the T-S curve is stable enough to estimate dynamic heights using temperature data alone. In the present study we show that this correlation exists also in the ACC region south of Africa ($r = 0.95$, significant at the 95% level). This relationship proves to be extremely useful because XBT data, which is limited to only the upper 800 m, can be used to derive dynamic heights at the surface. To test this relationship, several average temperatures within pressure ranges were assessed (e.g. 100-200 dbar, 300-400 dbar, 100-600 dbar, 600-700 dbar and 0-600 dbar). The strongest correlation exists when utilizing the average temperature between 0-600 dbar and the dynamic height at the surface (relative to 2500 dbar). Moreover, the 0-600 dbar level was best suited to maximise the data available, instead of extending the level to 700 or 800 dbar. Figure 2.8 shows the empirical relationship between the temperature averaged between 0-600 dbar and the dynamic height at the sea surface, relative to 2500 dbar, using data from the six CTD sections completed in the Atlantic sector south of Africa (see Figure 2.2). Four of these CTD sections were used because they were sampled in adjacent areas of the GoodHope transect, while the remaining two CTD sections were occupied along the GoodHope transect. The fact that the sections are not sampled in precisely the same location has no significant impact on deriving dynamic height using these proxy methods. This is because the upper ocean average temperature is a proxy for a streamline of the ACC and we assume that conservation in the streamline will occur to some extent upstream and downstream of the GoodHope transect.

Although the CTD sections were occupied in different seasons, the data collapse onto a single curve, confirming that this relationship is stable for this region of the Southern Ocean. The shape of the curve, between approximately 4-7°C, generally reflects the meridional variation of temperature from ˜46°S to 42°S. The drop in dynamic height below 4°C results in a steep dynamic height gradient, which is caused primarily by the southward increase in upper ocean salinity (34.3 to 34.7) and fall in meridional ocean temperature between 46°S and 55°S. The larger scatter

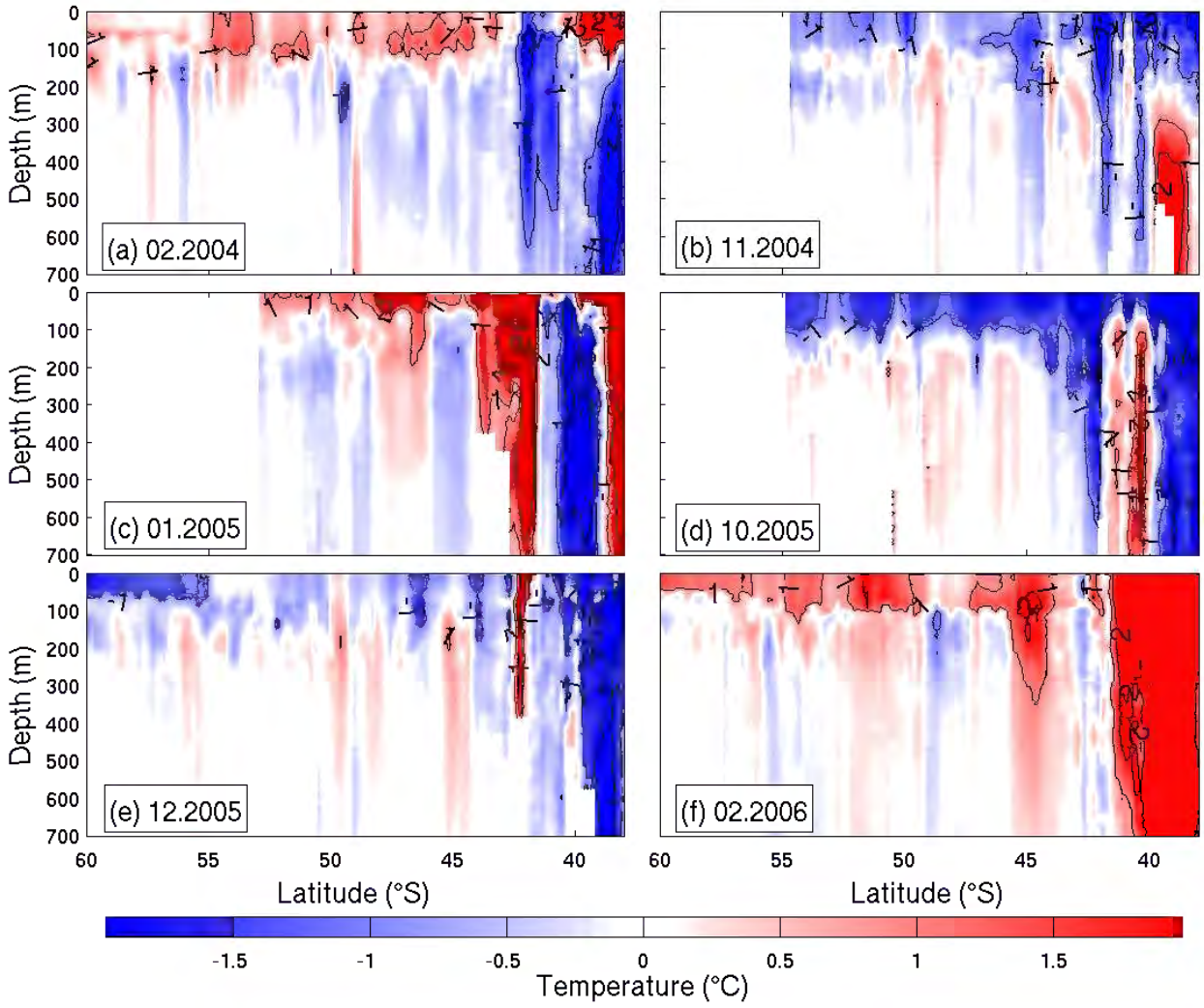

Figure 2.7: Temperature anomaly sections for the following transects: (a) GoodHope 1: February 2004, (b) GoodHope 2: November 2004, (c) GoodHope 3: January 2005, (d) GoodHope 4: October 2005, (e) GoodHope 5: December 2005, (f) Antarctica-Cape Town (AA-CT): February 2006.

of points, where temperatures exceed 7°C, is due to the influence of Agulhas Water introduced by Agulhas Rings north of the STF. The mean dynamic height decline across the ACC for the six CTD sections is 1.1 ± 0.06 dyn m (1 dyn m = 10 $m^2.s^{-2}$). The northern and southern boundaries of the ACC are taken as the position of the STF and southern boundary (SBdy), respectively (from *Orsi et al.*, 1995).

We plot the average ocean temperature, between 0-600 dbar (T_{0-600}), from the 18 available XBT sections, to investigate their latitudinal dependence (Figure 2.9). The data points fall on a relatively tight curve over the ACC, but diverge at the northern and southern ends. North of the ACC domain (∼40°S), the presence of a highly energetic field of anticyclonic and cyclonic eddies largely originating from the Agulhas Retroflection area (as already mentioned in Section 2.3), allows for a zonal and meridional exchange of Atlantic, Indian and Southern Ocean water masses. The upper ocean thermal structure in this region is thereby variable, causing the upper ocean temperature range to spread significantly. The SBdy marks the frontier separating waters flowing in the ACC from those found in the cyclonic sub polar Weddell Gyre. Poleward of the SBdy, the gradient in dynamic height tends to zero. Two XBT sections ($IX3_1$ and $IX3_2$) cross the Maud Rise, located at 65°S, 3°E. The upper ocean average temperatures are higher than sections located further away from the Maud Rise (see Figure 2.9). *Gordon and Huber* (1995) note that a quasi-stationary pool of relatively warm Weddell Deep Water (WDW) appears immediately west of the Maud Rise. This feature is derived from the flow of warm WDW around the flanks of Maud Rise. The rise in upper ocean temperature identified in the XBT data, over the Maud Rise, has a direct influence on overestimating the dynamic height data later on. This overestimate, however, does not have any bearing on the dynamic heights estimated over the ACC.

In order to estimate dynamic height from the available XBT sections, we exploit the empirical correlation, shown in Figure 2.8, by applying a smoothing spline to the data. Fifth and eighth order polynomial fits were also tested and applied to the data. However, the smoothing spline provides a better method for the approximation of values for this dataset. In recent years, it has been generally accepted (*Emery and Thomson*, 2001) that the smoothing spline is the most effective approximation method.

To assess the ability of this method to infer dynamic height from XBT temperature data, we first compare the actual dynamic height, relative to 2500 dbar, to the estimates predicted by the regression relationship for the six available CTD transects. In order to avoid bias, we withhold each of the six CTD section's dynamic height values from the empirical relationship, before predicting the dynamic height using the temperature observations. The results and corresponding root mean square difference (RMSD) over the ACC domain are shown in Figure 2.10. The mean of the RMSD for the six CTD sections is 0.05 dyn m. The agreement between the two estimates is excellent and the RMSDs are small. Discrepancies between the two estimates are largest near the northern and southern boundaries of the ACC, where the empirical relationship is less tight. This is likely due to the mixing of different water masses found at the boundaries and where the spread of upper ocean temperature increases (as shown in Figure 2.9). Due to the higher spatial resolution of the two CTD sections (∼50 km), occupied along the GoodHope cruise track, mesoscale features are better resolved, causing the dynamic height data to vary more than found in the remaining four CTD sections, that have lower spatial resolutions. The ACC fronts, especially the SAF and APF are well represented in the dynamic height gradients.

Dynamic heights are now estimated from the 18 XBT sections using the empirical relationship. These estimates have a marked latitudinal dependence, particularly within the ACC domain, and compare closely with true dynamic heights from the CTD sections (Figure 2.11). Once again, the values north of the STF exhibit a large dispersion due to the large temperature range in the upper ocean associated with this region. For the purpose of this study,

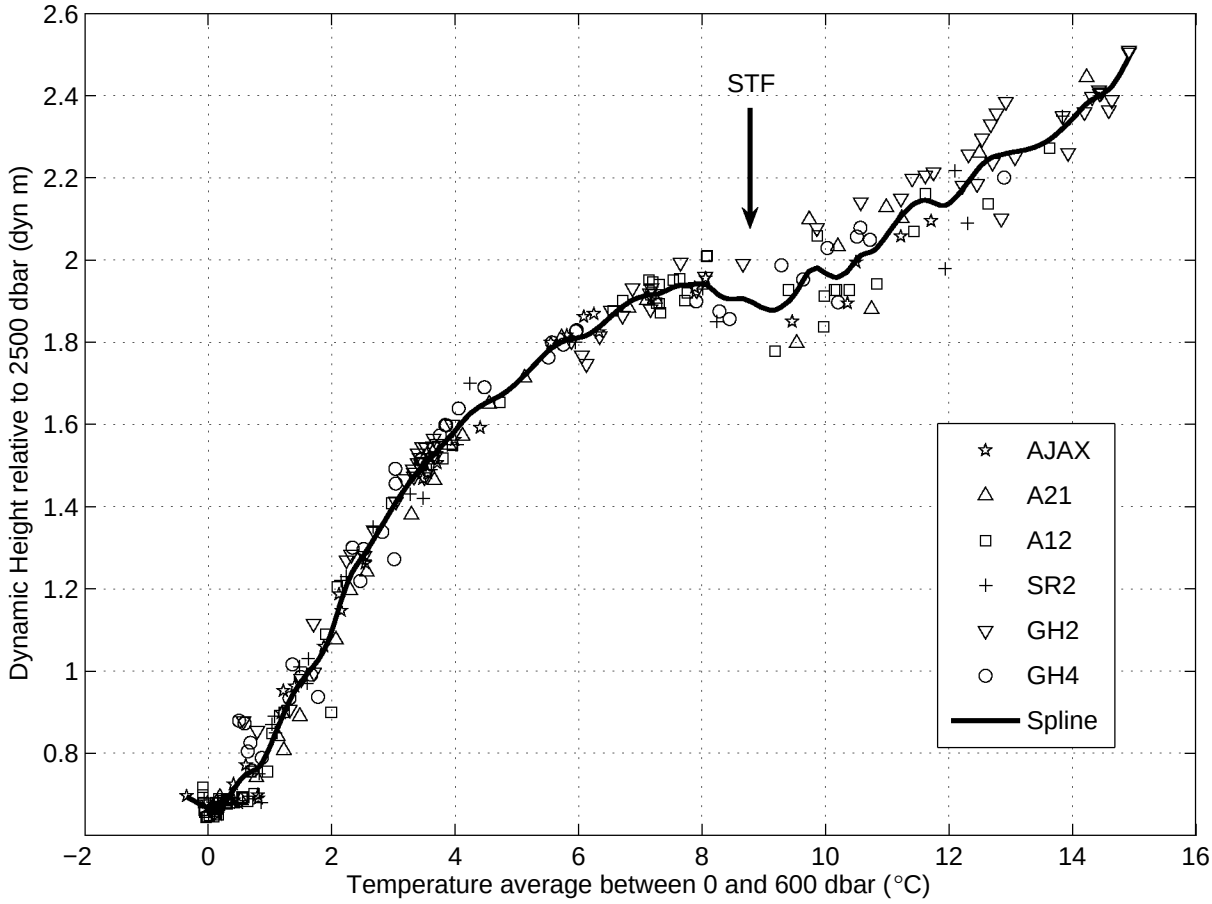

Figure 2.8: Dynamic height at the surface, relative to 2500 dbar, versus temperature averaged between the surface and 600 dbar. Data comes from six CTD transects completed in the south Atlantic: AJAX (stars), A21 (triangles), A12 (squares), SR2 (crosses), GH2 (down triangles), GH4 (circles). The solid curve depicts a smoothing spline fit to the data.

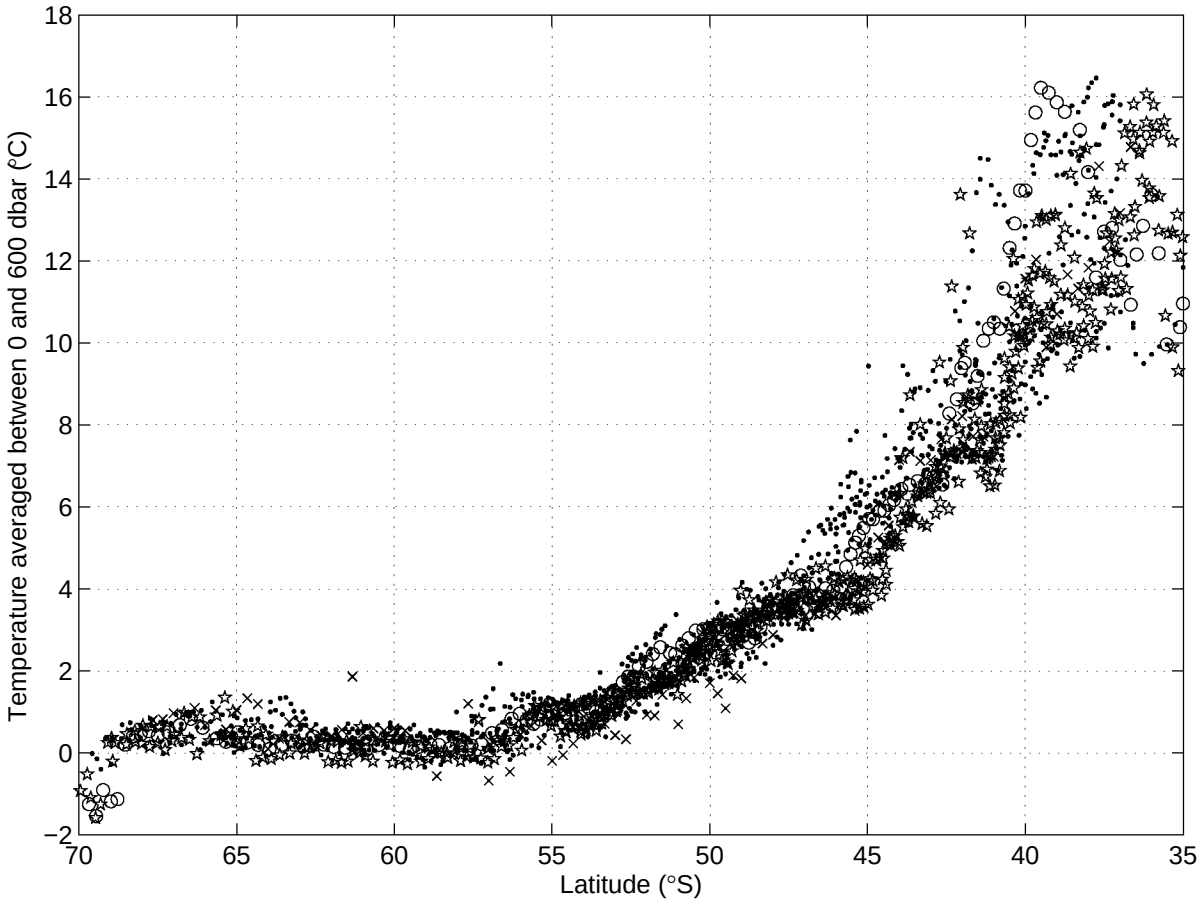

Figure 2.9: Average temperature, between 0 and 600 dbar, versus latitude for 18 XBT sections, completed in the South-East Atlantic. Data comes from repeat GoodHope sections (stars), AA-CT section (circles), AWI sections (dots) and an AARI section (crosses).

we focus specifically on the ACC, i.e. on the domain between the STF and the currents southern boundary, where the empirical relationship is particularly stable.

We illustrate the dynamic height estimates for the five GoodHope repeat XBT transects in Figure 2.12. The mean net dynamic height drop from the northern to the southern boundary of the ACC for the five XBT sections is 1.1 ± 0.065 dyn m, which is the same as the mean CTD dynamic height drop off. The range of the dynamic height drop across the ACC is between 1.01 dyn m in February 2004 to 1.20 dyn m in November 2004. This indicates a range of 0.19 dyn m variability over the ACC. The three inner frontal (SAF, APF and sACCf) positions are marked along the dynamic height profiles. Local maxima in the dynamic height gradient can be seen over the SAF, during the GH2 (November 2004) and GH3 (January 2005) transects. The dynamic height drop across the APF and sACCf is well reproduced during all the transects. The rise and fall in the dynamic height, between the STF and SAF, is mostly induced by the presence of mesoscale eddies (i.e. Agulhas Rings) that were crossed during the first and third GoodHope transects. In addition to the maximum gradient in the dynamic height over the identified 'classical' fronts, we see further drops in the dynamic height. These are mostly associated with the APF and suggest that the 'classical' ACC fronts could be associated with additional baroclinic jets as suggested by *Sokolov and Rintoul* (2007a) south of Australia. The identification of these additional jets is explained, in more detail, in Section 2.7.

The evidence shown here indicates that we can determine the Southern Ocean frontal positions where large gradients in dynamic heights are encountered. This suggests the position of the fronts can be determined from gradients of satellite SSH.

2.5 Baroclinic transports from XBT data

In order to derive baroclinic transports of the ACC from temperature data alone, we derive a second empirical relationship between dynamic height, relative to 2500 dbar (DH_{2500}), and cumulative baroclinic transport, integrated northward and above the 2500 dbar isobath (CT_{2500}) (Figure 2.13). This relationship is constructed using data from five of the CTD transects completed in the South-East Atlantic. We did not make use of the baroclinic transport data from the SR2 section, since a large proportion of the stations did not reach 2500 dbar. This method has been used to derive baroclinic transports from altimeter data for the region south of Australia (*Rintoul et al.*, 2002). Similarly to *Rintoul et al.* (2002), we use 2500 dbar as the reference level because it is the deepest depth that lies above the height of the mid-ocean ridge. The correlation between the two variables is very tight ($r = 0.98$, significant at the 95% level), meaning we can estimate baroclinic transports using dynamic height data. Again a smoothing spline is applied to the data.

We evaluate the accuracy of inferring baroclinic transports from upper ocean temperature data. The empirically derived dynamic heights for the CTD sections were first computed using upper ocean temperature data by exploiting the $T_{0-600} - DH_{2500}$ relationship and then applying it to the $DH_{2500} - CT_{2500}$ relationship to derive baroclinic transports. These transports were then compared to baroclinic transport estimates derived from the five CTD sections, relative to 2500 dbar. Resulting baroclinic transports and RMSDs are shown in Figure 2.14. The mean RMSD for the five tested sections is 6.0 Sv (1 Sv = 10^6 $m^3.s^{-1}$). This RMS error between baroclinic transports is relatively high, however, the total end transports, cumulated from south to north, compare well. The mean baroclinic transport for the five sections is 87.9 ± 3.9 Sv compared with $DH_{2500} - CT_{2500}$ derived baroclinic transports, which averaged 91.5 ± 1.2 Sv. On average, cumulative baroclinic transport values obtained from the $DH_{2500} - CT_{2500}$ relationship exceed CTD derived baroclinic transports by 3.5 Sv, or only 4% higher.

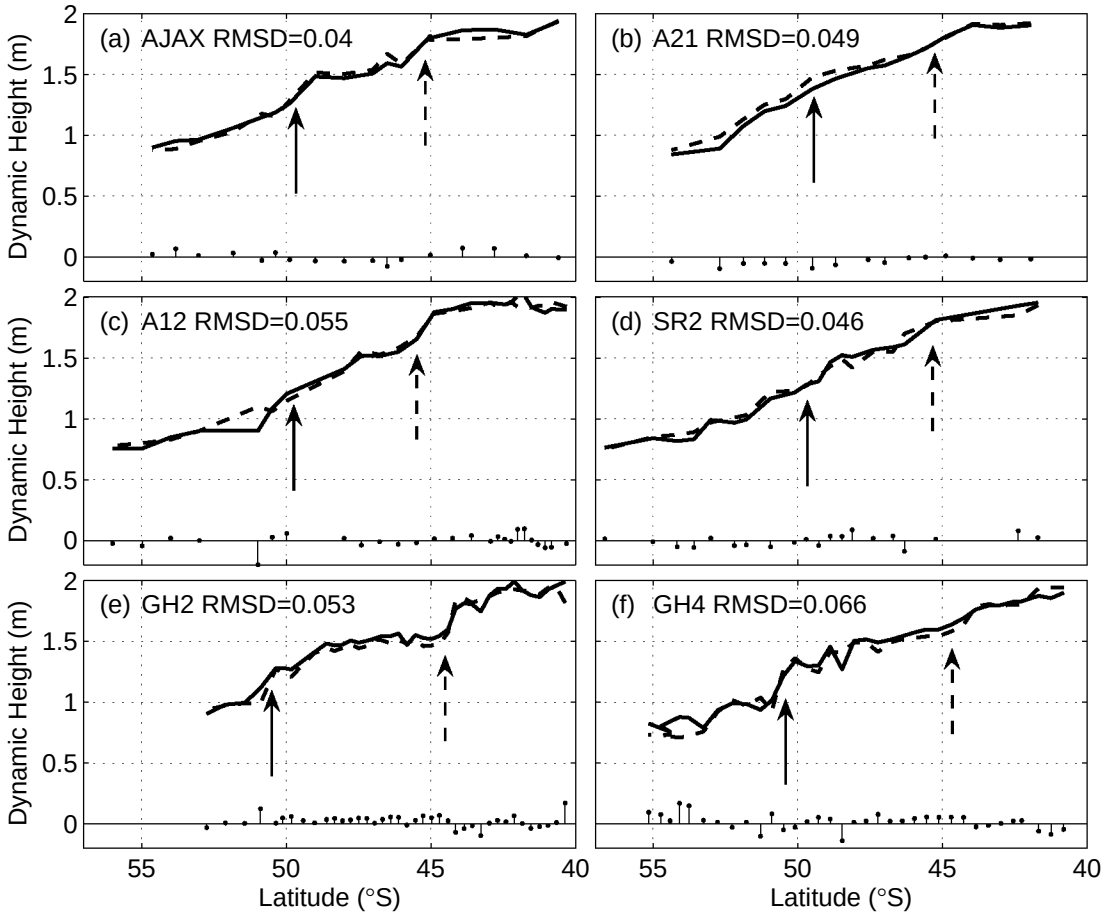

Figure 2.10: Comparison of 'true' dynamic height, above 2500 dbar (solid line), and dynamic height derived from the empirical relationship (dashed line) between upper ocean temperature and dynamic height in Figure 2.8. The dashed and solid arrows represent the positions of the SAF and APF, respectively. Differences between the two dynamic heights are shown along the x-axis. The RMSDs are given in dyn m.

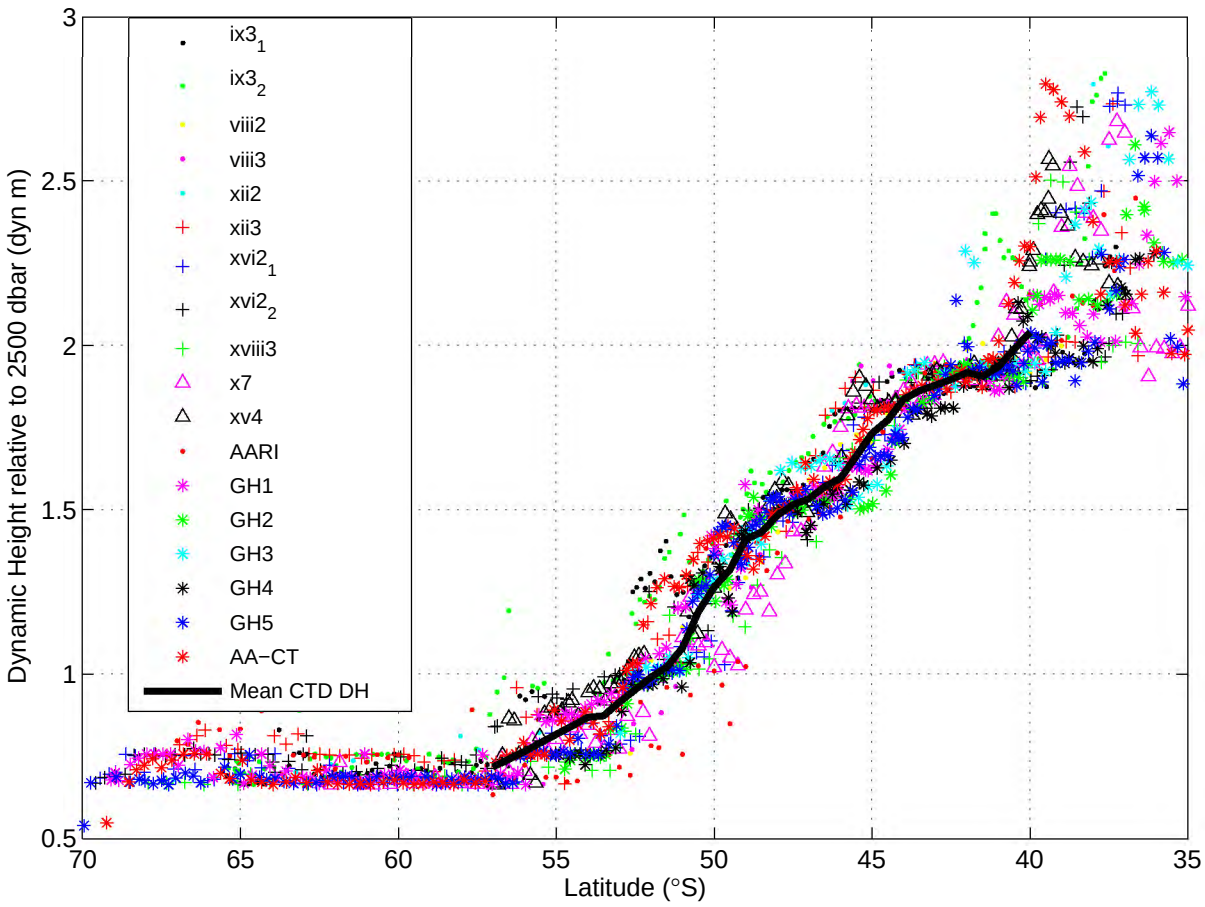

Figure 2.11: Dynamic height at the surface, relative to 2500 dbar, calculated using the empirical relationship in Figure 2.8, versus latitude for 18 XBT sections. The solid line represents the mean dynamic height calculated from temperature and salinity data from the six CTD transects.

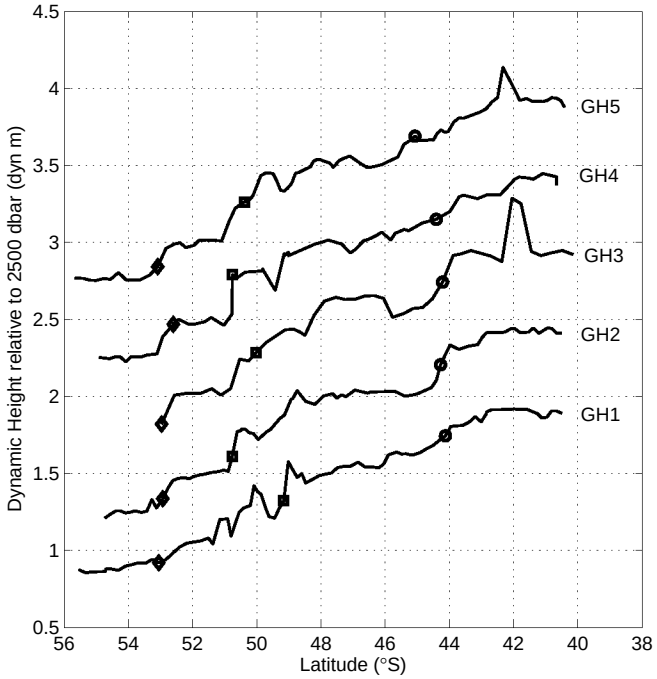

Figure 2.12: Dynamic height at the surface, referenced to 2500 dbar, for five repeat GoodHope XBT sections (2004-2006), estimated using the regression relationship in Figure 2.8. The estimated dynamic heights between sections are offset by 0.5 dyn m for clarity. The offset begins from the first section (GH1). The markers along each profile represent the latitudes (found using the temperature sections) of the SAF (circles), APF (squares) and the sACCf (diamonds).

We apply this proxy method to 18 XBT sections located in close proximity to the CTD transects. Several XBT sections are situated further eastward of the CTD transects. These sections exhibit a poleward shift in the STF in this region causing the average northern ACC limit on the XBT lines to be displaced southward relative to the average value from the CTD transects (41.8°S versus 40.3°S) (*Legeais et al.*, 2005). The XBT-inferred ACC baroclinic transports (above and relative to 2500 dbar; Tr_{2500}) range from 85.2 Sv to 94.7 Sv, with a mean of 90.0 $\pm$ 2.4 Sv. This is only 2.1 Sv (or 2.3%) higher than the 87.9 $\pm$ 3.9 Sv average from the CTD sections. Figure 2.15, shows the baroclinic transport for the five repeat GoodHope sections and the Antarctica-Cape Town (AA-CT) section between February 2004 and February 2006. Differences in baroclinic transport, at each station pair, are represented by the stems. Large increases in net baroclinic transport occur over the main fronts of the ACC. The substantial increase and then decline in baroclinic transport near the northern end of the GH3 section is as a result of the intense Agulhas Ring that was crossed. These baroclinic transport estimates are biased towards the summer months when sampling primarily occurred.

There is no clear inter-annual pattern in net baroclinic transport. The net baroclinic transport does, however, tend to increase during the mid to late summer months when compared to sections completed in the early summer/spring months of the same season. The temperature sections show that the isotherm gradients steepen as the seasonal progression warms the upper ocean layers. This increases the horizontal gradient in the dynamic height, which in turn intensifies the eastward baroclinic flow. The temperature at the southern end of the section is relatively constant with time, and, therefore, an increase in baroclinic transport tends to correspond to the presence

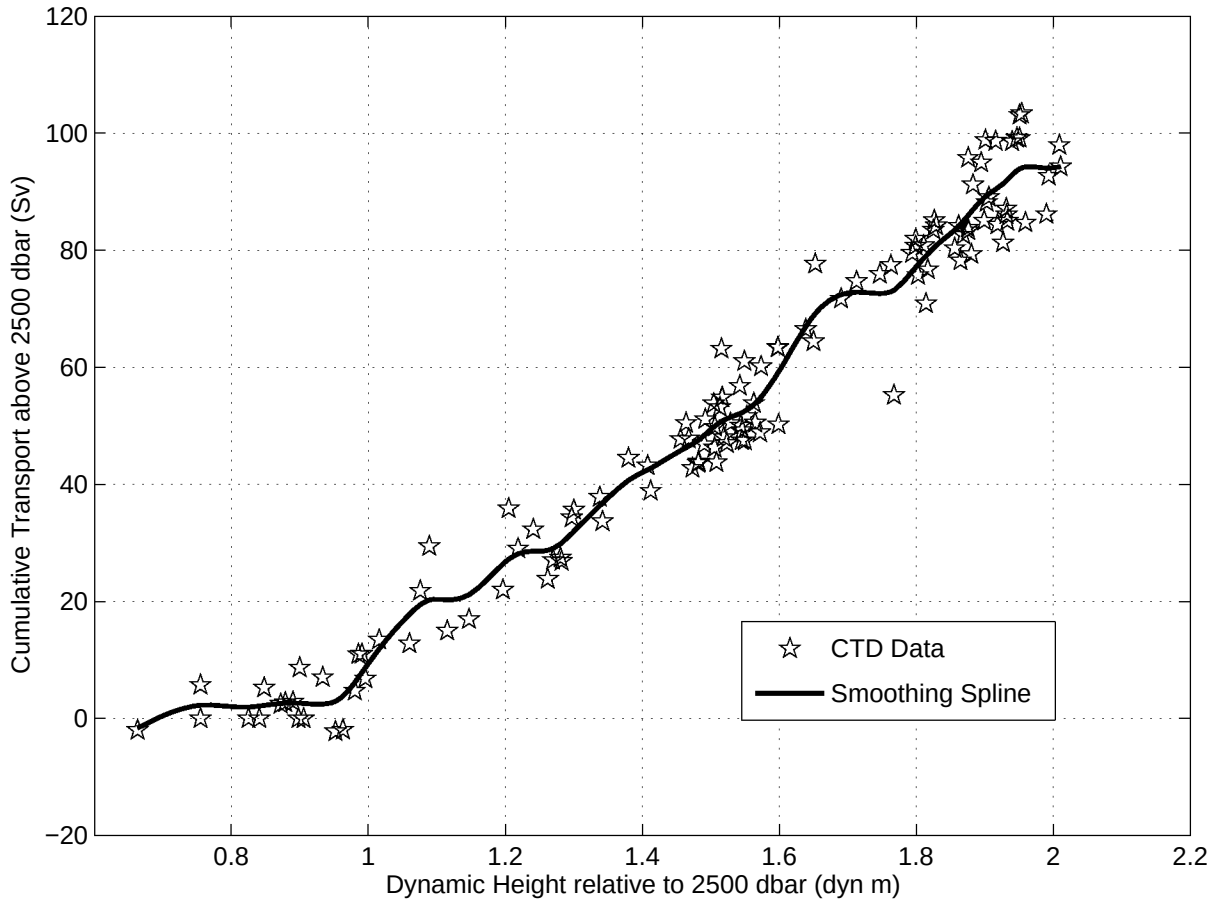

Figure 2.13: Northward baroclinic cumulative transport (above and relative to 2500 dbar) versus dynamic height at the sea surface, relative to 2500 dbar, of five CTD transects completed in the South-East Atlantic (including two occupations of GoodHope). The solid curve depicts a smoothing spline fit to the data.

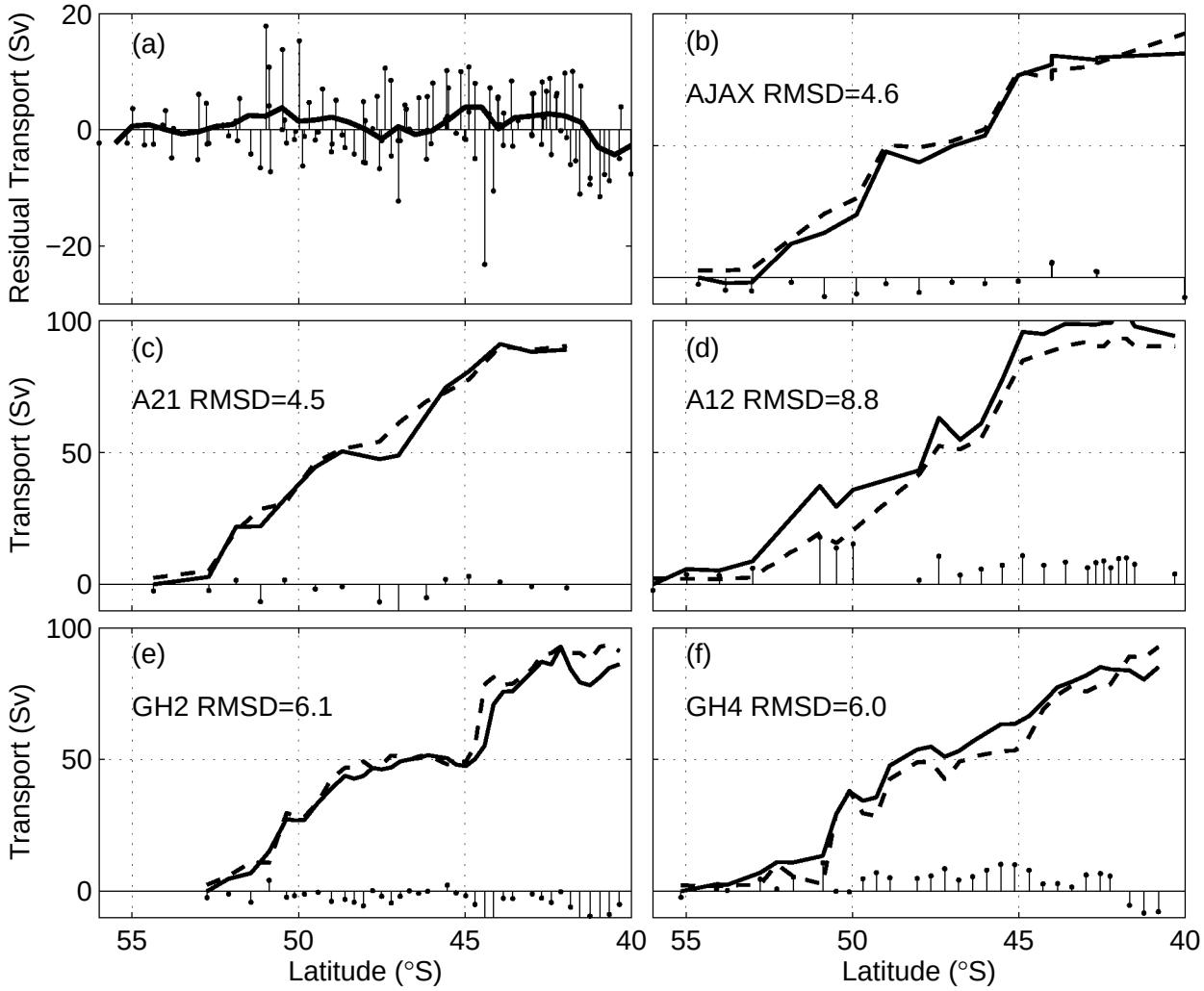

Figure 2.14: Comparison of baroclinic transport, relative to 2500 dbar (solid line), from CTD data, and baroclinic transport, derived from the empirical relationship (dashed line) in Figure 2.13. The comparisons are made from five CTD sections. Differences between the two transports are shown along the x-axis. The RMSDs are given in Sv. The differences between the curves (in Sv) are shown along the x-axis and are summarised in (a). The solid line, in (a), shows the mean residual plotted as a function of latitude.

of higher temperatures (and temperature gradients) in the northern domain of the ACC.

The mean XBT baroclinic transport estimate, made here, is 7.5 Sv lower than that measured by *Legeais et al.* (2005). Our empirical relationships are constructed, partially, using the South-East Atlantic historic CTD sections used by *Legeais et al.* (2005), however, we include two additional recent repeat CTD sections conducted along the GoodHope cruise track. The historic CTD sections are occupied at a lower spatial resolution and are not located along the GoodHope cruise track, which may, in part, be the cause of the final transport disparity. The GoodHope CTD sections do display net baroclinic transport estimates that are ∼4 Sv less than the historic CTD estimates. Additionally, thermal changes in the upper ocean layers, incurred during the temporal gap (9-18 years) between the recent and the historic CTD occupations, may lead to the transport differences between the two studies.

The average of the bottom referenced transport for four CTD sections is 145.0 ± 9.4 Sv. Due to the fact that CTD casts did not reach the bottom in the majority of the stations comprising the second CTD occupation of the GoodHope cruise track, no baroclinic transports relative to the bottom could be obtained for this section. The ratio between the baroclinic transport above 2500 dbar and to the bottom is almost constant and averages approximately 0.62 ± 0.055. This ratio proves to be a useful parameter to estimate the full depth baroclinic transports (Tr_{bottom}) from XBT-inferred transports at 2500 dbar. When applying the 62% Tr_{2500}/Tr_{2500} ratio, the bottom XBT-inferred ACC baroclinic transport ranges between 139 and 153 Sv, with a mean of 145 ± 3.9 Sv, for the 18 XBT crossings. These estimates agree with those obtained by *Legeais et al.* (2005), who use the I6 CTD section conducted along 30°E, in addition to the three historic CTD sections conducted in the South-East Atlantic, to derive bottom referenced transports form XBT data. This ratio has also been observed in other regions of the ACC. Along the SR1 transect in Drake Passage the ratio is found to be 67.6 ± 1.3% (*Sokolov et al.*, 2004) for four CTD occupations or 0.60 ± 0.02 for six CTD occupations (A. C. Naviera Garabato, personal communication). In a study by *Rintoul et al.* (2002) the ratio is 65.8 ± 2.1% for six CTD occupations of the SR3 transect south of Tasmania.

2.6 Meridional baroclinic transport distribution

We now present results on the distribution of baroclinic transport over the meridional extent of the GoodHope section and show the contribution of transport within each frontal domain. The latitudinal distribution of the across section cumulated baroclinic transport for each repeat XBT section is shown in Figure 2.16. It is evident that throughout the sections there are anomalous periods of westward flow over small spatial ranges. The most prominent of these westward flows are located at the northern end and can be attributed to Agulhas Rings (refer to Section 2.3). This occurs during the third and fifth GoodHope transects, where eddies were identified in the temperature sections (refer to Figure 2.4). The most prominent of these was crossed during the third GoodHope transect and which produces large opposing baroclinic transports of 34 Sv westward at 41.5°S and 46 Sv eastward at 42°S. The magnitude of these transports supports the view that this feature is an Agulhas Ring, which has invaded the northern part of the ACC. Similar transport features have been recorded by surface drifters and subsurface floats (at approximately 800 m depth) in the region of 41°S (*Richardson*, 2007).

The mean baroclinic transport, for five GoodHope XBT transects, has been divided into half a degree latitudinal bands over the ACC extent (Figure 2.17a). Again, it is evident that the mean flow at the northern end of the section (north of 42°S) is found to have a strong mean westward flow. The mean westward flow north of 42°S is 6.1 Sv. Two broad peaks of eastward baroclinic transport are found between the latitudinal ranges of the SAF and APF

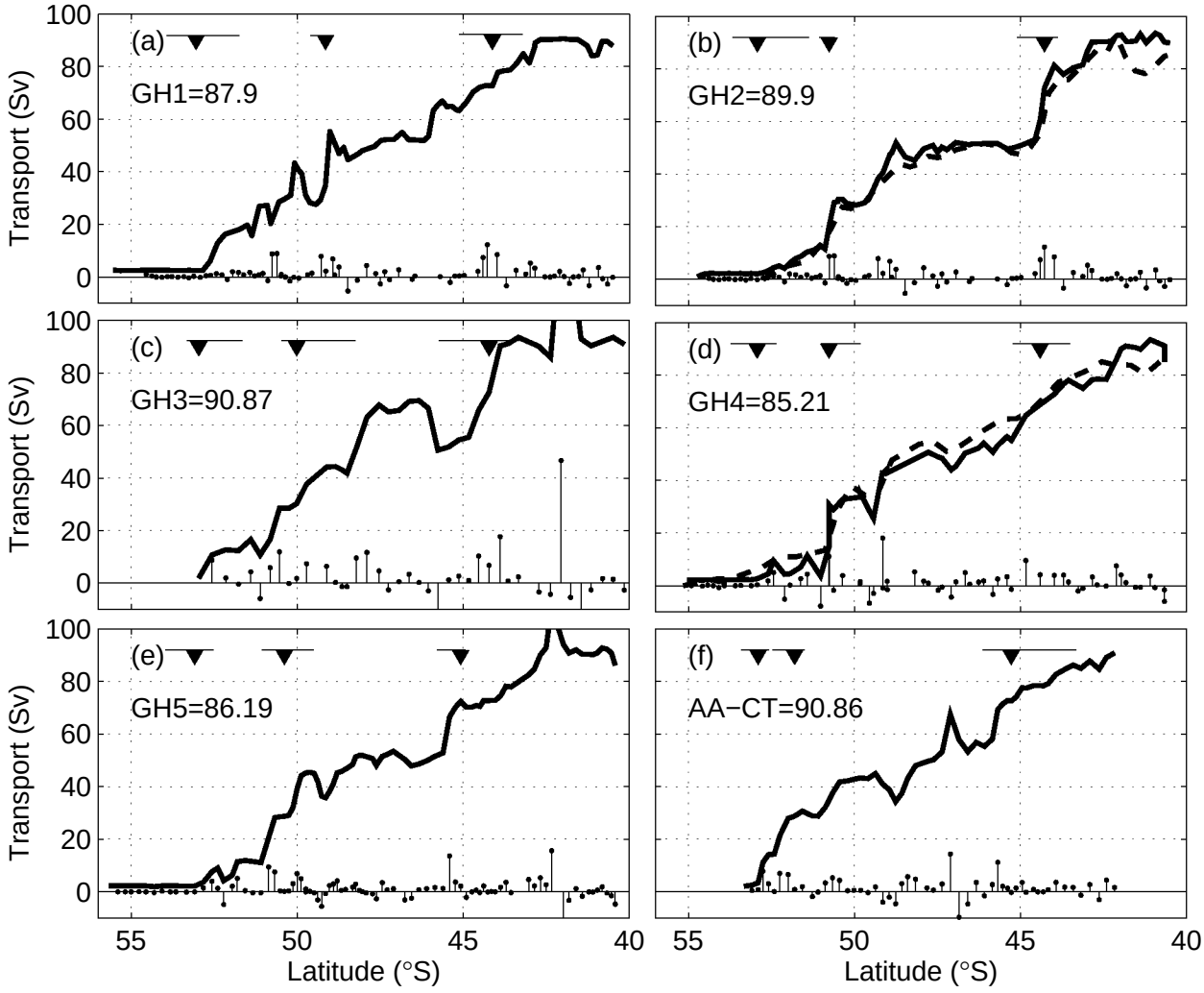

Figure 2.15: Northward cumulative baroclinic transport (referenced to 2500 dbar) for five repeat GoodHope XBT transects and the AA-CT section (bold line). The equivalent geostrophic transports from the CTD sections are shown for GoodHope 2 and 4 (dashed line). Differences in transport at each station pair are shown along the x-axis. The net cumulative baroclinic transport (in Sv) is given next to each section label. The positions of the three inner ACC fronts, determined from the temperature sections, are represented by the arrows (from south to north: sACCf, APF, SAF). The transport integration limits for each of these fronts is represented by the bar, placed above each arrow.

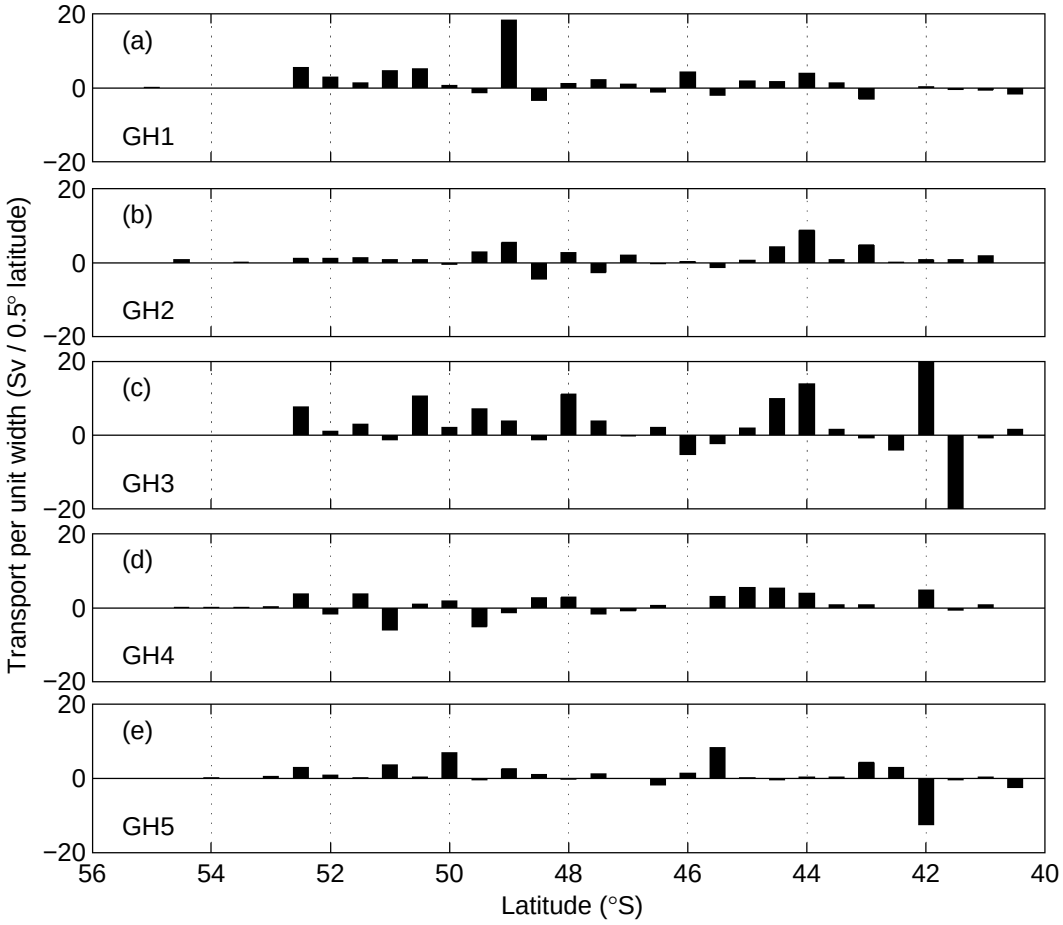

Figure 2.16: Baroclinic transport across the GoodHope sections per half degree latitude for five repeat occupations of GoodHope. Eastward flow is positive.

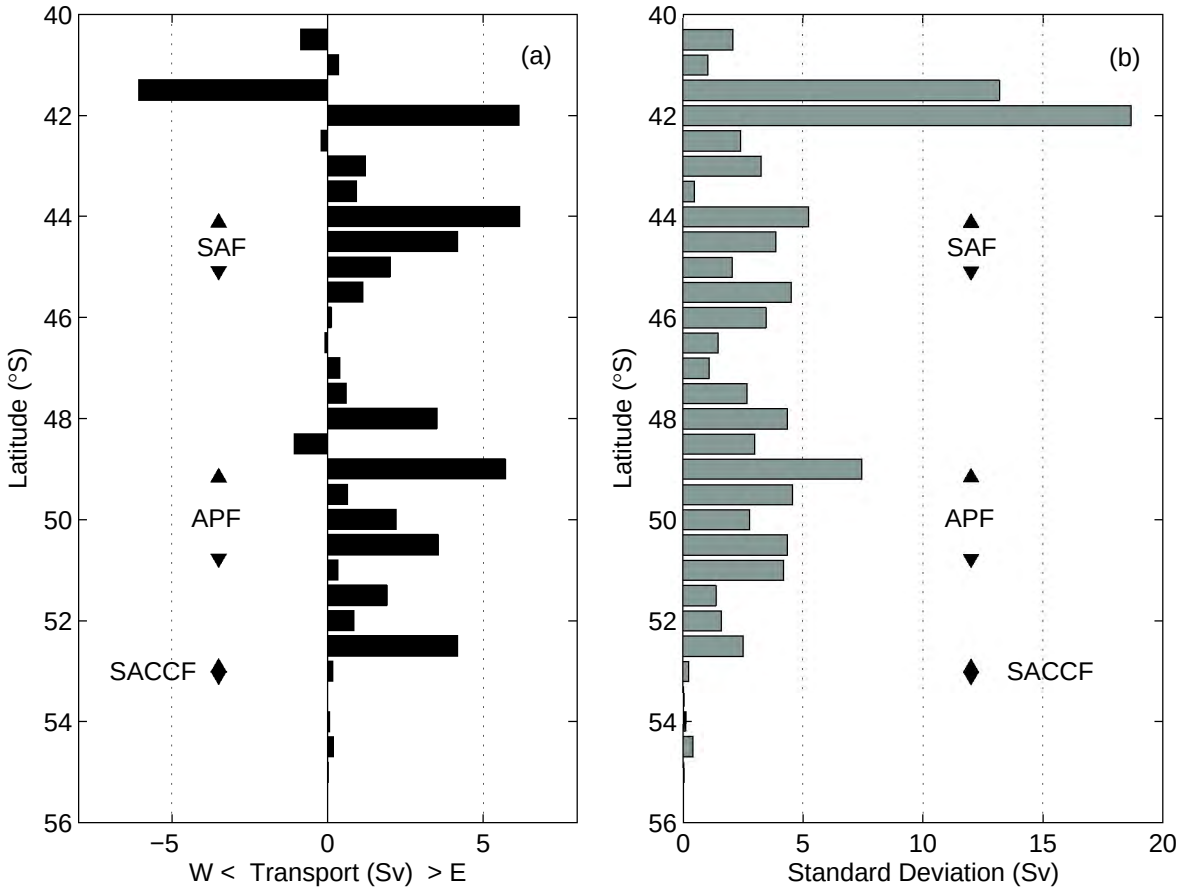

Figure 2.17: (a) Mean baroclinic transport, relative to 2500 dbar, per half degree latitude for five occupations of GoodHope. Eastward flow is positive. (b) The standard deviation of cumulative baroclinic transport for the half degree latitude bands is given. The arrows indicate the latitudinal range of the three inner ACC hydrographic fronts (SAF, APF sACCf), during five repeat GoodHope occupations.

(arrow ranges in Figure 2.17). The local maximum in eastward flow at the 52.5°S band is associated with the sACCf. There is little mean additional eastward baroclinic flow (<1 Sv) south of the sACCf and at the SBdy.

The meridional distribution of variability in the baroclinic transport (Figure 2.17b) is the highest in the region north of ∼42.5°S due to the east-west fluctuations in flow associated with the meandering STF and intruding Agulhas eddies. In this region, the standard deviation exceeds 12 Sv. Large standard deviations are also found over the SAF, SAZ and the APF and may reflect either meridional shifts in the frontal positions, changes in current strength, and/or eddy genesis and activity. This was similarly shown to be the case along the SR3 and SURVOSTRAL sections completed south of Tasmania (*Rintoul et al.*, 2002). South of 51°S, the variability is, as expected, substantially less (standard deviations less than 3 Sv), where the gradient in dynamic height, over the southern most ACC fronts (sACCf and SBdy), is substantially less than those to the north (SAF and APF), therefore, transport variations in these fronts constitute lower standard deviations.

The baroclinic transports associated with the three inner ACC fronts (SAF, APF and sACCf), and their contribution to the net ACC baroclinic transport are calculated for each GoodHope transect and displayed in Table 2.3. This was done by accumulating the baroclinic transport between the point where the baroclinic transport was

Table 2.3: Mean position of the three inner ACC fronts and associated contribution of each front to the XBT-derived baroclinic transport of the ACC (in Sverdrups and percentage of net ACC baroclinic transport, relative to 2500 dbar).

Front	Mean Position (°S)	Transport (Sv)	% Transport of ACC
SAF	44.6 ± 0.5	28.8 ± 8.8	32.3 ± 9.1
APF	50.4 ± 0.9	24.8 ± 7.4	28.4 ± 9.0
sACCf	52.8 ± 0.4	9.8 ± 5.9	11.1 ± 6.6
Total	-	63.4	72

found to be zero or flowing westward, to the south and north of the axial front position. This allowed us to estimate the baroclinic transport directly related to the position of the front, located using the temperature criteria of *Orsi et al.* (1995). The integration limits are indicated on Figure 2.15 for each of the three inner ACC fronts. The XBT-inferred frontal contributions largely match those deduced from the CTD sections. The contribution from the SAF and sACCf for the XBT-inferred baroclinic transports are 5.4% and 4.5% less, respectively. An overwhelming fraction (72%) of the net ACC baroclinic transport is accounted for by the three inner ACC fronts of which the SAF and APF dominate with a 32% and 28% contribution, respectively. This emphasises the key role the fronts play in determining the total baroclinic transport of the ACC.

Legeais et al. (2005), reveal that the sACCf contributes more to the net ACC transport (21%) than this study shows (11%). *Legeais et al.* (2005), make use of polynomial fits to estimate the baroclinic transport from XBT data. This type of fitting is significantly less precise at following the undulations in dynamic height linked to each front, which may be responsible for over-estimating the contribution made by the sACCf. In addition, the dynamic height gradient from XBT data obtained before 2004 seems to be somewhat greater between 52-55°S, than the most recent XBT data (see Figure 2.11). This would, in part, be responsible for the higher sACCf transport contributions made by *Legeais et al.* (2005).

Both the SAF and APF are primarily responsible for the variability associated with the total transport of the ACC. These two fronts have large baroclinic transport ranges, which exceed 20 Sv (SAF: 21.7-42.9 Sv; APF: 15.9-34.4 Sv), and their standard deviations are 8.8 Sv and 7.4 Sv (or 9%), respectively. The transport contribution of the STF and SBdy constitutes only a small fraction of the total transport, with each front contributing 4.4% and 1.3%, respectively. A large proportion of the remaining 22% of the total baroclinic transport may be accounted for by additional ACC jets, which are not taken into account when using the integration method used in this section. There are instances when a front appears to be separated into two or more branches of flow. The first GoodHope XBT transect provides such an example. The transports associated with the APF seem to be split into two distinct jets. One of these is located over the temperature front (∼49°S) and the other at ˜50°S, with a region of westward flow in-between the two eastward flowing jets. These additional transport jets are discussed in more detail in Section 2.7.

2.7 Baroclinic transports inferred from satellite altimetry data

An aim of this paper is to show that baroclinic transport estimates of the ACC, at a substantially improved temporal resolution, can be achieved. Hydrographic data are collected in the Southern Ocean primarily in the summer months, which creates the risk of aliasing high frequency variability. Annual XBT and CTD 'snapshot' sampling are not frequent enough to resolve the substantial ACC baroclinic transport variability that can be

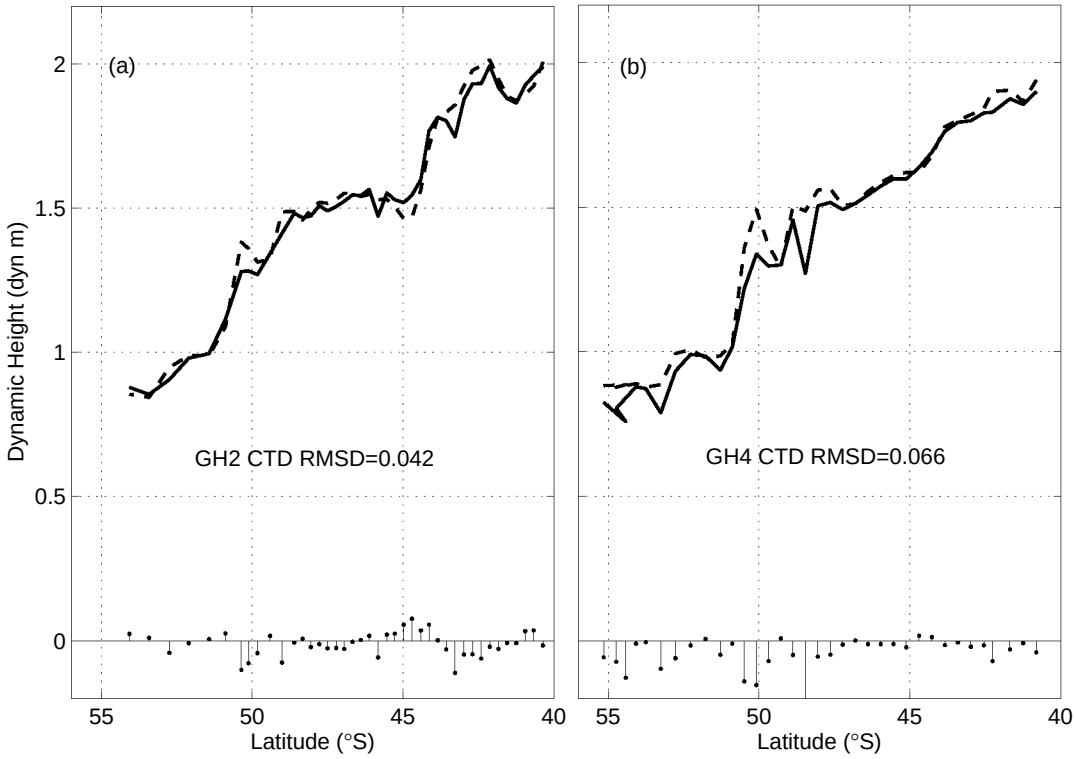

Figure 2.18: Comparison of surface dynamic height, relative to 2500 dbar, from CTD data (solid line) and from the ADT produced using altimetry data (dashed line), for two occupations of the GoodHope cruise track. The differences between the two estimates are shown along the x-axis.

expected at smaller temporal scales. A continuous time series of absolute dynamic topography (ADT), at weekly intervals, between 1992-2007, is created. This is done by adding the altimeter sea level anomalies (multi-mission gridded SSH product from AVISO; see Section 2.2.3.1) to the mean surface dynamic height, relative to 2500 dbar, calculated from two CTD and five repeat GoodHope XBT sections. The gradient of the ADT compares closely with the CTD (Figure 2.18) and XBT dynamic height gradients. The ADT product is somewhat 'smoother' than the hydrographic dynamic heights and in some cases mesoscale features are less well resolved. The hydrographic dynamic height estimates are relative to 2500 dbar and include only the baroclinic signal above this level. The altimeter derived ADT, however, may reflect changes in the density field below 2500 dbar. Differences between the ADT and hydrographic dynamic heights may, therefore, in part originate from the baroclinic field below 2500 dbar, and the barotropic field. Without an accurate estimate of the geoid, we are unable to separate the baroclinic and barotropic components of the satellite altimeter measurements. The differences may also reflect temporal and spatial sampling discrepancies, mapping errors and tides which have not been entirely removed from the altimeter signal, as well as sampling errors incurred in attaining the CTD and XBT data. Similarly, this was the case when SSH anomalies, inferred from CTD and altimeter measurements, were compared south of Australia (*Rintoul et al.*, 2002). Despite these factors, hydrographic estimates of dynamic height and the ADT are very similar (mean RMSD is 0.063 dyn m). This suggests that the ADT largely reflects baroclinic changes in the upper 2500 m of the water column.

Before we attempt to estimate the baroclinic transports from the full time-series of ADT data, we explain the

method of defining the ACC spatial limits and ACC fronts, using satellite altimeter products. Given that the ACC, south of Africa, is unbounded by any continental landmasses, it has an open ocean current structure. This becomes an advantage when estimating baroclinic transports using satellite altimetry products because no flow is omitted that occurs too close to coastal areas where altimeter data becomes unreliable due to tidal errors. This problem was encountered by *Rintoul et al.* (2002) south of Tasmania, where the flow between 45°S and the Tasmanian coast was excluded due to near-coast altimeter limitations.

More recently, high resolution hydrographic and satellite sampling have revealed that the ACC consists of multiple branches or filaments, which merge and split and vary in intensity, along the circumpolar course (*Hughes and Ash*, 2001; *Sokolov and Rintoul*, 2007a; 2007b). Analysis of the altimeter-derived surface velocity magnitude ($\sqrt{(u^2 + v^2)}$) and the MADT along the second GoodHope transect (Figure 2.19a) makes it clear that more than one velocity jet exists per ACC front. The highest gradients in the MADT are, as expected, located over the main velocity jets, identified by the vertical solid grey lines in Figure 2.19a. We supplement this with high resolution *in situ* temperature data (Figure 2.19b) whereby CTD and XBT temperature data are combined to better resolve the finer horizontal thermal gradient found over the velocity jets identified in Figure 2.19a. The high resolution temperature data reveals that the velocity jets, identified in Figure 2.19a, associate closely with regions of strong thermal gradients. This is especially the case with the dominant velocity jets of the SAF and APF. This suggests we can determine the multiple jet structure of the ACC using high resolution temperature sections south of Africa, in addition to that already undertaken in a study south of Australia (*Sokolov and Rintoul*, 2007a). A time series of altimeter-derived surface velocity magnitude and MADT along the GoodHope transect is presented in Figure 2.20. The isolines of MADT (thin black lines) closely follow the surface velocity magnitudes of the main ACC jets (surface colour plot). This means we can, with accuracy, follow specified isolines of MADT to locate the boundaries between each of the ACC fronts, except that of the STF. South of Africa, the STF experiences considerable spatial variability induced by the presence of eddies (see Section 2.3). This provides us with difficulty in defining the northern limit of the ACC using satellite altimeter data when we do not have information of the vertical thermal or salinity structure, provided by *in situ* hydrographic sections. Figure 2.20 confirms that there are no consistent surface velocity jets or isolines of MADT to use to track the limits of the STF, but rather episodic surface velocity maxima consistent with the presence of eddies and front meandering. This forces us to limit the northern domain of the ACC to the northern boundary of the SAF when we use satellite altimeter data alone. The boundaries between each ACC front are overlaid onto the surface velocity magnitude and MADT data, in Figure 2.20, using thick black lines. The isolines of MADT, used to define the front boundaries, are given as follows: northern limit of the SAF = 1.35 dyn m, SAF-APF = 0.94 dyn m, APF-sACCf = 0.31 dyn m, sACCf-SBdy = 0.0 dyn m, southern limit of the SBdy = -0.13 dyn m. The northern limit of the SAF and the limit between the SAF and APF experience the highest latitudinal variability (± 0.79-0.85°), while the limits of the sACCf and the SBdy experience the least latitudinal variability (± 0.35-0.38°). It must be noted that on certain occasions (late 1992, 2000, 2001, 2003 and 2005), the SBdy domain is invaded by sea-ice. During these short periods, we locate the southern limit of the SBdy as the mean location during the 14 year time series of latitudes. The mean position and associated standard deviations can be found in Table 2.4.

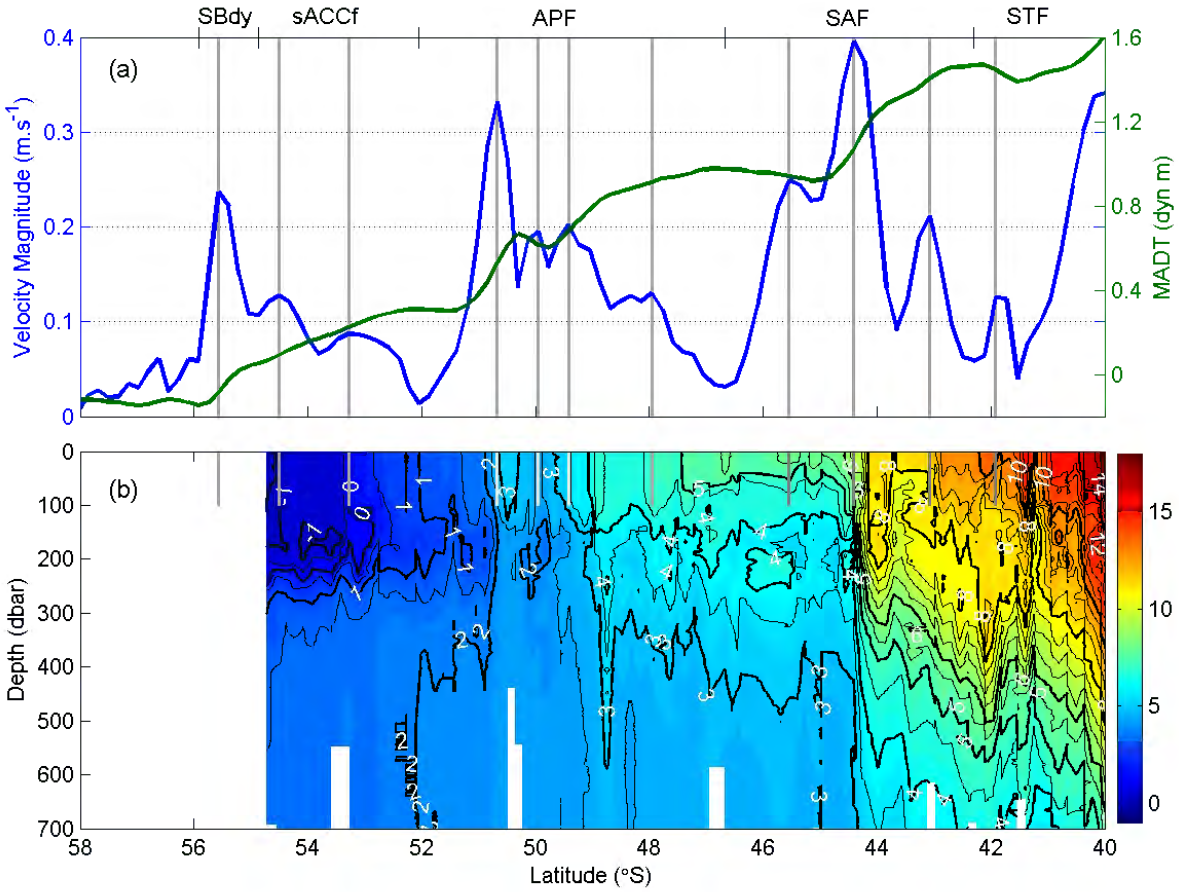

Figure 2.19: (a) Surface velocity magnitudes (solid blue line) and MADT data (solid green line) identify the transport jets (marked with vertical solid grey lines), associated with the ACC fronts. The proposed limits of each front, associated with this example, are indicated on the upper x-axis. (b) High resolution temperature data (combination of CTD and XBT temperature profiles; in °C) obtained during the second GoodHope crossing are used to show the vertical thermal structure associated with the transport jets identified in the upper figure panel.

We use the empirical relationship between dynamic height and cumulative baroclinic transport to estimate the baroclinic transport of the ACC (relative to 2500 dbar) from the ADT data. To test this approach, we compare the baroclinic transport estimated from the ADT data and from five XBT occupations along the GoodHope track (Figure 2.21). Both the transports and the form of the two curves are well reproduced. The accumulation of baroclinic transport over the SAF and APF is particularly well represented. The station pair differences are generally less than 8 Sv but increase over sections that have a low station density. Sections with largely spaced stations cause more abrupt changes in the dynamic height over latitude (specifically the third GoodHope XBT section; Figure 2.21d). The mean RMSD between the two transport estimates is 7.1 Sv and 10.1 Sv for the CTD and XBT sections, respectively. Near the fronts (namely the SAF and APF), the ADT deduced baroclinic transport gradient is greater (i.e. greater transport gains with latitude). This may, in part, reflect the deep structure of fronts, which extend closer to the sea floor than the rest of the ACC regime, and which are responsible for a significant proportion of the ACC's net baroclinic transport (see Section 2.6). Other differences between the ADT and hydrographically derived baroclinic transports may be due to deep baroclinic flow (>2500 dbar), and mapping errors and tides, which have

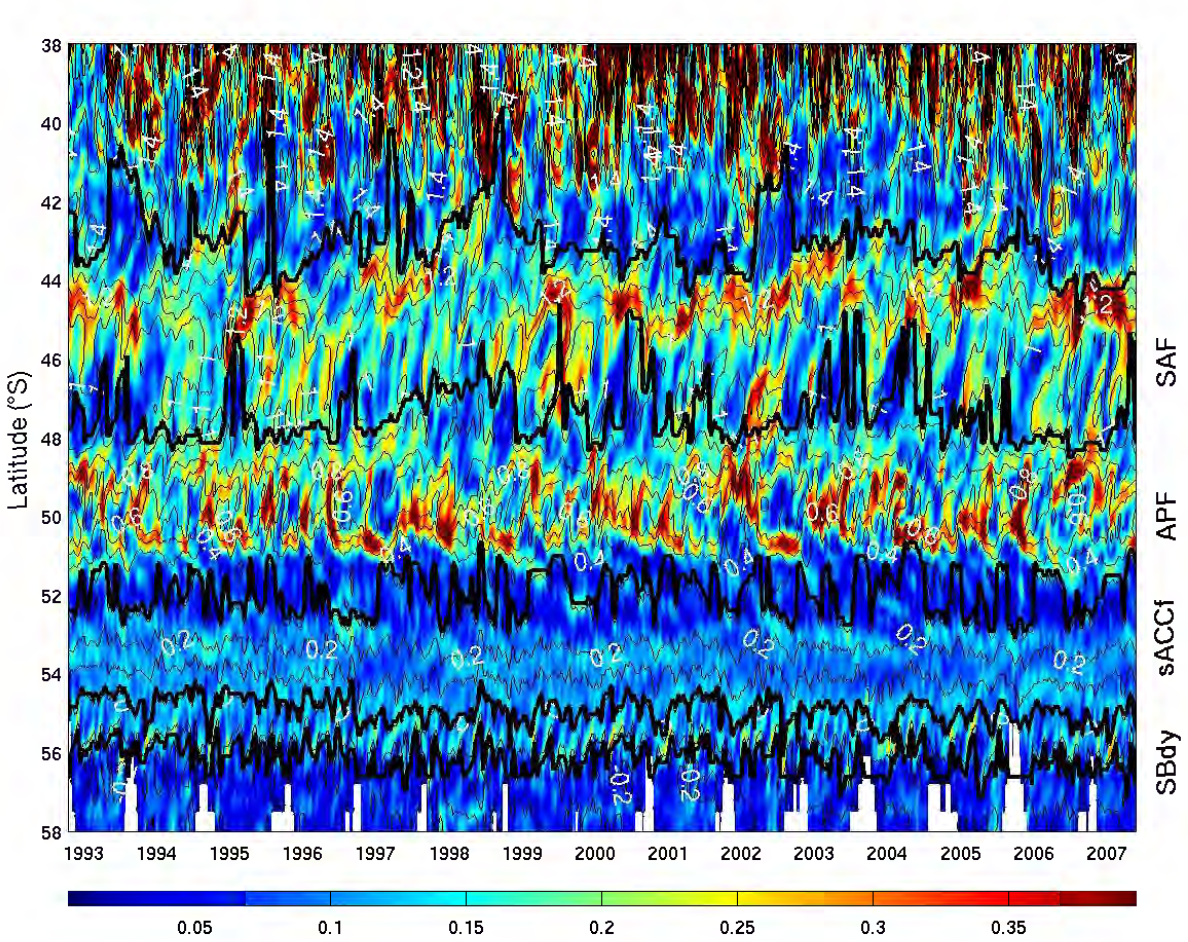

Figure 2.20: Time series of velocity magnitudes (colour surface plot; in $m.s^{-1}$) and MADT (thin black lines; in dyn m) over the GoodHope cruise track. The boundaries between each ACC front (excluding the northern STF) are illustrated using the thick black lines.

Table 2.4: Mean position and standard deviation of the boundaries of each front, as defined using satellite altimetry.

Front Boundary	Mean Position (°S)	Standard Deviation (° latitude)
STF-SAF	43.0	0.85
SAF-APF	47.4	0.79
APF-sACCf	51.9	0.57
sACCf-SBdy	54.9	0.35
southern SBdy	56.2	0.38

not been removed from the altimeter signal. The difference between the two curves may also be attributed to the barotropic component of the flow captured in the altimeter signal and which is reproduced in the ADT product. We are unable to accurately estimate the contribution the deep baroclinic flow, mapping errors and tides have on the dynamic height and transport residuals. We, therefore, are not able to estimate the barotropic component of the transport found in the altimeter signal. In recent times, there has been slow progress made in determining the barotropic flow of the ACC. A significant contribution to determining the absolute transport structure of the ACC will be made once we have the ability to measure the barotropic component in the satellite altimetry data.

2.8 Continuous time series of net ACC baroclinic transport

The ADT is used to estimate a 14 year continuous time-series of baroclinic transport, relative to 2500 dbar, over each front and the whole ACC extent (Figure 2.22; Table 2.5) by exploiting the empirical relationship in Figure 2.13. The baroclinic transports are cumulated for each of the fronts, using the limits defined in Section 2.7, and between the southern limit of the SBdy and the northern limit of SAF for the whole ACC sector. The time series extends, at weekly intervals, between October, 14, 1992 and May, 23, 2007. The combined transport contribution is only 1.8 ± 0.8 Sv for the SBdy and 8.7 ± 2.2 Sv for the sACCf. The SAF and APF are responsible for a much higher mean transport contribution. The SAF and APF contribute 33.3 ± 3.1 Sv and 40.9 ± 2.4 Sv, respectively. The mean baroclinic transport estimate (relative to 2500 dbar) for the ACC is 84.7 ± 3.0 Sv. This is on average 2.8 Sv lower than the mean baroclinic transport estimate inferred from the XBT data. This 'missing' transport can largely be attributed to the fact that we limit the cumulated transports to the northern limit of the SAF and not to the STF, as was done with the hydrographic derived baroclinic transports.

The SAF and APF are characterised by high frequency transport variability when compared to the sACCf and SBdy. The dynamic height gradient over the SAF and APF is considerably larger than the sACCf and SBdy. This means that changes in the dynamic height gradient over the southern most fronts leads to smaller transport variations. Additionally, a portion of the transport variability may be associated with the latitudinal variability of the front limits. The transport contribution by the APF is, on average, 7.6 Sv higher than the SAF. This is in contrast to the frontal contributions made by the XBT-inferred transport estimates. In order to avoid subjectivity, we only associate the transport contribution located either side of the axial front location from the XBT-inferred transports (see Section 2.6). This may, therefore, underestimate the transport contributions for fronts that have multiple transport jets, which seems to be the case for the APF. The SAF, on the other hand, is characterised as having one main core transport jet (and two smaller transport jets), so little transport contribution is missed using the method described in Section 2.6.

The mean latitudinal distribution and standard deviation of the baroclinic transports, between 1992-2007, are represented in Figure 2.23. The SAF contains one distinct transport core located at ∼44°S. Two small transport

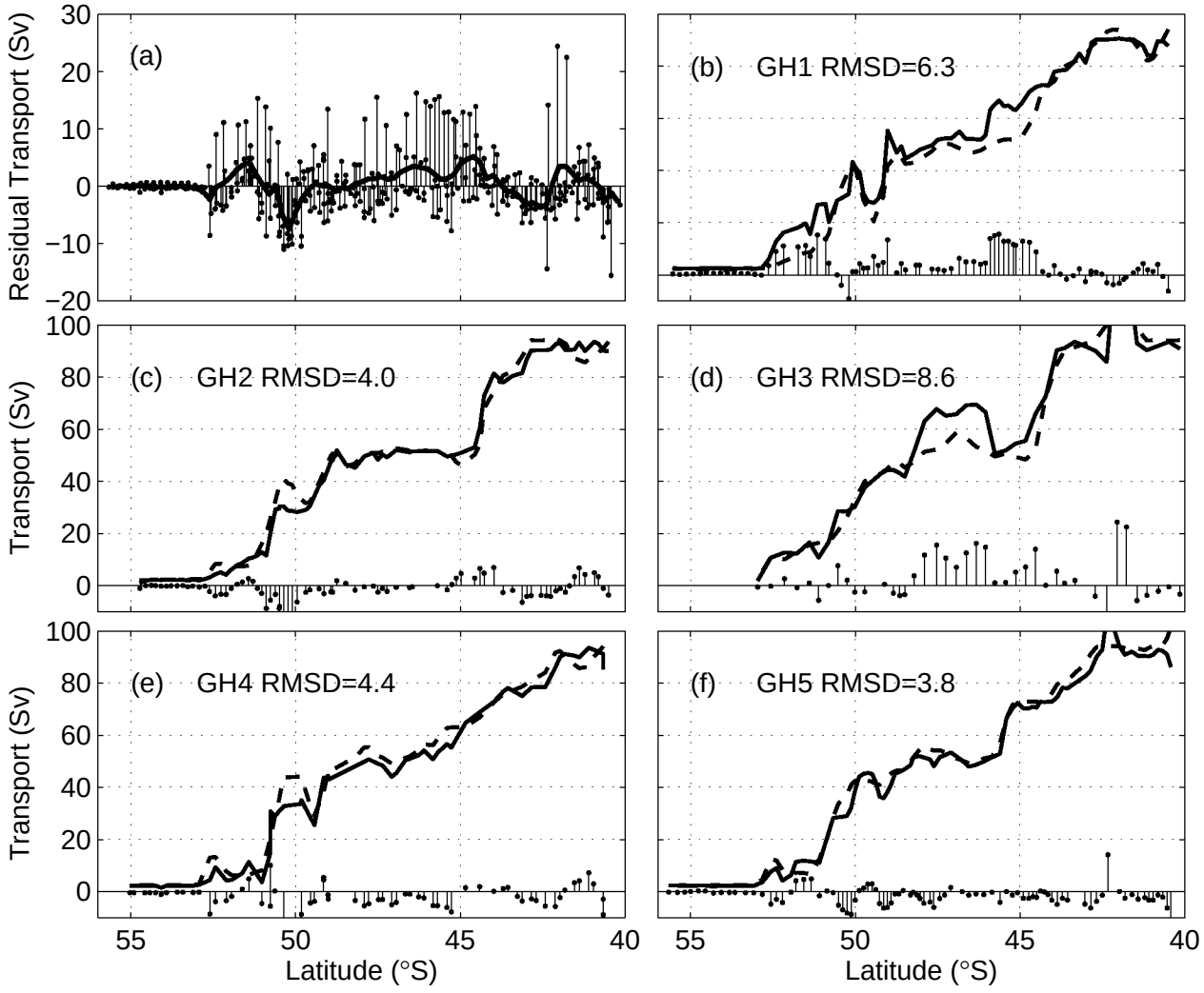

Figure 2.21: Comparison between baroclinic transport estimated from the ADT (dashed line) and from XBT dynamic height data (solid line; b through f), for five occupations of the GoodHope track. The differences between two transport estimates (in Sv) are shown along the x-axis and summarised in (a); the solid line is the mean residual plotted against latitude.

Table 2.5: Mean contribution of baroclinic transport by each front to the net baroclinic transport of the ACC derived from satellite altimetry data (in Sv and percentage, relative to 2500 dbar). The contribution of each front to the net transport standard deviation is given in percent.

Front	Transport (Sv)	% Transport of ACC	% of total standard deviation
SAF	33.3 ± 3.1	39.2 ± 2.5	50.7
APF	40.9 ± 2.4	48.4 ± 3.3	32.7
sACCf	8.7 ± 2.2	10.2 ± 2.6	13.6
SBdy	1.8 ± 0.8	2.2 ± 0.9	3.0

jets can be seen to the north and south of the main jet. These are located at ∼43°S and ∼44.5°S. In contrast, the APF has three distinct transport jets. The most prevalent of these is located at ∼50.8°S, followed by one at ∼49°S, and the smallest jet located at ∼48°S. The sACCf contains two main transport jets, which cores lie at approximately 51.5°S and 52.5°S, respectively. The small transport jet, located at ∼55.5°S, is associated with the SBdy. Periodic occurrences of westerly transport are found at the SAF and APF limit and in between the APF transport jets. This is likely caused by eddy shedding at the front and jet boundaries. The dominant transport standard deviations are found at the main jets of each front, which may reflect the meridional movement and change in current strength of these jets. The highest transport standard deviations, for the region, occur at the SAF. The SAF accounts for over 50% of the latitudinal transport standard deviations of the ACC. This suggests that the transport variations in the SAF are responsible for a large proportion of the spatial baroclinic transport variability related to the ACC. The APF accounts for 33% of the total transport variance per latitude. This means the APF is over 35% more stable than the SAF, when concerning latitudinal transport variability even though the APF has a greater overall baroclinic transport contribution to the ACC. The sACCf and SBdy follow suit with a contribution of 14% and 3% to the total standard deviation, respectively. The front contributions to the net baroclinic transport and standard deviation of the ACC are summarised in Table 2.5.

2.9 Summary

The exploitation of data is extremely important in the Southern Ocean, where it is especially hard to obtain due to its isolation and hostile environment. This study demonstrates how repeat CTD sections allow us to derive proxy techniques to determine the variability of the ACC, using XBT and remotely sensed data alone. These alternative methods are used to make accurate estimates of baroclinic transport with high spatial and temporal resolution.

First, we showed that a close correlation exists between upper ocean temperature and dynamic height. Surface dynamic heights were, therefore, derived from XBT profiles, which compared closely to the 'true' dynamic heights calculated from CTD data. The agreement between the two estimates were excellent and differences were small (mean RMSD <0.05 dyn m). These differences were highest towards the southern and northern end of the sections, where communication between several water masses containing different temperature and salinity signatures, was most extensive. The resulting dynamic heights showed close correspondence with the location of the ACC fronts (where local maxima in gradients were experienced). Additionally, the dynamic height data were accurate at resolving mesoscale features evident in the temperature sections.

A similar empirical relationship between surface dynamic height and cumulative baroclinic transport was used to derive, with minimal error, the baroclinic transport from all available XBT dynamic height profiles. These transports were found only to be, on average, 2.3% higher than the actual geostrophic measurements. The ratio

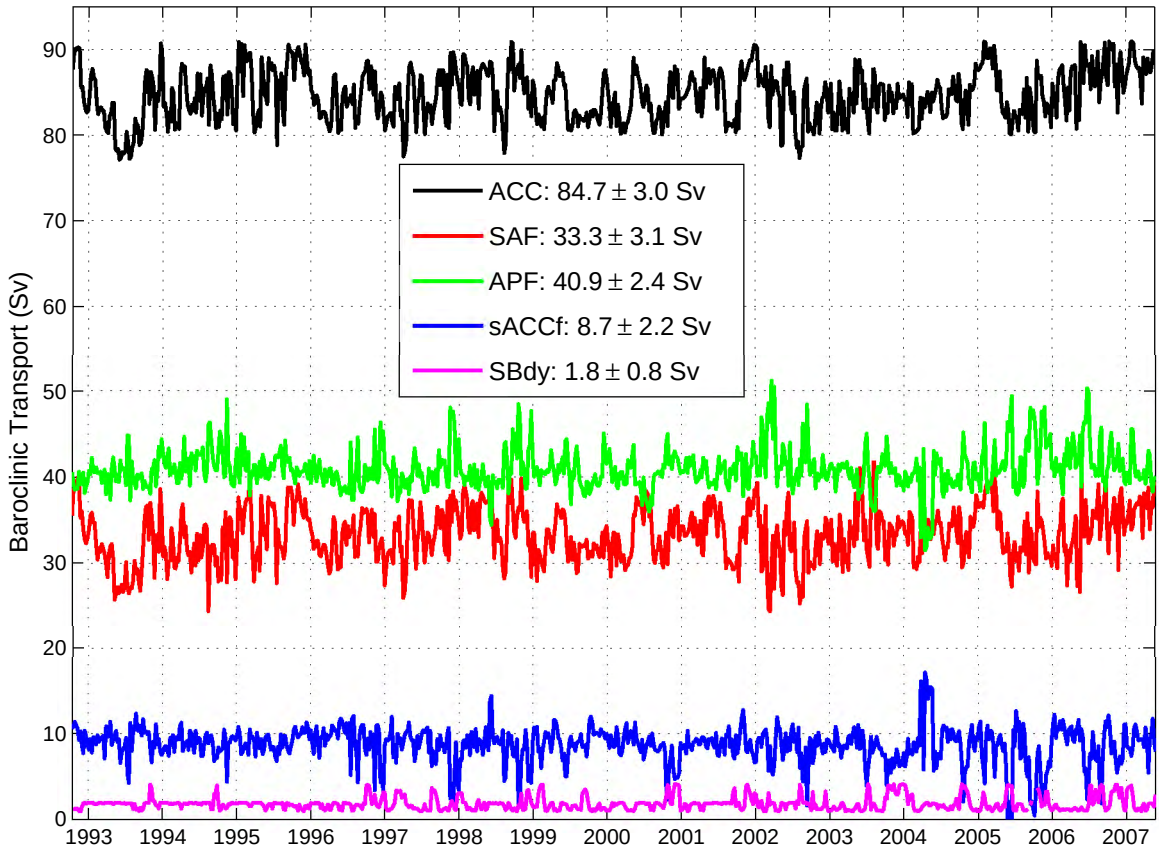

Figure 2.22: Time series of baroclinic transport, relative to 2500 dbar, for each ACC front and for the whole ACC domain (cumulated from the southern limit of the SBdy to the northern limit of the SAF), between 1992-2007. The legend depicts the mean transport and standard deviation of the transport time series for each respective domain.

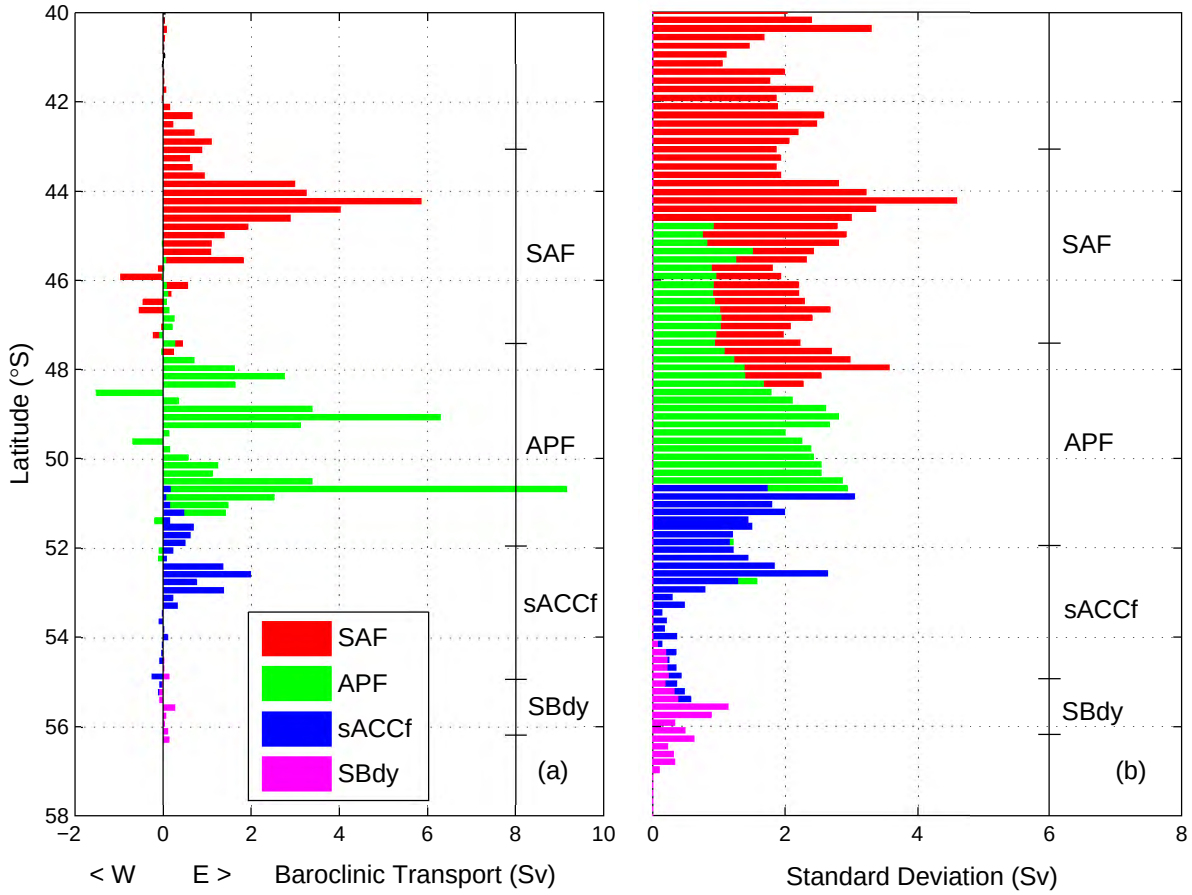

Figure 2.23: (a) Mean baroclinic transport per ACC front derived using the ADT data (between 1992-2007), plotted as a function of latitude. Eastward flow is positive. (b) The standard deviation of the baroclinic transport, plotted as a function of latitude. The mean frontal limits, as defined in Figure 2.20, are indicated on each plot.

between 2500 dbar and bottom referenced CTD transports was relatively constant (67%), thereby allowing us to reference the XBT baroclinic transports to full depth. The mean baroclinic transport, relative to 2500 dbar, for 18 XBT sections was 90 ± 2.4 Sv, while the bottom referenced baroclinic transport estimate was 145 ± 3.9 Sv.

The mean distribution of baroclinic transport with latitude exhibited broad bands of eastward flow associated with the three inner ACC fronts. As expected, these fronts also contributed to extensive amounts of variability in the ACC flow. The most northern part of the sections displayed periods of extreme flow reversals contributing to the highest amounts of transport variability. These occurrences were attributed to south-westward propagating Agulhas Rings, which penetrated the northern domains of the ACC along the GoodHope transect.

The ADT data, over the ACC, was created by adding SSH anomaly data to a mean surface dynamic height. The ADT compared closely with dynamic heights from CTD and XBT data (mean RMSD of 0.063 dyn m). Similarly, we applied the ADT to the empirical relationship between dynamic height and cumulative baroclinic transport to obtain a 14 year time series of net baroclinic transport estimates for the ACC. Intense mesoscale variability, in the form of eddies propagating from the Agulhas Retroflection, made it difficult to accurately define the northern limit of the ACC. Instead, we chose to cumulate the baroclinic transports to the northern limit of the SAF in order to provide a more accurate account of the net ACC baroclinic transport. The altimetry derived mean baroclinic transport of the ACC, relative to 2500 dbar, was 84.7 ± 3.0 Sv. The transports estimated per front, show that the SAF and APF contribute the bulk of the ACC baroclinic transport (∼88%), while the sACCf and SBdy add the remaining ∼12%. The mean latitudinal distribution of the transports reveals that each front is characterised by multiple eastward flowing jets that together, make up the total circumpolar flow. Interestingly, the SAF was found to contribute over 50% of the baroclinic transport variability of the ACC, even though its net transport contribution to the ACC was 9% less than the APF. The use of satellite altimetry products, to identify the front limits, proves to be a valuable tool in accurately defining the role and contribution each front has in determining the total baroclinic transport and associated variability of the ACC.

As shown by *Rintoul et al.* (2002) and *Sokolov et al.* (2004), these proxy techniques are appreciably promising and justify added effort to refine them further. The progression of the GoodHope programme in coming years will improve these methods through supplementary hydrographic sections. These proxy techniques highlight the value remote sensing techniques have on monitoring the transport and associated variability of the ACC, in a data sparse and remote expanse, like the Southern Ocean.

Acknowledgements

The successful completion of the hydrographic surveys would not have been possible without the invaluable assistance of the captains, officers, crew and scientists of the MV S.A. Agulhas and RV Akademik Sergey Vavilov. We are grateful to Silvia Garzoli and NOAA/OCO for their support to implement the XBT deployments in high density mode, to Molly Baringer and Qi Yao for their assistance in the quality control of the data at NOAA/AOML, and to Steven Cook, Robert Roddy, Craig Engler and Jim Farrington for their logistics support with XBT deployments. S. Swart especially thanks S. Speich for the support during a total of eight months stay at the Laboratoire de Physique des Oceans, UBO, France and J.-F. Legeais for technical assistance. The work presented here is supported by the South African National Antarctic Programme (SANAP) and the Russian Academy of Sciences (Grant Meridian Plus #18.17.3) through the provision of funds and facilities. The authors also thank Dr A. Sokov for his effort in helping implement this programme and the Alfred Wegener Institute for Polar and Marine Research for the partial provision of data used in this study. Lastly, we would like to thank three anonymous reviewers for their comments, which helped improve the manuscript.

Chapter 3

Paper II: An altimetry-based Gravest Empirical Mode south of Africa Part 1: Development and validation

This chapter is based on the work published as:
Swart, S., S. Speich, I. J. Ansorge and J. R. E. Lutjeharms (2009), An altimetry-based Gravest Empirical Mode south of Africa. Part 1: Development and validation, *J. Geophys. Res.*, doi:10.1029/2009JC005299.

Abstract

In Part 1 of this study, hydrographic transects of the Antarctic Circumpolar Current (ACC) south of Africa are projected into baroclinic stream-function space parametrised by pressure and dynamic height. This produces a two-dimensional Gravest Empirical Mode (GEM) that captures more than 97% of the total density and temperature variance in the ACC domain. Weekly maps of absolute dynamic topography data, derived from satellite altimetry, are combined with the GEM to obtain a 16-year time series of temperature and salinity fields. The time series of thermohaline fields are compared with independent *in situ* observations. The residuals decrease sharply below the thermocline, and through the entire water column the mean rms error is 0.15°C, 0.02 and 0.02 kg.m^{-3} for temperature, salinity and density, respectively. The positions of ACC fronts are followed in time using satellite altimetry data. These locations correspond to both the observed and GEM-based positions. The available temperature and salinity information allow one to calculate the baroclinic zonal velocity field between the surface and 2500 dbar. This is compared with velocity measurements from repeat hydrographic transects at the GoodHope line. The net accumulated transports of the ACC, derived from these different methods are within 1-3 Sv of each other. Similarly, GEM-produced cross-sectional velocities at 300 dbar compare closely to the observed data, with the rms difference not exceeding 0.03 m.s^{-1}. The continuous time series of thermohaline fields, described here, are further exploited to understand the dynamic nature of the ACC fronts in the regions, and which is found in Part 2 of this study.

3.1 Introduction

The Antarctic Circumpolar Current (ACC) connects all three major ocean basins of the world and the exchanges that take place provide a vital mechanism for the Global Meridional Overturning Circulation. To date, observational studies in the Southern Ocean have relied largely on individual hydrographic transects that are often beset by low horizontal spatial resolutions caused by logistical constraints and harsh working conditions. Additionally, the ARGO float program, while improving the observational coverage in recent years, still has a course spatial resolution and the data are only available from approximately 2003 (and 2004 for the region south of Africa). This proves problematic where basin scale analysis is needed to recover transports and fluxes in the Southern Ocean. We attempt to address this problem in this study. Remotely sensed variables, such as altimetry, have in our opinion, been underutilized in providing information of the subsurface structure in the Southern Ocean, and notably the ACC. Weekly maps of sea-surface-height (SSH) data from 1992, sampled at a relatively high spatial resolution, provide us with a base with which to investigate the dynamic variability and structure of the ACC system.

Localised strong meridional gradients in thermohaline properties (otherwise known as baroclinic fronts) are an ubiquitous feature of the Antarctic Circumpolar Current. An Eulerian approach to monitoring these fronts reveals high levels of temporal variability associated with their recurrent meandering and shifting, caused by mesoscale eddy shedding, as well as seasonal to inter-annual variations. To overcome this problem, hydrographic sections should be aligned with a common origin, such as the position of a baroclinic front determined using specified criteria.

We can project hydrographic sections onto a baroclinic stream-function coordinate $\Gamma(p, \phi)$ (in this case dynamic height at the sea surface, referenced to a common pressure, ϕ_{2500}) in order to give us insight into the subsurface thermohaline structure of the ACC. Thus, this method allows one to obtain the thermohaline properties of the water column from any particular measurement of dynamic height. This projection is called the Gravest Empirical Mode (GEM) and was first introduced to Southern Ocean hydrography through a series of studies: *Sun and Watts*, 2001; *Watts et al.*, 2001; *Sun and Watts*, 2002. The GEM is specifically advantageous for removing a large fraction of the temporal variability associated with small-scale and transient features. This is appealing for general circulation studies as only the modal field is represented. The GEM projected field is also time-invariant, vertically coherent, and equivalent barotropic (*Sun and Watts*, 2001).

The focus of this study lies in the ocean region south of Africa. The GoodHope (GH) monitoring program (*Ansorge et al.*, 2004; *Speich and Arhan*, 2007; *Swart et al.*, 2008; *Gladyshev et al.*, 2008; Figure 3.1) provides the ideal platform to combine the GEM with satellite altimetry SSH data and demonstrate the ability of this method to recreate *in situ* observations. This method provides us with a valuable 16-year time series (weekly intervals) of temperature and salinity fields at the GH line, which can be used to improve our understanding of the ocean dynamics in this least understood 'chokepoint' of the ACC. Previous studies have already provided evidence that show that subsurface ocean information (such as upper ocean temperature and baroclinic transports) is closely correlated with the SSH signal (*Rintoul et al.*, 1997; *Rintoul et al.*, 2002; *Sokolov et al.*, 2004; *Legeais et al.*, 2005; *Swart et al.*, 2008). This emphasizes that SSH is representative of the density signal of the water column and that further information of the subsurface structure may be available by utilising knowledge of the SSH.

3.2 A synopsis of the hydrography at the GH line

Compared with Drake Passage and the oceanic region south of Australia, the African chokepoint constitutes the most variable of the Southern Ocean. South of Africa, three oceanic regimes dominate the hydrography: the

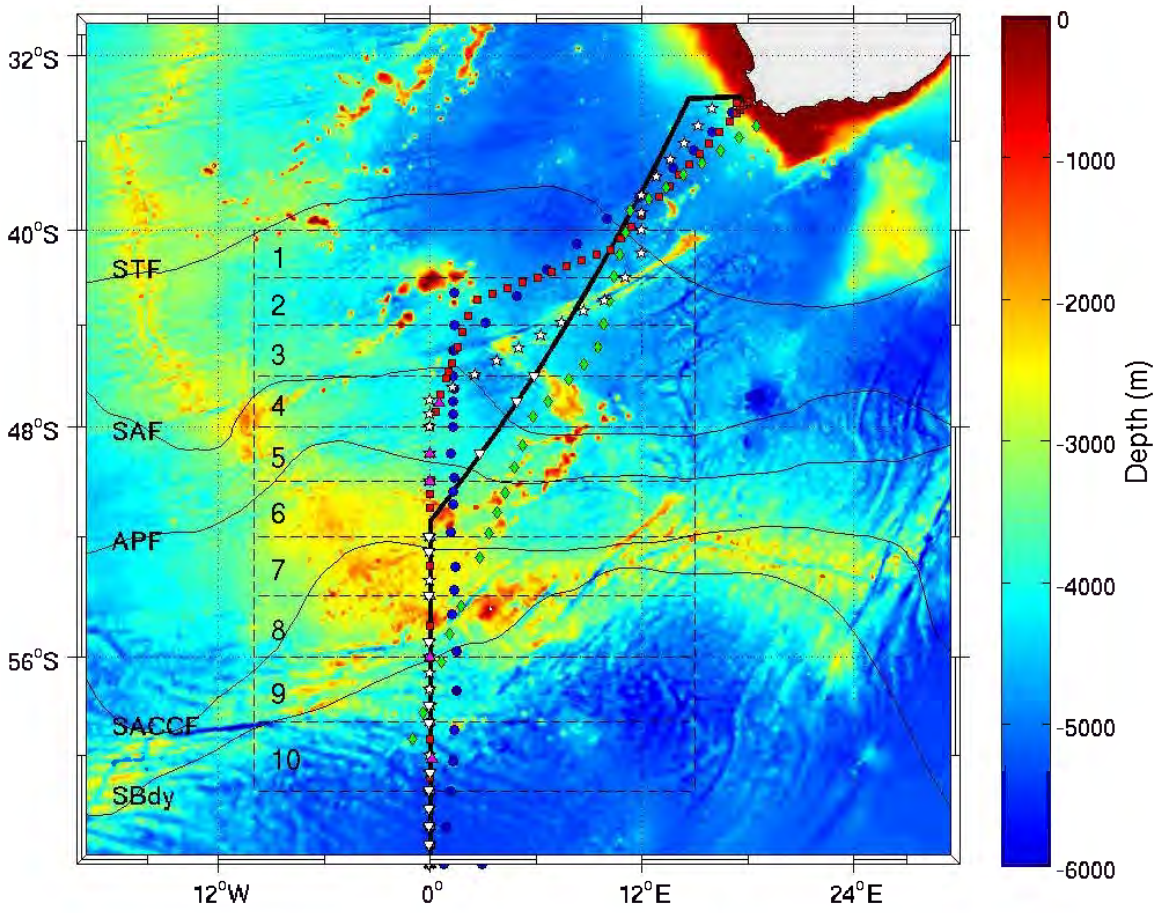

Figure 3.1: Locations of the eight CTD sections used in this study. The AJAX section (blue circles), A21 section (green diamonds), the 1992 A12 section (red squares), the 1999 A12 section (magenta triangles), the 2000 A12 sections (white stars), the 2002 A12 section (white triangles). The solid black line represents the repeat cruise track of the GH CTD and XBT sections. Traces of the ACC fronts, by *Orsi et al.* (1995), and the bathymetry (in meters) has been overlaid: STF (Subtropical Front), SAF (Subantarctic Front), APF (Antarctic Polar Front), SACCF (southern ACC front), SBdy (southern boundary of the ACC). The gridded boxes represent the latitudinal zones from which ARGO float data were extracted to derive a seasonal model for the region.

Agulhas Current, the ACC, and the Weddell Gyre. The Agulhas Current, which lies along the south-eastern edge of the African continental shelf, is regarded the strongest western boundary current in the southern hemisphere. Its westward termination is marked by a region of extreme mesoscale variability (*Lutjeharms*, 2006) in the form of eddy shedding that is associated with the current retroflecting back towards the east (*Gordon*, 1985; *Duncombe-Rae*, 1991; *Lutjeharms*, 1996; *de Ruijter et al.*, 1999; *Boebel et al.*, 2003). The Agulhas Retroflection produces an intermittent stream of Agulhas Rings (*Lutjeharms and Gordon*, 1987; *Lutjeharms*, 1996; *de Ruijter et al.*, 1999), which are occluded from the Agulhas Retroflection, and propagate generally in a north-westward direction (*Schouten et al.*, 2000), and intersect the GH line in the subtropical domain (*Gladyshev et al.*, 2008; *Swart et al.*, 2008). On occasions an Agulhas Ring detaches from the Agulhas Retroflection and propagates in a west to south-west direction (a time series of altimetry data shows this to happen on average 2.7 occasions per year; see Part 2, *Swart and Speich*, 2009; *Dencausse et al.*, 2009). These features have been observed crossing the GH track between 39-42°S and are often observed well into the Subantarctic Zone (SAZ) (*Swart et al.*, 2008; *Gladyshev et al.*, 2008).

The ACC is characterized by a series of eastward jets associated with baroclinic fronts, which denote the positions of the maximum meridional thermohaline gradients (*Deacon*, 1937; *Nowlin and Clifford*, 1982; *Orsi et al.*, 1995; *Belkin and Gordon*, 1996). In the African sector of the Southern Ocean, four primary fronts exist - the Subtropical Front (STF), the Subantarctic Front (SAF), the Antarctic Polar Front (APF), and the southern ACC front (SACCF). Additionally, the southern boundary of the ACC (SBdy) marks the boundary separating flow between the ACC and Weddell Gyre system (*Orsi et al.*, 1993). The presence and spatial structure of the STF south of Africa is complicated by the presence of Agulhas Rings, particularly in the region of the GH line. At this location, the presence of the STF is made up by an almost continual 'stream' of eddies (*Lutjeharms*, 1988; *Lutjeharms and Valentine*, 1988; *Belkin and Gordon*, 1996; *Dencausse*, 2009).

The hydrographic structure and frontal systems between Africa and Antarctica have been relatively well studied and described. Sea-surface temperatures (e.g. *Lutjeharms and Valentine*, 1984), numerous XBT sections (e.g. *Lutjeharms and Emery*, 1983; *Lutjeharms*, 1985; *Swart et al.*, 2008), some densely spaced CTD sections (e.g. *Whitworth and Nowlin*, 1987; *Read and Pollard*, 1993; *Belkin and Gordon*, 1996; *Swart et al.*, 2008; *Gladyshev et al.*, 2008) and satellite observations (e.g. *Moore et al.*, 1999) have been used to describe the average geographic locations, average hydrographic characteristics and variations to all of these in substantial detail.

The thermohaline structure, along the GH transect, is represented here by the second CTD occupation, completed in October 2005 (Figure 3.2). Each ACC temperature front, as defined by *Orsi et al.* (1995), is indicated on the figure. The CTD transect, unfortunately, did not cross the SBdy of the ACC so we are unable to represent it here. However, we choose to include this section because it is one of two sections in the region that is sampled at a high spatial resolution. This is important for clearly identifying more fine scale features that can be missed by low spatial resolution CTD sections. The temperature and salinity sections clearly identify the principal water masses spanning the length of the section. The most obvious of these include warmer, saltier intrusions of Agulhas Water (consisting of Tropical Indian Surface Water and Subtropical Indian Surface Water) found north of ∼40°S, Antarctic Intermediate Water (AAIW) characterized by a salinity minimum (<34.4) layer extending north of ∼50°S, and the temperature minimum layer at ∼100 dbar located south of the APF placed at ∼50.5°S.

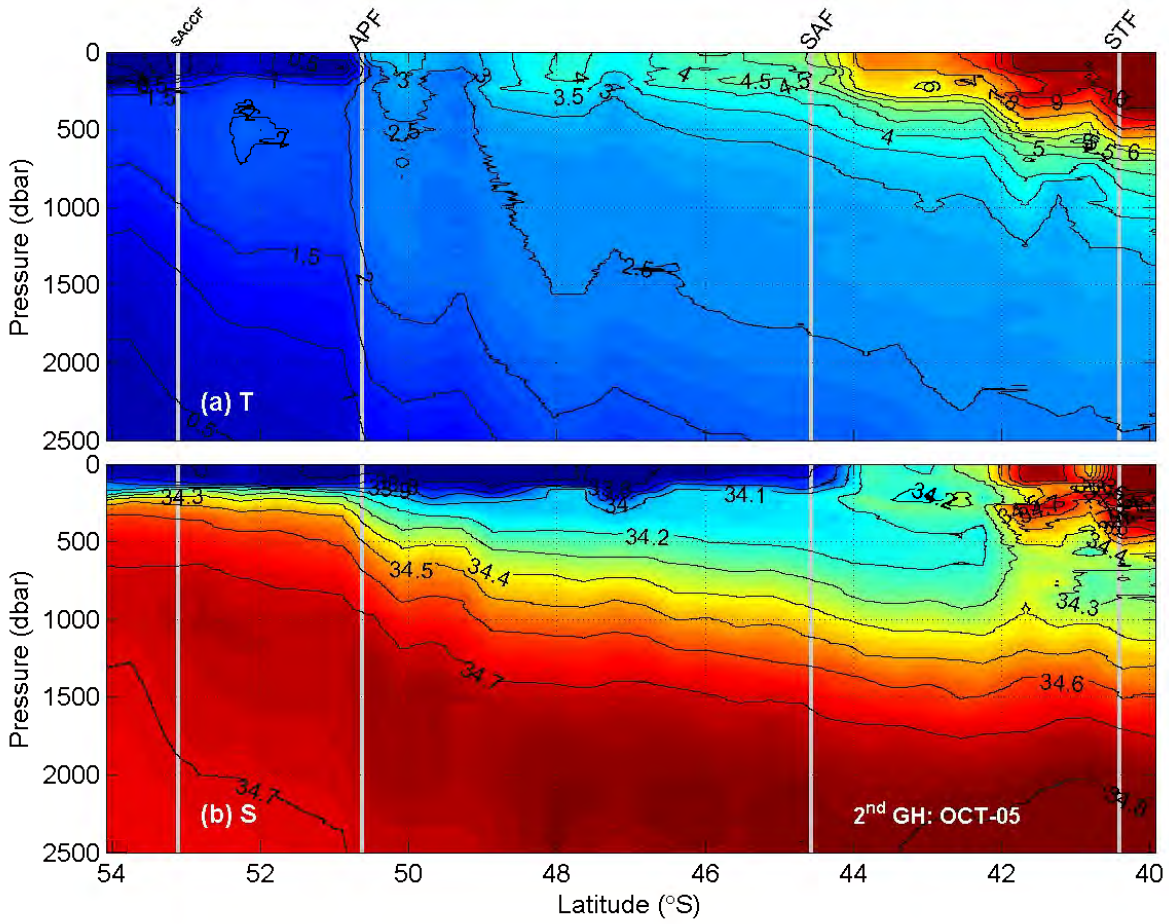

Figure 3.2: Temperature (a) and salinity (b) section from the second GH CTD section completed in October 2005. The ACC front locations, as determined using the criteria of *Orsi et al.* (1995), are indicated by the vertical grey lines.

Table 3.1: Summary of the CTD sections used in this study

Section	Date	Chief Scientist/Reference
AJAX	Jan. 1984	T. Whitworth/*SIO*, 1985
A21	Jan. - Mar. 1990	W. Roether/*Roether et al.*, 1990
A12 1992	May - Aug. 1992	P. Lemke/*Lemke*, 1992
A12 2000	Dec. 2000	E. Fahrbach/*WOCE*, 2002
A12 2002	Dec. 2002	E. Fahrbach/*WOCE*, 2002
GH1	Nov. 2004	S. Gladyshev/*Gladyshev et al.*, 2008
GH2	Oct. 2005	S. Gladyshev

3.3 Data

3.3.1 Conductivity-Temperature-Depth (CTD) data

Data from eight CTD sections, completed between 1984-2005 (Table 1), are used to set up the GEM projection south of Africa. Most of the sections encompass the region between the south-western tip of South Africa and the Antarctic continent (see Figure 3.1), while some of the sections do not extend completely to Antarctica. The sections provide a relatively good coverage of the seasonal variability expected for the region. The two most recent sections were completed at the GH line and have a higher spatial resolution (∼50 km) than those completed earlier (∼80 km). In most cases, there was tighter station spacing over regions of shallow or steep bottom topography. In total, data from 296 CTD casts (of which 199 stations lie within the ACC domain) were used in this study. Data for the A12 sections, completed between 1999-2002, were obtained from the CLIVAR and Carbon Hydrographic Data Office (details pertaining to the sections can be found at http://whpo.ucsd.edu/). For further details regarding station spacing, CTD calibration and problems encountered refer to the following technical reports and papers: *SIO*, 1985; *Roether et al.*, 1990; *Lemke*, 1992; *WOCE*, 2002; *Swart et al.*, 2008; *Gladyshev et al.*, 2008.

3.3.2 Satellite altimetry data

3.3.2.1 Sea Level Anomaly

The 'Maps of Sea Level Anomaly (MSLA)' product from CLS/AVISO, a weekly SSH anomaly map on a 1/3° Mercator grid that incorporates data from T/P, Jason-1, ERS-1/2 and Envisat altimeters, was used in this study. This data set extends, at weekly intervals, from 14 October 1992 to 23 January 2008, yielding 798 weeks of data. Because the ACC is characterized by mesoscale structures and variability we choose to use the "up-to-date" data processing that makes use of all the satellite data available for each period. The satellite altimetry data, for this time series, are not homogeneous in number per unit time, but for long periods they provide an improved resolution and data accuracy compared with the classical "referenced" data set. These multi-mission gridded SSHs are referenced to a seven year (1993-1999) mean. For details on mapping methods and error corrections applied to these fields, refer to *le Traon et al.* (1998), *le Traon and Ogor* (1998), and *Ducet et al.* (2000).

3.3.2.2 Absolute Dynamic Topography

The 'Maps of Absolute Dynamic Topography (MADT)' product from CLS/AVISO has the same temporal and spatial resolution as the data set described in Section 3.3.2.1. The MADT is the sum of the sea level anomaly data and a mean dynamic topography (Rio05–Combined Mean Dynamic Topography (CMDT); *Rio and Hernandez*,

2004). The CMDT is a combined product using *in situ* measurements (hydrographic and surface drifter data), altimetry data and the EIGEN-GRACE 03S geoid. The CMDT is computed over a seven year period (1993-1999). We also make use of the absolute geostrophic velocities calculated from the MADT data that are available from CLS/AVISO.

3.3.3 ARGO float data

ARGO profiling float data, from a quadrant located around the GH line and within the ACC (Figure 3.1), was used to set up a seasonal model for the region. The data comes from the Coriolis Operational Oceanography Center, which is one of two Argo Global Data Assembly Centres (GDAC) worldwide. Extensive quality control has been performed on the data, under the auspices of the GH observing program (M. Arhan and A. Prigent, personal communication). A total of 7120 individual profiles of temperature and salinity were located within this quadrant between January 2004 and October 2007. The profiles were then interpolated onto a regular pressure grid and placed within 2° latitudinal bands between the northern and southern ACC limits.

3.3.4 Expendable Bathythermograph (XBT) data

The XBT data originates from six high-density sections completed at the GH line between February 2004 and March 2008. The XBTs were deployed to measure the upper ocean thermal structure at spatial intervals of 25 km, increasing the frequency to 15 km over the frontal regions of the ACC. The 4000 km transect between Africa and Antarctica was on average completed within two weeks, with each section providing a roughly synoptic picture of the upper thermal layer in this sector of the Southern Ocean.

Extensive quality control procedures have been applied to the XBT data by AOML/NOAA in the United States. Adjacent temperature profiles were compared with each other and to the regional Levitus climatology (*Levitus*, 1982). For more details on the AOML quality control procedures, refer to *Daneshzadeh et al.* (1994) and *Bailey et al.* (1994), and for more information on the XBT sections, refer to *Swart et al.* (2008).

3.4 The gravest empirical mode south of Africa

3.4.1 Projection in stream function space

The GEM is created by projecting the hydrographic data from eight CTD transects for the region, onto streamline co-ordinates of pressure and dynamic height (Figure 3.3a-c and Figure 3.4a-c). The figures illustrate the robust empirical relationship between the surface dynamic height and the vertical structure of temperature and salinity and the tendency for CTD data to cluster around a functional curve. We use 2500 dbar as the reference level because it is the deepest point that lies above the mid-ocean ridge and also allows us to exploit CTD data that were not sampled to the bottom due to time constraints and harsh weather conditions experienced during several of the cruises.

In order to obtain a two-dimensional field using this projection method, we apply a cubic smoothing spline of equal parameter (Figure 3.3a-c and Figure 3.4a-c) to each of the relationships between temperature/salinity and dynamic height, extending from the surface to 2500 dbar, at intervals of 5 dbar. The resulting two-dimensional fields for temperature and salinity are represented in Figure 3.3d and Figure 3.4d, and are called GEM fields. Note that because these fields are represented using dynamic height, no explicit spatial information can be drawn from

these sections. Although the GEM fields tend to suppress the fine-scale features associated with the ACC, the basic thermohaline structures are still present. The most distinct reproduced features are the subsurface temperature minimum layer located in the upper 200 dbar (Figure 3.3d), the surface salinity minimum layer, and the low saline waters associated with AAIW, which extend between the surface and ∼1000 dbar (Figure 3.4d).

In comparison to previous GEM constructions south of Australia (SR3 section; *Sun and Watts*, 2001), the streamfunction relationships are very similar (Figure 3.3a-c and Figure 3.4a-c). In this study region, there is a greater scatter of temperature at the 1000 dbar interval, for values greater than the 2 dyn m interval (Figure 3.3b). Similarly, the salinity structure experiences the same scattering, but at all shown pressure levels. This is primarily due to the close proximity of subtropical water masses bordering the northern limit of the ACC south of Africa, which introduce warmer, saltier waters through mesoscale variability at the STF and intruding Agulhas Rings (*Swart et al.*, 2008; *Swart and Speich*, 2009). Besides the higher temperature and salinity signatures at dynamic heights greater than 1.8 dyn m, the respective GEM fields in Figures 3.3d and Figure 3.4d are comparable to those south of Australia (*Sun and Watts*, 2001), while their GEM representations at 0°E are very similar to our GEM fields, although somewhat smoother likely due to different sampling resolutions and smoothing parameters used.

3.4.2 A seasonal model south of Africa

Higher rms residuals are associated with the upper mixed layer and are mainly caused by the seasonal cycle in both temperature and salinity. The CTD data have a seasonal bias because sampling generally takes place in spring-summer in the Southern Ocean, with the exception of the A12 1992 section. We therefore, rely on float data from the region to build a seasonal model in temperature and salinity, in the upper 500 dbar, to reduce this bias.

ARGO float profiles, gathered between 2004 and 2007, were grouped into 2° latitudinal bands between 40-60°S (Figure 3.1). This was done in order to preserve the changing seasonal model with change in latitude, while still acquiring enough profiles to create a sound seasonal pattern in that band. The data, averaged monthly, were replicated three successive times before a 3-month running mean was applied to the data to remove the intra-seasonal variability. The middle year was extracted from the data set to avoid start and end transients during the filtering process. This mean cycle was then removed from the CTD data before being used to produce the GEM relationships. Therefore, all GEM data presented in this study have been parametrized by the seasonal model presented here. *Watts et al.* (2001) first employed this method for acoustic travel time, temperature and salinity data south of Australia.

The seasonal cycle of temperature, combined for all latitudinal bands, (Figure 3.5a & 3.5b) shows a clear sinusoidal signal due to the surface warming (cooling) during austral summer (winter). At the surface, the transition from a warm to cool state takes place around mid-May while the reverse effect occurs during late-November. A lag in this transition (∼5 months at 300 dbar) increases with pressure due to the delay in mixing to the deeper levels with time. The extent of the cool state, extends deeper than the summer warm state. This is likely due to stronger mixing and convective mechanisms taking place in the winter months, which allows for cooling to take place beyond 300 dbar. The magnitude of the summer warming in the upper 100 dbar is, on average, ∼0.2°C higher than the winter cooling.

The latitudinal differences in the annual cycle of salinity are more complicated than the temperature cycle. In order to avoid confusion, we only illustrate the annual salinity cycle between 56-58°S (Figure 3.5c). The general structure of the salinity cycle is similar to the temperature cycle except that the salinity cycle supersedes the temperature cycle by approximately 2 months. The deep extent of the salinity anomalies is likely caused by the

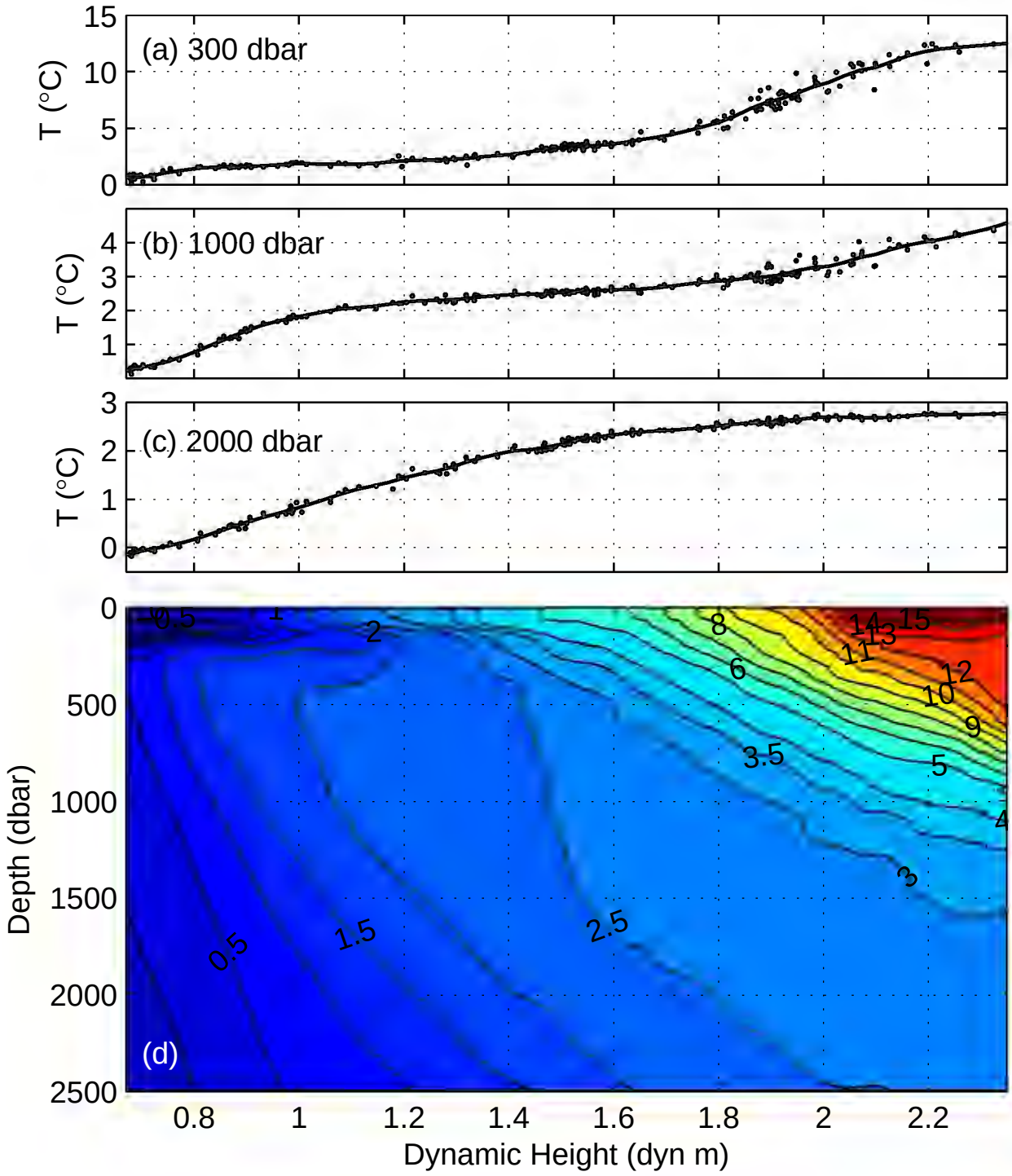

Figure 3.3: The available CTD temperature data plotted at three pressures, (a) 300 dbar, (b) 1000 dbar, and (c) 2000 dbar, as a function of dynamic height. A smoothing spline has been fitted to the data (solid curve). The same data are used to create the GEM temperature field shown in (d).

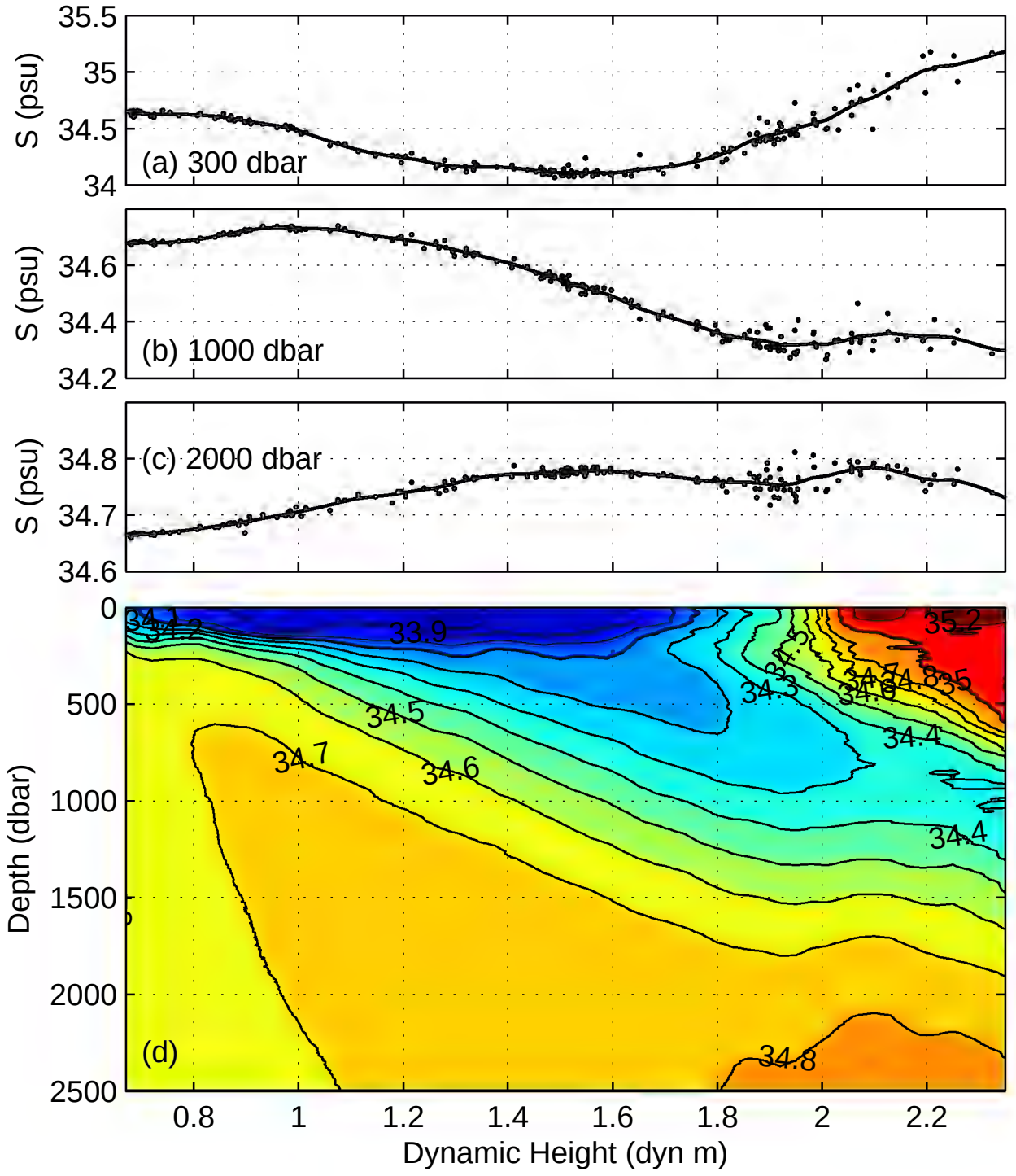

Figure 3.4: The same as Figure 3.3, but for salinity.

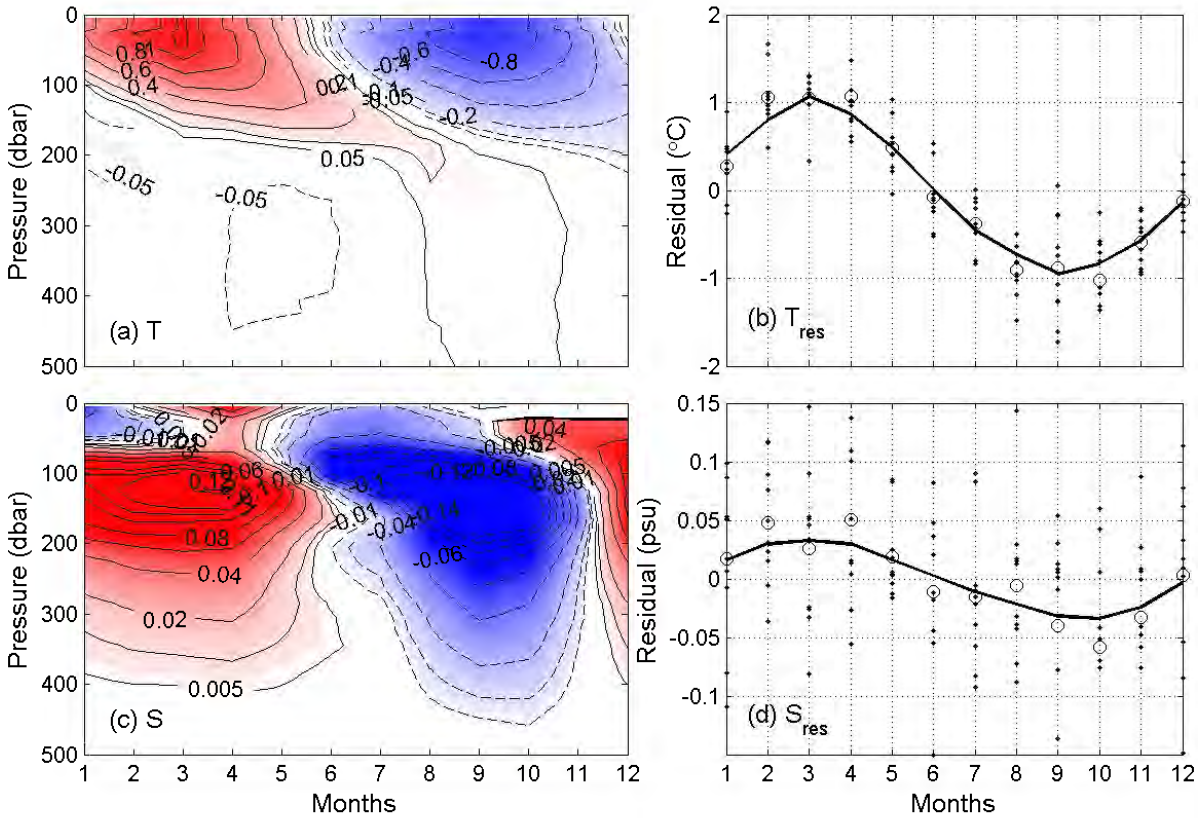

Figure 3.5: The annual march of (a) temperature and (c) salinity anomalies are deduced from available float data for the ACC region. The temperature plot represents the annual march over the whole latitudinal band (40-60°S), while the salinity plot represents the latitudinal range between 56-58°S. The mean seasonal residuals between 0-100 dbar of (b) temperature and (d) salinity are plotted for each latitudinal zone using black dots. Circles in (b) represent the mean of the residuals represented by the black dots and in (d) they represent the mean residuals between 100-200 dbar in the latitudinal range 56-58°S. A 3-month running mean is applied to the data (solid line) to filter out any interseasonal noise existing in the data.

extensive mixing of the upper ocean layers at the high latitudes where wind speeds are especially high.

After applying the seasonal correction, the temperature rms residual in the surface layer (0-300 dbar) is reduced from 0.22°C to 0.12°C. The salinity seasonal cycle has alternating positive and negative effects on reducing the rms residual in the upper layers. In the upper 200 dbar, the seasonal correction causes the rms residual to increase from 0.057 to 0.06, meanwhile, between the 200-300 dbar, the rms residual decreases from 0.05 to 0.04. On average, applying the salinity seasonal correction reduces the rms residuals in the upper layers and so it is used in this study even if its benefits are small.

3.4.3 Comparison against direct measurements

The GEM-derived temperature and salinity profiles were computed from the dynamic height, calculated from measurements of temperature and salinity at each station during the second GH CTD section. Note that prior to calculating the GEM-derived temperature and salinity profiles, the GEM fields were recalculated by excluding

the observed section in order that the profiles be independent of the directly measured data. The GEM-derived profiles were then plotted using the spatial co-ordinates (longitude, latitude) of the original CTD stations (Figure 3.6) and can be compared to the directly measured section in Figure 3.2. A number of hydrographic structures in the GEM-reproduced temperature and salinity sections compare closely with those found in the observed data. Features, such as the fronts, the thermocline depth and the temperature minimum layer, are very similar to the observed sections. The axial positions of the STF, SAF and APF in the GEM fields are within approximately 30 km of the observed positions. The GEM reconstructions do tend to filter out small-scale features, such as the isolated 2°C isotherm located at 52°S in the observed data. However, an anticyclonic anomaly can still be seen in the GEM fields at 50°S, although its intensity is somewhat reduced compared to the observed data sets. On the other hand, the core of an anticyclonic feature, observed at 42°S during the first GH CTD section, is exaggerated by the GEM fields (not shown), while the structure of an anticyclonic feature, crossed between 38-40°S (*Gladyshev et al.*, 2008), has been remarkably well represented by the GEM even though this feature is found outside the domain of the ACC and where information of the thermohaline properties and dynamic heights do not exist in the original GEM relationships. As the errors are largest in this region, we are unable to explain why this particular feature is well represented in the GEM fields as it does not occur on the norm. The rms residuals of temperature and salinity (Figure 3.6) are mostly confined to the upper 300 dbar, where uncertainties in the mixed layer are greatest due to seasonal changes and the interaction between the atmosphere and upper ocean. Additionally, the inability of the GEM to reproduce the exact depth of the capped temperature minimum water south of the APF in early summer, leads to some increased subsurface residuals in temperature and salinity in the southern parts of the section. The increased residuals in the upper mixed layer are clearly identifiable in the residual plots south of Australia, by *Sun and Watts* (2001). The residuals in both studies increase towards the northern latitudes, however, at the GH line, the increase is more abrupt and localised in the northern SAZ where the shape of the deepening residuals clearly represents the presence of mesoscale eddies in the section. The subsurface errors in the *Sun and Watts* (2001) study extend deeper (>1500 dbar) than those south of Africa (sudden decrease in residuals at ∼250 dbar).

To assess the accuracy of the GEM at representing the 'true' temperature and salinity properties of the ACC, we conduct the same examination process as *Watts et al.* (2001), which calculates the percentage of the hydrographic variance that is captured by the GEM fields (Figure 3.7). The variance is represented as

$$variance(p) = 1 - \frac{\sigma^2_{res}}{\sigma^2_{hyd}}\,, \tag{3.1}$$

where σ^2_{res} is the variance of the residuals in the GEM fields and σ^2_{hyd} is the total variance of the hydrographic sections. The percentage of variance captured in each property increases quickly with pressure and shows improvement in the layers least affected by surface forcing and seasonality (below the thermocline). On average, up to 94% of the temperature and the density, and 85% of the salinity variance is captured by the GEM in the upper 500 dbar. This increases sharply to 99%, 95% and 98% for temperature, salinity and density, between 500-2500 dbar, respectively. The ratio between the low observed variance of the deeper water masses (like Circumpolar Deep Water) and constant GEM residual variance causes the salinity and density variance captured to decrease in the deeper levels (>1500 dbar). This was similarly noted south of Australia (*Sun and Watts*, 2001), where the minimum variance captured by the salinity occurs slightly deeper (2000 dbar) than in the African sector. In this study, the captured salinity variance in the upper layers is much lower (∼80%) than the estimates made by *Sun and Watts* (2001) at the SR3 transect (∼96%). The disproportionately high difference in ACC water mass salinities from those

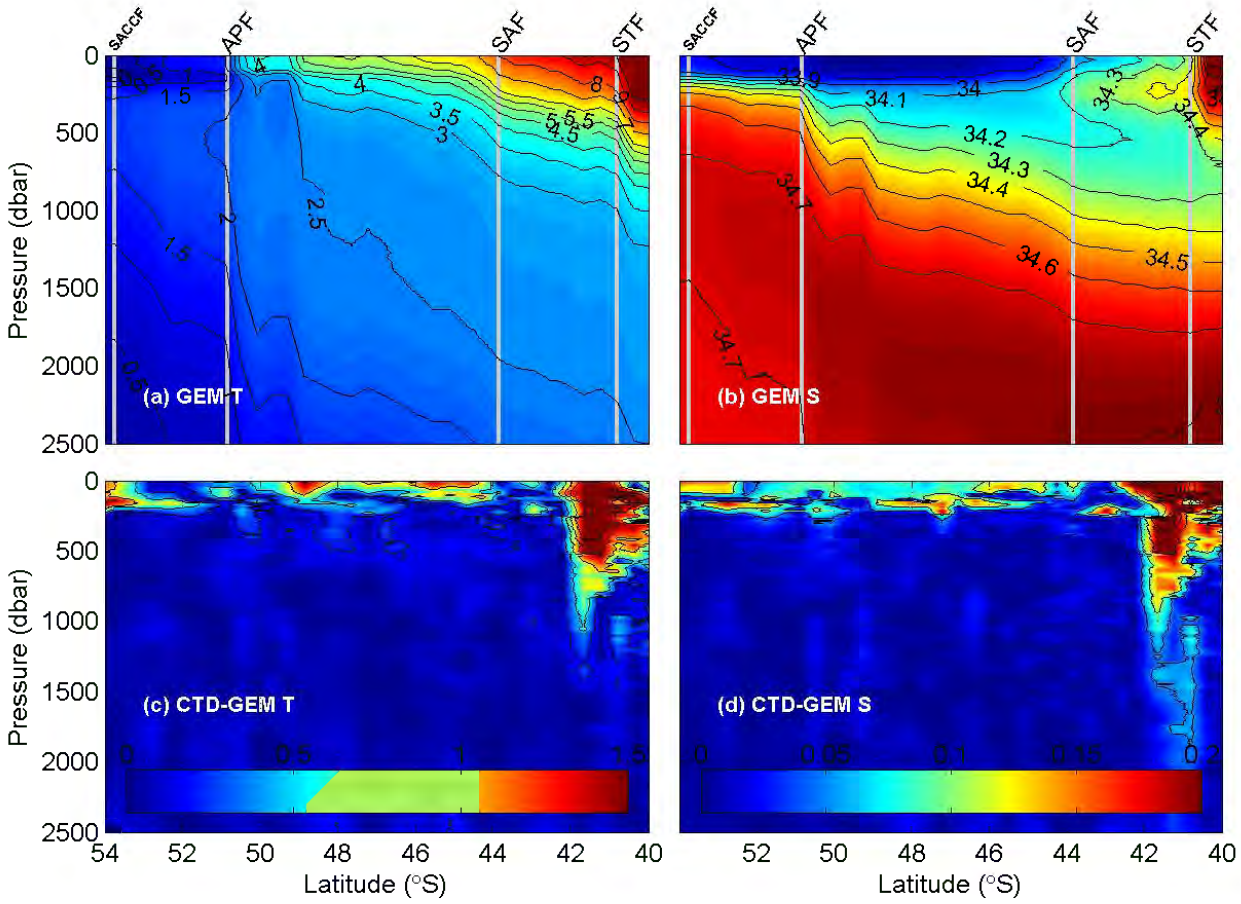

Figure 3.6: GEM-estimated sections of (a) temperature and (b) salinity pertaining to the CTD dynamic height data from the second GH occupation. The ACC front locations, as determined using the criteria of *Orsi et al.* (1995), are indicated by the vertical grey lines. The rms difference between the *in situ* CTD and GEM produced sections are shown for (c) temperature and (d) salinity, in °C and psu, respectively. The ACC front locations, as determined using the criteria of *Orsi et al.* (1995), are indicated by the vertical grey lines.

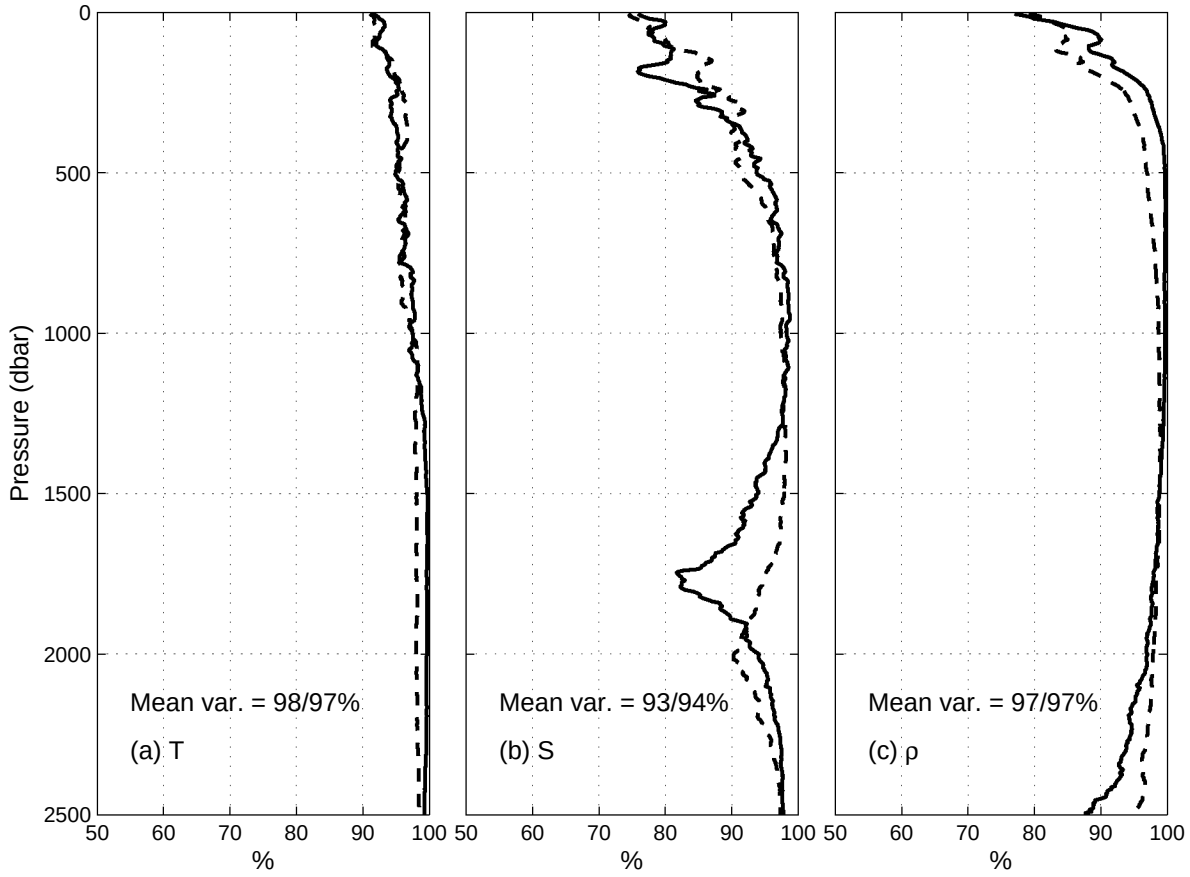

Figure 3.7: Percentage of hydrographic data variance captured by the GEM (solid curves) and AGEM (dashed curves) fields of (a) temperature, (b) salinity, and (c) density. The mean variance captured through the water column is displayed for the GEM and AGEM, respectively.

of subtropical origins introduced in the SAZ may cause some of the lower captured variance in the upper 1000 dbar, as the GEM struggles to represent the water mass properties with accuracy. The mean variance captured by the GEM, through the entire water column, is shown for each property, in Figure 3.7.

3.5 Applying satellite altimetry to the GEM

3.5.1 A time evolving absolute dynamic topography

To investigate the possibility of extending the temporal range and resolution of the GEM, we apply an altimetry derived absolute dynamic topography (ADT) data set to the empirical GEM relationships. The ADT is produced by adding a mean dynamic height state, created from repeat hydrographic sections at the GH line (see *Swart et al.*, 2008 for further details), to altimeter SSH anomalies. The ADT is representative of the entire water column and therefore, may additionally reflect both changes in the density field below 2500 dbar and a barotropic component. One cannot ignore supplementary errors introduced by temporal and spatial sampling discrepancies and interpolation, mapping errors and tides not entirely removed from the altimeter signal. Despite these factors, the ADT data are very similar

to the hydrographic estimates of dynamic height (mean rms error is 0.063 dyn m, from *Swart et al.*, 2008). This suggests that the ADT largely reflects baroclinic changes in the upper 2500 dbar of the water column.

AGEM (Altimetry + GEM) is the name we assign to the product that combines the ADT data with the GEM empirical relationships. The primary reason for creating the AGEM rests in the fact that data time series in the Southern Ocean, and particularly in the African sector, are so rare. To date, the large majority of ship board observations take place solely in the austral summer months. Profiling float data are helping to address this problem, however, profiles remain scarce when compared to the vast expanse of the Southern Ocean. For the first time, the AGEM is able to provide information on the subsurface baroclinic structure of the ocean at eddy resolving spatial and temporal scales.

Before this continuous time series of ADT data are used to render time evolving profiles of temperature and salinity, we accurately delineate the ACC front positions space and time.

3.5.2 Positioning the ACC fronts using satellite altimetry

Given that the ACC, south of Africa, is unbounded by any continental landmasses, its ocean boundaries or fronts have to be accurately defined using remote sensing techniques. In recent studies, high-resolution hydrographic and satellite sampling have been able to accurately locate the ACC fronts in space and time (*Sokolov and Rintoul*, 2002; *Sokolov and Rintoul*, 2007a; 2007b; 2009a; 2009b). *Swart et al.* (2008), briefly describe the use of altimetry data and *in situ* data to identify the ACC frontal zones, along the GH line. Previously, we have described that altimetric SSH data are largely representative of the maximum baroclinic shear in the water column. This means that regions of increased horizontal gradients in dynamic height are representative of the local maximums in the baroclinic shear and therefore, associated frontal jets or branches.

The mean meridional gradient in MADT data, along the GH line, reveals the dominant frontal regions (Figure 3.8). In the mean gradient, the SAF is represented by one core front (at 44.4°S), followed by two distinct branches of the APF, located at 48.9°S and 50.5°S. Further south, the SACCF is located at 53.5°S and the SBdy of the ACC is located at 55.6°S. An additional branch of the SAF, not shown in the mean MADT gradient, is sporadically present in time, south of the core SAF (seen on a portion of the MADT gradient plots and located, on average, at ∼48.2°S). On occasions, this branch may merge with the northern branch of the APF, located on average, just 87 km to the south (identified in mean plots of MADT geostrophic velocities and MADT eddy kinetic energy of the region). The mean gradient in dynamic height related to the main branch of the SAF and the APF are approximately 0.8 dyn m per 100 km, while due to the reduced intensity of the southern ACC fronts, the gradients over the SACCF and SBdy are ∼0.65 dyn m per 100 km. The northernmost peak in the MADT gradient may be associated with the northern branch of the STF, but it is not constantly present in time because it is made of a continual 'stream' of cyclones and Agulhas Rings originating at the Agulhas Retroflection (*Belkin and Gordon*, 1996; *Swart et al.*, 2008; *Dencausse*, 2009). The position of these fronts can be compared to the meridional distribution of the ACC's baroclinic transport, represented in latitudinal bins along the GH line, and found in *Swart et al.* (2008).

Similarly to the principles of the GEM, the conservation of streamlines means values of dynamic height will coincide with constant water mass properties and thus fronts. Like *Sokolov and Rintoul* (2002, 2007a), we examine the distribution of the MADT gradient at the GH line and find that constant values of MADT (streamlines) match localised MADT gradient maximums. The location of these gradient maximums and associated isolines of MADT are very similar to the front positions located in hydrographic data and defined by the *Orsi et al.* (1995) criteria (i.e. the major front cores at the GH line match the definition provided by *Orsi et al.* (1995)). We adapt the mean

Table 3.2: The mean value of MADT, used to follow the fronts in the MADT time series, as well as the mean latitudinal position of each front and their standard deviations are listed.

Front	Mean MADT (dyn m)	Front Position (°S)	Standard Deviation (° latitude)
STF	1.41	39.9	1.51
SAF	1.15	44.3	0.36
APF	0.49	50.4	0.27
SACCF	0.18	53.4	0.21
SBdy	-0.07	55.5	0.32

dynamic height in 5-year periods, between 1992-2008, in order to take into consideration the temporal variability in dynamic height space that might occur over the 16-year time series. The mean fixed values of MADT that have been used to locate the fronts, as well as their mean positions and standard deviation, can be found in Table 2.

To test the consistency of using this method, we overlay the fronts position onto the MADT velocity magnitude ($\sqrt{(u^2+v^2)}$; Figure 3.9). The fronts consistently follow the highest velocity magnitudes induced by the baroclinic shear of the fronts. Furthermore, Figure 3.10 provides a representation of the frequency at which the altimeter-derived fronts match the localised MADT gradient maximum associated with the front for the whole altimetry time series (1992-2008). Apart from the STF, the fronts are found at the exact position or within 0.2° latitude (20 km) of the maximum gradient between 52-73% of the time. Of these fronts, the worst performers are the two southernmost fronts (SACCF and SBdy), which is likely due to their weaker gradients, thus making it harder to 'pin point' their exact location. However, none of the main ACC fronts are found more than 2° latitude away from the maximum gradient. As expected, the STF is the worst performer with only 3% of the front positions matching the exact location of the maximum gradient and over 28% of the time the front position is located over 2° latitude away. It must be noted that these inaccuracies are exaggerated because (1) Agulhas Rings and other mesoscale features found just north of the STF cause large MADT gradients that dominate the generally weaker 'true' frontal gradients, and (2) because the latitudinal range of the STF overlaps the latitudinal range of the SAF by ∼1° latitude. This means that in some cases the maximum MADT gradient is incorrectly associated with the SAF and not the STF, thereby resulting in higher inaccuracies. The STF is generally a weaker front than the SAF and so this form of error exaggeration is particularly true in this case.

There are additional, yet smaller and less consistent jets present in the MADT velocity magnitude and gradient plots. Examples include the additional branches of the SAF and APF that are depicted in Figures 3.8 and 3.9. Comparatively, Sokolov and Rintoul (2002, 2007a) locate many more front branches south of Australia (e.g. 3 SAF branches, 2 APF branches, and 2 SACCF branches) than seem to be present in the African sector. This is partially justified by the deeper topography found south of Australia (such as the Australian-Antarctic Basin), which would allow for increased front destabilisation and jet separation. However, a more in-depth analysis on the front structures south of Africa may reveal many more jets, but for the purpose of this study, we only require locating the major fronts of the ACC.

3.5.3 Comparing ACC front positions

We now attempt to verify the frontal positions represented in the AGEM sections, using hydrographic sections. This indicates how accurately the AGEM represents the baroclinic boundaries in the ACC throughout the water column. The criteria used to locate the ACC fronts from the hydrography and the AGEM produced temperature

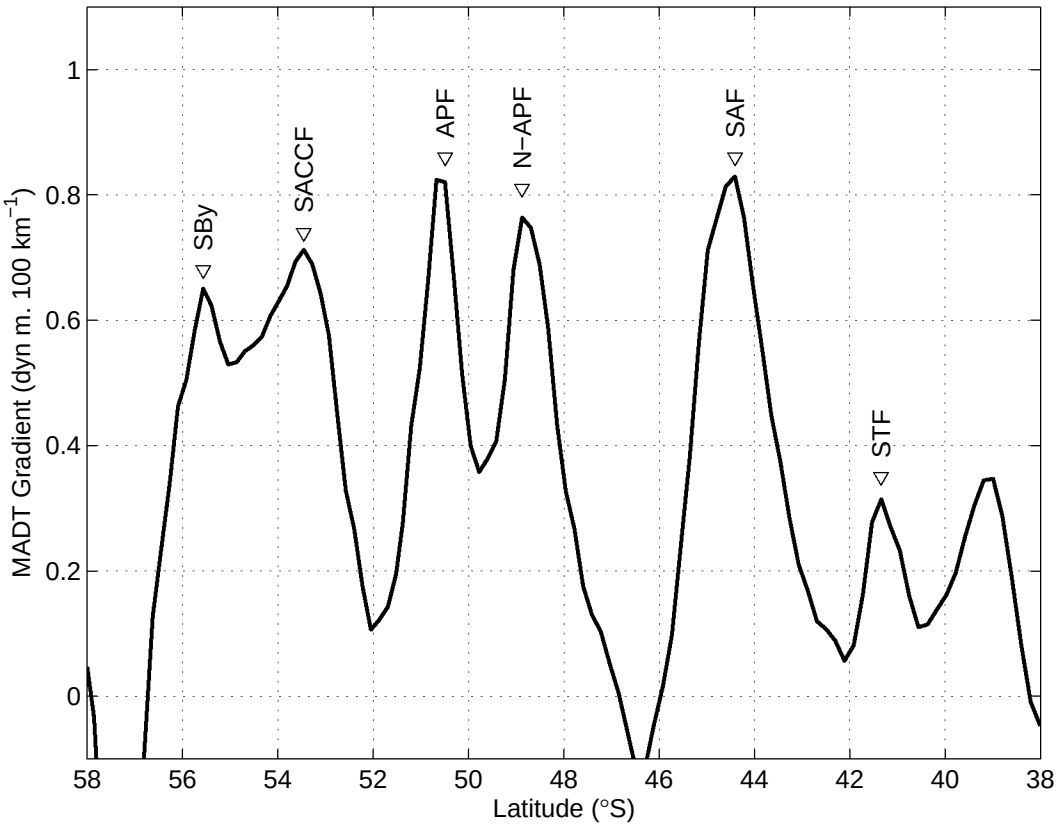

Figure 3.8: The mean MADT gradient (in dyn m. 100 km^{-1}), at the GH line, marks the positions of the ACC fronts (marked and labeled).

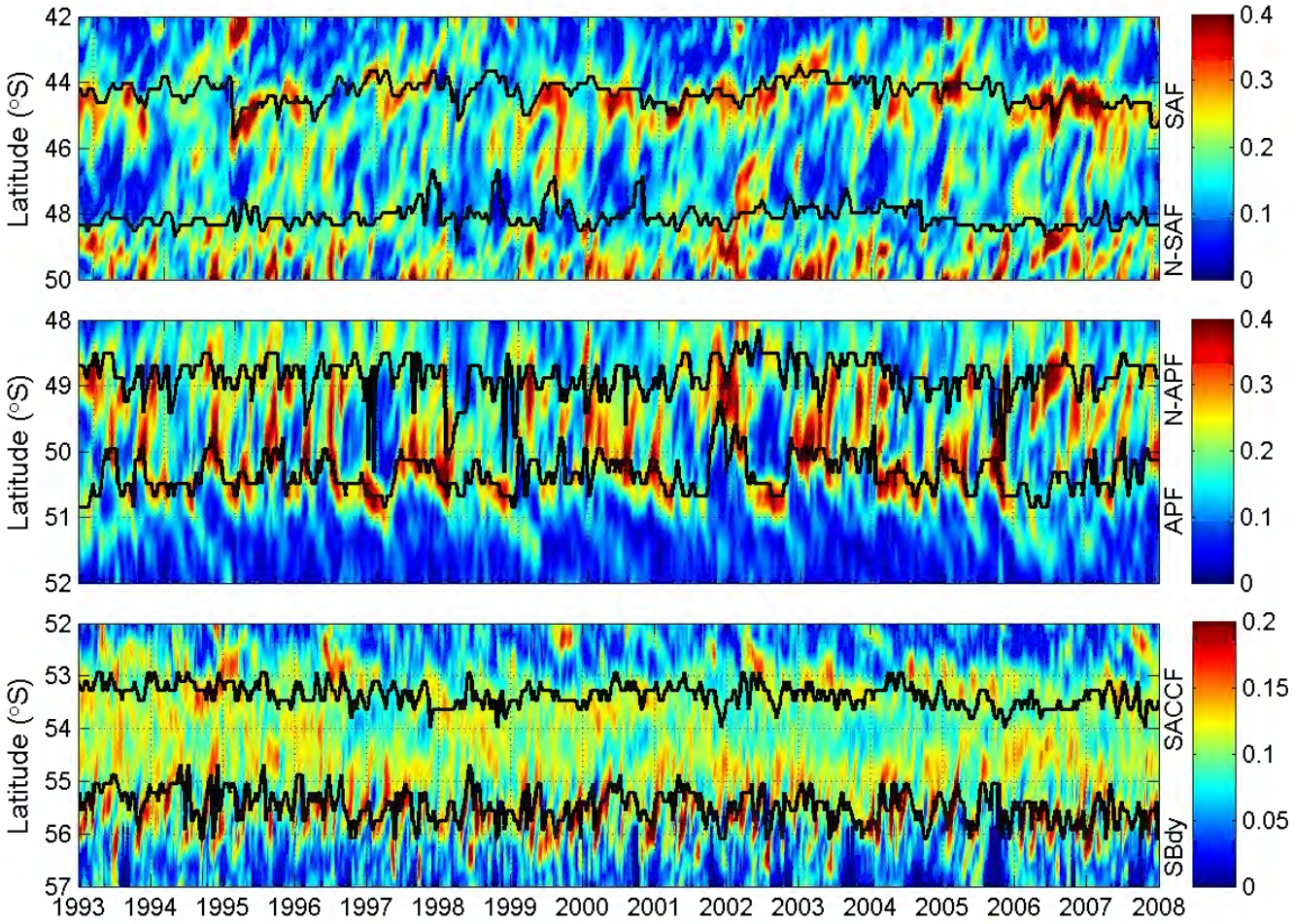

Figure 3.9: The positions of the ACC fronts, determined using the methods described in Section 3.5.2, are overlaid (black curves) on the MADT velocity magnitude (color plot; in $m.s^{-1}$) at the GH line.

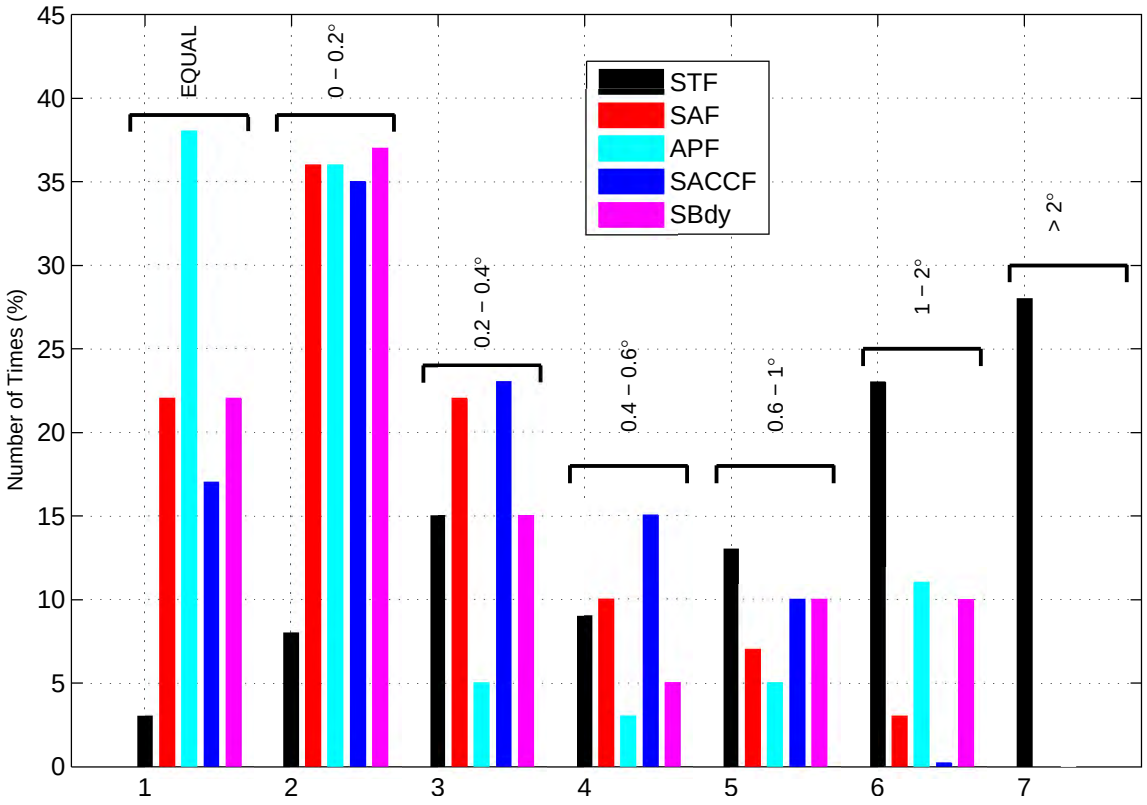

Figure 3.10: The frequency (in percent) of categorized distances between the position of the MADT-deduced ACC front and the local maximum in the MADT gradient, expected to be associated with that particular front. The categorized distances are displayed in the figure.

sections come from *Orsi et al.* (1995), and are the same fronts located by the localised peaks in the MADT gradient described in Section 3.5.2 and shown in Figure 3.8.

The positions of the ACC subsurface temperature fronts, from six GH XBT occupations, are shown in Figure 3.11. The position of the ACC fronts, determined using the AGEM temperature sections, as well as from the satellite altimetry (described above) are also shown in the figure for comparison. No altimetry-derived front positions are available for the last hydrographic section because the MADT data were not yet available for that period. However, AVISO "near real-time" altimetry data[1] (released within seven days), obtained during the cruise (BONUS-GH section) (*Speich and Dehairs*, 2008), were used to derive AGEM sections and the fronts positions, which allowed for comparison to the hydrographic front positions. This was the first documented occasion the AGEM was used on a research cruise to accurately determine the subsurface position of fronts and the subsurface structure of mesoscale features prior to arrival with the research vessel. This allowed for optimal spacing of subsequent CTD and biogeochemisty sampling stations during the voyage.

In Figure 3.11 the AGEM is for the most part effective at determining the latitudinal positions of the ACC fronts. Position matching, using MADT tracking, is least successful for the STF, where intense mesoscale variability and meandering in the front induces erratic meridional shifting. However, the AGEM still provides accurate positions when being compared with the *in situ* hydrographic positions. The AGEM positions of the SAF and APF are, on many occasions, the same as the MADT derived positions, which suggests the maximum gradients in the MADT are describing the subsurface temperature gradients correctly. On average, the SAF hydrographic front positions are found slightly further south than the two other methods. This may be caused by the fact that the subsurface expression of the front is not always found directly beneath to the surface expression (*Lutjeharms*, 1985), causing a spatial discrepancy between the maximum gradient in the altimetry SSH signal and the maximum gradient in the subsurface temperature. The positions of the APF overlap with considerable accuracy (only 30 km separating the observed and AGEM positions and 35 km separating the observed and MADT position) using all three methods, albeit the first XBT occupation. The weak nature of the SACCF and SBdy lead to determining the positions with less accuracy using the AGEM and MADT tracking, compared with the more baroclinically 'intense' SAF and APF. Furthermore, the fact that the SBdy was not reached during all the hydrographic transects, may lead to additional inaccuracies in determining its position using the AGEM. The SBdy was not reached during the second and third XBT occupations so we are unable to compare its observed position with the AGEM and MADT positions.

3.5.4 Validating the AGEM

The 16-year time series of ADT data, described in Section 3.5.1, are applied to the GEM empirical relationships to render time evolving profiles of temperature and salinity.

To assess the ability of the AGEM method to capture the thermohaline structure of the ACC accurately, we compare the measured data with time coherent AGEM temperature and salinity profiles. It is important to note that in order to provide an independent validation, the CTD data that are being compared are withheld from the empirical relationships used to infer the thermohaline information. The temperature and salinity sections produced by the AGEM (Figure 3.12) at the time of the second GH occupation can be compared with the observed CTD sections in Figure 3.2. The AGEM-reconstructed sections are remarkably similar to the observed sections. All water mass boundaries are well represented and major mesoscale features are accurately captured by the AGEM.

[1]It must be noted that using the "near real time" altimetry data does not allow for the exact knowledge of the satellite orbit and therefore its precision is less accurate than the "delayed time" data. However, such precision was not necessary for use on the research vessel.

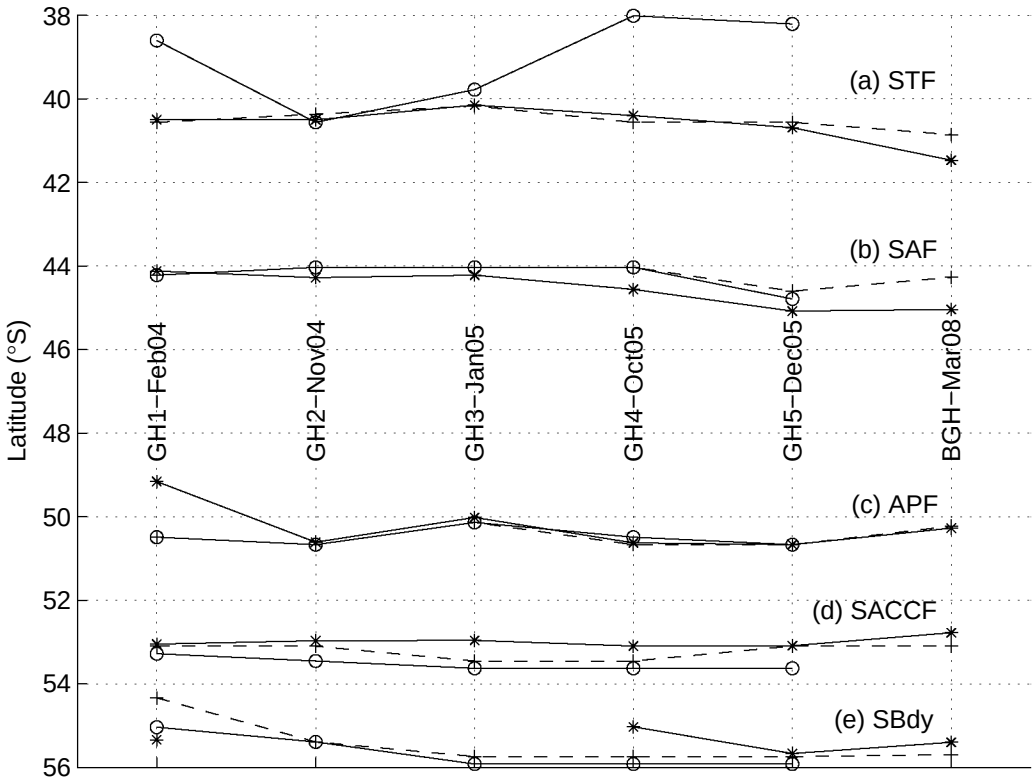

Figure 3.11: Latitudinal positions of the major ACC fronts determined; from six repeat XBT occupations at the GH line (stars), from the AGEM-estimated temperature sections (crosses), from satellite altimetry MADT data (circles).

In particular, the depth of the thermocline is correctly placed by the AGEM. This is similarly the case for the extent of the salinity minimum layer and its progression with depth towards the north. The representation of some mesoscale features is also reproduced accurately. A weak anticyclonic feature, crossed just north of the APF, is 'picked up' by the AGEM representations, although the AGEM does seem to exaggerate the strength of this feature to some extent. Additionally, an isolated 'patch' of warmer water, centered at ∼52°S and 500 dbar pressure, is also represented by the AGEM temperature section. However, slightly higher temperatures and greater salinities are created in the upper 150 dbar layer in the AGEM sections. This is responsible for the broad band of errors found in the upper layer extending between the SAF and SACCF. The latitudinal distribution of errors are spaced out relatively evenly, except for north of the SAF. The AGEM is expected to introduce greater inaccuracies, north of the SAF, where different water masses extraneous to the ACC are introduced by mesoscale activity, causing the relationship between the dynamic height and temperature and salinity to become multi-valued. Deeper residuals, located in the southern parts, are sporadic in nature (associated with an anticyclonic feature already mentioned) and are not found in the mean distribution of error with depth.

The rms of the residuals between the GEM and AGEM estimates and the *in situ* hydrography, for all the CTD stations used in this study, is summarized in Figure 3.13. In both methods, larger residuals are found in the upper 300 dbar, where seasonal and atmospheric effects increases the variability. The residuals decrease sharply for all properties, below the thermocline. The AGEM residuals are, on average, greater than those of the GEM. It is likely that sampling errors (see Section 3.5.1) introduced in the ADT data, when compared with *in situ* CTD derived dynamic heights, cause these higher residuals, especially between 300-1500 dbar for salinity and density. The higher residuals in the deep layers are not entirely caused by altimeter sampling errors but more due to the combination of the following two factors. The first factor is due to the very nature of the GEM projection, which removes a large fraction of the temporal variability associated with transient features, such as smaller-scale mesoscale eddies (*Sun and Watts*, 2001). This is especially evident in the northern domains of the ACC, where deep mesoscale features (Agulhas Rings) invade the SAZ. This variability is captured by the satellite altimeter and the error is projected to the deeper layers. Additionally, the ACC front positions vary more extensively in the northern domains. These variations are associated with at the least the upper 2000 m of the water column and therefore these changes are incorporated in the altimeter signal. The few CTD sections used to construct the GEM limit the extent to how much of this variability is captured in the GEM fields. The second factor is that the altimetry data includes the barotropic signal of the water column, which may cause additional error in the deeper layers by computing the AGEM-derived temperature and salinity baroclinic changes without the barotropic component. In the upper 500 dbar, the mean errors for both the GEM and AGEM in temperature, salinity and density are 0.4°C, 0.06 and 0.04 kg.m^{-3}, respectively. This is drastically reduced, by about ∼80%, to 0.07°C, 0.015 and 0.08 kg.m^{-3} for the same properties, between 500-2500 dbar.

Similarly to the GEM, we calculate the hydrographic variance captured by the AGEM in Figure 3.7. Surprisingly, by comparing the GEM and AGEM in Figure 3.7, the AGEM, at many depths, performs better than the GEM. Although only slightly, the AGEM captures more of the variance in the upper thermal and salinity layers but under performs in the upper density layer. The variance captured in the deeper salinity layer (>1000 dbar) performs better in the AGEM, where the percentage does not drop below 90%, while for the GEM, the variance captured drops to below 83% at ∼1750 dbar. The better performance of the AGEM in the deeper layers may be caused by the AGEM capturing a greater portion of the mesoscale variability (due the high spatial and temporal resolution of the altimetry data set), found predominantly in the northern ACC domains, compared with the CTD-derived

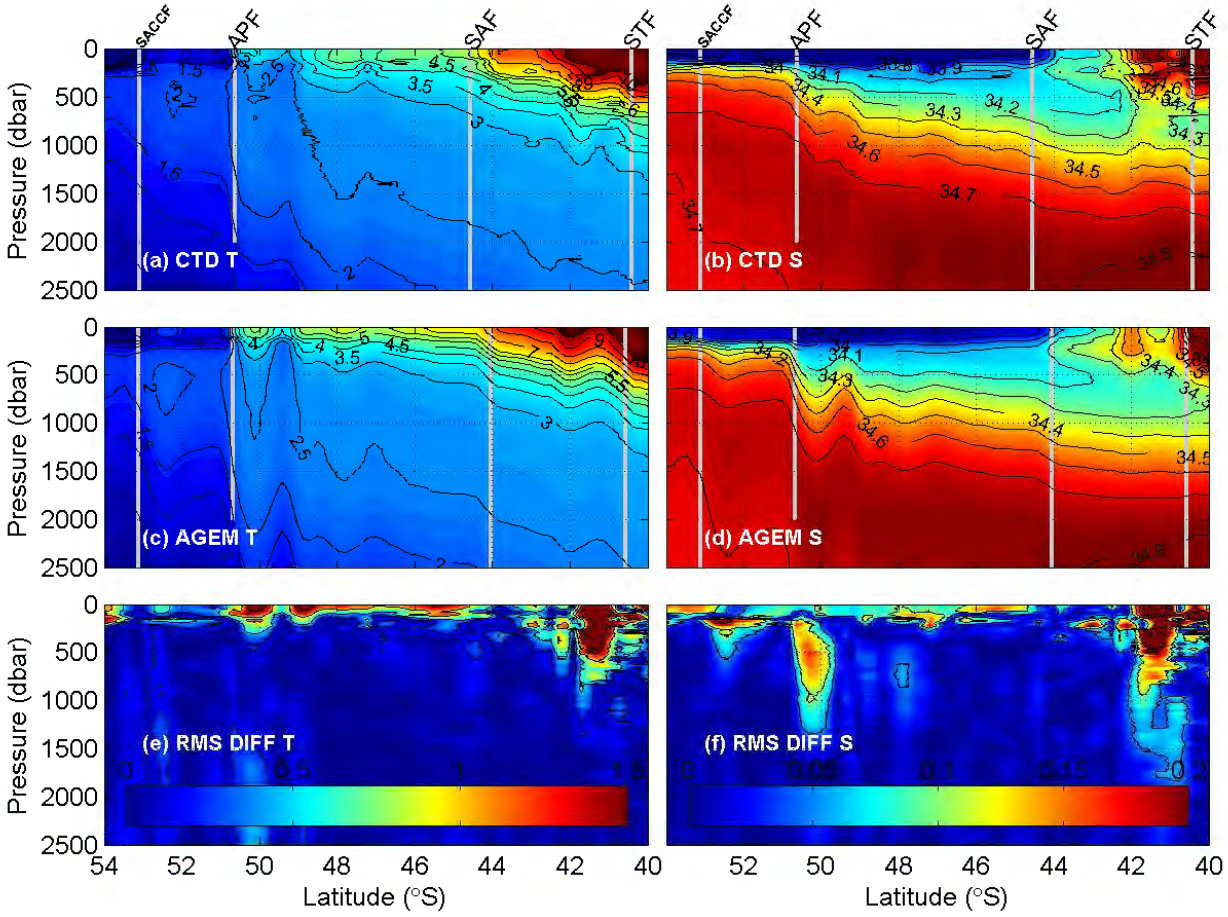

Figure 3.12: Comparison of the observed (a) temperature (in °C) and (b) salinity (in psu) sections with that of the AGEM produced sections (c & d) using solely the altimetry derived ADT data, from the time the observed section (second GH CTD transect) was carried out. The rms difference between the observed and AGEM-estimated sections of temperature and salinity are displayed in the bottom left and right panels, respectively (e & f). The ACC front locations, as determined using the criteria of *Orsi et al.* (1995), are indicated by the vertical grey lines.

GEM fields. This is enhanced in the deeper layers by the mesoscale features, which easily extend to over 2000 m deep. On average, up to 95% of the temperature, 86% of the salinity and 91% of the total variance is captured by the AGEM in the upper 500 dbar. Again, the percentage increases sharply below the thermocline (500-2500 dbar) to 97% for the temperature and density, and 94% for the salinity variance.

3.5.5 A baroclinic velocity field created using the AGEM

A sound method in which to test the performance of the GEM and AGEM is to relate its reproduced sections to the geostrophic velocity equation, which can assess whether the reproduced fields have correctly determined the baroclinic shear. This is done by comparing the GEM and AGEM velocity fields at depth and the total transport of the ACC, along the prime section upon which the GEM is built (GH line), to observed velocities and volume transports.

Firstly, we compute the total accumulated baroclinic transport of the ACC from the two CTD occupations of the

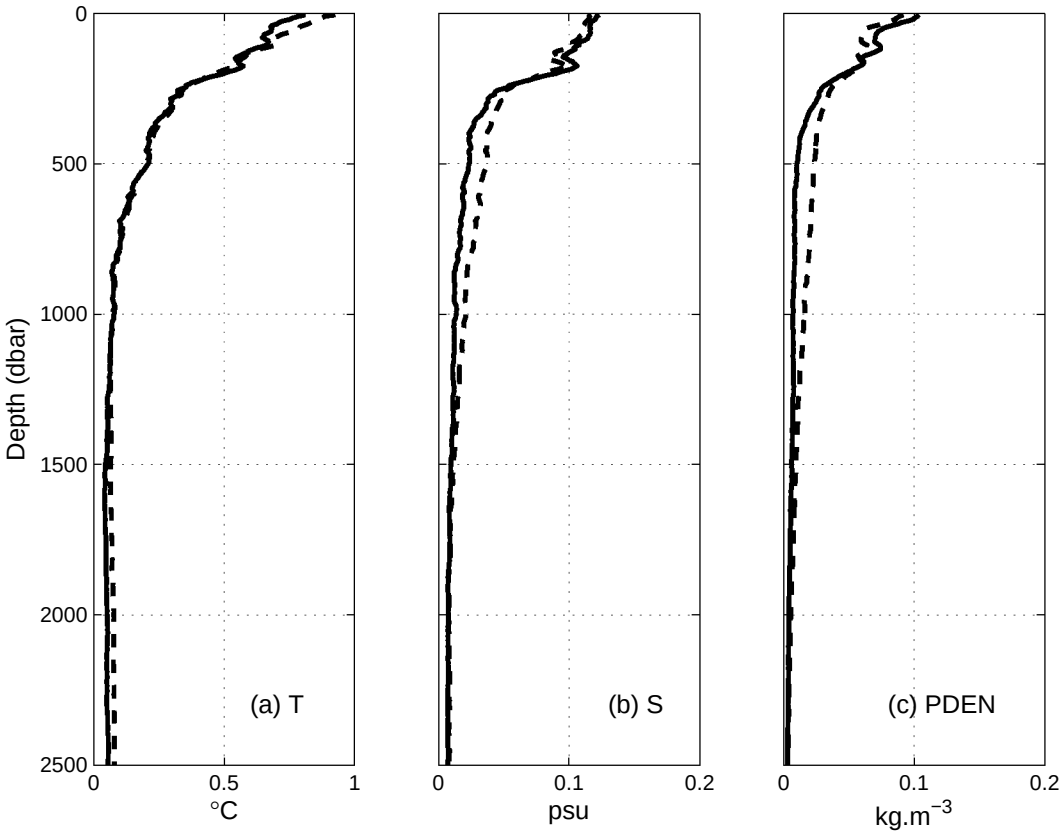

Figure 3.13: The mean rms residuals between the GEM (solid curve) and the AGEM (dashed curve) and the *in situ* hydrography are compared for (a) temperature, (b) salinity, and (c) density.

GH transect with the GEM and AGEM reproduced transports (Figure 3.14a & b). The transports are computed relative to 2500 dbar and accumulated from the SBdy to the STF, as determined using the criteria of *Orsi et al.* (1995), from the CTD sections. Again, in order to provide an independent validation, the CTD data that are being compared, are withheld from the empirical relationships when deducing the GEM temperature and salinity sections.

A general description of the accumulated transport shows that the main gains in transport are over the ACC fronts, particularly the SAF and APF (located on Figure 3.14a & b using arrows). The transport curves produced by the GEM, AGEM and observed estimates follow each other closely. Eddy variations in the transports are captured by all three methods, however, these variations are exaggerated by the AGEM method. A reason for this may be the temporal and spatial sampling difference between *in situ* dynamic heights and those derived using altimetry data. For example, the difference in sampling an eddy at its core or at its edges may lead to small differences in the calculated dynamic height that can lead to differing baroclinic transport curves. This is particularly evident in the transport curves (Figure 3.14b) due to the 'eddy like' feature that was crossed just north of the APF ($\sim$50°S) in the second GH CTD occupation (see Figure 3.2). Due to this anomalous feature, the maximum difference between the observed transport and the AGEM-derived transport reaches up to 15 Sv. In addition, higher AGEM transports may, in part, come from the SSH signal that includes a barotropic component, which we are yet unable to isolate due to a lack of information about the Earth's geoid (*Swart et al.*, 2008). The difference in baroclinic transport between the CTD estimates, and the GEM (crossed stems) and AGEM (circled stems) estimates are indicated along the x-axes in Figure 3.14a & b. The largest differences are found in the AGEM estimates, mostly near the fronts where eddy activity is greatest (mean rms difference is 2.9 Sv). Small differences, seldom exceeding 2.5 Sv (mean rms difference is 1.4 Sv) are found between the *in situ* and GEM transport curves. The overall differences between the methods are cancelled because the integrated transport over the ACC depend only on the end points, while the net transports are within 1-2.6 Sv of eachother. The end transports are given in Figure 3.14a & b and average 84.8 Sv and 94.4 Sv for the first and second occupation, respectively.

The AGEM-derived accumulated baroclinic transports are extended to the whole ADT time series and compared to the accumulated transports taken from *Swart et al.* (2008) who use a different approach (Figure 3.14c). The *Swart et al.* transport time series is estimated by exploiting an empirical relationship between the dynamic height (relative to 2500 dbar) and the accumulated baroclinic transport of the ACC from regional CTD sections and applying the ADT data at the GH line to this relationship to render continuous transport estimates. Both transport estimates are accumulated between the SBdy and the northern limit of the SAF (see *Swart et al.*, 2008 for more details on front limit determinations) in order to eliminate the large variability and associated errors found in the region of the STF. The AGEM-derived net transports average 94.2$\pm$3.1 Sv, which is roughly 10 Sv higher than the estimates made by *Swart et al.* (84.7$\pm$3 Sv). In the study by *Swart et al.*, the empirically-derived transports were often $\sim$8 Sv lower than the CTD-estimated transports. This means that the higher AGEM transport estimates are likely more accurate than the *Swart et al.* estimates when compared to the 'true' CTD estimates. Although the scale of variability between the two estimates is approximately the same, the short term variations in the transports are not very similar. These differences are likely caused by the more basic structure of the empirical relationship used in the study by *Swart et al.*, which may fail to record a portion of the smaller spatial scale variations in the accumulated transport. None-the-less, in time, further transport comparisons may help us to understand the complex nature of the ACC flow in space and time.

Secondly, the cross-sectional velocities, at 300 dbar, as deduced from the three methods, are shown in Figures 3.15a & 3.15b. For clarity, the three velocity estimates are offset from one another in the figure. Similarly for

the baroclinic transports, the highest zonal velocities occur over the ACC fronts, indicated on the figure. In most places, the fine velocity structures compare closely with one another in space. The mean rms difference between the observed and GEM produced velocities is only 0.01 m.s^{-1}. This error increases to 0.03 m.s^{-1} between the observed and AGEM produced velocities. The mean differences in the two methods for both GH occupations are summarized in Figure 3.15c. The highest errors are again located over the front regions, where eddy activity is higher and a large addition in error is attributed to the mesoscale feature crossed during the second CTD occupation along the GH transect, as discussed above. On two occasions in the first GH occupation, the AGEM transports within the ACC are approximately twice as large as the observed transports. Out of the ACC domain (north of ∼40°S), the errors increase due to the introduction of water masses that are characterized as having different T-S to dynamic height signatures, compared to those found in the ACC.

Finally, Figure 3.16 shows the 16-year mean structure of the zonal velocities along the GH transect deduced from the AGEM sections. Several well-defined velocity cores are identified across the span of the ACC. These core jets are closely associated with the mean positions of the main ACC fronts identified in Section 3.5.2 and indicated by the labeled arrows in the figure. The position of additional smaller velocity cores can be identified in the mean velocity field and are represented by small arrows in Figure 3.16. The velocity cores of the SSAF and NAPF (briefly mentioned in Section 3.5.2) can also be clearly made out. We are unable to identify the smaller cores in the mean MADT and velocity magnitude distribution plots in Section 3.5.2, however, they exist in the mean AGEM velocity field. The southern jets are, in some places, interspersed with velocity reversals that may be associated with eddy velocity reversals due to eddy genesis taking place near the fronts. This representation emphasizes the strength of the main ACC fronts that, on average, extend to pressures greater than 2000 dbar. The deepest reaching front is the APF, where mean velocities are greater than 0.8 cm.s^{-1} and often the velocities exceed 1.5 cm.s^{-1} at 1500 dbar. The smaller velocity cores are considerably weaker and do not extend far beyond 1000 dbar in pressure.

A future study will make use of the AGEM to zonally expand the velocity field to include the meridional velocity component. This will be able to help answer questions related to meridional exchanges of heat and fresh-water in the Southern Ocean.

3.6 Summary

Major current systems, such as the ACC, experience high temporal variability, yet the dominance of the GEM in these systems illustrates that thermohaline fields are remarkably organised in streamfunction space, as previously shown by *Book* (1998), *Meinen and Watts* (2000), *Sun and Watts* (2001). This gives us confidence in the GEM's ability to capture most of the system's variability.

The ACC is well suited to exploiting the GEM method because each value of dynamic height is characterised by a particular T-S curve, thereby illustrating that source waters have undergone similar physical processes to arrive at a particular streamfunction (*Watts et al.*, 2001). This becomes more complicated in confluence regions where different source waters advect and converge, supplying different thermohaline properties along the same vertical coordinate at different times. This is precisely what occurs in the northern domains of the GH line, where subtropical Agulhas waters enter the ACC system and supply warm, salty water masses to the cooler, fresher environment of the SAZ (*Gladyshev et al.*, 2008; *Swart et al.*, 2008; *Swart and Speich*, 2009; *Dencausse et al.*, 2009). This was previously noted south of Africa by *Sun and Watts* (2001) where, in the upper thermal layer, temperature residuals where more than twice that of those found in the Australia sector of the Southern Ocean.

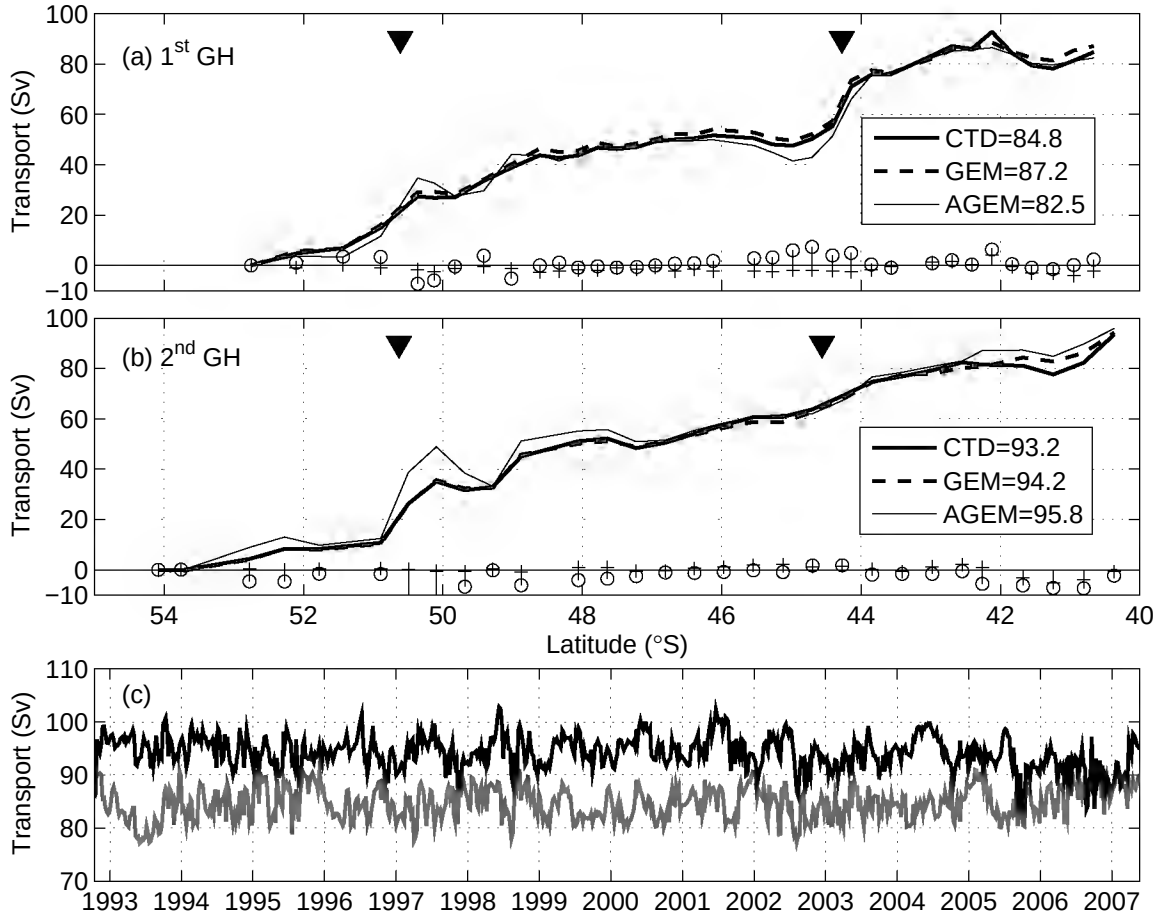

Figure 3.14: Comparison between accumulated baroclinic transports of the ACC, estimated from the (a) first and (b) second GH CTD occupations (solid curves), and those estimated using the GEM-estimated sections (dashed curves), and AGEM-estimated sections (thin curves). The difference between the GEM and hydrographic estimates (crossed stems), and the AGEM and hydrographic estimates (circled stems), are displayed along the x-axis. The hydrographic latitudinal positions of the SAF and APF are marked by northern and southern arrows, respectively. (c) The AGEM-derived net accumulated transports for the ACC (black curve) are compared with the estimates made by *Swart et al.* (2008) (grey curve).

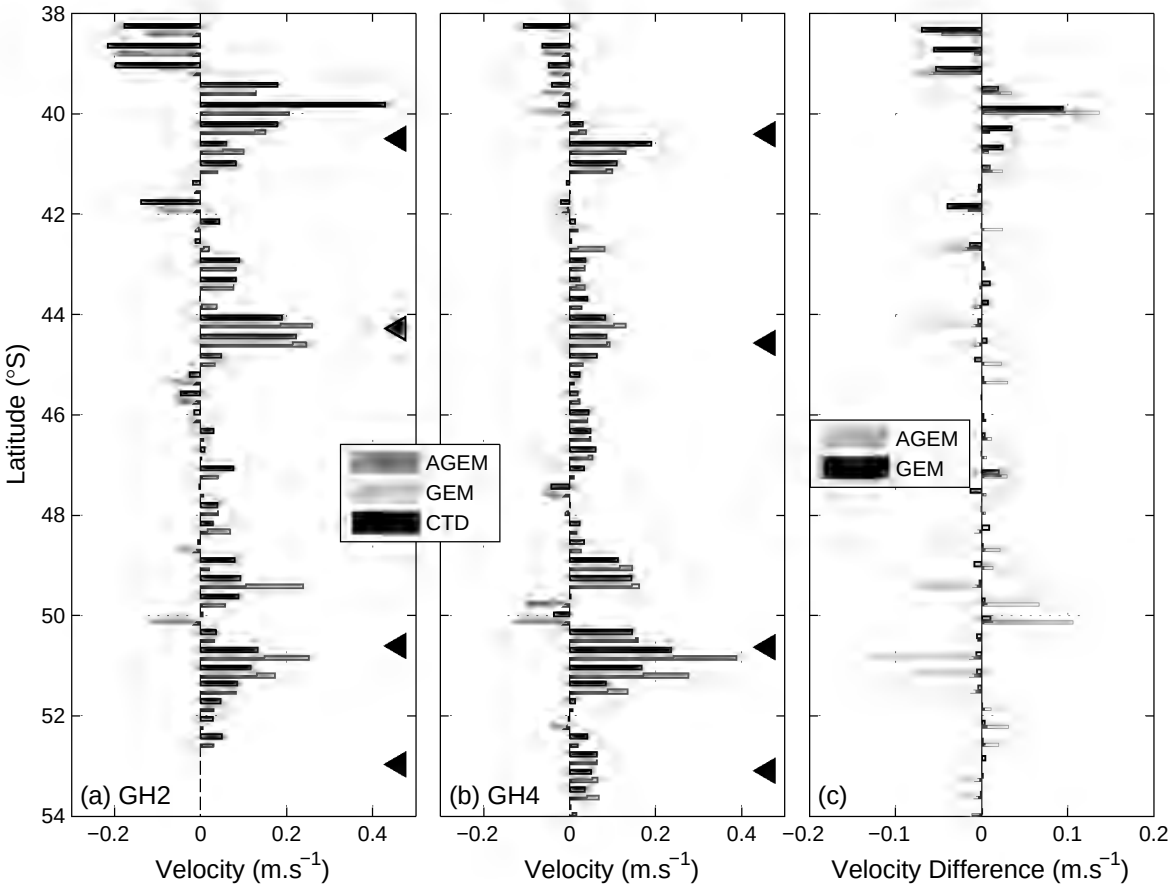

Figure 3.15: The cross-sectional velocities at 300 dbar (in m.s^{-1}), estimated from the (a) first and (b) second GH CTD occupations (black bars) are compared with the velocities estimated from the GEM- (light grey bars), and AGEM-derived (dark grey bars) sections. The latitudinal positions of the ACC fronts, determined from the CTD temperature sections are indicated on the figure from north to south as follows: STF, SAF, APF, SACCF. The mean velocity difference between the CTD-estimated velocities and those estimated from the GEM and AGEM-derived sections are summarised in the right-hand panel (c).

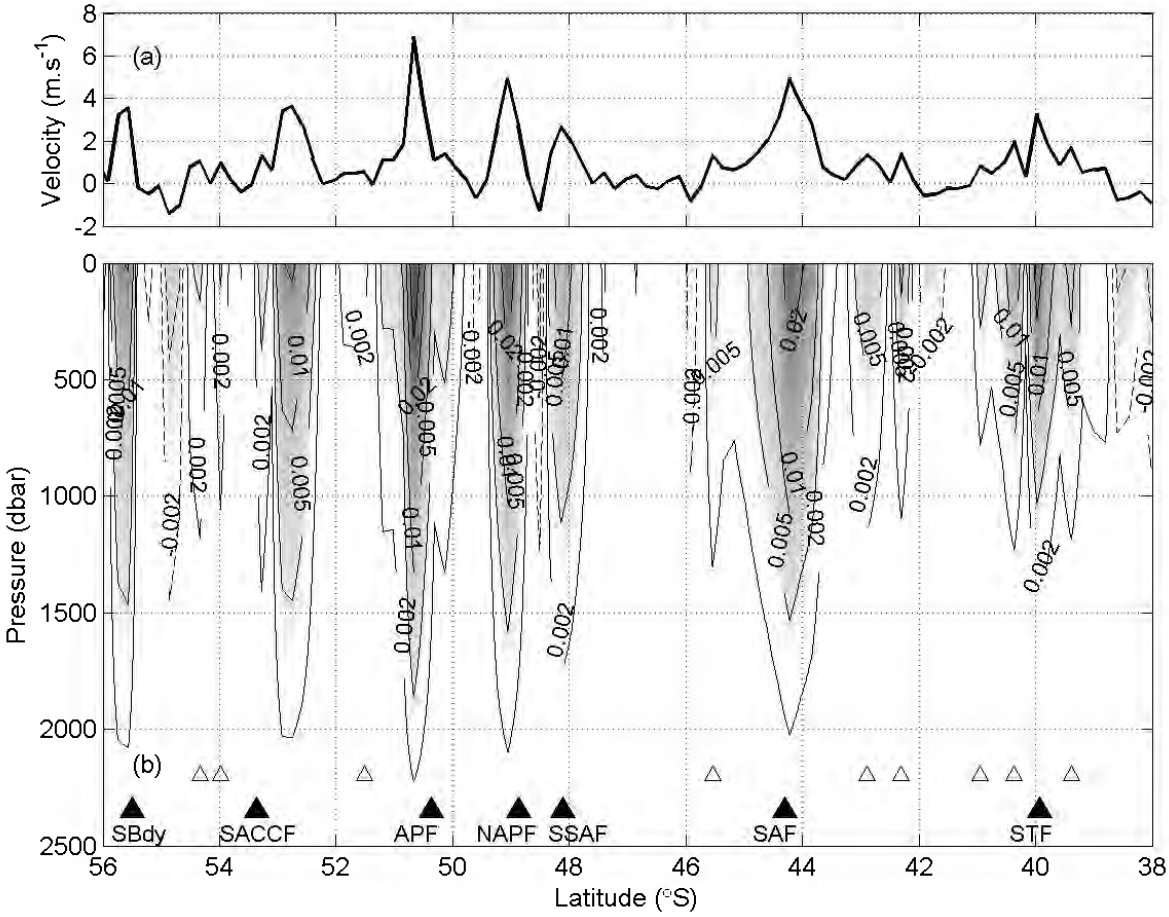

Figure 3.16: (a) The sum of the time-averaged (1992-2008) latitudinal distribution of the cross-sectional velocities (in m.s^{-1}) at the GH line shown in (b). The large arrows show the mean positions of the major ACC fronts, identified by the ADT, while smaller arrows show those additional jet-like structures that are not clearly seen in the MADT velocities, presented in Figure 3.9.

Despite these intrusions, the GEM-based correlations, produced from a large assemblage of hydrocasts, are sensitive to the variability and changes occurring within the region of interest, conserving all the thermohaline structures found in the hydrography and even capturing transient structures with small vertical scale. The GEM captures more than 96% of the hydrographic variance below the thermocline. The rms error in the upper 300 dbar for temperature and salinity are 0.54°C and 0.09, respectively. This decreases to, on average, 0.07°C and 0.02 below the thermocline. The GEM has shown its strength at determining, with great accuracy, the locations of maximum baroclinic shear and hence the positions of the ACC fronts. This is further tested by comparing baroclinic transports and velocities with pressure, which shows that the GEM methods produce closely comparable end transports of the ACC and the rms errors in the velocity field, at 300 dbar, are less than 0.01 and 0.03 $m.s^{-1}$ for the GEM and AGEM, respectively.

The extensive time series of altimetry data have to be more readily exploited in the Southern Ocean, where *in situ* data are so sparse and sampling is limited to the austral summer months. The combination of satellite altimetry data to the GEM greatly improves the spatial and temporal sampling resolution of the region, while giving us much needed insight into the time-varying subsurface structure of the ACC. In Part 2 of this study (*Swart and Speich*, 2009), the continuous time series of thermohaline fields are used to estimate the heat and salt content variability at the GH line and therefore the physical processes that dominate the behavior of the ACC. These estimates provide insight into the subsurface thermohaline variations of each ACC front and frontal zone, which previously has not been undertaken at such high spatial and temporal resolutions.

The ARGO float program is for the first time providing relatively good spatial coverage in the Southern Ocean. In time, these combined with hydro casts, will provide a large quantity of T-S profiles, which will greatly enhance the use of the GEM in all regions of the Southern Ocean and allow for extensive testing of numerical ocean models, that presently have little data to perform validations on.

The combination of the AGEM sections and velocities, and the positions of the ACC fronts and spatial boundaries, defined using altimetry data, provides a powerful scientific tool towards improving our understanding of the variability occurring within the ACC. The accuracy of the AGEM to reproduce subsurface thermohaline conditions serves as a catalyst to further studies that utilize time series analysis (e.g. *Swart and Speich*, 2009). The 16-year time series of AGEM observations will also allow for statistical decomposition of variance signals found in these results.

Acknowledgement

This research forms part of the first author's PhD, completed at the University of Cape Town, and supported by the South African National Antarctic Program (SANAP) and INSU-CNRS, France. We are grateful to C. Kermabon for her help with data processing and to A. Prigent for preparing the ARGO float data, which were supplied by the Coriolis Operational Oceanography Center, France. S. Swart thanks CNRS in funding research visits to the Laboratoire de Physique des Océans (LPO), Université de Bretagne Occidentale, France. Thanks are extended to S. Gladyshev and A. Sokov for their efforts in implementing the GH CTD sections. J. R. E. Lutjeharms thanks the STIAS (Stellenbosch Institute for Advanced Study) for a fellowship during which his contribution was finalised. The altimetry products are supplied by the CLS Space Oceanography Division, Toulouse, France. Lastly, the authors would like to thank two anonymous reviewers for their time in reviewing this paper.

Chapter 4

Paper III: An altimetry-based Gravest Empirical Mode south of Africa Part 2: Dynamic nature of the ACC fronts

This chapter is based on the work published as:
Swart, S. and S. Speich (2009), An altimetry-based Gravest Empirical Mode south of Africa. Part 2: Dynamic nature of the ACC fronts, *J. Geophys. Res.*, doi:10.1029/2009JC005300.

Abstract

In Part 1 of this study, altimetry data are applied to the gravest empirical mode south of Africa to yield a 16-year time series of temperature and salinity sections. In this part of the study, the time series of temperature and salinity sections are used to derive weekly estimates of heat content (HC) and salt content (SC) at the GoodHope meridional transect of the Antarctic Circumpolar Current (ACC). These estimates compare favorably to observed data. The resulting 16-year time series of HC and SC estimates are used to explain the subsurface thermohaline variability at each ACC front and frontal zone. The variability at the Subantarctic Zone (SAZ) is principally driven by the presence of Agulhas Rings, which occur in this region approximately 2.7 times per annum and are responsible for the longest and highest scales of observed variability. The variability of the SAZ is responsible for over 50% and 60% of the total ACC HC and SC variability, respectively. Poleward of the SAZ, the variability is largely determined by the influence of the local topography on the fronts of the region and can be explained by the conservation of potential vorticity. Wavelet analysis is conducted on the time series of meridionally integrated HC and SC in each ACC front and frontal zone, revealing a consistent seasonal mode that becomes more dominant towards the southern limit of the ACC. The lower frequency signals are compared with two dominant modes of variability in the Southern Ocean. The Southern Annular Mode correlates well with the HC and SC anomaly estimates at the Antarctic Polar Front, while the Southern Oscillation Index appears to have connections to the variability found in the very southern domains of the ACC.

4.1 Introduction

The Antarctic Circumpolar Current (ACC) consists of multiple branches and filaments that are grouped together to represent the main ACC fronts (*Sokolov and Rintoul*, 2007a, 2007b, 2009a, 2009b; *Swart et al.*, 2008). The fronts often exhibit considerable latitudinal variability on their circumpolar path, as was first noticed by *Deacon* (1933) over 70 years ago. These forms of variability are dominant in the mesoscale band induced by front meandering and eddy genesis (*Mackintosh*, 1946; *Joyce et al.*, 1978; *Lutjeharms and Valentine*, 1988; *Stammer*, 1998; *Moore et al.*, 1999; *Philips and Rintoul*, 2000; *Morrow et al.*, 2004) and are vital to meridional fluxes of heat and salt within the Southern Ocean. This suggests that a large portion of the variability of the ACC is determined by the individual behavior of the ACC fronts and, to a lesser degree, the regions between the fronts. To date, little work has been done to better understand the fronts' regional and temporal variability, notably in the African sector of the Southern Ocean (*Koshlyakov et al.*, 1985; *Nowlin and Klinck*, 1986; *Gouretski and Danilov*, 1994; *Ansorge et al.*, 2006).

Previous measurements of heat content (HC) and salt content (SC) in the Southern Ocean have been based on few synoptic hydrographic transects, the majority of which were completed in austral summer only. To overcome the poor temporal and spatial resolution of measurements in the African sector of the Southern Ocean, we make use of the gravest empirical mode (GEM) method, first described for the Southern Ocean by *Sun and Watts* (2001), and apply this technique to weekly composites of satellite altimetry data. The GEM method makes use of all available hydrographic casts from the south-eastern sector of the Atlantic Ocean and projects the data into a baroclinic stream function space, parametrized by pressure and dynamic height. Further details can be found in Section 4.2.2. The development and validation of this method is described in Part I of this study (Swart, S., S. Speich, I. J. Ansorge and J. R. E. Lutjeharms, 2009, in review, JGR; hereinafter referred to as SSAL09). From the GEM, we derive the subsurface HC and SC structure, along a permanent geographic locale, enabling us to better understand the temporal variability associated with the region and the ACC system. The GoodHope (GH) line is the geographic locale used in this study (*Ansorge et al.*, 2004; *Speich and Arhan*, 2007). The GH program provides the ideal platform to combine the GEM with satellite altimetry, as demonstrated by SSAL09.

The GH line crosses the south-east Atlantic Ocean, which is recognised one of the most dynamic and variable ocean domains in the world (*Wunsch and Stammer*, 1995; *Boebel et al.*, 2003). This region is identified as the meeting point of the eastward flowing ACC and the Agulhas Current, acknowledged as one of the world's strongest western boundary currents (*Bryden et al.*, 2005; *Lutjeharms*, 2006). The Agulhas Current's westward termination is marked by the Agulhas Retroflection, which produces an intermittent stream of Agulhas Rings (*Gordon*, 1985; *Lutjeharms and Gordon*, 1987; *Duncombe-Rae*, 1991; *Lutjeharms*, 1996; *de Ruijter et al.*, 1999; *Boebel et al.*, 2003; *Lutjeharms*, 2006) that generally propagate in a north-westerly direction (*Schouten et al.*, 2000). Irregularly Agulhas Rings propagate on a west to south-west course. These features directly influence the stability and continuity of the Subtropical Front (STF) (*Lutjeharms*, 1988; *Lutjeharms and Valentine*, 1988; *Belkin and Gordon*, 1996; *Dencausse*, 2009) and have been located and sampled in the Subantarctic Zone (SAZ) (*Swart et al.*, 2008; *Gladyshev et al.*, 2008). These anomalies may play a significant role in the local variability of the northern ACC region, which has implications for the behavior of local biology and bio-geochemistry.

The GEM-produced sections of temperature and salinity are used in this study to quantify the property signatures of these features and the possible impact they may have in the region. We also evaluate the role elevated topography and bathymetric passages may have in bringing about instabilities to the flow of the ACC fronts, at the GH line. The final parts of this study make use of meridionally integrated GEM-estimates of HC and SC

to quantify the variability experienced in the region. An attempt to connect the long-term variability with the well-known modes of southern hemisphere atmospheric variability is also briefly covered.

4.2 Material and Methods

4.2.1 Data

Data from eight conductivity-temperature-depth (CTD) sections, conducted between 1984-2005, are used to set up the GEM fields for the oceanic region connecting the south-western tip of South Africa and the Antarctic continent via the Greenwich Meridian (see SSAL09). Included are two repeat high-resolution (average station spacing is ∼50 km) CTD sections along the GH line (*Gladyshev et al.*, 2008; *Swart et al.*, 2008).

The 'Maps of Sea Level Anomaly (MSLA)' and 'Maps of Absolute Dynamic Topography (MADT)' data, available from CLS/AVISO have been used in this study. Both products are constructed on a 1/3° Mercator grid and are available between 14 October 1992 and 23 January 2008, at weekly intervals. This yields a continuous time series of 798 weeks of data. We choose to use the 'up-to-date' data files that make use of all the altimeter data available for each period because it is best suited at resolving the fine-scale structures and variability associated with the ACC.

4.2.2 The GEM and AGEM

Hydrographic casts of temperature and salinity are projected into stream function space, parametrized by pressure and dynamic height. This method demonstrates the remarkable relationship between the surface dynamic height (relative to 2500 dbar) and the subsurface thermohaline structure, which has been tested across the ACC south of Africa by SSAL09. Parameterising hydrographic data in this way captures more than 97% of the temperature and density variance and 93% of the salinity variance between the surface and 2500 dbar (SSAL09).

The GEM fields retain many of the characteristic hydrographic features normally identified when observed data are represented in geographic space. To emphasise this, a comparison between the vertical profile of the hydrographic variables and the GEM fields is shown in Figure 4.1. Each set of vertical temperature and salinity profiles (thin curves) are representative of a dynamic height cluster that has a range of 0.01 dyn m (1 dyn m = 10 $m^2.s^{-2}$). The grey curve represents the mean GEM vertical structure within the same dynamic height range as those of the observed temperature and salinity profiles. The consistency between the two representations emphasizes the ability to parametrize thermohaline variables by dynamic height in this region. Examples of these include the subsurface temperature minimum layer in the upper 200 dbar, located south of the Antarctic Polar Front (APF) and the characteristically low saline waters, associated with the Antarctic Intermediate Water layer, extending between the surface and approximately 1000 dbar. The variations between the two representations is directly related to the amount of mixing between different water masses. The profiles, for example, within the 1.9 dyn m grouping, exhibit less defined vertical structure in the upper 600 dbar, due to more pronounced interaction between subtropical and subantarctic water masses, while the profiles, within the 0.7 dyn m grouping, display very similar structure below ∼200 dbar, where water mass communication is infrequent. The GEM reveals its efficiency at removing the small scale variations in the vertical structure that are represented as the small fluctuations in the real data.

Parameterising the data by pressure and dynamic height allows us to apply this method to altimeter-derived absolute dynamic height (ADT) data. This yields a continuous time series of temperature and salinity profiles, across the ACC (1992-2008), and forms the basis for the analysis in this study. The ADT is produced by combining

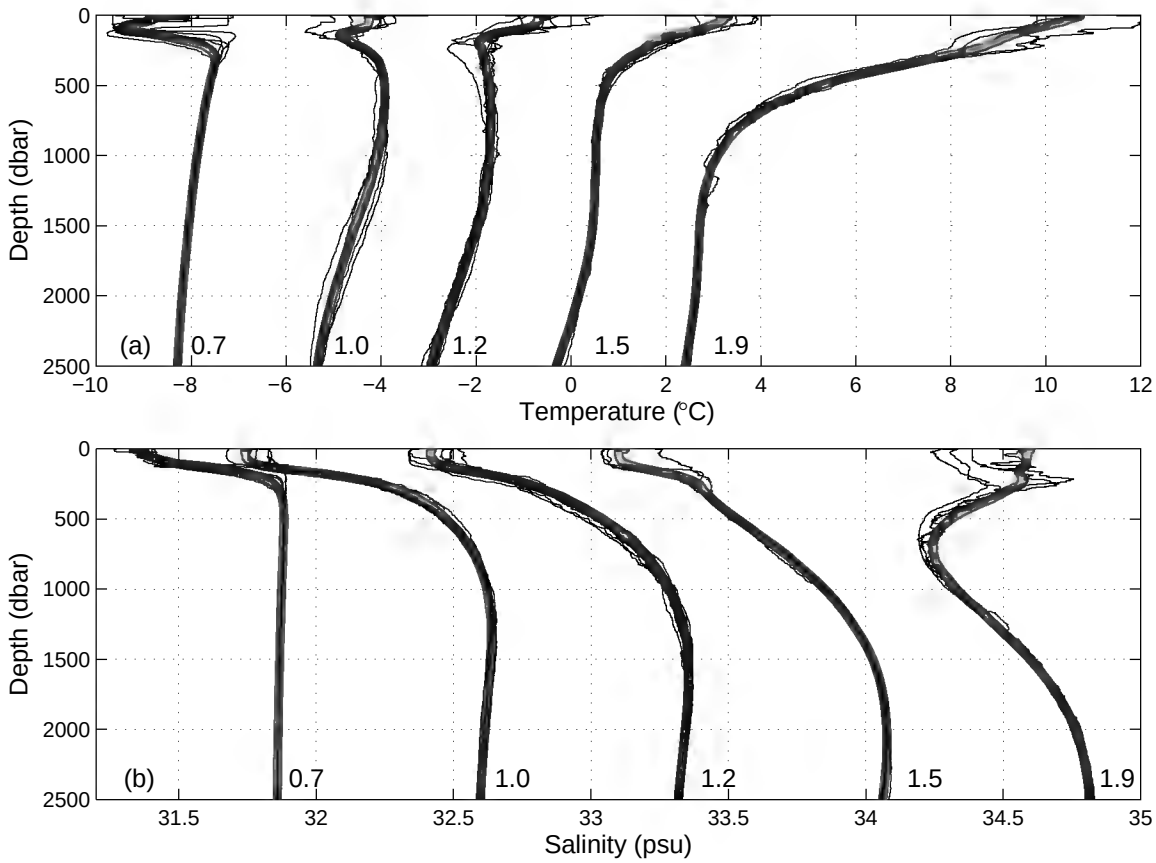

Figure 4.1: Groupings of observed (a) temperature and (b) salinity profiles (thin black curves) that are found within 0.01 dyn m of the central values displayed. The thick grey curves show the corresponding GEM-estimated profiles. The temperature profiles are each offset to the left by 2°C and the salinity profiles are each offset to the left by 0.7.

altimeter Sea Surface Height (SSH) anomalies to a mean dynamic height state, derived from repeat hydrographic sections (CTD and XBT), at the GH line (*Swart et al.*, 2008). The ADT is combined with the GEM to create the AGEM (Altimetry Gravest Empirical Mode). For further details on the construction of the ADT and the AGEM, refer to *Swart et al.* (2008) and SSAL09, respectively.

4.2.3 Front Positions

Altimetry SSH data has proven to be largely representative of the baroclinic shear in the water column. This indicates that local maxima in the dynamic height gradient are representative of the maximum baroclinic shear, associated with fronts (*Hughes and Ash*, 2001; *Sokolov and Rintoul*, 2007a; 2007b; 2009a; 2009b; *Swart et al.*, 2008). In this study we make use of both the core positions of the ACC fronts, and the frontal boundary zones (region between two limits that consistently capture the maximum frontal velocities). These boundaries are located by exploiting both the height and geostrophic velocity information from the MADT data, at the GH line. A complete description of the methodology used to define the core position of the ACC fronts can be found in SSAL09. The methodology used to define the frontal boundary zones has been described by *Swart et al.* (2008). In brief, these limits are defined as follows: continuous isolines of MADT data follow the lowest velocity magnitudes in between the

Table 4.1: Abbreviations, latitudinal ranges and mean widths of the frontal zones described in this study.

Frontal Zone	Abbreviation	Latitudinal Range (°S)	Mean Width (km)
Subantarctic Zone	SAZ	38.2-46.8	540
Antarctic Polar Frontal Zone	APZ	43.7-51.2	573
Southern ACC Zone	SACCZ	47.6-54.9	440
Southern Boundary Zone	SBZ	51.8-57.8	217

main fronts throughout the altimetry time series. These MADT isolines, therefore, depict the boundary between successive fronts. This allows us to define the spatial volume of each individual front, thus providing a more accurate measurement of the HC and SC related to that particular front. Table 4.1 outlines all frontal zones discussed in this study, including their abbreviations, latitudinal ranges and mean widths.

4.2.4 Heat and Salt Content

The HC and SC is integrated throughout the upper 2500 dbar of the water column. The HC is calculated in the conventional manner:

$$HC = \int_{0}^{2500} \rho \, C_p \, T \, dz \, , \tag{4.1}$$

where ρ is the density of seawater (1027 $kg.m^{-3}$), C_p is the heat capacity of seawater at constant pressure (4000 $J.kg^{-1}.K^{-1}$), dz is the thickness of the water column, and T is the potential temperature (in °C). The SC is estimated as:

$$SC = \int_{0}^{2500} 0.001 \, \rho \, S \, dz \, , \tag{4.2}$$

where S is the salinity.

4.3 Comparing the GEM-derived heat and salt content with direct observations

The ability of the AGEM to accurately capture the thermohaline structure of the ACC south of Africa has been demonstrated in the first part of this study (SSAL09). To further validate the results presented in this paper, we compare the HC and SC, deduced from temperature and salinity sections produced by the AGEM, to *in situ* observations from repeat CTD occupations at the GH line (Figure 4.2 and 4.3). Prior to calculating the HC and SC, using the AGEM, the GEM fields are recalculated, after excluding the observed section to which it is being compared to. This is to ensure that the reproduced data are fully independent of the directly measured data.

The HC and SC meridional gradients in the observed and AGEM-produced data sets compare well. The representations are particularly similar at the Antarctic Polar Frontal Zone (APZ) (between ∼44-49°S) where HC gains and mesoscale perturbations are especially weak (to be illustrated in Section 4.4). Elevated differences (shown along the x-axis in Figure 4.2 and in Figure 4.3c) are located over the APF at approximately 50°S. This may be

explained by the higher mesoscale variability found at this front (explained in more detail in Section 4.4). Within the ACC domain, the highest differences are found in the Subantarctic Zone (roughly between 40-45°S). The intrusion of subtropical waters by eddy features and strong meanders at the STF, and on occasions Agulhas Waters (*Swart et al.*, 2008; *Gladyshev et al.*, 2008) by Agulhas Rings, reduce the accuracy of the GEM in this region. This is because the GEM relies on the principle that temperature and salinity values be aligned with a single value of dynamic height (*Sun and Watts*, 2001). The large discrepancy of >200 $kg.m^{-2}$ in SC at ∼41°S, for the second CTD occupation, is caused by the inability of the AGEM to accurately capture the salinity magnitude associated with an Agulhas Ring that was crossed during the CTD transect (see *Swart et al.*, 2008 and SSAL09 for further details on the hydrographic and altimetric structure of this particular feature). North of ∼40°S and extraneous to the ACC, the GEM's accuracy to determine the observed thermohaline structure decreases sharply. This is due to the high level of mixing of very different water masses associated with the known mesoscale turbulence and Indo-Atlantic exchange taking place in this region (*Duncombe-Rae*, 1991; *Lutjeharms*, 1996; *de Ruijter et al.*, 1999; *Boebel et al.*, 2003). The consequence of this is that the relationship between temperature and salinity and the dynamic height changes and is no longer one-to-one. The rms error in HC and SC, due to the presence of Agulhas Rings between 38-42°S, is estimated as 4.22 $\times 10^9 \pm 1.4 \times 10^8$ $J.m^{-2}$ and 170.6 ± 24 $kg.m^{-2}$, respectively.

Eddy variations in the HC and SC are captured by the AGEM, yet these variations are somewhat exaggerated (refer to SSAL09 for a more detailed description of AGEM exaggeration of mesoscale features). A portion of the differences throughout the ACC could be explained by errors introduced to the altimeter data used to create the ADT time series (*le Traon et al.*, 1998). Further discrepancies could, in part, come from the SSH signal that includes a barotropic component, which we are yet unable to isolate in *in situ* observations due to a lack of information about the Earth's geoid (*Swart et al.*, 2008). Lastly, differences in spatial and temporal sampling between the altimeter and *in situ* observations may introduce additional errors. The mean rms differences between the observed and AGEM-estimated HC and SC, between the surface and 2500 dbar, are 1.22 $\times 10^9$ $J.m^{-2}$ and 39.8 $kg.m^{-2}$, respectively. Major differences are associated with the upper layers, where variability at all scales is the largest. Nonetheless, the rms represents less than 10% of the signal. We can therefore trust the method and reconstruct the subsurface thermohaline structure of the water column at the GH transect using the whole altimetry time series.

4.4 Hovmöller analysis of heat and salt content

The methods presented in Section 4.2.4 are applied to the time series of AGEM-produced sections of temperature and salinity to derive the HC and SC, respectively, between 0-2500 dbar, along the latitudinal extent of the GH line. The temporal mean of both HC and SC at each latitudinal grid point have been removed from this time series to yield the heat content anomaly (HCA) salt content anomaly (SCA) estimates, respectively.

4.4.1 Heat and salt content anomaly

We illustrate the HCA and SCA throughout the upper 2500 dbar of the water column in Figure 4.4. The positions of the ACC fronts, as determined using altimetry data (refer to SSAL09 for methodology), are depicted using solid black lines. For simplification, we make use of the 'classical' ACC fronts that have been described by *Orsi et al.* (1995) and not the multi-frontal structure defined by *Sokolov and Rintoul* (2007a; 2009a; 2009b). Indeed, the discussion of the heat and salt content behavior for the fewer classically-defined fronts is simpler and more robust when associated to large-scale modes of variability compared with a more refined study for each secondary frontal

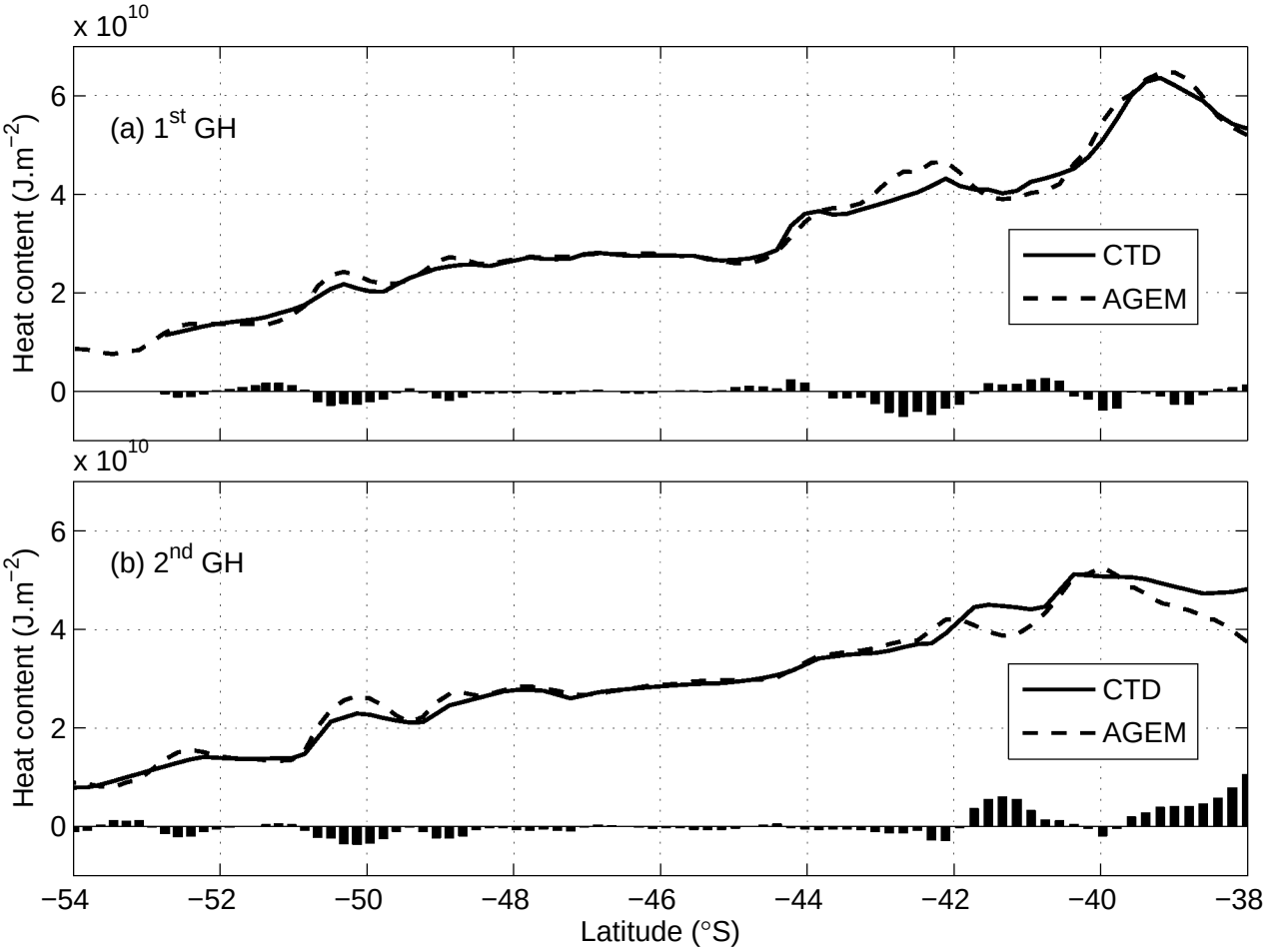

Figure 4.2: Comparison between observed (solid curve) and AGEM-estimated (dashed curve) heat content between the surface and 2500 dbar for the (a) first and (b) second GH occupations, completed in November 2004 and October 2005, respectively. The difference between the hydrographic and AGEM estimates (bars) are displayed along the x-axis.

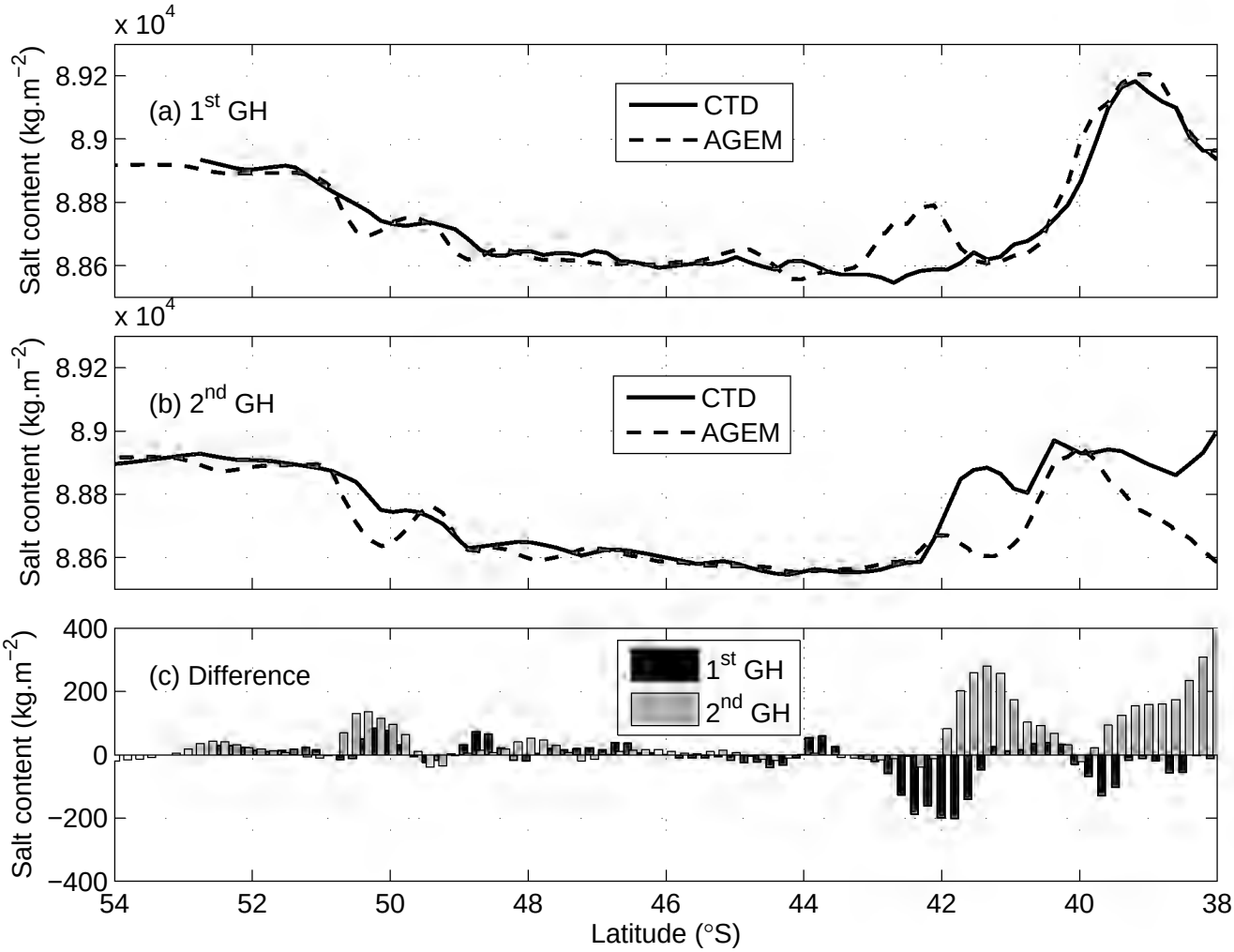

Figure 4.3: Comparison between observed (solid curve) and AGEM-estimated (dashed curve) salt content between the surface and 2500 dbar for the (a) first and (b) second GH occupations. The difference between the hydrographic and AGEM estimates (bars) are summarised in panel (c) where black bars are for the first occupation and the grey bars are representative of the second occupation.

structure. Furthermore, *Swart et al.* (2008) show that each of the most dominant multi-frontal structures found in each front region relate to the temperature and salinity criteria of the 'classical' ACC fronts given by *Orsi et al.* (1995).

The STF is characterised by sudden and erratic changes in space from one week to another, which makes its difficult to accurately locate its position using altimetry data. This is because the STF south of Africa and particularly in this region is often only present as a series of Agulhas Rings and eddies (*Lutjeharms and Valentine*, 1988), which pass through the northern extremes of the GH line (*Belkin and Gordon*, 1996; *Swart et al.*, 2008; *Dencausse*, 2009). The positions of the other ACC fronts are more stable in nature (*Lutjeharms and Valentine*, 1984) and can be more accurately defined in horizontal space. A detailed description of the position, standard deviation, and behavior of the ACC fronts, derived using this method, can be found in *Swart et al.* (2008) and in SSAL09.

The behavior of the HCA and that of the SCA are quite different from eachother (Figure 4.4). This is particularly true at the fronts and in the frontal zones. The short-term variability of the SAZ is dominated by the presence of mesoscale eddies and meanders, originating from the STF, and of Agulhas Rings, which arrive from the west or west-south-west. In Section 4.4.2, the short term variability found in the SAZ is explained in more detail.

Compared with the SAZ, the range of HCA and SCA values are considerably reduced within the APZ. Anomalous events in this region are principally driven by the behavior of the Subantarctic Front (SAF). Figure 4.5 is used to better understand the mean state of the ACC and fronts in the region of the GH line. The color plot represents the rms of the MADT data, while the surface geostrophic velocities are shown by the arrows. Topography contours of 1000 m, 2000 m and 3000 m are overlaid and velocity streamlines (blue lines) are also included. In addition, the front positions, given by *Orsi et al.* (1995), have been depicted in the illustration. Apart from the STF, the altimetry derived front positions (SSAL09) in Figure 4.5 do not overlap those derived by *Orsi et al.* (1995) at the GH line. This may be due to some inaccuracies in positioning the fronts using the criteria of *Orsi et al.* (1995). This is especially the case for the SAF, where recent high-density hydrographic transects have positioned the SAF north of the Meteor Rise (*Ansorge et al.*, 2004; *Gladyshev et al.*, 2008; *Swart et al.*, 2008).

Subsequent to crossing the Mid-Ocean Ridge, the SAF experiences some fragmentation downstream possibly due to a loss of the strong topographic control that could be caused by the meridional steering of the flow by underlying bathymetry and, thereby leading to the genesis of meanders and eddies (*Hogg and Blundell*, 2006). These perturbations are carried southward due to a meridional shift in the SAF upon reaching the Meteor Rise at 2°E (see Figure 4.5), thereby distributing anomalous features, in a band, between 46-48°S. The SCA in the APZ are opposite in sign to the HCA. This is because mesoscale anomalies originating from the SAF propagate south, carrying with them low salinity intermediate waters of which the mean salinity is considerably lower than the surrounding Circumpolar Deep Water (CDW) found further south. This produces negative SCAs when integrated through the upper 2500 dbar water column and emphasises the fact that these features originate from regions further north. If we investigate the SCA solely in the upper 400 dbar (not shown), interestingly, the variability in the APZ, is overwhelmingly dominated by the mesoscale anomalies discussed above and indicate their confinement to the upper ∼600 dbar. Besides the presence of these features, the APZ has substantially less anomalous episodes of salt content in the upper 2500 dbar.

The high frequency variability in the HCA and SCA, located in the region of the APF and shown in Figure 4.4 is, with the exeption of the SAZ, considerably higher than in other regions of the ACC. These events typically last in the order of approximately 8 weeks, while some large events can subsist for up to one year (such as the cool,

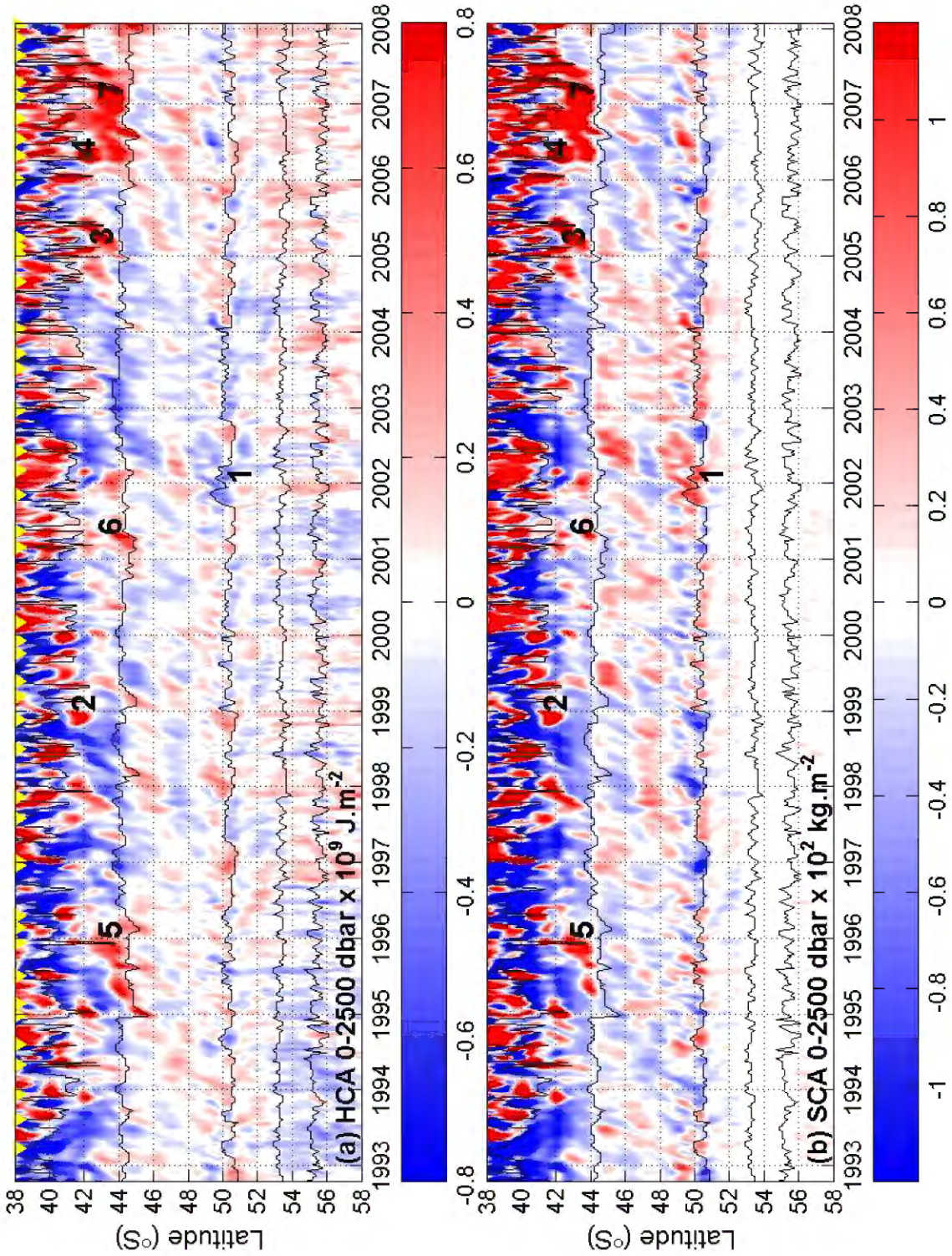

Figure 4.4: A Hovmöller representation of the (a) HCA and (b) SCA between the surface and 2500 dbar, at the GH line, from 1992-2008. The latitudinal positions of the ACC fronts (thin black lines) are from north to south: STF, SAF, APF, SACCF, SBdy. The numbers are referred to in the text.

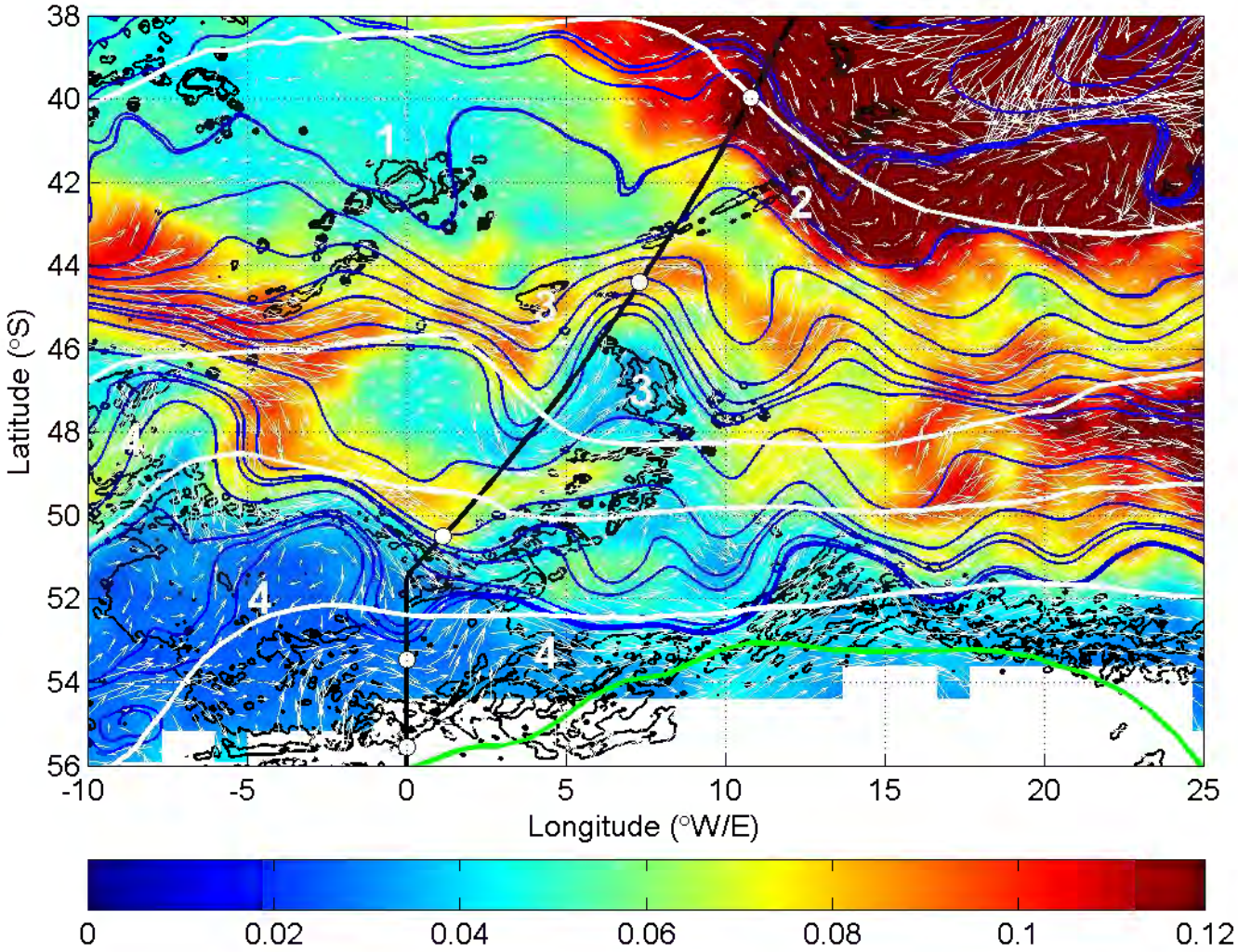

Figure 4.5: The rms of the MADT (in dyn m) over a 16-year period is shaded in color, while the mean surface geostrophic velocities are represented by the white arrows. The 1000 m, 2000 m and 3000 m bathymetry contours are overlaid (thin black lines) and geostrophic velocity streamlines (blue lines) have been added. The GH line is shown by the thick black line. White spaces represent regions where sea-ice was intermittently present during the altimetry time series. The 'classical' ACC fronts, as described by *Orsi et al.* (1995), have been overlaid using solid white curves, apart from the SBdy, which is depicted for clarity as a solid green curve. A white dot located over the GH line depicts the mean front position derived from the time series of MADT data. From north to south, these fronts and those of *Orsi et al.* (1995) are as follows: STF, SAF, APF, SACCF, SBdy. Important bathymetric features are numbered as follows: (1) Discovery Seamount, (2) Agulhas Ridge, (3) Meteor Rise, (4) Mid-Ocean Ridge.

saline event beginning in mid-2001; labeled '1' in Figure 4.4). This form of variability is characteristically mesoscale in nature and we now attempt to provide evidence for this statement. Referring to Figure 4.5, the impeding Mid-Ocean Ridge, at ∼50°S; 10°W, exerts strong topographical control over the path of the APF and forces the mean geostrophic flow northwards. This is as a result of the flow being forced across isolines of planetary vorticity, which causes an input of relative vorticity to the water column by the shrinking of vortex lines (*Moore et al.*, 1997, 1999) due to the decrease in depth. Further downstream, the APF follows contours of f/h, roughly along the edge of the 2500 m isobath before a loss of topographic control occurs prior to reaching the GH line. Downstream of the Mid-Ocean Ridge, this input of relative vorticity is likely balanced through nonlinear processes such as eddy genesis and Rossby waves (*Hughes*, 1995, 1996). Thus, elevated mesoscale variability is found in this region resulting in the band of mesoscale-type signals found in the HCA and SCA. This evidence is supplemented by the existence of a branch of elevated MADT rms extending over the GH line in Figure 4.5. This high level of rms associated with the APF is also shown by *Moore et al.* (1999) who explain that the position of the APF varies significantly (and therefore is unstable) at the Greenwich Meridian, subsequent to crossing the Mid-Ocean Ridge.

South of the APF, the SCA variability in the upper 2500 dbar, is considerably lower. This is because the variability present at the surface is dampened by the monotonic salinity structure below the halocline, which is located between 200-300 dbar. If we remove the majority of the relatively high saline, monotonic layer by computing the SCA between the surface and 400 dbar (not shown), we are able to reveal the true SCA variability in the upper ocean layer. A large portion of the temporal variability of salinity, between the APF and SBdy, originates in the mesoscale band. Additional interannual signals in the variability can be seen in both the HCA and SCA and will be discussed in Section 4.5.1 using time series analysis.

Elevated eddy kinetic energy (EKE) has been noted downstream of major topographic features (*Daniault and Menard*, 1985; *Patterson*, 1985; *Chelton et al.*, 1990; *Morrow et al.*, 1994). The kinetic energy budget at the GH line is illustrated to emphasise this point. The deviations of u' and v' from the mean ($\bar{u}$, $\bar{v}$) allow one to estimate the EKE per unit mass:

$$EKE = \frac{1}{2}(u'^2 + v'^2) \tag{4.3}$$

The kinetic energy, per unit mass, of the mean flow is referred to as the mean kinetic energy (MKE) and is defined by *Richardson* (1983):

$$MKE = \frac{1}{2}(\bar{u}^2 + \bar{v}^2) \tag{4.4}$$

A Hovmöller diagram representing the anomaly of the surface EKE along the meridional extent of the GH line (Figure 4.6) highlights the increased kinetic energy produced by the passage of mesocale meanders and eddies, which cause deviations of the u and v components of the the mean flow, in the region of the APF, while to the north a wider and less defined band of elevated EKE depicts the SAF. Furthermore, this illustration clearly indicates the intensity of the EKE magnitude difference between the extremely active mesoscale region associated with the subtropical domains and passage of Agulhas Rings with that of the major ACC fronts beginning just a few degrees further south (to be discussed further in Section 4.4.2). In some instances, the ring structure of the most southern propagating Agulhas Rings can be made out in Figure 4.6. The distribution of the mean surface kinetic energy budget, at the GH line, is shown in Figure 4.7. This clearly highlights the different behavior of the SAF and APF. At the SAF, the largest contribution to the total kinetic energy (TKE) comes from the mean kinetic energy (MKE),

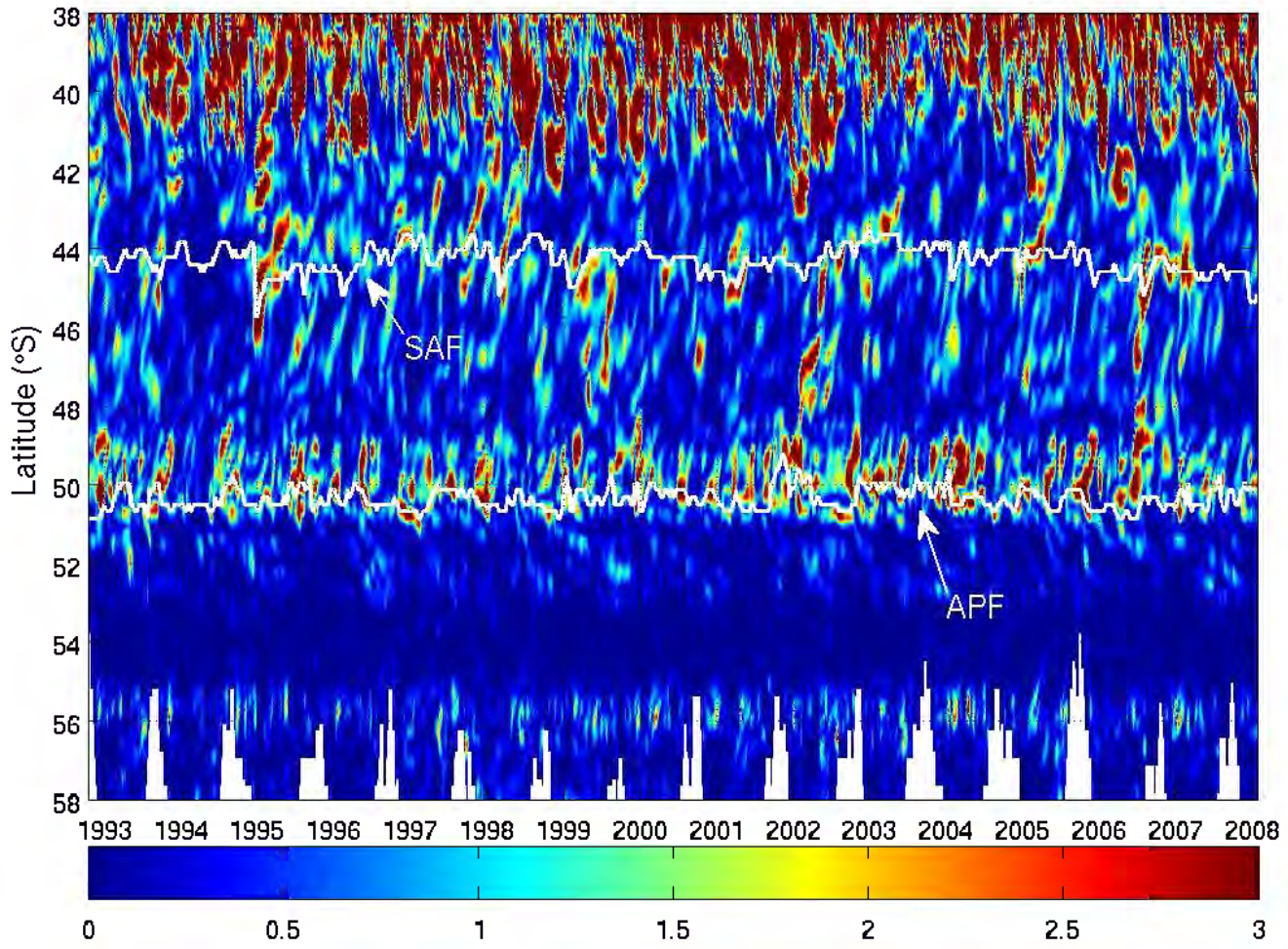

Figure 4.6: A Hovmöller representation of the surface eddy kinetic energy at the GH line, from 1992-2008. The latitudinal positions of the SAF and APF, determined using altimetry data, are overlaid (white lines).

which is the kinetic energy related to the time- and zonal-mean motion, likely due to the topographic steering caused by the Meteor Rise that constricts the flow into a zonal-dominent jet at the crossing of the GH line. To the contrary, the EKE is particularly high at the APF (double the EKE at the SAF; $>1.5\ cm^2.s^{-2}$) when compared with the rest of the ACC south of the STF. This is likely as a result of the meridional motion caused by the passing of eddies, generated on an almost continual basis, while the MKE at the APF, downstream of the Mid-Ocean Ridge, is approximately $0.5\ cm^2.s^{-2}$ less than at the SAF. The southern ACC front (SACCF) and the southern boundary of the ACC (SBdy) are also represented in the kinetic energy budget. The SACCF is largely dominated by the MKE, suggesting little mesoscale variability in the mean flow, while the EKE is considerably higher at the SBdy, symptomatic of increased mesoscale activity. The EKE at the region around the STF is disproportionately higher than the MKE, which is as a result of the intense mesoscale activity found at the unstable STF, largely due to the passage of Agulhas Rings. Remnants of the mean position of the northern and southern branches of the STF are likely represented by the elevation of MKE at 39°S and 41.5°S, respectively.

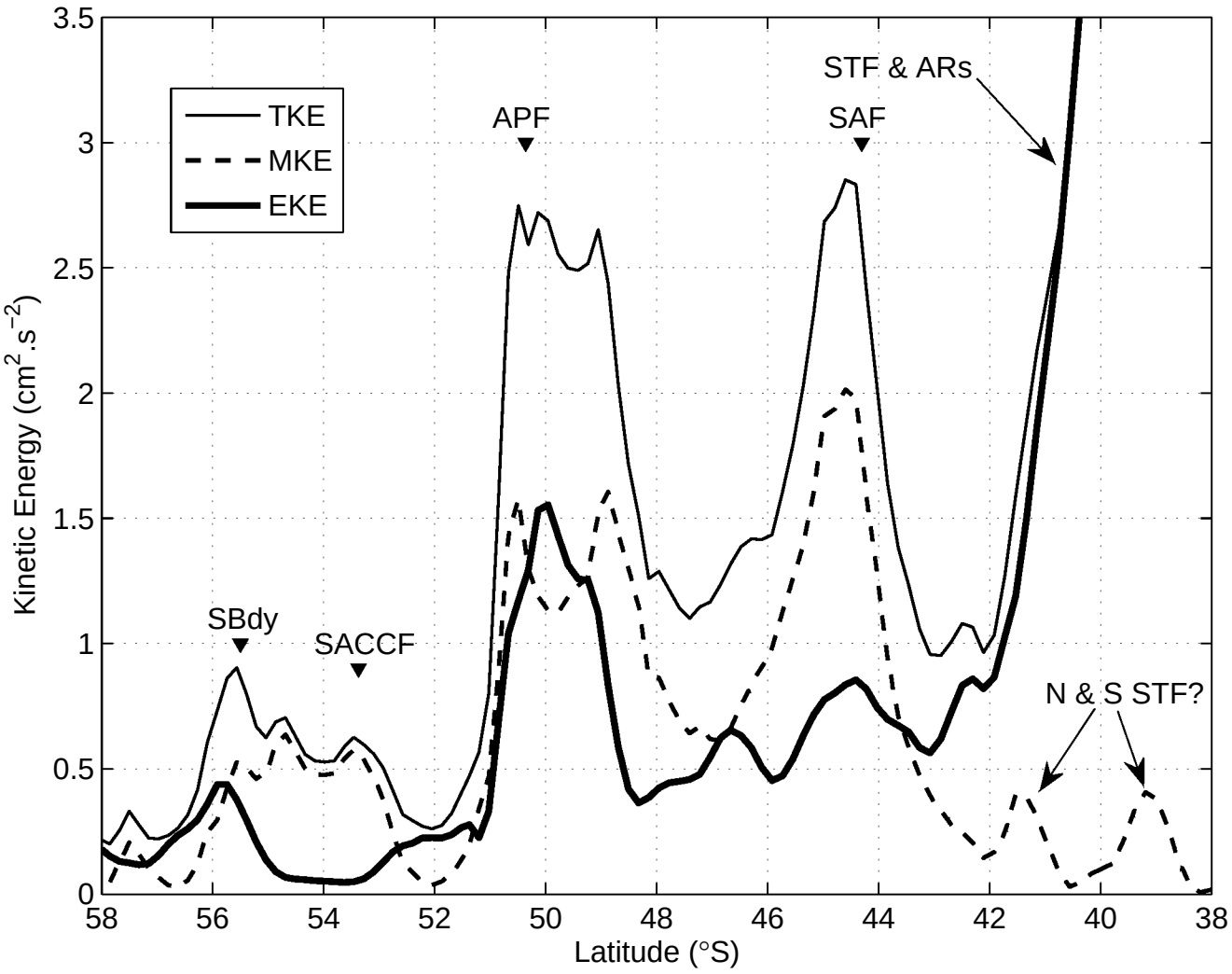

Figure 4.7: The latitudinal distribution of the 16-year mean surface kinetic energy at the GH line is separated into the total kinetic energy (thin solid curve), mean kinetic energy (dashed curve) and eddy kinetic energy (thick solid curve). The mean positions of the ACC fronts, determined using altimetry data, are indicated by the arrows. The abbreviation 'AR' stands for 'Agulhas Ring'.

4.4.2 Dominant forcing of dynamic variability in the SAZ

Extensive analysis of MADT data, in conjunction with both the HCA and SCA time series, are used to identify two dominant aspects that force the variability within the SAZ. These dominating aspects are firstly the westward or west-south-westward propagating Agulhas Rings into the SAZ and the second is eastward propagating eddies that have their origin in the unstable STF upstream (west) of the GH line. A time series of MADT 'snapshots' are included to help clarify the following discussion (Figure 4.8).

The northern parts of the SAZ (∼40-42°S) are subjected to generally short (∼2 months), yet intense episodes of elevated HCA that occur approximately 2.7 times per year (Dencausse et al. (2009) estimated 2.6 in an independent study). These episodes are also clearly identifiable as intense peaks in the surface EKE, illustrated in Figure 4.6. On some occasions, these anomalous features can remain in the region for extensive periods of time (up to 14 months). These features are identified as Agulhas Rings using MADT data, as well as back-tracking their trajectories to confirm their origins are within the Agulhas Retroflection region (see Figure 4.8). Confidence in this form of analysis is further given by *Swart et al.* (2008) who matched the Agulhas Rings, identified in the MADT data, with *in situ* XBT sections in order to describe their vertical temperature structure. In total, 43 individual Agulhas Rings are located in the MADT data and seen crossing the GH line between 40-43°S, during the 16 years of available data. Three Agulhas Rings that are found quite far south in the SAZ, are identified in Figure 4.4 by labels '2', '3' and '4'. During these instances, the HCA at a single vertical profile increases to $>2.3 \times 10^{10}$ $J.m^{-2}$. The frequency of their presence in the SAZ is not always uniform, as shown by an observation in 1999 when Agulhas Rings are found on four occasions within the SAZ, followed by a quiescent period between May 2000 and January 2001, when no Agulhas Rings are located. To give an indication of their frequency, yellow arrows in Figure 4.4 indicate the presence of an Agulhas Ring in the SAZ.

The presence of Agulhas Rings south of the STF seem to play a large role in the HCA and SCA of the SAZ. The values of integrated HCA and SCA in the SAZ are isolated during the 43 instances when the Agulhas Rings have their maximum presence in the SAZ (i.e. they are at their most southern extent) and compared to the mean HCA and SCA during the 16-year time series. The mean HCA (SCA) throughout the time series is -1.9 $\times 10^{10}$ $J.m^{-1}$(-586 $kg.m^{-1}$). The mean HCA (SCA), during periods when the Agulhas Rings are present in the SAZ, is calculated as 2.86 $\times 10^{10}$ $J.m^{-1}$(451 $kg.m^{-1}$). This shows that the presence of Agulhas Rings in the region increase the HCA and SCA by 4.76 $\times 10^{10}$ $J.m^{-1}$ and 1037 $kg.m^{-1}$, respectively. Additionally, the HCA (SCA) is greater than the mean 80% (82%) of the time an Agulhas Ring is present in the SAZ.

On average, the entire spatial extent of an Agulhas Ring tends to cross the GH line in approximately 56-70 days (or 8-10 weeks), which equates to a propagation speed of ∼0.04 $m.s^{-1}$. On rare occasions (such as for the feature labeled '2' and '3' in Figure 4.4) the Agulhas Ring propagates over the GH line at a much reduced speed of ∼0.023 $m.s^{-1}$ and may take between 90-130 days to cross the cruise track. This is approximately 40% slower than the normal propagation speed. The slower propagating Agulhas Rings cross the GH line further south than their faster moving northern brothers. Inspection of the MADT time series shows that the Agulhas Rings located further south are initially occluded from the Agulhas Retroflection slightly further south than the average Ring. This leads to the Agulhas Ring being 'trapped' by the shallow topography, associated with the Agulhas Ridge (centered at ∼42°S; 13°E and ∼2000 meters deep at its shallowest), thereby considerably slowing its propagation speed. The Agulhas Ring then moves over the Agulhas Ridge and continues on its north-westward path, and on its way it crosses the GH line, located approximately 3° west of the Agulhas Ridge (see Figure 4.5 for bathymetry references).

Ten average size and average behaving Agulhas Rings, that crossed the GH line in the SAZ, are further analysed

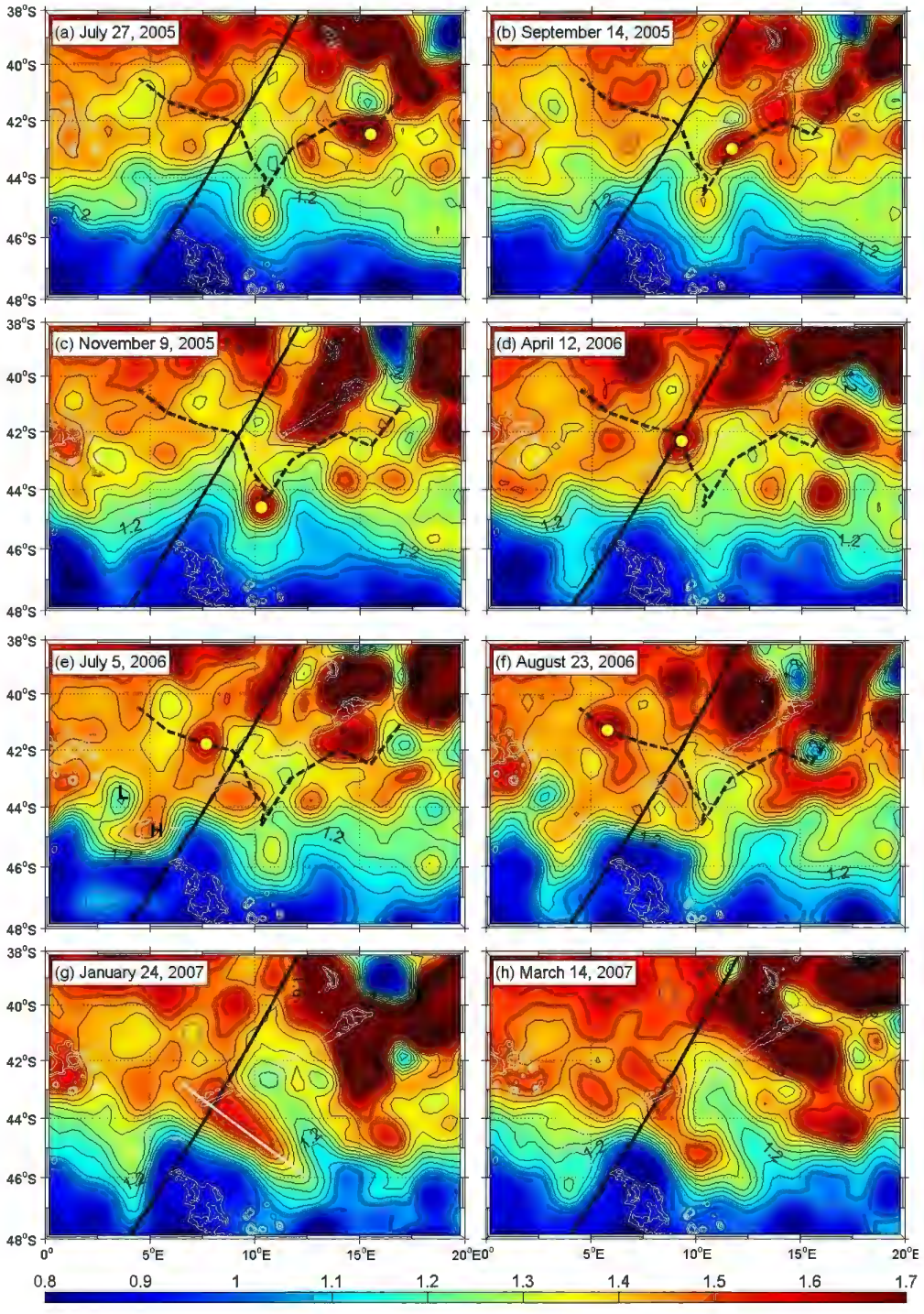

Figure 4.8: A sequence of maps, between 27 July 2005 and 14 March 2007, illustrating the weekly MADT data (in dyn m) for the region near the GH line. The propagation of an Agulhas Ring is identified with a yellow dot near its core. The black dashed curve, in panels (a) to (f), represents the approximate path (from east to west) of the Agulhas Ring between 13 July 2005 and 6 September 2006. The GH line is marked by the thick black curve and topography for the region (1000 m, 2000 m and 3000 m isobaths) is marked with thin white lines. The dynamic height values have a contour interval of 0.05 dyn m. The thick white line in panel (g) depicts the approximate length of the warm anomalous feature described in Section 4.4.2.

Table 4.2: Comparison between the mean hydrographic state (1992-2008) and the average hydrographic state when Agulhas Rings are present in the SAZ. The standard deviation for the ten sampled Agulhas Rings is shown.

	T-surface (°C)	T-200 dbar (°C)	S-surface (psu)	S-200 dbar (psu)	Diameter (km)
Mean Hydrography	10.6	8.8	34.48	34.52	-
Agulhas Ring	15.7	12.4	35.24	35.24	190
Standard Deviation	0.73	0.77	0.13	0.13	60
Difference	5.1	3.6	0.76	0.76	-

to estimate their hydrographic impact on the region. This is undertaken by comparing the Agulhas Rings mean hydrographic state to the 16-year mean hydrographic state of the SAZ, at the average location where Agulhas Rings cross the GH line. These results are summarised in Table 4.2. Note also that when an Agulhas Ring is present, the temperature (salinity) at the surface and at 200 dbar increases to 5.1°C (0.76) and 3.6°C (0.56), respectively.

The HCA variability found in the southern parts of the SAZ is forced by mesoscale perturbations in the form of large meanders and eddies that occur within the SAF and SAZ further upstream of the GH line. It is likely that these instabilities are caused following the SAF's path over the Mid-Ocean Ridge at ∼44°S; 12°W. A complete analysis of MADT data and its geostrophic velocity component is done to analyse the nature of the positive anomalies labeled '5' and '6' in Figure 4.4. Preceding these warm events, the MADT data shows the formation of a large meander in the SAF upstream of the GH line (not shown). In some cases, this meander may pinch off to form a warm eddy, which carried by the mean easterly flow of the SAF and ACC, propagates downstream. This eddy is then steered quite sharply northward by the rise in topography, associated with the Meteor Rise. The 'slanted' spread of positive HCA in the Hovmöller representations (Figure 4.4), is caused by the feature crossing the GH line from the southwest. Greater detail on the behavior of these anomalous features is described below.

We now attempt to explain the complex nature of the intensely positive HCA and SCA values found in the SAZ, which began in March 2006 and remained in the region until October 2007 (labeled '7' in Figure 4.4). Figure 4.9 shows a 'zoom' of the HCA, between the surface and 2500 dbar, for this particular event in order to detail its structure more precisely. The initial increase in the HCA (labeled 'A' in Figure 4.9) is caused by an Agulhas Ring crossing the GH line between March and June 2006. A set of MADT 'snapshots' are shown in Figure 4.8 to identify the Agulhas Ring mentioned here, which for clarity is marked with a yellow dot near its core. The Agulhas Ring propagates in a WSW direction from the Agulhas Retroflection (Figure 4.8a), seemingly guided by the Agulhas Ridge (Figure 4.8b) before merging with a warm eddy (centered at 45°S; 11°E) that is positioned on the leeward side of the SAF meander (located over the GH line), thereby intensifying its MADT gradient (Figure 4.8c). The feature remains quasi stationary at this location for ∼10 weeks before progressing in a northwest direction and crossing the deepest part of the Agulhas Ridge and then intersecting the GH line in April 2006 (Figure 4.8d).

Shortly after crossing the Agulhas Ridge (∼1 month), the Agulhas Ring appears to split into two independent parts (Figure 4.8e; indicated by label 'B' in Figure 4.9). The northern part continues to advance to the northwest and away from the region, while the southern part is fed by flow originating from the STF, before likely being influenced by the strong mean easterly flow and returning back to the southeast (southeast of the GH line). At approximately the same time as the splitting of the Agulhas Ring, a large meander in the SAF is pinched off to form a warm and cold eddy, labeled 'H' and 'L' in Figure 4.8e, respectively. This warm eddy clearly moves downstream and crosses the GH line from the southwest, at the beginning of July 2006 (labeled 'C' in Figure 4.9). This eddy merges with the already present southern portion of the Agulhas Ring resulting in an intense, elongated anomaly that consequently produces elevated HCA and SCA values in the region for approximately one year (November

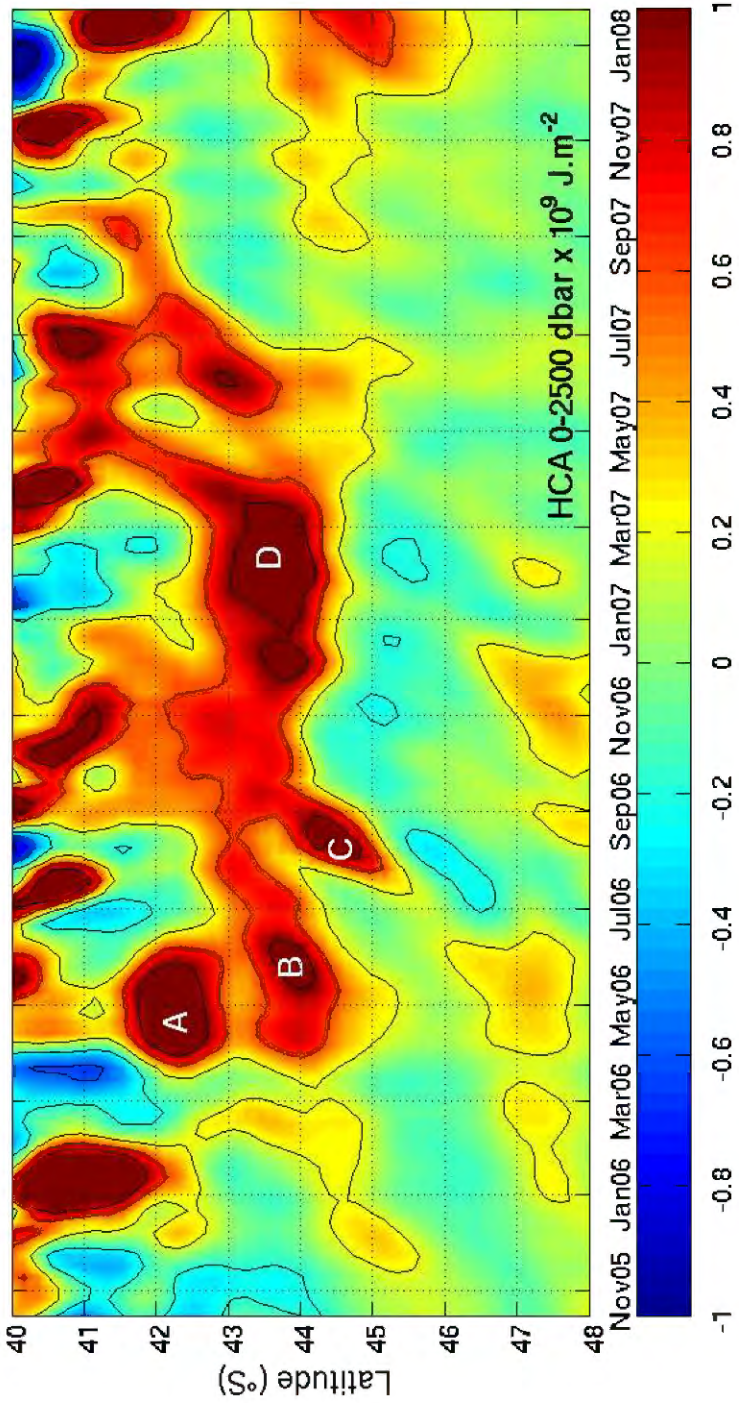

Figure 4.9: A Hovmöller representation of the HCA between the surface and 2500 dbar, at the GH line, focusing on an anomalous feature found roughly between April 2006 and September 2007. The letters given in the figure are described in Section 4.4.2.

2006-October 2007; labeled 'D' in Figure 4.9). The feature has a maximum length of ∼950 km and width of ∼220 km. At its peak intensity in February 2007, this feature elevates the HCA at an individual vertical profile to ∼1.4 $\times 10^9$ $J.m^{-2}$ and the SCA to 320 $kg.m^{-2}$.

The time series of GEM-produced hydrographic sections are used to analyse the anomalous temperature and salinity subsurface structure associated with this positive feature. The mean temperature and salinity between March 2006 and March 2007 are subtracted from the mean for the whole period (16 years) and shown in Figure 4.10a and c, respectively. Over this period, the maximum anomalous temperatures and salinities occur near the surface and are approximately 3°C and 0.5 above the mean, respectively. A localised subsurface maximum is associated with the northern boundary of the Agulhas Ring and found at ∼500 dbar. The extent of the positive feature reaches roughly 1500 dbar. The latitudinal anomalous temperature and salinity is averaged between 0-1000 dbar and shown in Figure 4.10b and 4.10d, respectively. At the core of the Agulhas Ring feature the anomalous temperature and salinity exceeds the mean by 1.75°C and 0.17, respectively. The feature appears to be strongly confined in space by the mean position of the SAF at 44.6°S (represented by the grey line in Figure 4.10a & c), as indicated by the strong thermal and saline gradient at its southern edge. This is likely due to the topographic steering of the SAF over the region of the GH line, thereby inhibiting the southward propagation of mesoscale features approaching from the north. A comparison of the T-S properties between the period of the anomalous feature and the 16-year mean depicts the departure of the T-S structure from one another at a fixed geographic position - 43.8°S (Figure 4.11). The deviation is most magnified in the surface waters but can also be clearly portrayed in the central and intermediate waters.

The presence of Agulhas Rings in this region is of particular interest due to the fact that they are able to transport large quantities of heat and salt from the subtropics to the SAZ, as well as that these features can remain in the region for as long as 14 months. The influence they may have on the local biology and bio-geochemistry structure of the region is yet to be understood and warrants further research.

4.5 Heat and salt content time series

In order to quantify the observed variability in the ACC, we estimate the integrated HCA and SCA in the following ways (only the integrated HCA is shown in this study): (1) the property integral between fronts, defined using altimetry, to derive the value for the frontal zones (thin curves in Figure 4.12) and; (2) the property integral between the northern and southern limit of each front to derive the value for the core region of the front (thick curves in Figure 4.12). These two integral methods allow us to understand the variability occurring between each front, which may be a contribution to frontal heat and salt exchange in the Southern Ocean as well as the variability occurring within the core of each jet and therefore the manifestation of variability in the zonal-dominant mode of the flow and the behavior of the front. Note that the northern and southern limits of each ACC front have been taken from *Swart et al.* (2008) and a brief explanation has been given in Section 4.2.3.

4.5.1 Time series and Wavelet Analysis

The continuous wavelet transform (CWT) has been extensively used in time series analysis of geophysical parameters within the last ten years. It is well adapted to the study of multi-scale, non-stationary phenomena occurring over finite spatial and temporal domains (*Lau and Weng*, 1995) and has been applied in meteorological and oceanographic studies to indicate modes of variability, such as the El Niño Southern Oscillation. *Torrence and Compo* (1998) and

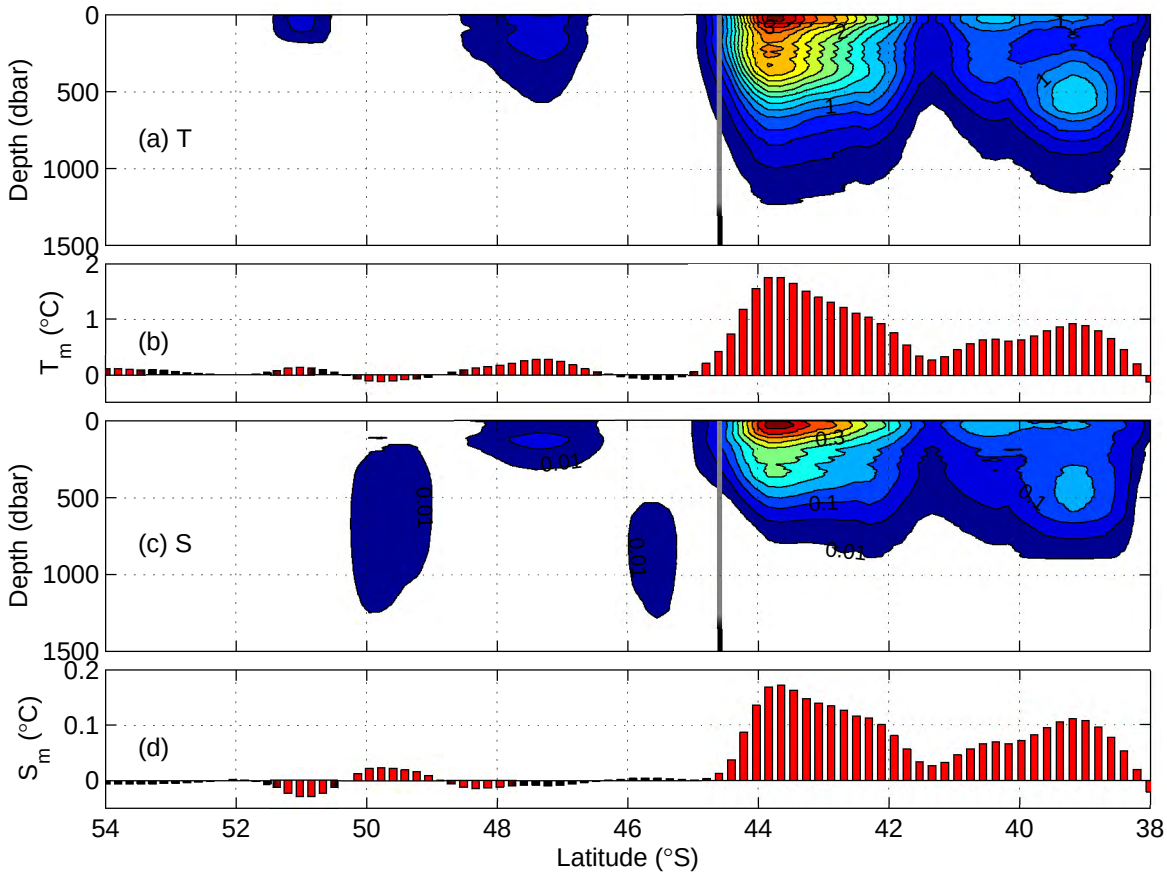

Figure 4.10: The anomalous subsurface structure of (a) temperature and (c) salinity for the anomaly evident in Figure 4.9 is shown for period between March 2006 and March 2007. The anomalous (b) temperature and (d) salinity is averaged between 0-1000 dbar. The grey line indicates the position of the SAF during the time when the anomalous feature was present. The contour intervals are 0.2°C and 0.05 for the temperature and salinity anomaly plots, respectively.

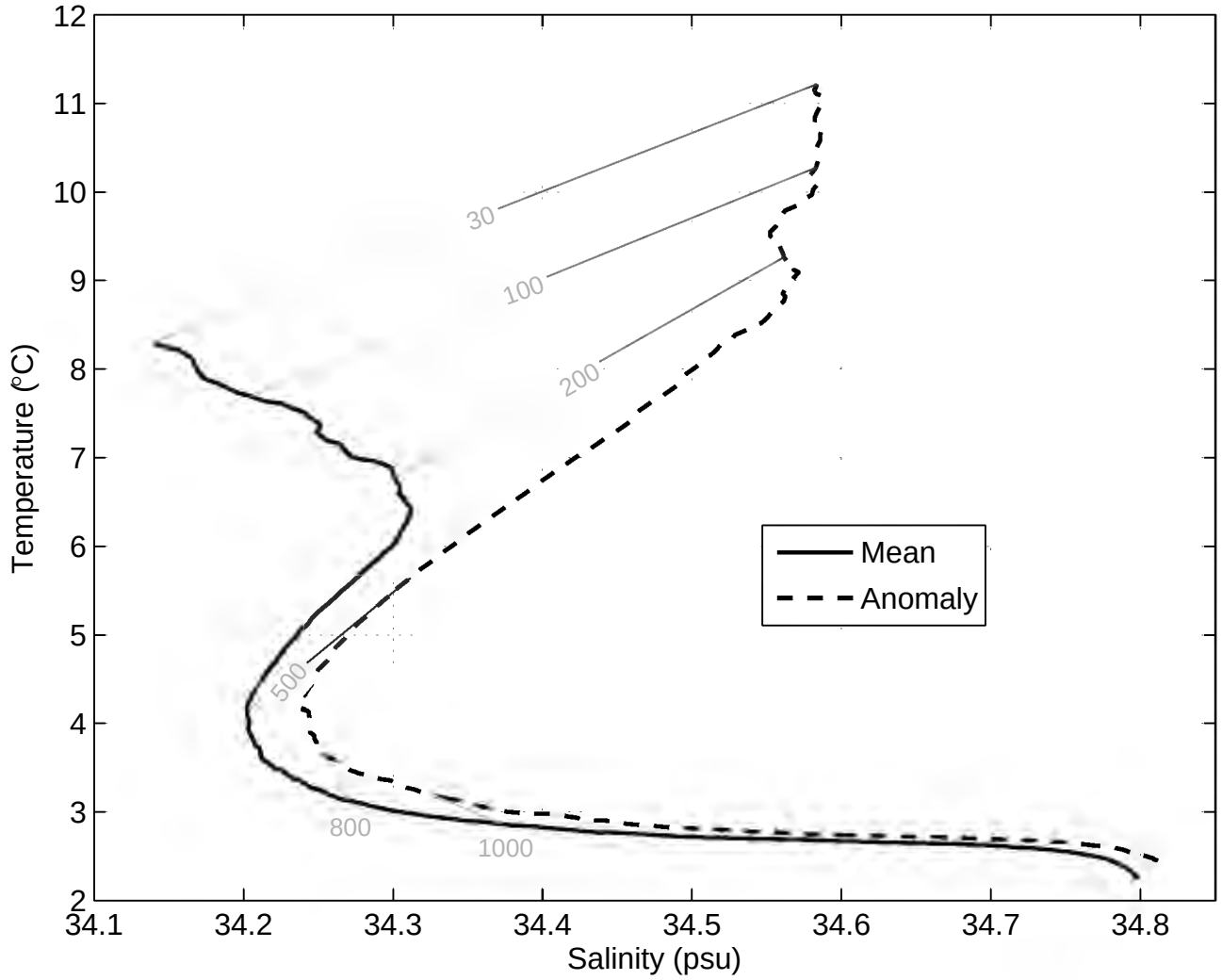

Figure 4.11: An AGEM-derived T-S diagram for a locale at 43.8°S indicating the 16-year mean structure (solid curve) and for the period the anomalous feature was present between March 2006 and March 2007 (dashed curve). The grey lines connect values of equal depth.

Daubechies (1992) provide a practical guide to wavelet analysis and provide more detailed explanations on its application to geophysical data. The Fourier Transform is not utilised in this study as it does not contain any time dependence of the signal and therefore cannot provide local information regarding the time evolution of its spectral characteristics (*Lau and Weng*, 1995).

The CWT allows for the decomposition of a signal $x(t)$ into elementary contributions localised in time and in frequency using mathematical tools, called wavelets. These wavelets are obtained from a single function Ψ by translations and dilations

$$\Psi_{b,a}(t) = \frac{1}{a}\Psi\left(\frac{t-b}{a}\right), \tag{4.5}$$

where $a > 0$ is the dilation parameter and b is the time translation parameter. The CWT expands the time series into a two-dimensional parameter space (b, a) and yields a measure of relative amplitude of local activity at scale a and time b (*Melice et al.*, 2001). More specifically, the Morlet wavelet is used in this study because it is best suited for analysis of geophysical data-sets (*Lau and Weng*, 1995). The Morlet wavelet is a complex exponential modulated by a Gaussian function

$$\Psi(t) = \pi^{1/4} e^{-t^2/2} e^{i\omega_0 t}, \tag{4.6}$$

with $i = (-1)^{\frac{1}{2}}$ and where $\omega_0 = \pi(2/ln2)^{\frac{1}{2}}$ (*Daubechies*, 1992) is chosen to be large enough to ensure that $\Psi(t)$ satisfies the admissibility condition, which practically is equivalent to

$$\int_{-\infty}^{\infty} \Psi(t)dt = 0. \tag{4.7}$$

By inverting the modulus scale, the wavelet becomes a time frequency analysis where the dilation parameter a corresponds to the period and the translation parameter b corresponds to the time.

Firstly, we analyse the time series of the integrated HCA (Figure 4.12) and SCA in each frontal zone at the GH line. The choices of wavelet figures displayed in this paper are those that are of most interest and/or contribute to explaining the largest proportion of the observed variability.

Agulhas Rings are partially a source of the high frequency variability experienced in the SAZ and are well resolved in the time series. These events have been previously described in detail in Section 4.4.2. The Agulhas Rings can increase the total SAZ HC and SC up to 1.4 $\times 10^{11}$ $J.m^{-1}$ and 5 $\times 10^{3}$ $kg.m^{-1}$ in the upper 2500 dbar, respectively. Some of these events stand out as isolated peaks in the time series due to their extraordinary intensity (such as the Agulhas Ring, which crossed the GH line between March – June 2006). Although the mean wavelet power spectrum, for the periods representing these events, is below the 95% significance level, the wavelet modulus (Figure 4.13a) does appear to show an increase in amplitude at the period at which the Agulhas Rings appear in the SAZ (2.7 occasions per year or at a period of ∼20 weeks). Throughout the HCA and SCA time series, the SAZ contains variability that has a period of approximately 80 weeks or 1.5 years, which is well above the 95% significance level, as indicated in Figure 4.13b. Variability with this period is limited to the SAZ alone. The Hovmöller representation of the HCA in Figure 4.4a shows that this period appears to be related to the changing positive to negative phases in the HCA and SCA in the central parts of the SAZ. The strong links this region appears to have with the south-west Indian Ocean Gyre (passage of Agulhas Rings) may strongly suggest that the origins of variability on this time scale lie within the subtropics. However, to date this remainsunclear.

The variability of the frontal zones is often quite different from that found at the fronts. At the SAF, for instance, the short term variability (integrated HCA STD = 3 $\times 10^{10}$ $J.m^{-1}$) is considerably reduced compared

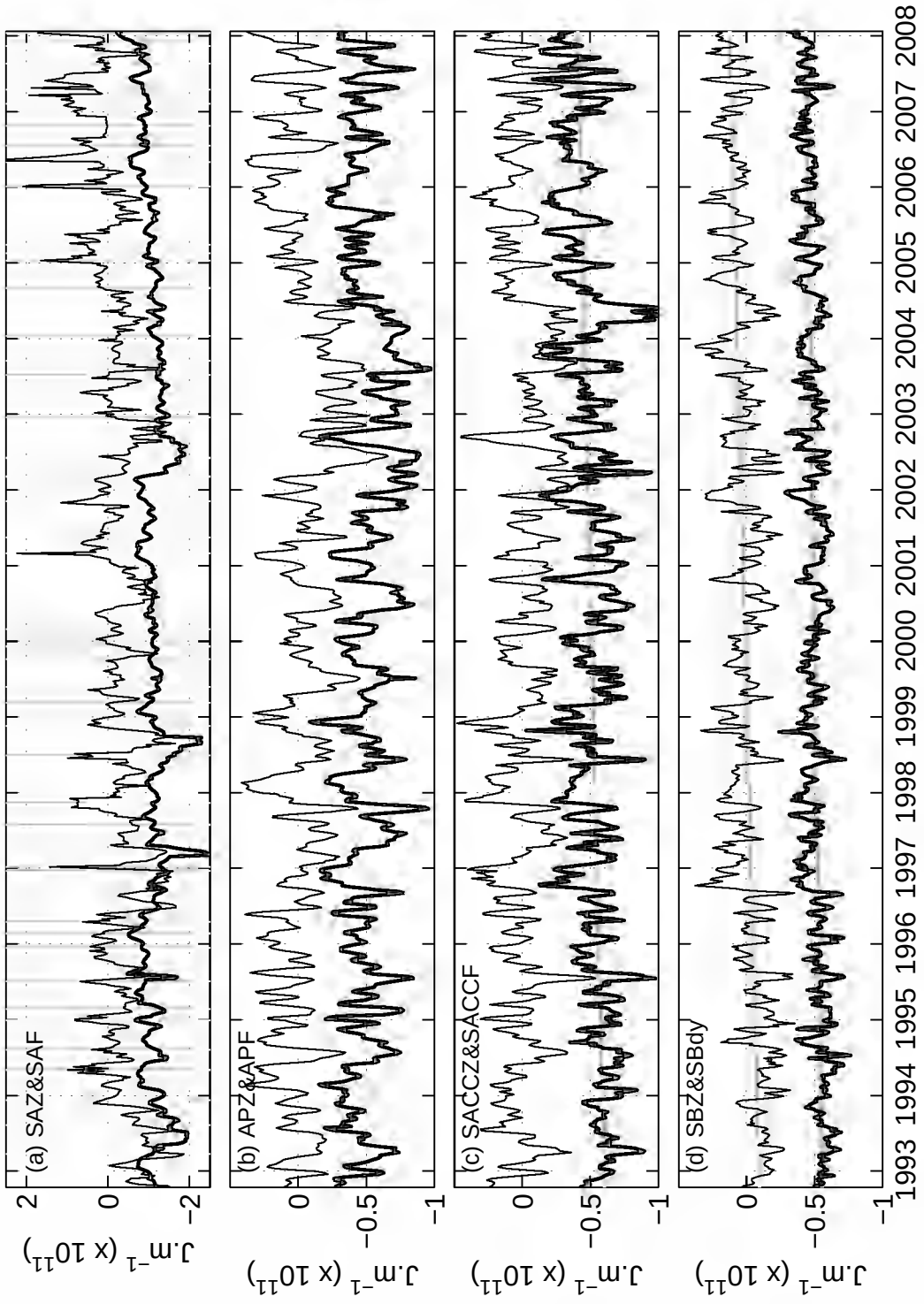

Figure 4.12: The time series of HCA is shown for each frontal zone (thin curve) and each ACC front (thick curve). The presence of an Agulhas Ring in the SAZ is marked by the grey lines in panel (a). The grey lines in panel (c) and (d) mark the trends in HCA for the respective fronts and frontal zones.

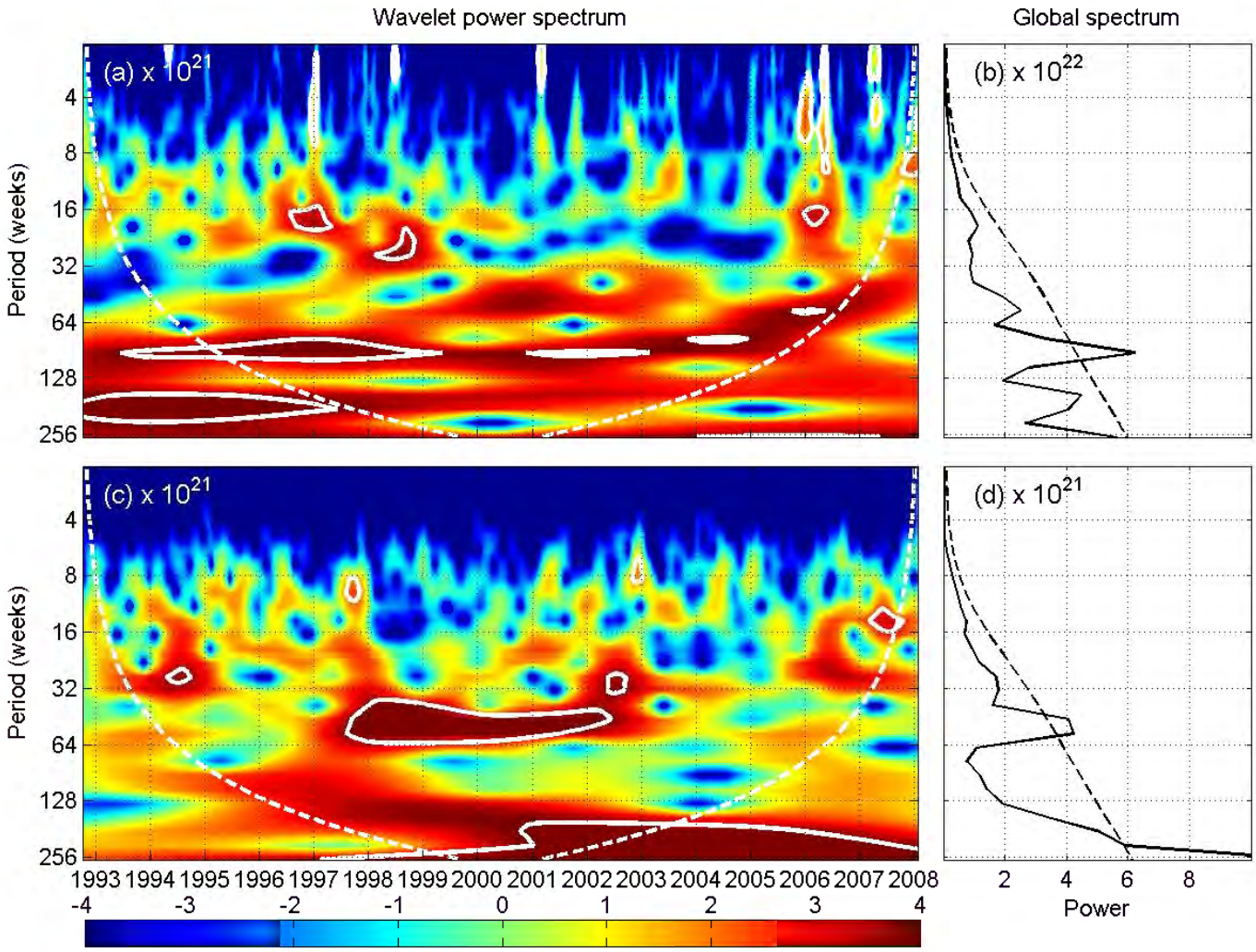

Figure 4.13: The modulus of the wavelet transform, using the Morlet wavelet, is shown for the SAZ (a) and the APZ (c), while the mean power of the global spectrum (solid curve) with the 95% significance level indicated (dashed curve) is shown for the SAZ (b) and APZ (d). White contours in (a) and (c) indicate where the wavelet amplitude is significant at the 95% level, while the white dashed curves represents the cone of influence.

with the SAZ (STD = 6.2 $\times 10^{10}$ $J.m^{-1}$). This is because the influence of Agulhas Rings and other mesoscale variability, associated with the STF, does not penetrate extensively south of the northern branch of the SAF. This may be because the strong baroclinic shear at the front acts as a boundary that blocks the southward propagating mesoscale features that induce the 4- to 12-week scale variability found further north.

The most significant form of variability in the SAF has a period of ∼5 years and is clearly depicted in the wavelet analysis as a continuous band in the modulus and a statistically significant peak in the mean spectrum (not shown). This pattern is characterised by a slow increase (decrease) in the HCA (SCA) over 4-6 years, followed by a sharp decrease (increase), which takes place over a relatively short time (<1 year). These events are unlikely related to the periodicity/intensity of features originating from north of the SAF because the SCA is of opposite sign to the HCA, which is not indicative of southward displacement of water masses from subtropical origins. However, the short extreme negative episodes in the HCA during mid-1995, early-1997 and late-1998 are of the same sign as the SCA.

The nature of the HCA and SCA time series variability found in the APZ and in the APF are similar and so the description given here is representative for both regions. The short term variability (in the order of 8 weeks) is dominant in the HCA and SCA time series (Figure 4.12b), while the wavelet modulus representing the HCA (Figure 4.13c), indicates a small contribution at the seasonal scale. Although the seasonal variability is present in the time series (localised peaks at the 52 week period in the wavelet power spectrum for the APZ; Figure 4.13c), it does not seem to contribute significantly to the observed variability. The differences between the seasoned and deseasoned data-sets (not shown) are small compared with the higher frequency variability found in the APF and APZ. Additionally, a new wavelet analysis was performed on the deseasoned data-sets for all regions, which revealed no new significant increases in the wavelet power spectrum. However, seasonal warming and cooling of the upper mixed layer may only marginally impact the dynamic height, referenced to 2500 dbar, thus translating to weak HC and SC signals. For this reason we are unable to accurately quantify seasonal variations but we can still provide an estimate as to which regions may undergo larger seasonal variations in comparison to their overall variability. Ongoing work hopes to evaluate, in more detail, the significance the seasonal changes have on the total variance in the region.

Apart from the seasonal cycle, variability with a period of ∼5 years (or 250 weeks) was found to be well above the 95% significance level in the mean wavelet power spectrum for the APZ (Figure 4.13d). This cycle can also be seen in the time series (Figure 4.12b) as a period of slow increasing and decreasing values around three long-term peaks (nadirs) in the HCA (SCA). The maximum peaks occur at approximately mid-1995, early 2001 and early 2006. Unfortunately, the length of the time series means that only three of these cycles can be distinguished and therefore only part of the wavelet power spectrum that is significant is located within the cone of influence (COI).

The mechanism driving this 5-year variability may be linked to the highly nonlinear nature of the ACC dynamics and could be potentially explained by interannual-to interdecadal intrinsic variability arising from the meridional topographical steering of the mean flow causing baroclinic instability (*Hogg and Blundell*, 2006). The role of topographic steering and baroclinic instability on the very rich ACC spatio-temporal spectra has been confirmed by more recent Quasi Geostrophic model simulations (*Thompson*, 2009).

The variance of the HCA and SCA seasonal cycle was compared to the variance of the HCA and SCA time series in other regions in order to evaluate the role the seasonal march may have on the observed variability. The calculated proportion of the HCA seasonal variance accounted for in the time series, on average, increased polewards and more than doubled between the extreme north of the ACC (SAZ ∼7%) and the region between the SACCF and

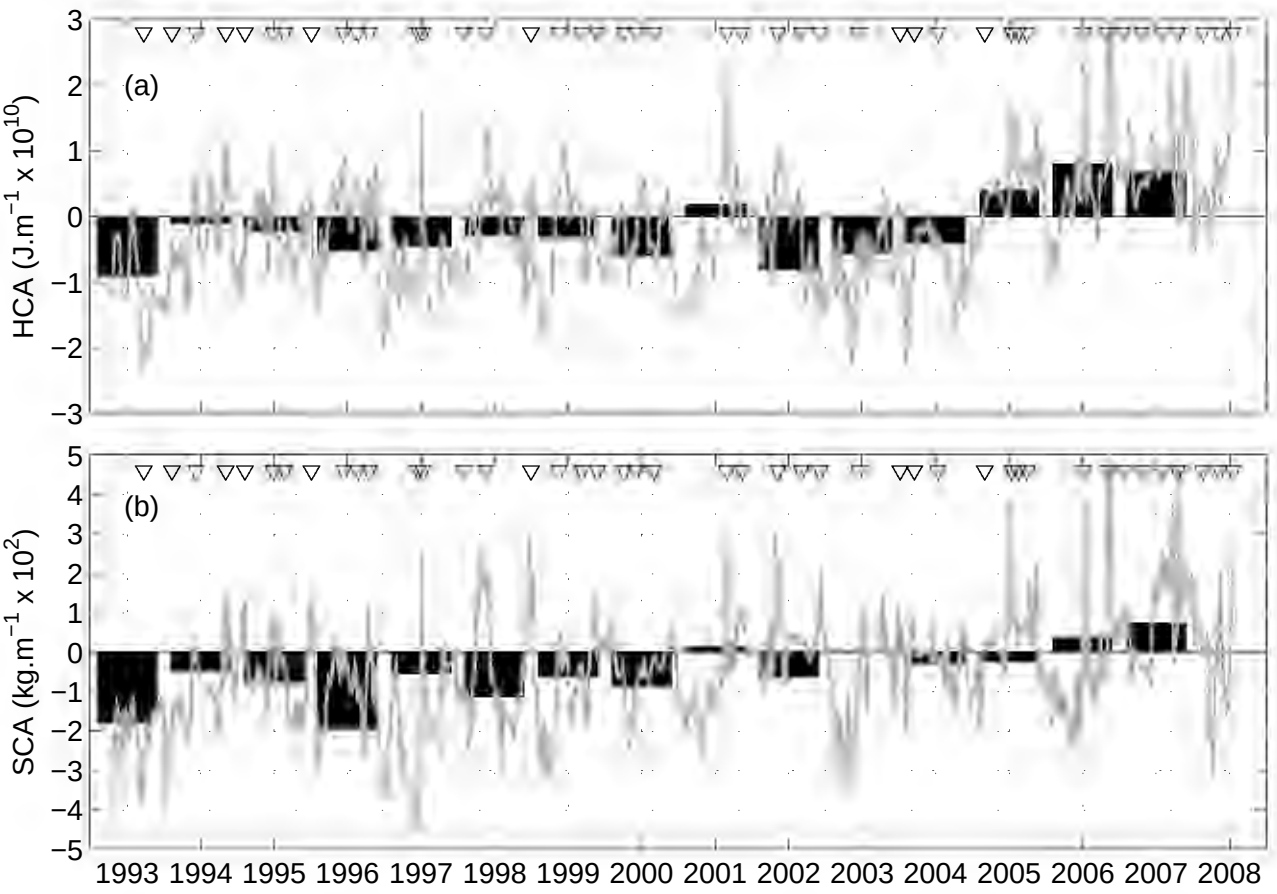

Figure 4.14: The time series of (a) HCA and (b) SCA are shown for the entire ACC domain (grey curves). The annual means are depicted by the bars. The presence of an Agulhas Ring in the SAZ is indicated by the arrows near the upper x-axis.

the SBdy (hereinafter, named the southern boundary zone; SBZ ∼18%), while the seasonal cycle of SCA progressed southward at a slower rate (SAZ ∼12%; SBZ ∼19%). Table 4.3 provides the percentage contribution of the seasonal variability to the total variance found in the time series of HCA and SCA in each frontal zone.

It is interesting to note that the annual mean time series of HCA depicts short-term positive trends (2004-2007) for all the frontal zones (the annual mean time series of HCA is not shown for each individual frontal zone but only for the entire ACC extent; Figure 4.14a). The HCA increase in the SAZ may be explained by the intense anomalous feature found in the region at the time (Section 4.4.2). However, as to why the other frontal zones experience a similar gain in HC remains unclear. This is matched by increases in the mean SCA in the SAZ but the SCA decreases in the APZ and the region between the SACCF and the APF, hereinafter named the southern ACC zone (SACCZ). This warm period can be seen across the entire meridional extent of the ACC in Figure 4.4a.

A positive (negative) trend in the HCA (SCA) are found in the southern parts of the ACC (linear trends are displayed in Figure 4.12c and d; not shown for SCA). This is limited to the SACCF, SBdy, and the SBZ. These trends are more likely induced by a regime shift, where the HCA (SCA) experiences a rapid increase (decrease)

Table 4.3: The variance contribution of the seasonal cycle to each frontal zone and the variance contribution of each frontal zone to the total variance of the ACC, for both HC and SC.

Frontal Zone	HC seasonal var. (%)	SC seasonal var. (%)	HC var. contrib. to ACC (%)	SC var. contrib. to ACC (%)
SAZ	9	12	55	65
APZ	12	7	18	20
SACCZ	11	14	16	14
SBZ	19	19	12	1

in the final quarter of 1996. In the SACCZ, the mean increase in HCA, between October 1992-October 1996 and between November 1996-January 2008, is 1.5 $\times 10^{10}$ $J.m^{-1}$, while the decrease in SCA is 24.2 $kg.m^{-1}$. The positive trends in the HCA seem to be consistent with a southward shift in the southern ACC fronts. Analyses of both altimetry trends in the position of the fronts in this study (not shown; and by *Sokolov and Rintoul*, 2009b) and CTD estimates (at the GH line) of frontal positions compared to historical data, show that where the fronts are more free to adjust (i.e. far from steep topography and deep narrow passages), they have had a clear southward shift since the early 1990s (probably due to ongoing climate change). This is especially the case for the subtropical region as well as the southward extent of the ACC and its associated fronts (not shown). Whether these differences are induced by an actual change in the system or by an anomalous spell up until 1997 remains unclear and cannot be answered due to the limited temporal extent of the altimeter time series.

Lastly, the HCA and SCA are integrated over the entire ACC band (between the SBdy and the STF) and displayed in Figure 4.14. The SAF and particularly the SAZ are the dominant role players in determining the HCA and SCA variability of the ACC. Clear peaks in both the HCA and the SCA found in the SAZ (Figure 4.12) are carried over into the ACC variability, while the long term (5-year) signals can also be detected. The warming and increasing salinity inclination from 2004-2008 is emphasised by the annual mean HCA and SCA, respectively. This results in the mean annual HCA and SCA peaking between 2007 and 2008 with values of $\sim$0.8 $\times 10^{10}$ $J.m^{-1}$ and $\sim$0.7 $\times 10^{2}$ $kg.m^{-1}$ above the mean, respectively. A breakdown of the variance contribution of each frontal zone to the entire ACC domain (Table 4.3) indicates that the SAZ is the dominant variability role player with a 55% (65%) contribution to the HCA (SCA) variance of the ACC. The mean variance contribution of HCA (SCA) declines sharply to 17.5% (20%) for the APZ, 15% (14%) for the SACCZ and 12% (1%) for the SBZ. This strong variance gradient is likely due to the order of magnitude difference in HC and SC found in the Subantarctic region compared with the region south of the APF. Furthermore, the contrasting strength of the T-S properties associated with mesoscale features originating from the subtropics (e.g. the Agulhas Current and STF) to water masses of the ACC will induce more intense anomalies than those found at higher latitudes. The weak meridional gradients of salinity in the CDW layer dominates the water column below $\sim$500 dbar and likely introduces the very low variance in SCA south of the SACCF. The percentage contribution of the variance in each frontal zone to the integrated ACC time series variance is shown in Table 4.3.

4.5.2 Modes of variability

This section briefly tests the extent to which the dominant modes of southern hemisphere atmospheric variability relate to the observed oceanic variability signals described in this study so far. The weekly time series of HCA and SCA data are used to produce monthly and annual means, for each front and frontal zone, before testing its correlation to the Southern Annular Mode (SAM) index and to the Southern Oscillation Index (SOI). The SAM index, as per *Marshall* (2003), has been incorporated in this study. In short, a true unbiased measure of the SAM has been calculated from the empirical definition of *Gong and Wang* (1999):

$$SAM = P^*_{40^\circ S} - P^*_{65^\circ S}\,, \tag{4.8}$$

where $P^*_{40^\circ S}$and $P^*_{65^\circ S}$ are the normalised monthly zonal mean sea level pressure (MSLP) at 40°S and 65°S, respectively. This has been slightly adjusted to values based on the mean of six station records near each of the two above mentioned latitudes (*Marshall*, 2003).

The SOI is the normalized difference in MSLP between Tahiti, French Polynesia and Darwin, Australia (*Troup*, 1965). These zonal pressure differences are principally set-up by the fluctuations in ocean temperatures during El Niño and La Niña phases (*Rasmusson and Carpenter*, 1982; *Philander*, 1990). Previous studies have shown that the SOI can strongly affect the southern hemisphere atmosphere extra-tropics, which can in-turn allow for an oceanic response (e.g. *Mo and White*, 1985; *Karoly*, 1989; *Mo*, 2000; *Yuan*, 2004).

The relation between the annual means of HCA at the APF and the annual mean of the SAM index (Figure 4.15) is explained by a correlation coefficient of 0.35 over the full time series. However, the first five years (1993-1997) are found to be anti-correlated (r=-0.22), while the remaining part of the time series (1998-2007) shows a relatively strong correlation coefficient (r=0.54) between the two variables. The general trend in the remaining ten years suggests that negative SAM years result in a cooling trend at the APF, and vice versa. The relation between the SAM index and the HCA/SCA in the remaining domains of the ACC do not show a strong connection, with correlation coefficients remaining positive but below 0.26. It may be that the correlation coefficients are higher at the APF because the maximum westerly wind stress occurs here. However, it remains unclear why the correlation coefficients are particularly low in the other ACC regions. These questions are currently being investigated in a study, which hopes to provide a clearer understanding of the relationship between the ACC and the SAM index (*Billany et al.*, 2009).

The SAM index shows a positive summer trend (1957-2005: *Marshall*, 2003, *Jones et al.*, 2009) with superimposed anomalies. *Sallee et al.* (2008) suggested that a positive anomaly of the SAM index translates into a southward shift of the APF in the Indian sector of the Southern Ocean. Their definition of the APF is related to a unique value of dynamic height for the entire Southern Ocean and not specific regional values, such as those defined recently by *Sokolov and Rintoul* (2009b) and in this study, thus they may miss part of the circumpolar variability. For the APF time series derived at the GH line, we see a marked southward shift in the front position. This shift seems to occur more clearly in 1998, with the onset of a positive SAM anomaly (http://jisao.washington.edu/data/aao/; *Thompson and Solomon*, 2002). It must be noted that the results of *Sallee et al.* (2008), on the regression of the Sea Level Anomaly onto the SAM index, displays a low correlation for the entire Atlantic sector, suggesting that the imprint of this mode of variability is low in the GH region, compared with the Indo-Pacific sector. On the other hand, *Meredith and Hogg* (2006) suggest a correlation between the SAM index and EKE in the ACC during 2000-2002, which is followed by a two-year delay relating to the positive SAM anomaly onset of 1998. Furthermore, they explain that the lag is due to the time taken for the SAM to influence the deeper ocean layers. If this increase in eddy activity is related to increases in wind stress (positive SAM anomaly: *Thompson and Solomon*, 2002) and if the Southern Ocean westerlies have a positive trend, as has been suggested by IPCC simulations (*Cai et al.*, 2003; *Rauthe et al.*, 2004) and various analyses of the NCEP wind field, it may suggest that the positive HCA trend may be explained by an increase in the poleward eddy-heat flux (*Meredith and Hogg*, 2006).

The SOI fails to describe any meaningful correlations with the integrated HCA between the STF and SACCF. The SBdy and SBZ, however, do display interesting connections with the SOI with a mean correlation coefficient of 0.45 between the annual mean values of HCA at the SBdy, and the SOI (Figure 4.16). Notably, if the correlation is performed for the period 1993-2001 the r- value increases to 0.67, whereas for the 2001-2007 period, the two time series appear anticorrelated (r=-0.56). The reason behind this is not entirely evident but, it suggests a modulation of the mechanism through which the SOI projects into the southern domain of the ACC, east of Drake Passage.

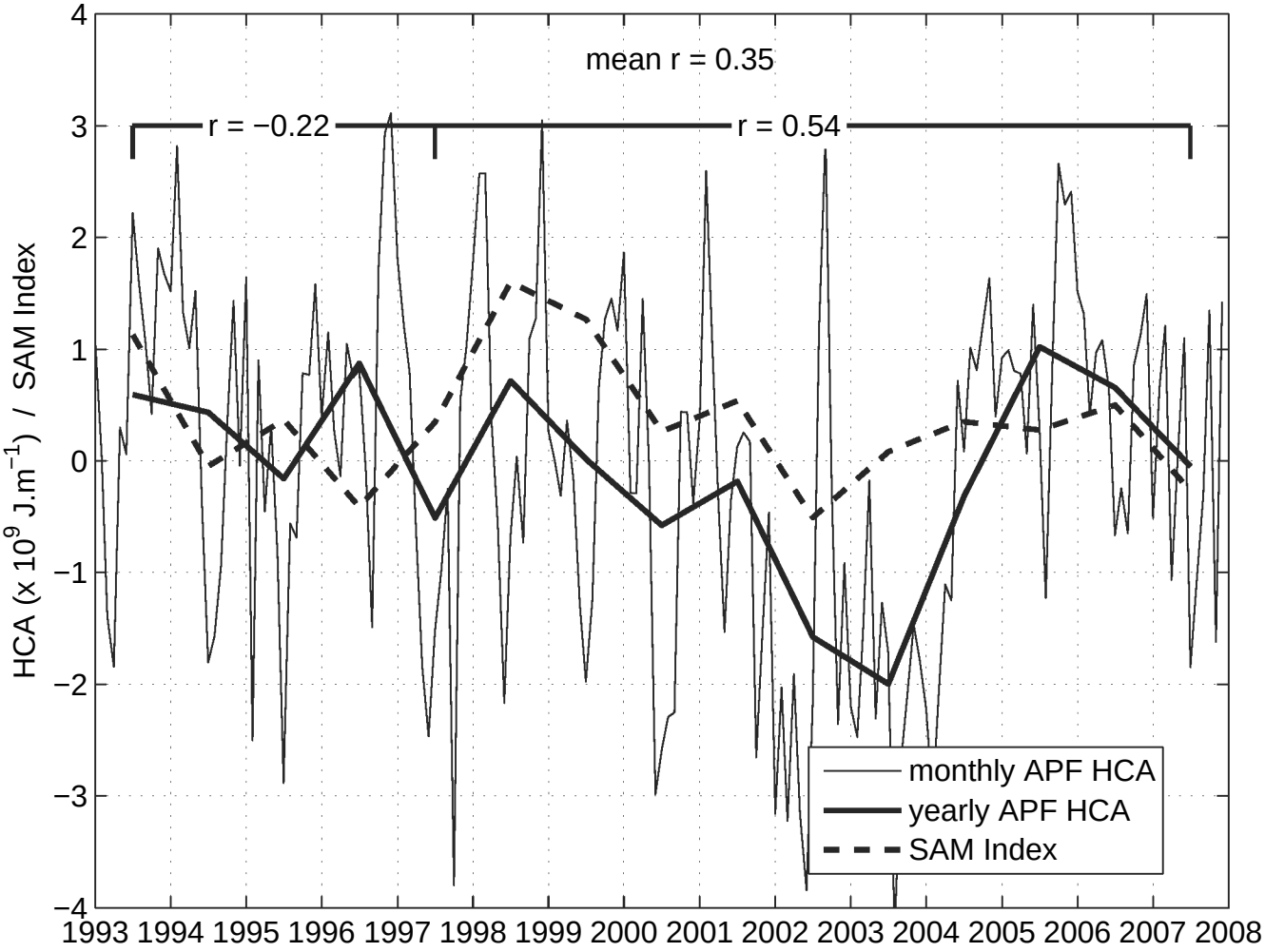

Figure 4.15: The relation between the yearly HCA at the APF (black curve) and the yearly SAM index (dashed curve). The grey curve represents the monthly HCA at the APF. The correlation coefficients are shown for the yearly data-sets between 1993-1997 and between 1997-2008, as well as for the entire time series.

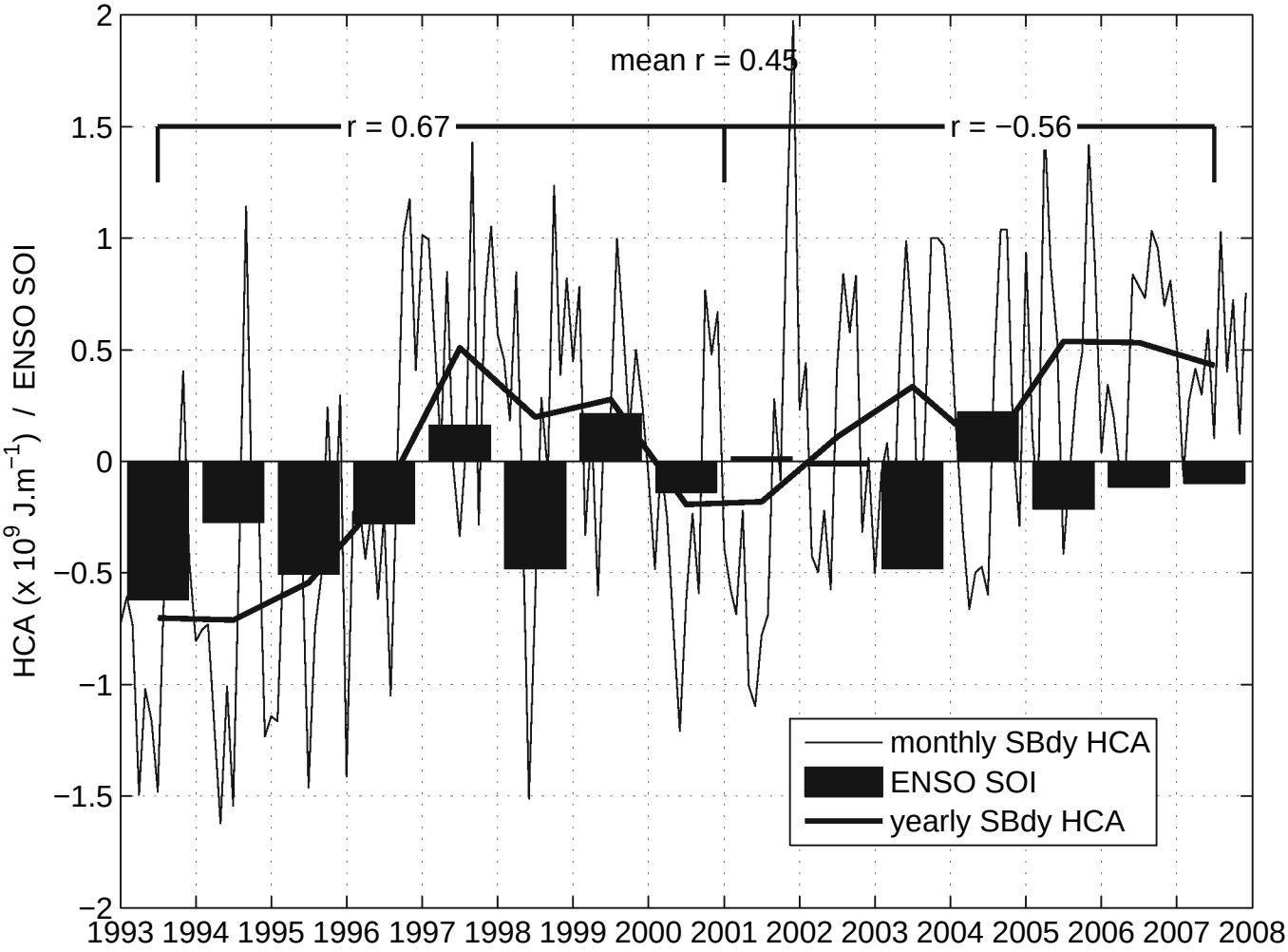

Figure 4.16: The relation between the yearly HCA at the SBdy (black curve) and the yearly SOI (bars). The grey curve represents the monthly HCA at the SBdy. The correlation coefficients are shown for the yearly data-sets between 1993-2001 and between 2002-2008, as well as for the entire time series.

4.6 Discussion and Summary

In this paper, we have studied how to make use of the SSH signal to better understand the role the fronts have in determining the heat and salt content variability of the ACC. This information allows us to determine the finer temporal and spatial component of the variability found at each front and frontal zone of the ACC. The behavior of the variability is noticeably different in each region and is largely a function of subtropical influences and of the underlying topography.

The Subtropical-Subantarctic dynamical regimes occurring across the GH transect are characterised by the injection of waters to the north-west (for the subtropical region) and to the south-west (for the SAZ) by Agulhas Rings. These features are very intense and are easily detectable using satellite altimetry products. Statistics are now available on the recurrence of such events during the entire satellite altimetric time series (*Dencausse*, 2009). From the altimetry time series, especially since the MADT product has been provided by CLS-AVISO (*Ducet et al.*, 2000; *Rio and Hernandez*, 2004), smaller mesoscale structures, and in particular cyclonic eddies, clearly appear (e.g. *Chelton et al.*, 2007). We observe such structures at every GH hydrographic cruise. Cyclonic eddies and smaller anticylonic structures, that develop poleward, are starting to be tracked through different methods in a more quantitative way. *Sokolov and Rintoul* (2009b) found that cyclones are more numerous than anticyclones, and *Roullet and Klein* (2009), in a very-high resolution numerical study of the ACC, found the same. The specific tracking of the cyclones has been initiated and finalised around the Southern African slope (*Rubio et al.*, 2009), which also shows a slight majority of cyclonic structures (that are ejected from the continental slope) over anti-cyclonic eddies in the Cape Basin. This type of analyses (in the form of regional modeling and altimetry data analysis) should be extended to the ACC sector of the GH region to quantitatively evaluate the mesoscale characteristics and associated transport of these features.

The propagation of Agulhas Rings into the northern domains of the ACC largely governs the anomalous behavior of the SAZ. These features are not consistently present in the region but on average they cross the GH line, south of the STF, 2.7 occasions per year. It is clear that the majority of the Agulhas Rings move out of the ACC region within a few months. However, a portion of their temperature, salinity and other property signals are likely to remain in the ACC, thereby providing an apparent mechanism for tropical-extratropical exchange. Furthermore, this study identifies an extremely anomalous episode of heat and salt content in the SAZ. The exploitation of the GEM allows us to better realise the impact these events have on the region by quantifying the subsurface temperature and salinity characteristics.

Key topographic obstructions, namely the Mid-Ocean Ridge, Agulhas Ridge and Meteor Rise, play a fundamental role in determining the behavior of the fronts at the GH line. The SAF experiences large-scale meandering as the jet is forced northwards by the Meteor Rise and generally inhibits the genesis of mesoscale eddies at the GH line. The opposite is true for the APF where, downstream of the Mid-Ocean Ridge, the input of relative vorticity is likely dissipated through nonlinear processes such as eddy action (*Hughes*, 1995). This seems to be the obvious heat and salt content variability signal found at the APF and may therefore, be a key region in the formation of warm and cold eddies in the ACC.

The time series of HCA and SCA within each front and frontal zone reveals the profound contribution the SAZ has to the total variability found in the ACC in the GH region (HC>50%, SC>60%). The proportion of variance introduced by the seasonal cycle was also calculated for each frontal zone. The results indicate that the seasonal cycle contributes a considerably greater portion of the total variance further to the south (∼20% of variance explained at the SBdy) compared with the SAZ (∼10%). This is likely caused by the higher amplitude

of the seasonal cycle in the higher latitudes but also reiterates that the variability in the Subantarctic regions may be driven more extensively by communications with the subtropical oceanic domains and, in more general, by the highly nonlinear character of the flow. Both satellite altimetry and high resolution modeling studies have uncovered that fine scale dynamics (mesoscale and submesoscale) play a major role in the Southern Ocean dynamics (*Hogg and Blundell*, 2006; *Chelton et al.*, 2007; *Thompson*, 2009; *Roullet and Klein*, 2009). The connection with atmospheric forcing and the large scale dynamics is therefore not as direct and linear as it was thought to be in previous studies (*Thompson and Solomon*, 2002; *Meredith et al.*, 2004; *Cai et al.*, 2003) and a dedicated study is needed to better understand this relationship.

Lastly, the use of wavelet analysis on the time series component of this paper shows that longer (>1 year) temporal modes of variability are present at the SAZ, APF and APZ. A short comparison with the two most well-known modes of variability in the Southern Ocean indicates that there may be some connection between the long-term variability found in the APF region and with the SAM index, while the SOI appears to be well correlated with the extreme southern parts of the ACC. A detailed comparison with surface wind speed data for the region may possibly yield some interesting results, but does not fit into the scope of the study presented here.

The exploitation of the proxy methods presented here are useful at improving our understanding of the subsurface properties that previously would have only been revealed by *in situ* sampling of the water column. However, we have to remain cautious in determining the scale of variability in the system using these techniques. The GEM is dependent on the height information at the sea surface to infer subsurface thermohaline information. As dynamic height is representative of the density signal throughout the water column, the GEM may not be able to precisely isolate variations in the heat and salt content within specific water masses and its strength is best suited at determining integrated property changes throughout the upper 2500 dbar of the water column. Additionally, at this stage we are unable to determine from what sources an increasing steric height signal may come from. This may be due to changes in the oceans heat content leading to thermal expansion of sea-water or from mass input originating from melting continental ice (*von Schuckmann et al.*, 2009). Moreover, it has recently been shown that mass input has a greater effect on steric height changes than initially thought (*Cazenave et al.*, 2008). Nevertheless, the use of data derived from proxy methods provides an important tool to study the variability and dynamics of the ACC system on a continuous basis and at an improved spatial resolution. These techniques justify added effort to refine them and to employ them to answer key scientific questions in Southern Ocean oceanography. These include better quantifying the meridional exchanges and fluxes of heat and fresh-water over the entire circumpolar path of the ACC.

Acknowledgement

This research forms part of the first author's PhD, completed at the University of Cape Town, and funded by the NRF and SANAP. This work is part of the international CLIVAR GoodHope project. S. Speich has been supported by the University of Brest, IRD and the national French Research Programme (LEFE). Thank you to I. J. Ansorge and J. R. E. Lutjeharms for helpful comment and guidance during this research. S. Swart thanks A. Naveira-Garabato and W. P. M. de Ruijter for a stay at the National Oceanography Centre, Southampton, UK, and IMAU, Universiteit van Utrecht, Netherlands, respectively. The wavelet analysis MatLab tools were obtained from *Torrence and Compo* (1998) and adapted by B. Backeberg. The monthly time series of the SAM and SOI indexes were obtained from KNMI climate explorer website (http://climexp.knmi.nl). Thanks are extended to R. Blamey and N. Hart for helpful comments during the writing of this manuscript. Lastly, the authors would like to thank two anonymous reviewers for their time in reviewing this paper.

Chapter 5

Conclusions

5.1 Summary

The Southern Ocean is a vital player in the global climate system and largely controls the balance of heat between the low and high latitudes. And yet, due to the vast distance between Africa and Antarctica and the lack of resources to conduct coordinated and regular research in the region, a knowledge gap in the Southern Ocean scientific community still exists. This formed part of the motivation for this study, which demonstrates how repeat hydrographic sections can be used to construct proxy relationships that can infer further information. These relationships have been employed to determine the variability of the oceanic region on finer temporal and spatial scales. Previous studies have tested similar proxy techniques in other regions of the Southern Ocean, namely the Drake Passage and south of Australia (e.g. *Rintoul et al.*, 2002; *Sokolov et al.*, 2004) but until now, none have been tested in the oceanic region south of Africa. It could be said that it is surprising that the extent of satellite altimetry coverage over the ocean has not been more vigorously employed to help solve some of the fundamental questions oceanographers have about Southern Ocean circulation and variability. This is especially true if one realises that altimetry data is the only extensive data-set that provides us with some insight into how the physical parameters vary below the surface, since the variability of the SSH signal is representative of the thermohaline changes occurring throughout the water column.

The first part of this thesis exploited upper ocean thermal data from XBT casts to accurately derive baroclinic transports of the ACC relative to 2500 dbar. The mean baroclinic transport, relative to 2500 dbar, for 18 XBT sections was 90 $\pm$ 2.4 Sv, while the estimate to the bottom was 145 $\pm$ 3.9 Sv. These estimates and those derived for each frontal zone corroborate other transport estimates for the region (discussed below), thereby providing confidence that these proxy techniques accurately provide information about the meridional baroclinic shear.

The proxy methods used here, are based on knowledge of the dynamic height signal. For this reason, weekly maps of altimetry data are used to render a 14-year time series of baroclinic transports of the ACC. These estimates agree well with simultaneous *in situ* estimates (rms difference in net transport of 5.2 Sv), suggesting that sea level anomalies largely reflect baroclinic transport changes in the upper 2500 dbar of the water column. The extended time series also allowed us to investigate the internal variability set up by the individual ACC fronts and frontal zones. This revealed that the SAF and APF are, by far, the main contributors to the ACC transport ($\sim$88%) and that the SAF contributes over 50% of the total transport variability of the ACC even though its net transport

contribution to the ACC is 9% less than the APF. We have shown that Agulhas Rings, propagating towards to west cause large transport reversals in the northern SAZ and result in high levels of variability.

In the Atlantic sector, volume transport measurements have occurred primarily in Drake Passage. *Whitworth* (1980) observed the baroclinic transport, relative to 2500 dbar, to average approximately 80 Sv, while *Nowlin and Clifford* (1982) obtained a range of between 86-88 Sv referenced to the same level. More recently, *Sokolov et al.* (2004) calculated the baroclinic transport to be 92.7 Sv, relative to 2500 dbar, from four CTD sections at the SR1 line, while upper ocean temperature derived baroclinic transports using proxy methods from these same data produced an estimate of 83.5 Sv. Our baroclinic transport estimates compare very closely with those of Drake Passage. These results suggest that there is no net gain or loss in the ACC volume along the South Atlantic basin or from the South Atlantic Gyre when regarding the circulation in the upper 2500 dbar. One must, however, keep in mind the uncertainties that may be created by temporal variations, and a barotropic transport contribution, when comparing the baroclinic transports along the longitudinal extent of the South Atlantic.

At deeper levels (>2500 dbar), between Drake Passage and the Greenwich Meridian, we found greater dynamical interaction for the water masses associated with the ACC and those found to the north. There are substantial variations in the bottom referenced baroclinic transport between Drake Passage, at 35°W, and at the Greenwich Meridian. Full depth mean baroclinic transports range between 134 ± 11 Sv (*Whitworth and Peterson*, 1985) and 137 ± 8 Sv (*Cunningham et al.*, 2003; *Sokolov et al.*, 2004) at Drake Passage, while at 35°W, a study by *Heywood and King* (2002) found the baroclinic transport to be 157 Sv. Our full depth baroclinic transport estimate in the region of the Greenwich Meridian is 145 Sv from both the CTD baroclinic flow and from the 18 XBT baroclinic transport estimates, which is the same as the values obtained by *Legeais et al.* (2005). This result may consequently reveal that approximately 20 Sv are gained within the ACC between Drake Passage and 35°W. This is ascribed to deep level injection of North Atlantic Deep Water (NADW) within the SAF in the western boundary region, as shown through water mass breakdown by *Heywood and King* (2002), and previously proposed by *Gordon* (1986). In addition, *Read and Pollard* (1993) showed some addition of NADW to the Circumpolar Deep Water (CDW) because of its higher salinity found further east at 40°E.

On the basis of isopycnal salinity distributions at deep levels (*Arhan et al.*, 2003), it has been suggested that the decrease from 157 Sv at 35°W to 145 Sv at the Greenwich Meridian (net loss of 12 Sv), reflects a northward loss of CDW by the ACC (*Legeais et al.*, 2005). If correct, this would be a partial compensation to the gain of NADW found to the west of 35°W, in the same depth range. Furthermore, the fact that transport estimates above 2500 dbar are similar between Drake Passage and the Greenwich Meridian supports the indication that net volume communication takes place in the deep ocean. There may also be a loss of Lower CDW (LCDW) from the ACC to the Weddell Gyre between 35°W and the Greenwich Meridian. Evidence shows that most of the water warmer than 0.2°C in the Weddell Gyre is an unmodified remnant of LCDW from the southern ACC (*Whitworth and Nowlin*, 1987). This idea is supported by $\theta - O_2$ diagrams from the Criva-2 stations, which show a discontinuity in $\theta - O_2$ slopes between LCDW and AABW (Park et al., 2001). Lastly, the bottom referenced baroclinic transport estimates of 157 Sv at 30°E (*Legeais et al.*, 2005), of 157 Sv (*Park et al.*, 2001) and of 159 Sv at 33°E (*Read and Pollard*, 1993) suggest that the ACC domain south of Africa gains between 9 to 14 Sv. *Read and Pollard* (1993) have suggested that this may be accounted for by a southward transfer of water across the STF south of the Agulhas Retroflection between 0° and 30°E.

The proxy techniques employed in the first paper were expanded to supply information on the subsurface thermohaline structure of the ACC. The ACC is well suited to exploiting the GEM method because each value of

dynamic height is characterised by a particular T-S curve, thereby illustrating that source waters have undergone similar physical processes to arrive at a particular streamfunction (*Watts et al.*, 2001). Altimetry data was combined with the GEM to produce 16 years worth of weekly fields of temperature and salinity across the meridional extent of the ACC. These fields were shown to compare closely with independent *in situ* observations of the water column, capturing more than 97% of the total temperature and density variance in the ACC domain.

The combination of the GEM with altimetry data provided a useful tool to study the heat and salt content variability of the ACC south of Africa. Specific emphasis was placed on determining the influence that subtropical mesoscale features, in particular Agulhas Rings, have on the oceanography of the Subantarctic region. The methods employed become more complicated in confluence regions where different source waters advect and converge, supplying different thermohaline properties along the same vertical coordinate at different times. This is precisely what occurs in the northern domains of the GH line, where subtropical Agulhas waters enter the ACC system and supply warm, salty water masses to the cooler, fresher environment of the SAZ (*Gladyshev et al.*, 2008; *Swart et al.*, 2008; *Swart and Speich*, 2009; *Dencausse et al.*, 2009). Despite these intrusions, the GEM-based correlations, produced from a large assemblage of hydrocasts, are sensitive to the variability and changes occurring within the region of interest, conserving all the thermohaline structures found in the hydrography and even capturing transient structures with small vertical scale. It was shown that, on average, Agulhas Rings were present south of the STF 2.7 occasions per annum. On one occasion, the Agulhas Ring appeared to merge with an eddy originating from the STF. This resulted in extremely high heat and salt signatures in the SAZ over a period of 1.5 years. These features likely provide a mechanism for tropical-extratropical exchange of heat and salt and the impact these types of phenomena have on the local biology and biogeochemistry of the region should be duly noted. The time series of thermohaline sections were also used to investigate the influence of the local bathymetry on the behavior of the ACC fronts. The variability at the APF was found to largely be caused by the Mid-Ocean Ridge further upstream, which caused the EKE to dominate the energy spectrum and suggested that this may be a region that allows for cross-frontal water mass exchange. Both satellite altimetry and high resolution modeling studies have uncovered that fine scale dynamics (mesoscale and submesoscale) play a major role in the Southern Ocean dynamics (*Hogg and Blundell*, 2006; *Chelton et al.*, 2007; *Thompson*, 2009; *Roullet and Klein*, 2009). The connection with atmospheric forcing and the large scale dynamics is therefore not as direct and linear as it was thought to be in previous studies (*Thompson and Solomon*, 2002; *Meredith et al.*, 2004; *Cai et al.*, 2003) and a dedicated study is needed to better understand this relationship.

The lack of observations south of Africa justify the use of the methods presented in this thesis. For the first time, we were able to investigate the longer-term variability of transports and thermohaline structure of the ACC at the African chokepoint. However, we have to remain cautious in determining the scale of variability in the system using these techniques. At this stage we are unable to determine from what sources the increasing steric height signal originates. This may be due to changes in the oceans heat content leading to thermal expansion of sea-water or from mass input originating from melting continental ice (*von Schuckmann et al.*, 2009). Moreover, it has recently been shown that mass input has a greater effect on steric height changes than initially thought (*Cazenave et al.*, 2008). With additional work refining these techniques we will be able to help answer the wealth of questions we have on the basin-scale circulation of the south-east Atlantic Ocean and understand its role in the hydrographic dynamics over the entire circumpolar path of the ACC.

5.2 Future work and study limitations

The use of the proxy methods described in this thesis makes use of observed data in order to set-up the required empirical relationships to render additional hydrographic information. This means that these methods can be continually improved and updated as new and more precise observations are recorded. A particular concern is that the vast majority of hydrographic profiles come from spring or summer months. This means that the variability captured by the proxy methods is biased towards the summer season and the addition of future winter observations will hopefully rectify this. This study does not make use of ARGO float data to derive any empirical relationships presented in this study (float data is only used to estimate the seasonal progression of variables for the GEM). This is mainly due to the time constrains of the thesis but also because float profiles have, until recently, been rare in the Southern Ocean (especially in this sector of the Southern Ocean where the seeding of profiling floats upstream of the Greenwich Meridian remains scarce). In time, the addition of hydrographic profiles by research expeditions and profiling floats will enhance the accuracy of the proxy techniques.

In the first Paper, the final sections use altimetry data to derive a 14-year time series of baroclinic transports of the ACC. This time series has been used to describe the variability contribution of each ACC front. However, due to length and time constraints, the study does not decompose the transport time series to better understand what affects the overall variability signal of the ACC. It is hoped that in the future, time series analysis techniques can be applied to the data in order to determine the effects of the atmospheric modes of variability (such as the El Ninõ Southern Oscillation and/or the Southern Annular Mode) and to calculate the lagged correlation coefficient due to the surface wind forcing (example, NCEP reanalysis wind data) to estimate the contribution made by the surface wind stress.

In this thesis, the use of the GEM is limited to the GoodHope line where observed data is most abundant. The incorporation of profiling float data would allow for the GEM to be expanded longitudinally into the Southern Ocean, thereby providing 3-dimensional views of ocean variables. This would be particularly useful at better understanding the advection of water masses throughout the Southern Ocean and their connection with exterior oceanic regions. Furthermore, the zonal influence of the subtropical ocean regions (i.e. the Agulhas Return Current) on the Southern Ocean can be conceptualised. A portion of the animations, presented in Appendix A, do expand the GEM several degrees zonally but none of this data is incorporated into any of the three presented Papers.

Resolving the ocean domains outside of the ACC have presented a challenge in this study. The proxy relationships frequently fail in very variable regions where there is extensive mesoscale activity, such as by Agulhas Rings propagating north of the STF to the south-west of South Africa. In these regions, at individual depths, multiple values of temperature and salinity coincide with one value of surface dynamic height. This means that when sea-surface-heights are used to estimate either the baroclinic transport or thermohaline structure in these regions, the technique is unable to define an exact value and often the error is much higher. It is possible that the relationships can be 'fine-tuned' in the future to allow some flexibility in these regions, but at present this problem remains unsolved.

Combining the GEM with altimetry data produces a vast amount of information on the hydrographic structure of the ACC. Paper III only uses a fraction of this data to unveil the subsurface heat and salt content variability along the GoodHope line over 16 years. It is hoped that more of the available information will be exploited to answer questions pertaining to the oceanography of the region. This data also has huge potential to assist other marine disciplines, such as biological and biogeochemistry studies, which rely on physical data to understand the underlying forcings revealed in its data. Additionally, it has been noted in the results of this thesis that the GEM has more

practical applications, such as predicting the approximate hydrographic environment prior to arrival by research ships, which determine their station placings and spatial resolution often to coincide with front positions or the occurrence of anomalous oceanographic features (example, large eddies or meanders). In the near future, detailed measurements of the Earth's field will become available, which will lead to a more accurate account of the Earth's geoid (Gravity Recovery and Climate Experiment: GRACE mission). This will greatly improve the application of proxy methods, such as the GEM. With an accurate account of the geoid, the baroclinic and barotropic components of the altimetry signal can be accurately separated. This means that our ability to estimate the absolute velocity and volume transport of the ACC can be achieved using these methods. The subject of a future paper will deal with attempting to derive absolute velocities in the ACC using the altimetry-GEM combination. These proxy methods are appreciably promising and justify added effort to refine them. These techniques also highlight the value remote sensing techniques have on monitoring the variability of the ACC, in a data sparse and isolated region, like the Southern Ocean.

Bibliography

Ansorge, I. J., S. Speich, J. R. E. Lutjeharms, G. J. Goni, C. J. Rautenbach, W. Froneman, M. Rouault, and S. Garzoli (2004), Monitoring the oceanic flow between Africa and Antarctica, *S. Afr. J. Sci.*, *101*, 29–35.

Ansorge, I. J., J. R. E. Lutjeharms, N. C. Swart, and J. V. Durgadoo (2006), Observational evidence for a cross-frontal heat pump in the Southern Ocean, *Geophys. Res. Lett.*, *32*, L14,603, doi:10.1029/2005GL22,588.

Arhan, M., H. Mercier, and Y.-H. Park (2003), On the deep water circulation of the eastern South Atlantic Ocean, *Deep Sea Res. Part I*, *50*, 889–916.

Bailey, R., A. Gronel, H. Philips, G. Meyers, and E. Tanner (1994), CSIRO Cookbook for quality control of expendable bathythermograph (XBT) data, *Tech. Rep. 220*, CSIRO Marine Laboratories, Hobart, Australia.

Beal, L. M., and H. L. Bryden (1999), The velocity and vorticity structure of the Agulhas Current at 32°S, *J. Geophys. Res.*, *104*, 5151–5176.

Belkin, I. M., and A. L. Gordon (1996), Southern Ocean fronts from the Greenwich meridian to Tasmania, *J. Geophys. Res.*, *101*, 3675–3696.

Billany, W., S. Swart, J. Hermes, and C. J. C. Reason (2009), Variability in Southern Ocean fronts at the Greenwich Meridian, *in prep.*

Boebel, O., J. Lutjeharms, C. Schmid, W. Zenk, T. Rossby, and C. Barron (2003), The Cape Cauldron: a regime of turbulent inter-ocean exchange, *Deep-Sea Res.*, *50*, 57–86.

Book, J. (1998), Kuroshio variations off southwest Japan, *Tech. rep.*, M.S. thesis, Graduate School of Oceanography, University of Rhode Island.

Bryden, H. L., L. M. Beal, and L. M. Duncan (2005), Structure and transport of the Agulhas Current and its temporal variability, *J. Oceanogr.*, *61*(3), 479–492.

Budillon, G., and S. R. Rintoul (2003), Fronts and upper ocean thermal variability south of New Zealand, *Antarctic Sci.*, *15*, 141–152.

Byrne, D. A., D. L. Witter, D. R. Watts, N. R. Pettigrew, C. M. D. Rae, and S. Baker-Yeboah (2006), Interocean heat and salt transports from the Agulhas Leakage: First results from ASTTEX, *Eos Trans. AGU, Ocean Sci. Meet. Suppl.*, *87(36)*(Abstract OS22C-03).

Cai, W. (2006), Antarctic ozone depletion causes an intensification of the Southern Ocean super-gyre circulation, *Geophys. Res. Lett.*, *33*, doi:10.1029/2005GL024,911.

Cai, W., P. H. Whetton, and D. J. Karoly (2003), The response of the Antarctic Oscillation to increasing and stabilized atmospheric CO2, *J. Clim.*, *16*, 1525–1538.

Callahan, J. E. (1972), Structure and Circulation of Deep-Water in Antarctic, *Deep-Sea Res.*, *19*, 563.

Cazenave, A., K. Dominh, S. Guinehut, E. Berthier, W. Llovel, G. Ramillien, M. Ablain, and G. Larnicol (2008), Sea level budget over 2003-2008: A reevaluation from GRACE space gravimetry, satellite altimetry and Argo, *Glob. Planet. Change*, *65*, doi:10.1016/j.gloplacha.2008.10.004.

Chelton, D. B., M. G. Schlax, D. L. Witter, and J. G. Richman (1990), Geosat altimeter observations of the surface circulation of the Southern Ocean, *J. Geophys. Res.*, *95*, 17,877–17,903.

Chelton, D. B., M. G. Schlax, R. M. Samelson, and R. A. de Szoeke (2007), Global observations of large ocean eddies, *Geophys. Res. Lett.*, *34*, L15,606, doi:10.1029/2007GL030,812.

Clarke, A. J. (1982), The Dynamics of Large-Scale, Wind-Driven Variations in the Antarctic Circumpolar Current, *J. Phys. Oceanogr.*, *12*, 1092–1105.

Cunningham, S. A., S. G. Alderson, B. A. King, and M. A. Brandon (2003), Transport and variability of the Antarctic Circumpolar Current in Drake Passage, *J. Geophys. Res.*, *108*(C5), doi:10.1029/2001JC001,147.

Daneshzadeh, Y.-H. C., J. F. Festa, and S. M. Minton (1994), Procedures used at NOAA-AOML to quality control real time XBT data collected in the Atlantic Ocean, *Tech. Rep. ERL AOML-78*, NOAA Atlantic Oceanographic and Meteorological Laboratory.

Daniault, N., and Y. Menard (1985), Eddy kinetic energy distribution in the Southern Ocean from altimetry and FGGE drifting buoys, *J. Geophys. Res.*, *90*, 11,877–11,889.

Darbyshire, M. (1963), Computed surface currents off the the Cape of Good Hope, *Deep-Sea Res.*, *10*, 623–632.

Daubechies, I. (1992), *Ten lectures on Wavelets*, 357 pp., Soc. for Ind and Appl. Math., Philadelphia, Pa.

de Ruijter, W. P. M., A. Biastoch, S. S. Drijfhout, J. R. E. Lutjeharms, R. P. Matano, T. Pichevin, P. J. van Leeuwen, and W. Weijer (1999), Indian-Atlantic interocean exchange: Dynamics, estimation and impact, *J. Geophys. Res.*, *104*, 20,885–20,910.

Deacon, G. E. R. (1933), A general account of the hydrology of South Atlantic Ocean, *Discovery Reports*, *7*, 171–238.

Deacon, G. E. R. (1937), The hydrology of the Southern Ocean, *Discovery Reports*, *15*, 1–124.

Deacon, G. E. R., and J. A. Moorey (1975), The boundary region between currents from the Weddell Sea and Drake Passage, *Deep-Sea Res.*, *22*, 265–268.

Dencausse, G. (2009), Echanges Indo-Atlantique d'Eau Subtropicale en Relation aux Structures Frontales et de Meso-echelle: utilisation de la Serie Temporelle Altimetrique de Niveau de la Mer, *Tech. rep.*, PhD, Universite de Bretagne Occidentale.

Dencausse, G., M. Arhan, and S. Speich (2009), Routes of Agulhas rings in the southeastern Cape Basin, *submitted, Deep-Sea Res. I.*

Ducet, N., P. Y. le Traon, and G. Reverdin (2000), Global high-resolution mapping of ocean circulation from TOPEX/Poseidon and ERS-1 and-2, *J. Geophys. Res.*, *105*, 19,477–19,498.

Duncombe-Rae, C. M. (1991), Agulhas retroflection rings in the South Atlantic ocean: an overview, *S. Afr. J. Mar. Sci.*, *11*, 327–344.

Emery, W. J., and R. E. Thomson (2001), *Data analysis methods in physical oceanography*, 2nd ed., Elsevier Science B. V., pages: 281-285.

Georgi, D. T., and J. M. Toole (1982), The Antarctic Circumpolar Current and the oceanic heat and freshwater budgets, *J. Mar. Res.*, *40*, 183–197.

Gill, A. E., and P. P. Niiler (1973), Theory of Seasonal Variability in Ocean, *Deep-Sea Res.*, *20*, 141–177.

Gille, S. T. (2002), Warming of the Southern Ocean since the 1950s, *Science*, *295*, 1275–1277.

Gladyshev, S., M. Arhan, A. Sokov, and S. Speich (2008), A hydrographic section from South Africa to the southern limit of the Antarctic Circumpolar Current at the Greenwich meridian, *Deep-Sea Res. I*, *55*, 1284–1303.

Gong, D., and S. Wang (1999), Definition of Antarctic oscillation index, *Geophys. Res. Lett.*, *26*, 459–462.

Gordon, A. L. (1967), Geostrophic transport through Drake Passage, *Science*, *156*, 1732.

Gordon, A. L. (1985), Indian-Atlantic transfer of thermocline water at the Agulhas Retroflection, *Science*, *227*, 1030–1033.

Gordon, A. L. (1986), Inter-Ocean Exchange of Thermocline Water, *J. Geophys. Res.*, *91*, 5037–5046.

Gordon, A. L., and B. A. Huber (1995), Warm Weddell deep water west of Maud rise, *J. Geophys. Res.*, *100(C7)*, 13,747–13,753.

Gordon, A. L., D. T. Georgi, and H. W. Taylor (1977), Antarctic Polar Front Zone in Western Scotia Sea - Summer 1975, *J. Phys. Oceanogr.*, *7*, 309–328.

Gordon, A. L., D. G. Martinson, and H. W. Taylor (1981), The wind-driven circulation in the Weddell-Enderby Basin, *Deep-Sea Res.*, *28A*, 151–163.

Gordon, A. L., J. R. E. Lutjeharms, and M. L. Grundlingh (1987), Stratification and circulation at the Agulhas Retroflection, *Deep-Sea Res.*, *34*(4), 565–599.

Gordon, A. L., R. F. Weiss, W. M. Smethie, and M. J. Warner (1992), Thermocline and Intermediate Water Communication Between the South-Atlantic and Indian Oceans, *J. Geophys. Res.*, *97*, 7223–7240.

Gouretski, V. V., and A. I. Danilov (1994), Characteristics of warm rings in the African sector of the Antarctic Circumpolar Current, *Deep-Sea Res. I*, *41*, 1131–1157.

Heywood, K. J., and B. A. King (2002), Water masses and baroclinic transports in the South Atlantic and Southern oceans, *J. Mar. Syst.*, *60*, 639–676.

Hogg, A. M., and J. R. Blundell (2006), Interdecadal variability of the Southern Ocean, *J. Phys. Oceanogr.*, *36*, 1626–1645.

Hughes, C. W. (1995), Rossby waves in the Southern Ocean: A comparison of TOPEX/POSEIDON altimetry with model predictions, *J. Geophys. Res.*, *100*, 15,933–15,950.

Hughes, C. W. (1996), The Antarctic Circumpolar Current as a waveguide for Rossby waves, *J. Phys. Oceanogr.*, *26*, 1375–1387.

Hughes, C. W., and E. R. Ash (2001), Eddy forcing of the mean flow in the Southern Ocean, *J. Geophys. Res.*, *106(C2)*, 2713–2722.

Jacobs, S. S., and D. T. Georgi (1977), Observations on the southwest Indian/Antarctic Ocean, *Voyage of Discovery-M. Angel, editor, Oergamon, New York*, (43-85).

Jones, J. M., R. L. Fogt, M. Widmann, and G. Marshall (2009), Historical SAM variability. Part I: Century length seasonal reconstructions, *submitted to J. Clim.*

Joyce, T. M., W. Zenk, and J. M. Toole (1978), The anatomy of the Antarctic Polar Front in the Drake Passage, *J. Geophys. Res.*, *83*, 6093–6113.

Karoly, D. J. (1989), Southern hemisphere circulation features associated with El Nino-Southern Oscillation events, *J. Clim.*, *2*, 1239–1252.

Klatt, O., E. Fahrbach, E. Hoppema, and G. Rohardt (2005), The transport of the Weddell Gyre across the Prime Meridian, *Deep-Sea Res.*, *52*, 513–528, doi:10.1016/j.dsr2.2004.12.015.

Koshlyakov, M. N., Y. M. Grachev, T. G. Sazhina, and M. I. Yaremchuk (1985), A cyclonic eddy in the Antarctic Circumpolar Current and heat transport across the Antarctic Front, *Oceanology*, *25*, 685–691.

Kostianoy, A. G., A. I. Ginzburg, M. Frankignoulle, and B. Delille (2004), Fronts in the Southern Indian Ocean as inferred from satellite sea surface temperature data, *J. Mar. Sys.*, *45*, 55–73.

Lau, K. M., and H. Weng (1995), Climate signal detection using wavelet transform: How to make a time series sing, *Bull. Amer. Meteorol. Soc.*, *76*(12), 2391–2402.

le Traon, P., P. F. Nadal, and N. Ducet (1998), An improved mapping method of multisatellite altimeter data, *J. Atm. Ocean. Tech.*, *15*, 522–534.

le Traon, P. Y., and F. Ogor (1998), ERS-1/2 orbit improvement using TOPEX/POSEIDON: The 2cm challenge, *J. Geophys. Res.*, *103*, 8045–8057.

Legeais, J.-F. (2005), Transport du Courant Circumpolaire Antarctique et distribution spatiale des fronts oceaniques, *MSc Thesis*.

Legeais, J.-F., S. Speich, M. Arhan, I. J. Ansorge, E. Fahrbach, S. Garzoli, and A. Klepikov (2005), The baroclinic transport of the Antarctic Circumpolar Current south of Africa, *Geophys. Res. Lett.*, *32(L24602), doi:10.1029/2005GL023271*.

Lemke, P. (1992), WHP Cruise Summary Information: A12, *Tech. rep.*, Alfred Wegener Institut fuer Polar- und Meeresforschung, Bremerhaven, Germany.

Levitus, S. (1982), *Climatological Atlas of the World Ocean*, NOAA Professional Paper No. 13.

Lutjeharms, J. R. E. (1985), Location of frontal systems between Africa and Antarctica: some preliminary results, *Deep-Sea Res.*, *32*, 1499–1509.

Lutjeharms, J. R. E. (1988), Meridional heat transport across the Sub-Tropical Convergence by a warm eddy, *Nature*, *331*(251-253).

Lutjeharms, J. R. E. (1996), *In: The South Atlantic: Present and Past Circulation*, chap. The exchange of water between the South Indian and South Atlantic oceans, Springer-Verlag, Heidelberg, pp. 125-162.

Lutjeharms, J. R. E. (2006), *The Agulhas Current*, Springer-Verlag, Heidelberg, 329 pp.

Lutjeharms, J. R. E., and R. C. V. Ballegooyen (1988), The Retroflection of the Agulhas Current, *J. Phys. Oceanogr.*, *18*, 1570–1583.

Lutjeharms, J. R. E., and W. J. Emery (1983), The detailed thermal structure of the upper ocean layers between Cape Town and Antarctica during the period Jan-Feb 1978, *S. Afr. J. Antarc. Res.*, *13*, 3–14.

Lutjeharms, J. R. E., and A. L. Gordon (1987), Shedding of an Agulhas Ring observed at sea, *Nature*, *325*, 138–140.

Lutjeharms, J. R. E., and H. R. Valentine (1984), Southern Ocean thermal fronts south of Africa, *Deep-Sea Res.*, *31*, 1461–1475.

Lutjeharms, J. R. E., and H. R. Valentine (1988), Eddies at the Sub-Tropical Convergence south of Africa, *J. Phys. Oceanogr.*, *18*, 761–774.

Lutjeharms, J. R. E., O. Boebel, and H. T. Rossby (2003), Agulhas cyclones, *Deep-Sea Res.*, *50*, 13–34.

Mackintosh, N. A. (1946), The Antarctic Convergence and the distribution of surface temperatures in Antarctic waters, *Discovery Reports*, *23*, 177–212.

Marshall, G. J. (2003), Trends in the Southern Annular Mode from observations and reanalysis, *J. Clim.*, *16*, 4134–4143.

McCartney, M. S. (1977), Subantarctic Mode Water, *Discovery Reports*, pp. 103–119.

Meinen, C. S., and D. R. Watts (2000), Vertical structure and transport on a transect across the North Atlantic Current near 42°N, *J. Geophys. Res.*, *105*(21), 21,869–21,891.

Melice, J. L., A. Coron, and A. Berger (2001), Amplitude and frequency modulations of the Earth's obliquity for the last million years, *J. Clim.*, *14*, 1043–1054.

Meredith, M. P., and A. M. Hogg (2006), Circumpolar response of Southern Ocean eddy activity to a change in the Southern Annular Mode, *Geophys. Res. Lett.*, *33*, L16,608, doi:10.10,029/2006GL026,499.

Meredith, M. P., P. L. Woodworth, C. W. Hughes, and V. Stepanov (2004), Changes in the ocean transport through Drake Passage during the 1980s and 1990s, forced by changes in the Southern Annular Mode, *Geophys. Res. Lett.*, *31*, L21,305, doi:10.1029/2004GL021,169.

Mo, K. (2000), Relationships between low-frequency variability in the Southern Hemisphere and sea surface temperature anomalies, *J. Clim.*, *13*, 3599–3610.

Mo, K., and G. White (1985), Teleconnections in the southern hemisphere, *Monthly Weather Rev.*, *113*, 22–37.

Moore, J. K., M. R. Abbott, and J. G. Richman (1997), Variability in the location of the Antarctic Polar Front (90°-20°W) from satellite sea surface temperature data, *J. Geophys. Res.*, *102*, 27,825–27,833.

Moore, J. K., M. R. Abbot, and J. G. Richman (1999), Location and dynamics of the Antarctic Polar Front from satellite sea surface temperature data, *J. Geophys. Res.*, *104 (C2)*, 3059–3073.

Morrow, R., R. Coleman, J. Bhurch, and D. Chelton (1994), Surface eddy momentum flux and velocity variances in the Southern Ocean from Geosat altimetry, *J. Phys. Oceanogr.*, *24*, 2050–2071.

Morrow, R., J.-R. Donguy, A. Chaigneau, and S. R. Rintoul (2004), Cold-core anomalies at the Subantarctic Front, south of Tasmania, *Deep-Sea Res., I*, *51*, 1417–1440.

Mosby, H. (1934), The waters of the Atlantic Antarctic Ocean, *Scientific Results of the Norwegian Antarctic Expedition*, *11*, 1–131.

Naveira-Garabato, A. C., E. L. McDonagh, D. P. Stevens, K. J. Heywood, and R. J. Sanders (2002), On the export of Antarctic Bottom Water from the Weddell Sea, *Deep-Sea Res.*, *49*, 4715–4742.

Nowlin, W. D., and M. Clifford (1982), The kinematic and thermohaline zonation of the Antarctic Circumpolar Current at Drake Passage, *J. Mar. Res.*, *40*, 481–507.

Nowlin, W. D., and J. M. Klinck (1986), The physics of the Antarctic Circumpolar Current, *Rev. Geophys. Space Phys.*, *24*, 469–491.

Olbers, D., and K. Lettmann (2007), Barotropic and baroclinic processes in the transport variability of the Antarctic Circumpolar Current, *Ocean Dynamics*, *57*, 559–578, doi:10.1007/s10,236–007–0126–1.

Olbers, D., and M. Visbeck (2005), A model of the zonally averaged stratification and overturning in the Southern Ocean, *J. Phys. Oceanogr.*, *45*, 1190–1205, doi:10.1175/JPO2750.

Olbers, D., and C. Wubber (1991), *In: Strategies for Future Climate Research*, chap. The role of wind and buoyancy forcing of the Antarctic Circumpolar Current, MPI, Hamburg, pp. 161-192.

Olbers, D., D. Borowski, C. Volker, and J.-O. Wolff (2004), The dynamical balance, transport and circulation of the Antarctic Circumpolar Current, *Antarctic Sci.*, *4*, 439–470, doi:10.1017/S0954102004002,251.

Orsi, A. H., W. D. Nowlin, and T. Whitworth (1993), On the circulation and ctratification of the Weddell Gyre, *Deep-Sea Res.*, *40*, 169–203.

Orsi, A. H., T. Whitworth, and W. D. Nowlin (1995), On the meridional extent and fronts of the Antarctic Circumpolar Current, *Deep-Sea Res.*, *42*, 641–673.

Park, Y. H., E. Charriaud, D. R. Pino, and C. Jeandel (1998), Seasonal and interannual variability of the mixed layer properties and steric height at station KERFIX, southwest of Kerguelen, *J. Mar. Sys.*, *17*, 571–586.

Park, Y. H., E. Charriaud, P. Craneguy, and A. Kartavtseff (2001), Fronts, transport, and Weddell Gyre at 30°E between Africa and Antarctica, *J. Geophys. Res.*, *106*, 2857–2879.

Patterson, S. (1985), Surface circulation and kinetic energy distribution in the Southern Hemisphere oceans from FGGE drifting buoys, *J. Phys. Oceanogr.*, *15*, 865–884.

Peterson, R. G. (1988), On the Transport of the Antarctic Circumpolar Current Through Drake Passage and Its Relation to Wind, *J. Geophys. Res.*, *93*, 13,993–14,004.

Peterson, R. G., and L. Stramma (1991), Upper-Level Circulation in the South-Atlantic Ocean, *Prog. Oceanogr.*, *26*, 1–73.

Philander, S. G. H. (1990), *El Nino, La Nina and the Southern Oscillation*, 289 pp, Academic Press, San Diego, CA.

Philips, H. E., and S. R. Rintoul (2000), Eddy variability and energetics from direct current measurements in the Antarctic Circumpolar Current south of Australia, *J. Phys. Oceanogr.*, *30*, 3050–3076.

Piola, A. R., and D. T. Georgi (1982), Circumpolar Properties of Antarctic Intermediate Water and Sub-Antarctic Mode Water, *Deep-Sea Res.*, *29*, 687–711.

Pond, S., and G. L. Pickard (1983), *Introductory Dynamical Oceanography*, 2 ed., Pergamon Press.

Rasmusson, E. M., and T. Carpenter (1982), Variations in tropical sea surface temperature and surface wind fields associated with the Southern Oscillation/El Nino, *Monthly Weather Rev.*, *110*, 354–384.

Rauthe, M., A. Hense, and R. Morrow (2004), A model intercomparison study of climate change signals in extratropical circulation, *Int. J. Climatol.*, *24*, 643–662.

Read, J. F., and R. T. Pollard (1993), Structure and transport of the Antarctic Circumpolar Current and Agulhas Return Current at 40°E, *J. Geophys. Res.*, *98*, 12,281–12,295.

Reid, J. L., and W. D. Nowlin (1971), Transport of Water Through Drake Passage, *Deep-Sea Res.*, *18*, 51.

Richardson, P. L. (1983), Eddy Kinetic Energy in the North Atlantic from surface drifters, *J. Geophys. Res.*, *88*(C7), 4355–4367.

Richardson, P. L. (2007), Agulhas leakage into the Atlantic estimated with subsurface floats and surface drifters, *Deep Sea Res. I*, *54*, 1361–1389.

Rintoul, S. R. (1991), South-Atlantic Interbasin Exchange, *J. Geophys. Res.*, *96*, 2675–2692.

Rintoul, S. R. (2007), Rapid freshening of Antarctic Bottom Water formed in the Indian and Pacific oceans, *Geophys. Res. Lett.*, *34, L06606*, doi:10.1029/2006GL028,550.

Rintoul, S. R., and S. Sokolov (2001), Baroclinic transport variability of the Antarctic Circumpolar Current south of Australia (WOCE repeat section SR3), *J. Geophys. Res.*, *106*, 2815–2832.

Rintoul, S. R., J. R. Donguy, and D. H. Roemmich (1997), Seasonal evolution of upper ocean thermal structure between Tasmania and Antarctica, *Deep Sea Res. Part I*, *44*, 1185–1202.

Rintoul, S. R., C. W. Hughes, and D. Olbers (2001), *In: Ocean circulation and climate: Observing and Modelling the Global Ocean*, ISBN-13: 9780126413519, Elsevier Science Ltd.

Rintoul, S. R., S. Sokolov, and J. Church (2002), A 6-year record of baroclinic transport variability of the Antarctic Circumpolar Current at 140°E from expendible bathythermograph and altimetry measurements, *J. Geophys. Res.*, *107*, C10, 3155, doi:10.1029/2001JC000,787.

Rio, M. H., and F. Hernandez (2004), A mean dynamic topography computed over the world ocean from altimetry, in situ measurements, and a geoid model, *J. Geophys. Res.*, *109*, C12,032, doi:10.1029/2003JC002,226.

Roether, W., M. Samthein, T. J. Muller, W. Nellen, and D. Sahrhage (1990), Sudatlantik-Zircumpolarstrom, Reise Nr. 11, 3 Oktober 1989-11 Marz 1990, Meteor-Ber. 90-2, *Tech. rep.*, University of Hamburg, Hamburg, Germany.

Roullet, G., and P. Klein (2009), Available potential energy diagnosis in a direct numerical simulation of rotating stratified turbulence, *J. Fluid Mech.*, *624*, doi:10.1017/S0022112008004,473.

Rubio, A., B. Blanke, S. Speich, N. Grima, and C. Roy (2009), Mesoscale eddy activity in the southern Benguela upwelling system from satellite altimetry and model data, *in press in Prog. Oceanogr.*

Sallee, J. B., K. Speer, and R. Morrow (2008), Southern Ocean fronts and their variability to climate modes, *J. Clim.*, *21*(12), 3020–3039.

Schmitz, W. J. (1996), On the Eddy field in the Agulhas Retroflection, with some global considerations, *J. Geophys. Res.*, *101*, 16,259–16,271.

Schouten, M. V., W. P. M. de Ruijter, P. J. van Leeuwen, and J. R. E. Lutjeharms (2000), Translation, decay and splitting of Agulhas rings in the south-eastern Atlantic Ocean, *J. Geophys. Res.*, *105*, 21,913–21,925.

SIO (1985), Cruise Report: AJAX, *Tech. rep.*, Scripps Institution of Oceanography/Texas A and M University, USA.

Sloyan, B. M., and S. R. Rintoul (2001), The Southern Ocean Limb of the Global Deep Overturning Circulation, *J. Phys. Oceanogr.*, *31*(1), 143–173.

Sokolov, S., and S. R. Rintoul (2002), Structure of Southern Ocean fronts at 140°E, *J. Mar. Syst.*, *37*, 151–184.

Sokolov, S., and S. R. Rintoul (2007a), Multiple jets of the Antarctic Circumpolar Current south of Australia, *J. Phys. Oceanogr.*, *37*, 1394–1412.

Sokolov, S., and S. R. Rintoul (2007b), On the relationship between fronts of the Antarctic Circumpolar Current and surface chlorophyll concentrations in the Southern Ocean, *J. Geophys. Res.*, *112*, C07,030, doi:10.1029/2006JC004,072.

Sokolov, S., and S. R. Rintoul (2009a), The circumpolar structure and distribution of the Antarctic Circumpolar Current fronts. Part 1: Mean circumpolar paths, *submitted to J. Geophys. Res.*

Sokolov, S., and S. R. Rintoul (2009b), The circumpolar structure and distribution of the Antarctic Circumpolar Current fronts. Part 2: Variability and relationship to sea surface height, *submitted to J. Geophys. Res.*

Sokolov, S., B. A. King, S. R. Rintoul, and R. L. Rojas (2004), Upper ocean temperature and the baroclinic transport stream function relationship in Drake Passage, *J. Geophys. Res.*, *109*(C05001), doi:10.1029/2003JC002,010.

Speich, S., and M. Arhan (2007), GOODHOPE/Southern Ocean: A study and monitoring of the Indo-Atlantic connections, *Mercator Newsletter*, *27*, 29–41.

Speich, S., and F. Dehairs (2008), MD166 International Polar Year BONUS-GoodHope Cruise Report, *Tech. rep.*, LPO-IFREMER-IPEV.

Speich, S., B. Blanke, and G. Madec (2001), Warm and cold water routes of an OGCM thermohaline conveyor belt, *Geophys. Res. Lett.*, *28*, 311–314.

Speich, S., B. Blanke, P. de Vries, S. Drijjfhout, K. Doos, A. Ganachaud, and R. Marsh (2002), Tasman leakage: A new route in the global ocean conveyor belt, *Geophys. Res. Lett.*, *29(10)*, doi:10.1029/2001GL014,586.

Speich, S., B. Blanke, and W. Cai (2007), Atlantic meridional overturning circulation and the Southern Hemisphere supergyre, *Geophys. Res. Lett.*, *34*, doi:10.1029/2007GL031,583.

Sprintall, J., R. Peterson, and R. Roemmich (1997), High resolution XBT/CTD measurements across Drake Passage, *WOCE Newsletters*, *29*, 18–20.

Stammer, D. (1998), On eddy characteristics, eddy transports, and mean flow properties, *J. Phys. Oceanogr.*, *28*, 727–739.

Sun, C., and D. R. Watts (2001), A circumpolar gravest empirical mode for the Southern Ocean hydrography, *J. Geophys. Res.*, *106*, 2833–2855.

Sun, C., and D. R. Watts (2002), Heat flux carried by the Antarctic Circumpolar mean flow, *J. Geophys. Res.*, *107(C9), 3119, doi:10.1029/2001JC001187*.

Sverdrup, H. U. (1940), Hydrology, *Report of B.A.N.Z. Antarctic Research Expedition*, *3*, 89–125.

Swart, S., and S. Speich (2009), An altimetry-based gravest empirical mode south of Africa. Part 2: dynamic nature of the ACC fronts, *J. Geophys. Res.*, p. doi:10.1029/2009JC005300.

Swart, S., S. Speich, I. J. Ansorge, G. J. Goni, S. Gladyshev, and J. R. E. Lutjeharms (2008), Transport and variability of the Antarctic Circumpolar Current south of Africa, *J. Geophys. Res.*, *113*(C09014), doi:10.1029/2007JC004,233.

Swart, S., S. Speich, I. J. Ansorge, and J. R. E. Lutjeharms (2009), An altimetry-based gravest empirical mode south of Africa. Part1: development and validation, *accepted, J. Geophys. Res.*

Thompson, A. F. (2009), Jet formation and evolution in baroclinic turbulence with simple topography, *submitted to J. Phys. Oceanogr.*

Thompson, D. W. J., and S. Solomon (2002), Interpretation of recent Southern Hemisphere climate change, *Science*, *296*, 895–899.

Torrence, C., and G. P. Compo (1998), A practical guide to wavelet analysis, *Bull. Amer. Meteorol. Soc.*, *79*, 61–78.

Trenberth, K. E., W. G. Large, and J. G. Olson (1990), The Mean Annual Cycle in Global Ocean Wind Stress, *J. Phys. Oceanogr.*, *20*, 1742–1760.

Troup, A. J. (1965), The Southern Oscillation, *Quart. J. Royal Meteorol. Soc.*, *91*, 490–506.

van Leeuwen, P. J., W. P. M. de Ruijter, and J. R. E. Lutjeharms (2000), Natal pulses and the formation of Agulhas rings, *J. Geophys. Res.*, *105*(C5), 6425–6436.

von Schuckmann, K., F. Gaillard, and P.-Y. le Traon (2009), Global hydrographic variability patterns during 2003-2007, *submitted to J. Geophys. Res.*

Warren, B. A. (1972), Insensitivity of Subtropical Mode Water Characteristics to Meteorological Fluctuations, *Deep-Sea Res.*, *19*(1), 1–19.

Watts, R. D., C. Sun, and S. R. Rintoul (2001), A two-dimensional gravest empirical mode determined from hrdrographic observations in the Subantarctic Front, *J. Phys. Oceanogr.*, *31*, 2186–2209.

Weijer, W., W. P. M. D. Ruijter, H. A. Dijkstra, and P. J. van Leeuwen (1999), Impact of interbasin exchange on the Atlantic overturning circulation, *J. Phys. Oceanogr.*, *29*, 3184.

Whitworth, T. (1980), Zonation and Geostrophic Flow of the Antarctic Circumpolar Current at Drake Passage, *Deep-Sea Res.*, *27*, 497–507.

Whitworth, T. (1983), Monitoring the Transport of the Antarctic Circumpolar Current at Drake Passage, *J. Phys. Oceanogr.*, *13*, 2045–2057.

Whitworth, T., and W. D. Nowlin (1987), Water Masses and Currents of the Southern-Ocean at the Greenwich Meridian, *J. Geophys. Res.*, *92*, 6462–6476.

Whitworth, T., and R. G. Peterson (1985), Volume Transport of the Antarctic Circumpolar Current from Bottom Pressure Measurements, *J. Phys. Oceanogr.*, *15*, 810–816.

WOCE (2002), World Ocean Circulation Experiment, Global Data, Version 3.0., *Tech. rep.*, WOCE International Project Office, Southampton, UK; published by U.S. National Oceanographic Data Center, Silver Spring, 180/02, DVD-ROM.

Worthington, L. V. (1972), Negative ocean heat flux as a cause of water-mass formation, *J. Phys. Oceanogr.*, *2*, 205–211.

Wunsch, C., and D. Stammer (1995), The global frequency-wavenumber spectrum of oceanic variability estimated from TOPEX/POSEIDON altimetric measurements, *J. Geophys. Res.*, *100*(C12), 24,895–24,910.

Wust, G. (1935), Schichtung und Zirkulation des Atlantischen Ozeans, *Meteor Reports 1925-1927*, *6*(2), 1–288.

Yuan, X. (2004), ENSO-related impacts on Antarctic sea ice: a synthesis of phenomenon and mechanisms, *Antarctic Science*, *16(4)*, 415–425.

APPENDIX A

Animation material

Throughout the study several data animations were constructed and viewed to clarify some questions about the dynamics and circulation of the oceanic region south of Africa. These animations have been placed on disk (attached) and can be viewed in any AVI compatible software, such as VLC (Linux) or Media Player (Windows).

The animations available on the disk are listed below. Slanted text represents scientific discussion relating to the data shown in the animations.

1. *video1_adt_gh_topo.avi*: Weekly 'Maps of Absolute Dynamic Topography' (MADT; in dyn m) are displayed for the region encompassing the GoodHope line. This animation runs from October, 14, 1992 to January, 23, 2008. The GoodHope line is represented using a thick black curve. The bathymetry for the region (2000 m and 3000 m isobaths) is marked using white contours. The MADT contour interval is 0.025 dyn m. For further details about the data, refer to the data sections of Papers I or II.
   This animation was principally used to track mesoscale features crossing the GoodHope line. These features were often tracked using this product to find their place of origin and to show how they dissipated. This data was specifically used to track Agulhas Rings that propagated in a west to west-south-west trajectory and were located in the SAZ when crossing the GoodHope line. Between roughly 40-55°S, the main ACC fronts can be approximately positioned where isolines of MADT are closely spaced (i.e. where the local meridional gradient of the MADT is greatest).

2. *video2_sla_gh.avi*: Weekly 'Maps of Sea Level Anomaly' (MSLA; in dyn m) are displayed for the region encompassing the GoodHope line. This animation runs from October, 14, 1992 to January, 23, 2008. The GoodHope line is represented using a black curve. For further details about the data, refer to the data sections of Papers I or II.

3. *video3_temp_gem.avi*: Altimetry data (weekly) is merged with the GEM (AGEM; Paper II) to render temperature sections along the GoodHope line (surface to 1000 dbar) in order to improve our understanding of the subsurface thermohaline structure and to record the depth to which some of the transient features extended.

4. *video4_salt_gem.avi*: Same as for video 3 but for salinity.
   The propagation of Agulhas Rings in the northern domain of the SAZ has been discussed extensively in Paper I and III. Video 3 and 4 can clearly show the 'pulsing' nature of Agulhas Rings moving over the GoodHope line when sudden peaks in the temperature and salinity, to depths that extend to 1000 dbar, are observed. Other transient mesoscale features can be seen further south. These are often associated close to the mean position of the APF.

5. *video5_sc_interm.avi*: The salt content, derived from the AGEM-produced sections of salinity (Paper III), is extended longitudinally (20°W to 25°E) to investigate the passage and behavior of mesoscale features in the region and the exchange of salt signatures between different oceanic domains. The mean salt content is found in the Antarctic Intermediate Water layer following the 1027.1 $kg.m^{-3}$ (upper limit) and 1027.3 $kg.m^{-3}$(lower limit) isopycnals. This animation runs from October, 14, 1992 to December, 28, 2005. The GoodHope line is represented using a dashed black curve. The bathymetry for the region (2000 m and 3000 m isobaths) is

marked using white contours. The salt content contour interval is 0.05 psu.
This animation allows us to focus on mesoscale features that bring about varying signatures of salt content in the Antarctic Intermediate Water layer. The most dominant features are Agulhas Rings, which can be seen propagating from the east. Interestingly, they indicate a possible path for fresh water to flow towards the north and into the southern Benguela region as well as onto the Agulhas Bank. We must keep in mind that the further away we create these GEM representations from the geographic location of the GoodHope cruise track, the more inaccuracies will be introduced. This is because the GEM empirical relationships have been constructed from data located at or near the GoodHope line. This means that the thermohaline structure may vary up- and/or downstream of the GoodHope line and, therefore, introduce additional errors. For this reason, we must be cautious with representations located away from the GoodHope line and outside the limits of the ACC.

6. *video6_hc_anom_sla.avi*: (left panel) Weekly plots MSLA (in dyn m) are displayed for the region encompassing the GoodHope line. (right panel) The AGEM-derived heat content anomaly is represented between the surface and 2500 dbar for the same domain as the MSLA plots. This animation runs from October, 14, 1992 to December, 28, 2005. The 100 and 500 m isobaths are displayed using yellow contours, while the 1000 and 2000 m isobaths are in green.

7. *video7_sla_gvel300.avi*: The geostrophic velocities at 300 dbar are derived from sections of density using the GEM method. These velocities (in $m.s^{-1}$) are plotted as arrows. The time-varying plots of altimetry SLA are overlaid in color (in dyn m). The bathymetry for the region (2000 m and 3000 m isobaths) is marked using white contours. This animation runs from October, 14, 1992 to January, 10, 1996.
It is interesting to note how the geostrophic velocities vary due to the propagation of mesoscale features across the GoodHope line. North of 40°S, the passage of Agulhas Rings causes large velocity reversals and increased variability.

APPENDIX B

GEM-produced XBT sections

In an additional approach at testing the efficacy of the GEM, XBT sections of temperature are reproduced by applying information of the surface dynamic height to the GEM. This also allows one to see whether the GEM will reproduce transient features not found the mean hydrographic structure. In total, seven XBT sections, conducted along the GoodHope line are compared here. The bottom panels of the first five figures show the rms difference between the observed data and the GEM-produced sections, while the remaining two figures show the difference.

The GEM-produced sections are, for the most part, very similar to the observed sections. In most cases, mesoscale features encountered in the observed data are reproduced accurately by the GEM. This includes the passage of Agulhas Rings in the northern domains. The largest errors are, as expected, located outside the limits of the ACC because the data used to construct the GEM comes predominantly from within the limits of the ACC. The GEM-deduced sections reproduce the temperature minimum layer located south of $\sim$50°S, although it is not always able to position its exact depth and intensity.

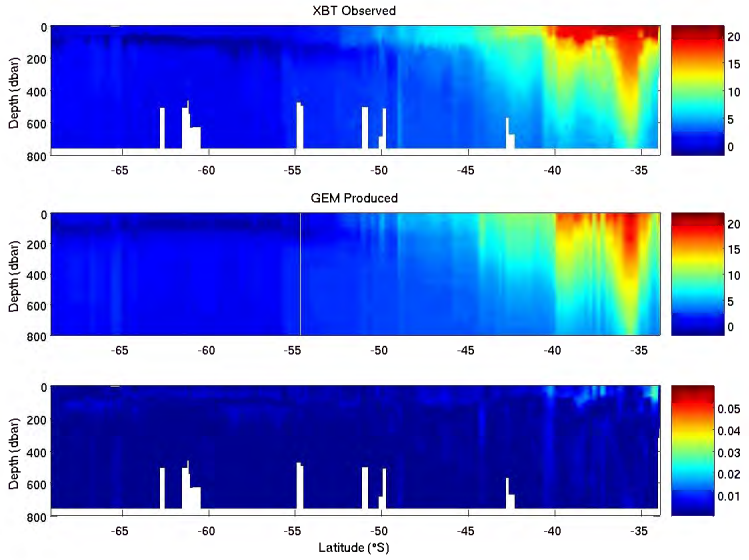

Figure 1: (upper panel) The first GoodHope XBT section (March 2004), (middel panel) the GEM-produced section from the dynamic height data derived from proxy methods and (bottom panel) the rms difference between the two representations.

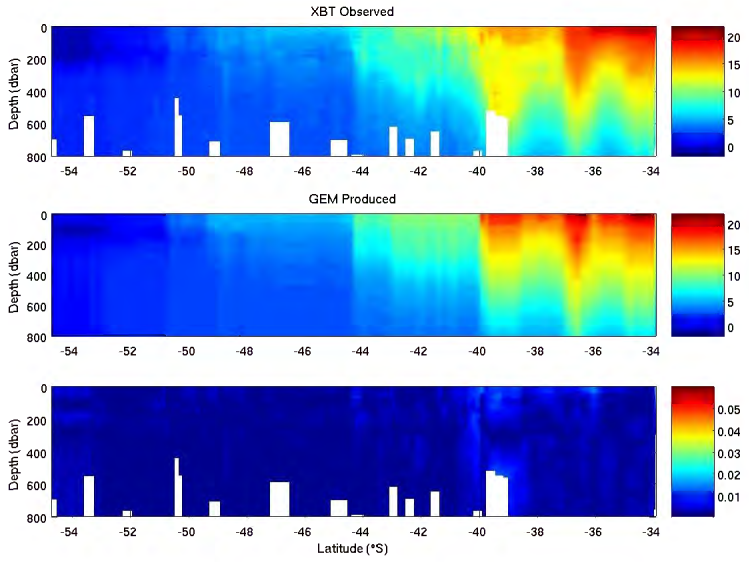

Figure 2: Same as Figure 1 but for the second GoodHope XBT section (November 2004).

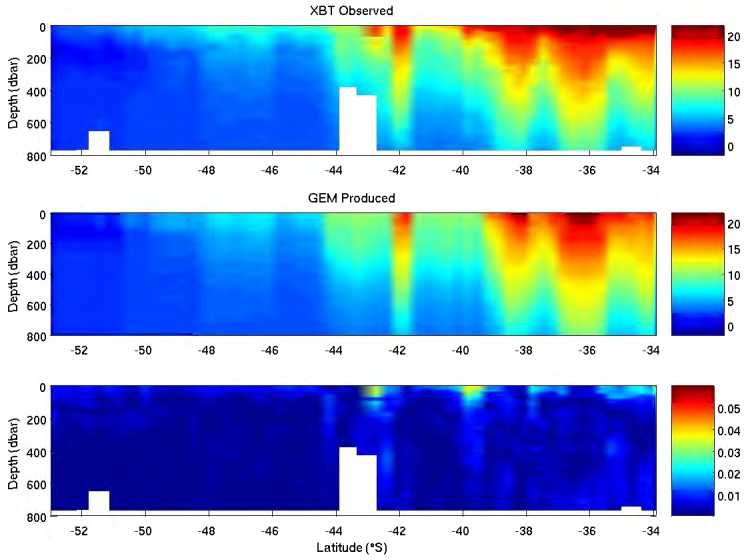

Figure 3: Same as Figure 1 but for the third GoodHope XBT section (January 2005).

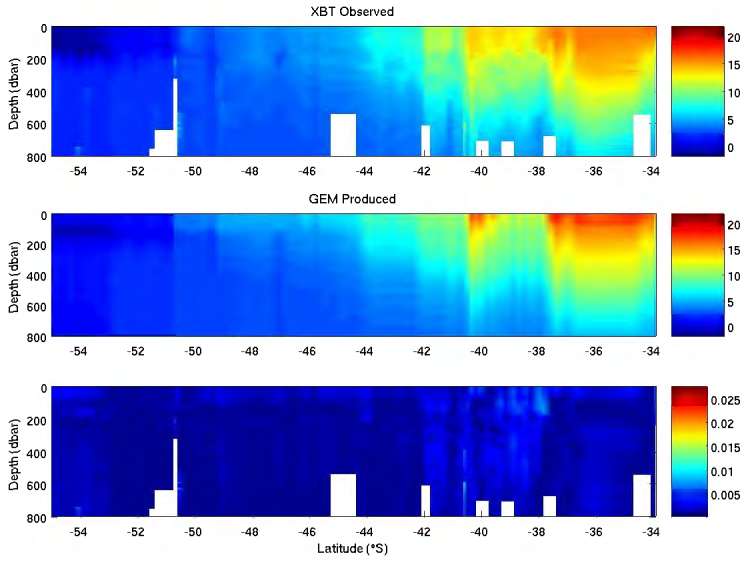

Figure 4: Same as Figure 1 but for the fourth GoodHope XBT section (October 2005).

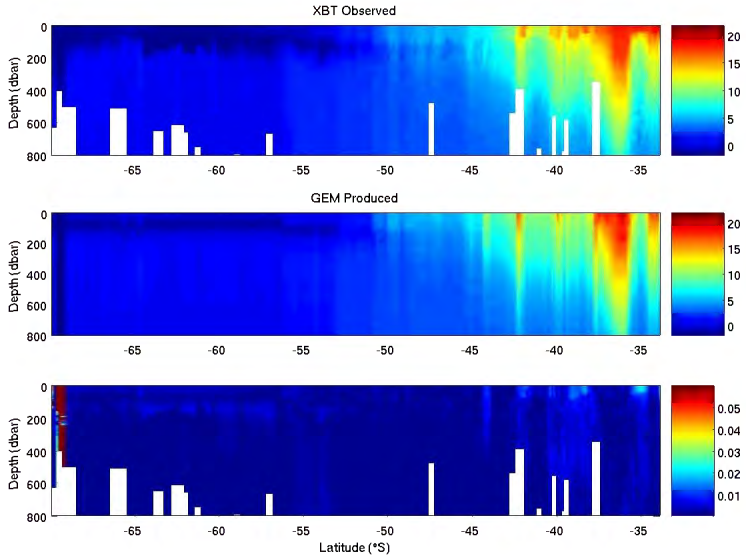

Figure 5: Same as Figure 1 but for the fifth GoodHope XBT section (December 2005).

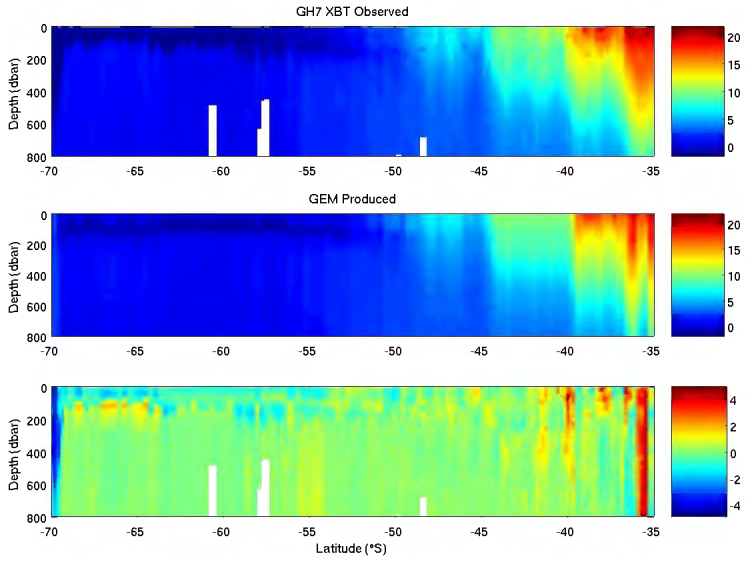

Figure 6: Same as Figure 1 but for the sixth GoodHope XBT section (October 2006). Note that the bottom panel represents the difference between the two upper representations and not the rms difference as for the previous figures.

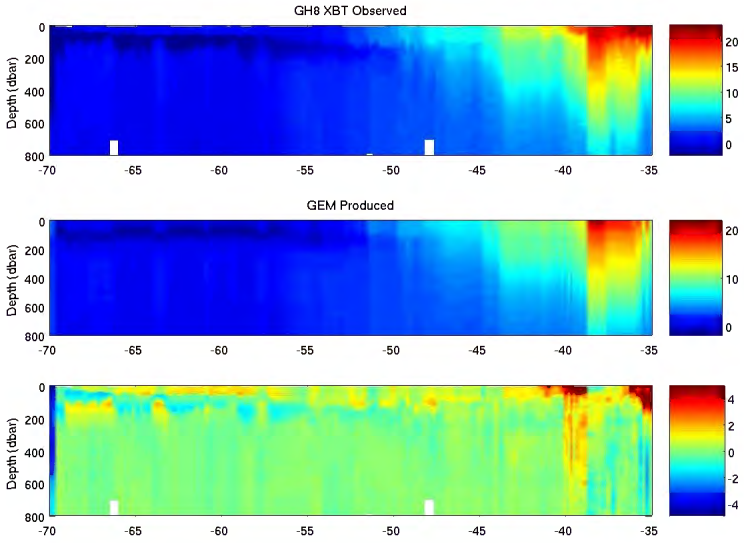

Figure 7: Same as Figure 6 but for the seventh GoodHope XBT section (December 2006).

APPENDIX C

Hovmöller plots of heat and salt content

In Paper III, the integrated heat and salt content between the surface and 2500 dbar is represented in Hovmöller diagrams. Due to length constraints of journal articles the heat and salt content integrated within other pressure layers are not shown. The figures presented in this appendix show the Hovmöller representations of heat and salt content not included in Paper III.

In many instances similarities can be found between the layers represented in this section to that found in Paper III. However, isolating different pressure and density layers does reveal varying intensities and behaviors of certain features.

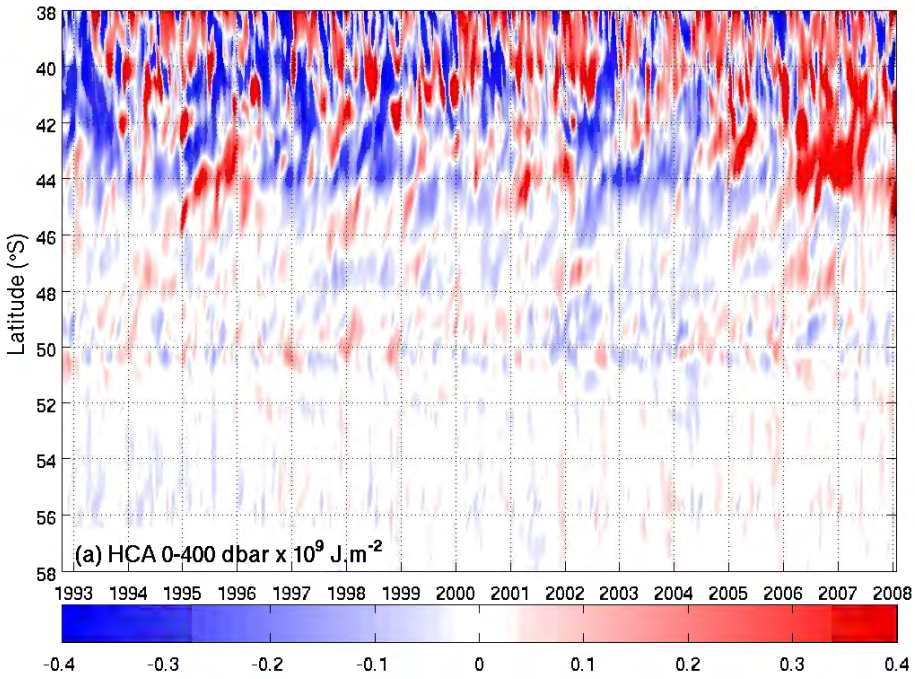

Figure 8: A Hovmöller representation of the heat content anomaly between the surface and 400 dbar, along the GoodHope line. The white space in the northern (southern) domain of the ACC represents the northern (southern) extent of the ACC, which can be defined as the position of the STF (SBdy). Values are expressed as $\times 10^9\ J.m^{-2}$.

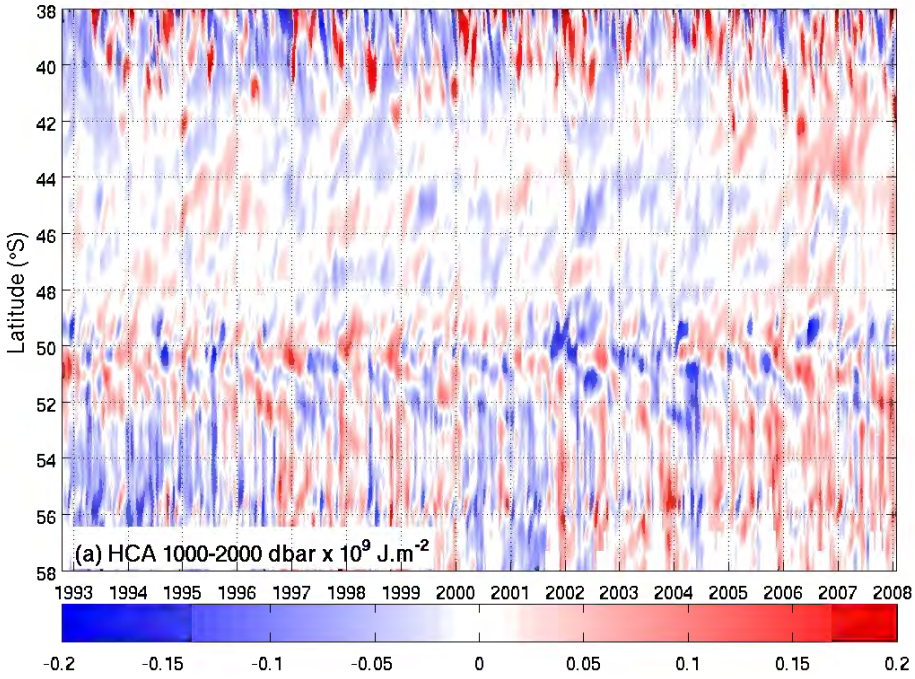

Figure 9: Same as for Figure 8 but between 1000 and 2000 dbar. Values are expressed as $\times 10^9\ J.m^{-2}$.

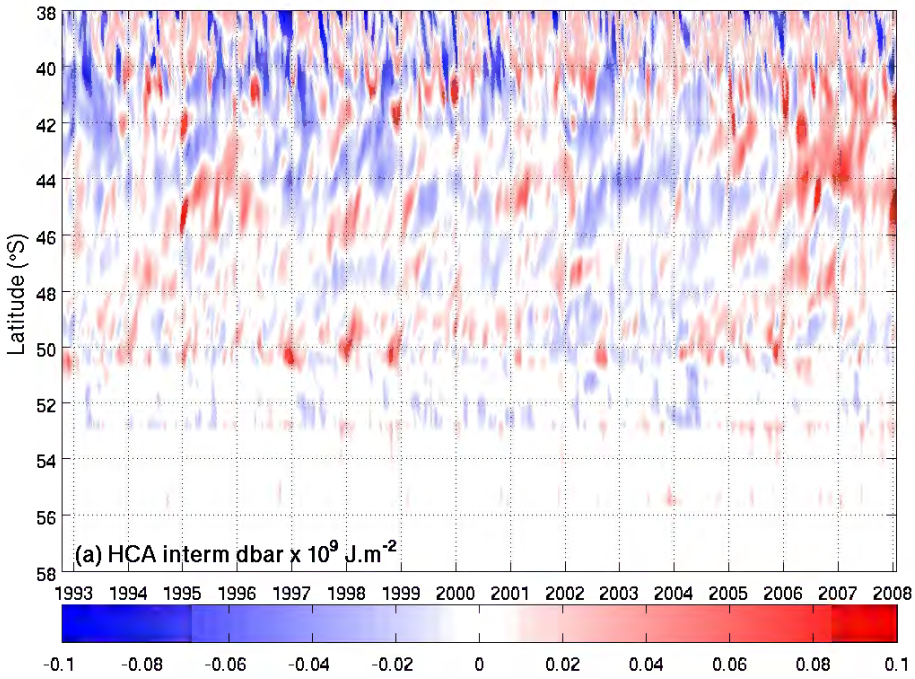

Figure 10: Same as for Figure 8 but between the upper (1024.1 $kg.m^{-3}$) and lower limits of the Antarctic Intermediate Water layer (1024.7 $kg.m^{-3}$). Values are expressed as $\times 10^9$ $J.m^{-2}$.

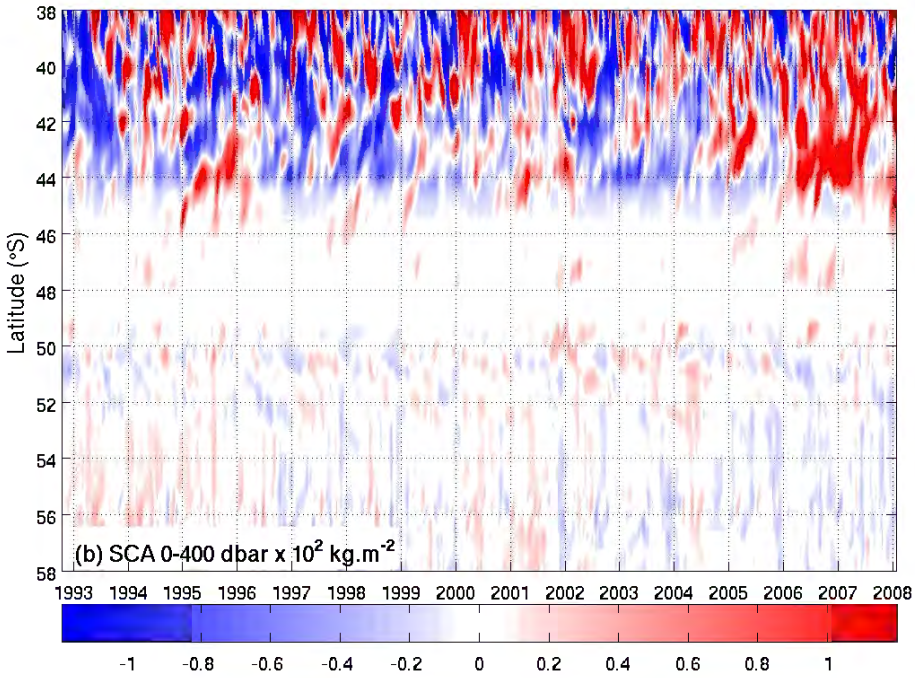

Figure 11: Same as for Figure 8 but for the salt content anomaly between the surface and 400 dbar. Values are expressed as $\times 10^2$ $kg.m^{-2}$.

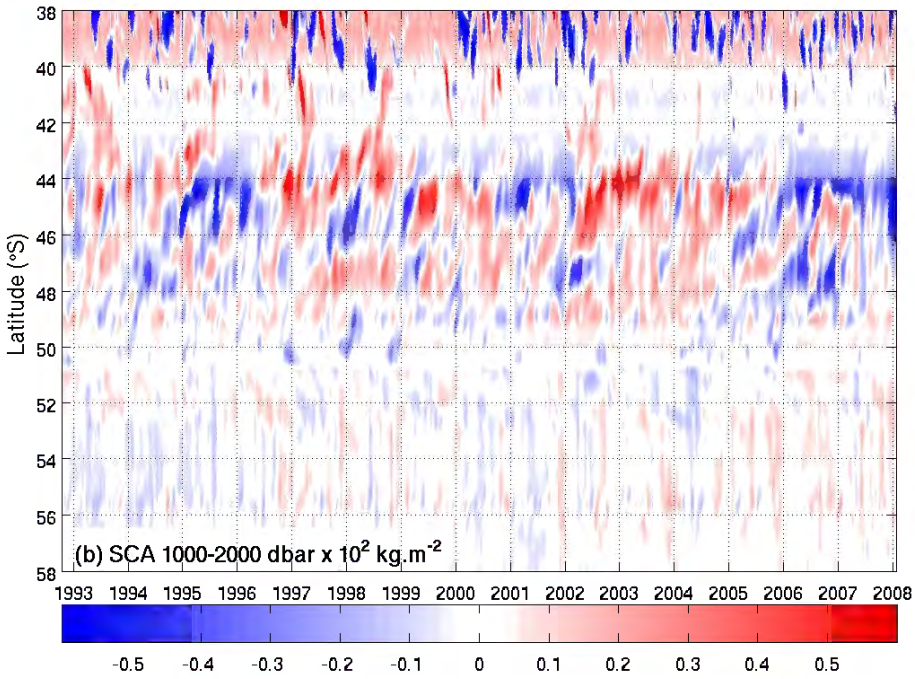

Figure 12: Same as for Figure 11 but between 1000 and 2000 dbar. Values are expressed as $\times 10^2\ kg.m^{-2}$.

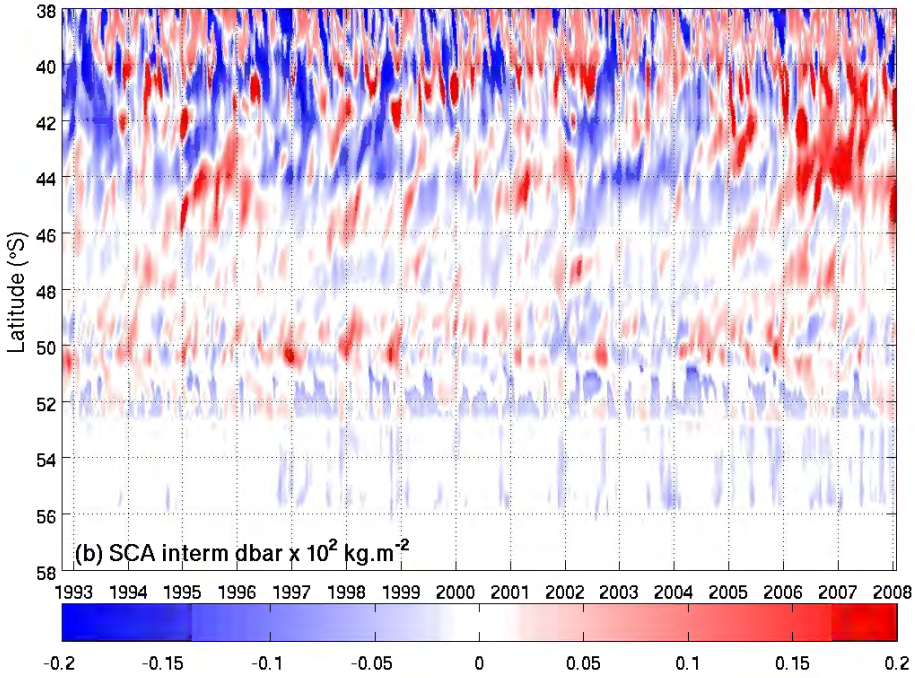

Figure 13: Same as for Figure 11 but between the upper ($1024.1\ kg.m^{-3}$) and lower limits of the Antarctic Intermediate Water layer ($1024.7\ kg.m^{-3}$). Values are expressed as $\times 10^2\ kg.m^{-2}$.

APPENDIX D

Annual mean time series of the heat and salt content anomaly

The annual mean heat and salt content anomaly is estimated for each frontal zone of the ACC and within each pressure and density layer.

In each of the figures below, the black bars and red line both represent the annual mean of the heat or salt content anomaly. The upper (lower) extents of the blue boxes represent the upper (lower) quartile of the data (upper=75% of data; lower=25% of data). The whiskers extending from the box are the upper and lower limits of the data. The thin red line in the box is the median. The red crosses are the outliers.

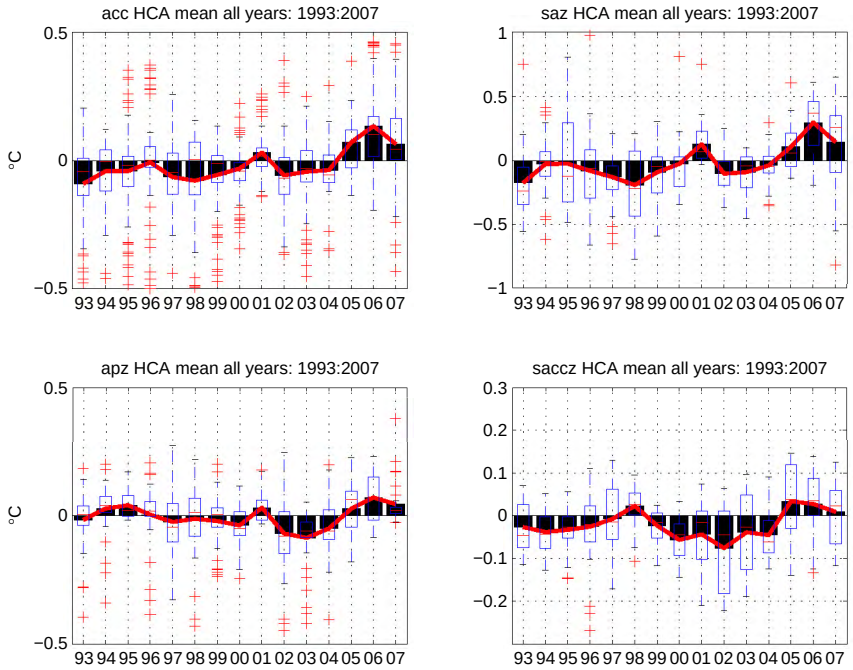

Figure 14: Box plots of the annual mean HCA, between the surface and 2500 dbar, for the whole ACC domain (upper left panel), the SAZ (upper right panel), the APZ (lower left panel), and the SACCZ (lower right panel).

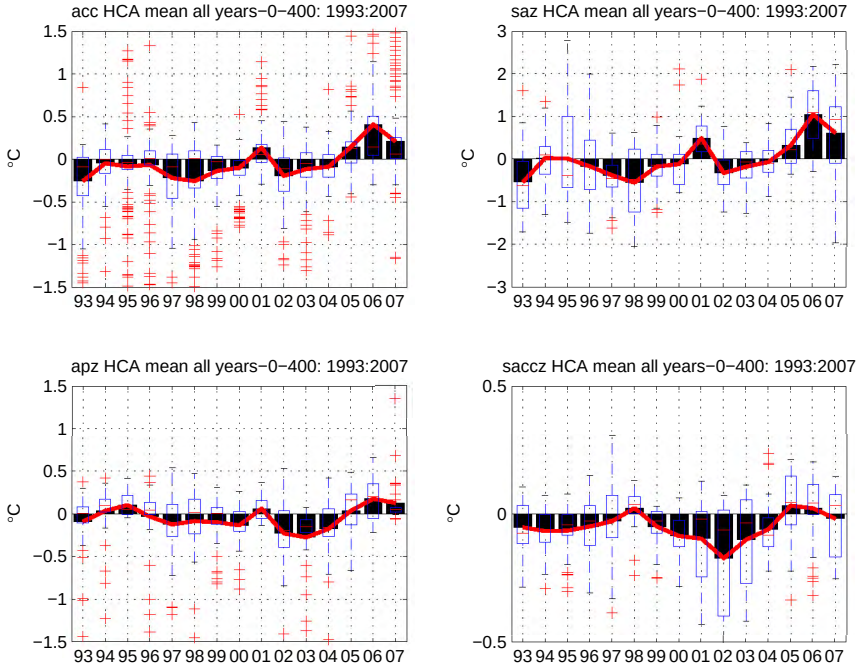

Figure 15: Same as for Figure 14 but between the surface and 400 dbar.

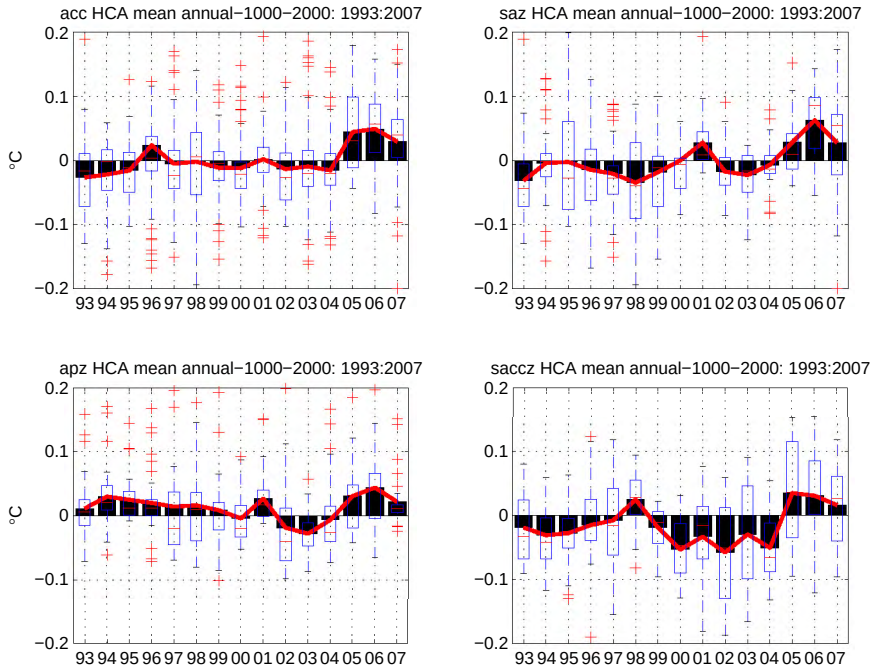

Figure 16: Same as for Figure 14 but between 1000 and 2000 dbar.

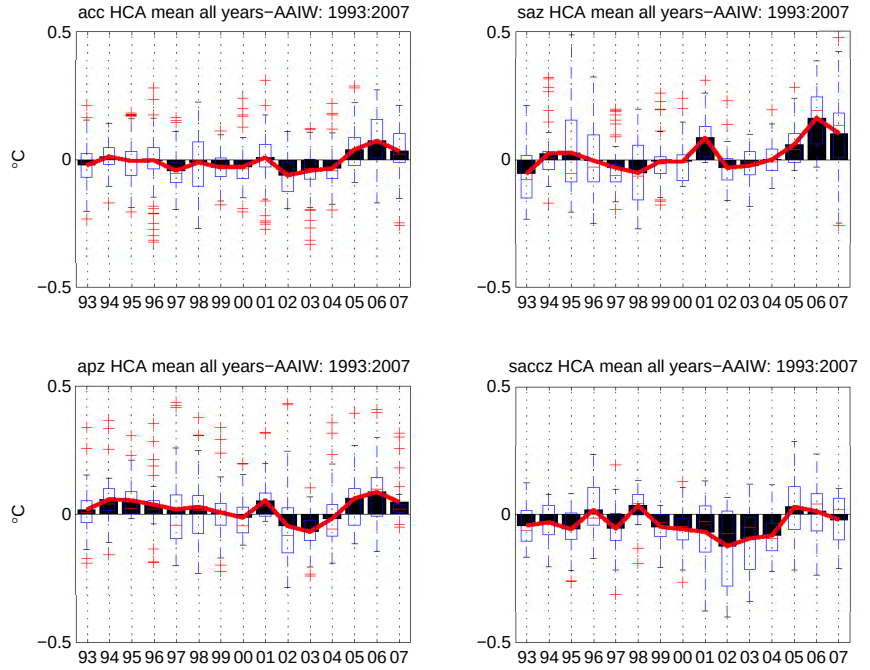

Figure 17: Same as for Figure 14 but for the Antarctic Intermediate Water layer.

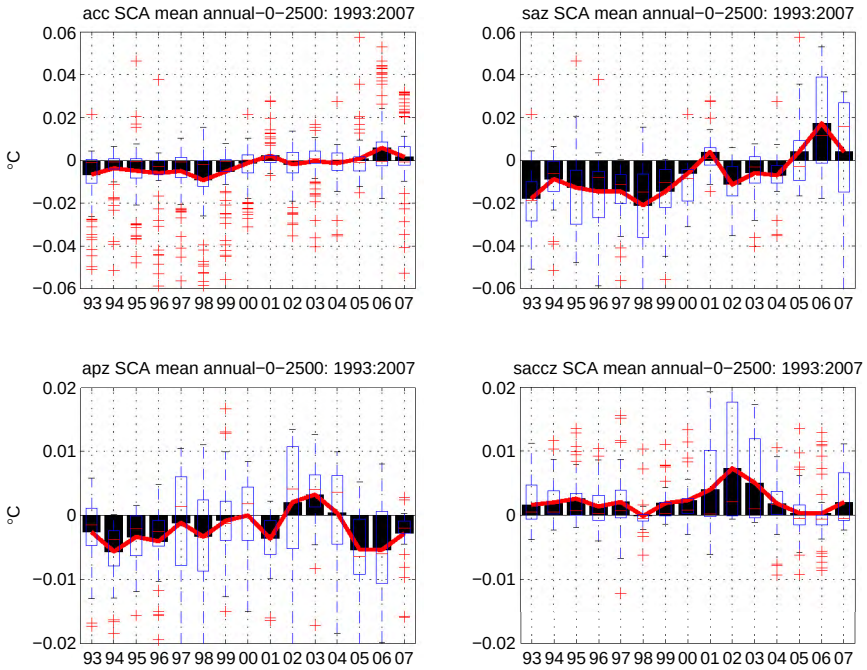

Figure 18: Same as for Figure 14 but for the salt content anomaly between the surface and 2500 dbar.

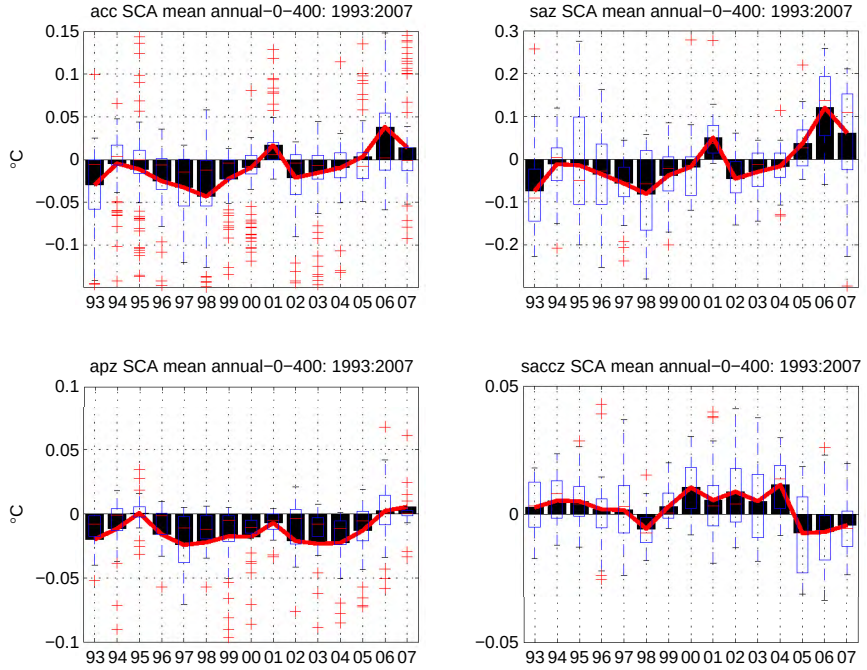

Figure 19: Same as for Figure 18 but between the surface and 400 dbar.

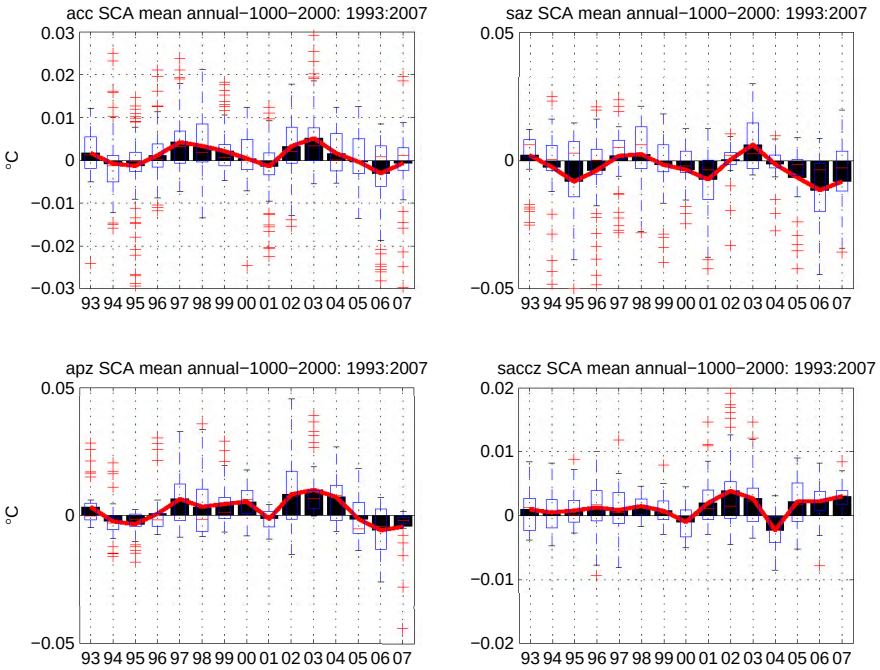

Figure 20: Same as for Figure 18 but between 1000 and 2000 dbar.

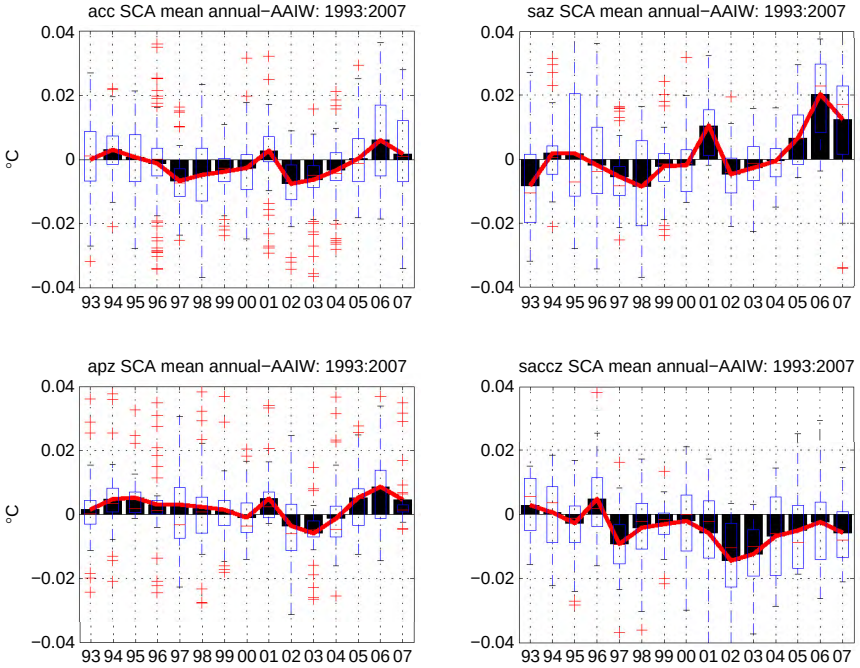

Figure 21: Same as for Figure 18 but for the Antarctic Intermediate Water layer.

APPENDIX E

Continuous wavelet analysis on the time series of heat content anomaly

Wavelet analysis is used in this study to separate the different scales of variability found in the heat content anomaly for different zones of the ACC. Some of these are represented in Paper III and those that are not can be found below.

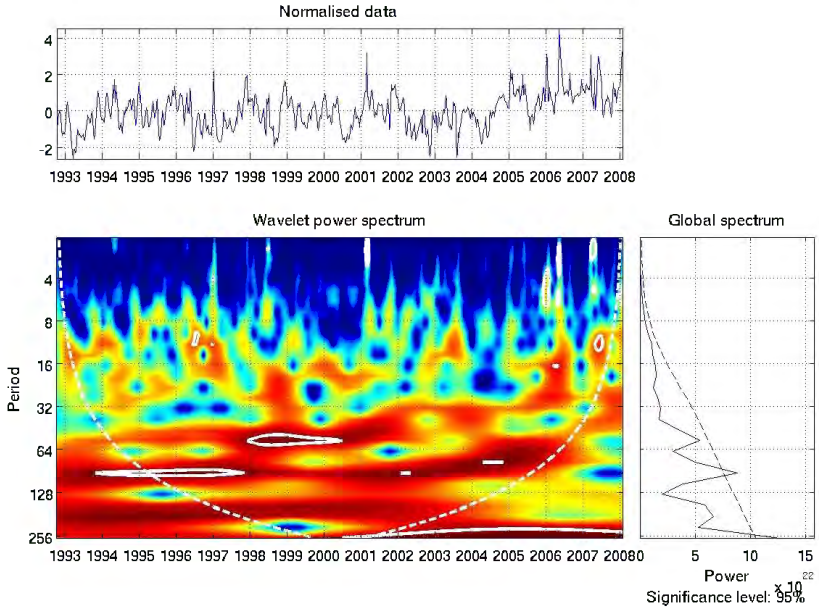

Figure 22: The continuous wavelet spectrum is presented for the heat content anomaly, between the surface and 2500 dbar, within the ACC domain. White contours indicate where the wavelet amplitude is significant at the 95% level, while the white dashed curve shows the cone of influence.

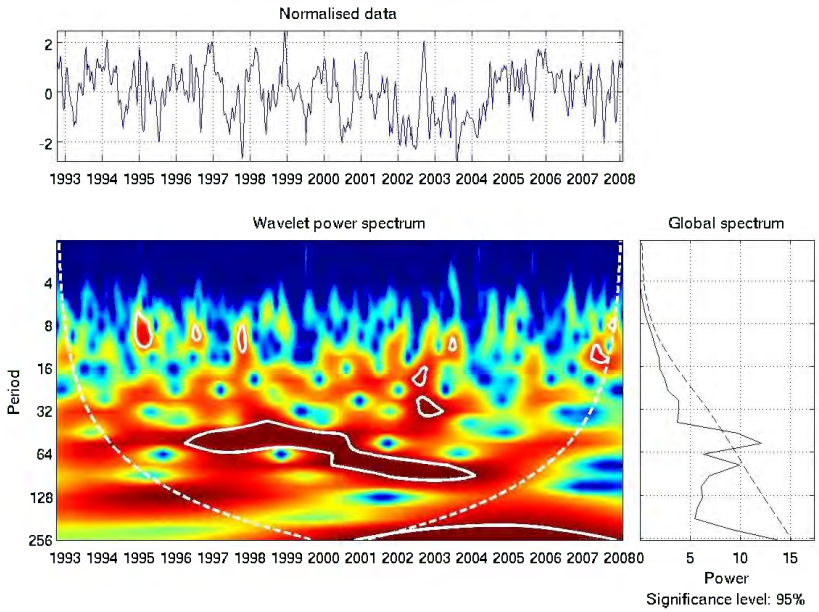

Figure 23: Same as for Figure 22 but for the APF.

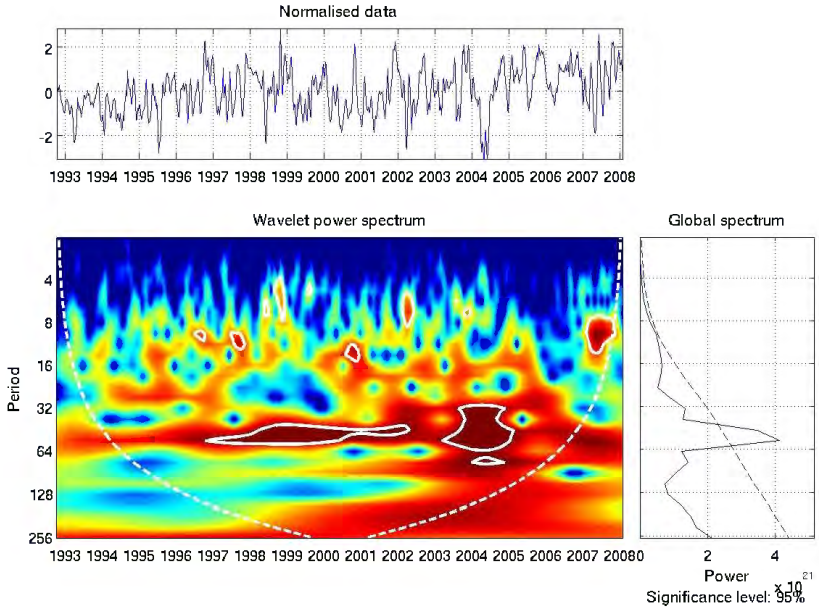

Figure 24: Same as for Figure 22 but for the SACCF.

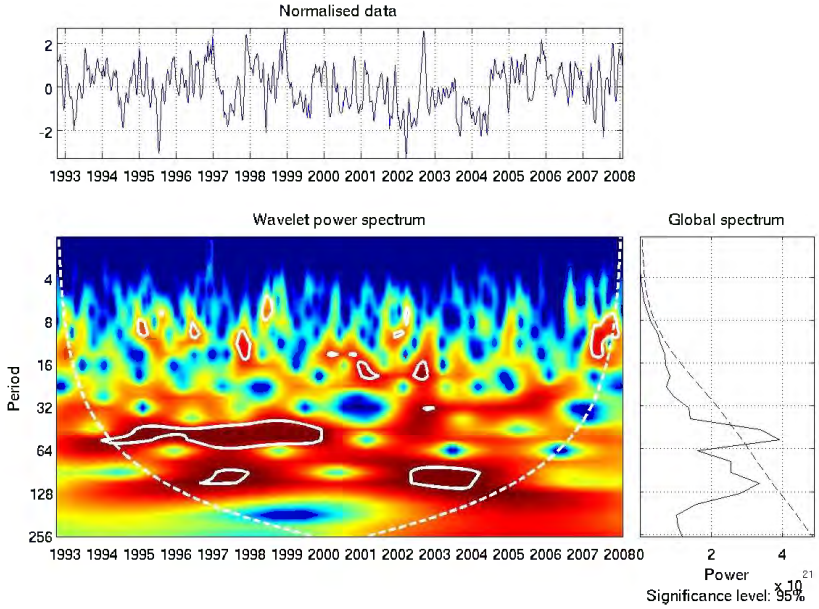

Figure 25: Same as for Figure 22 but for the SACCZ.

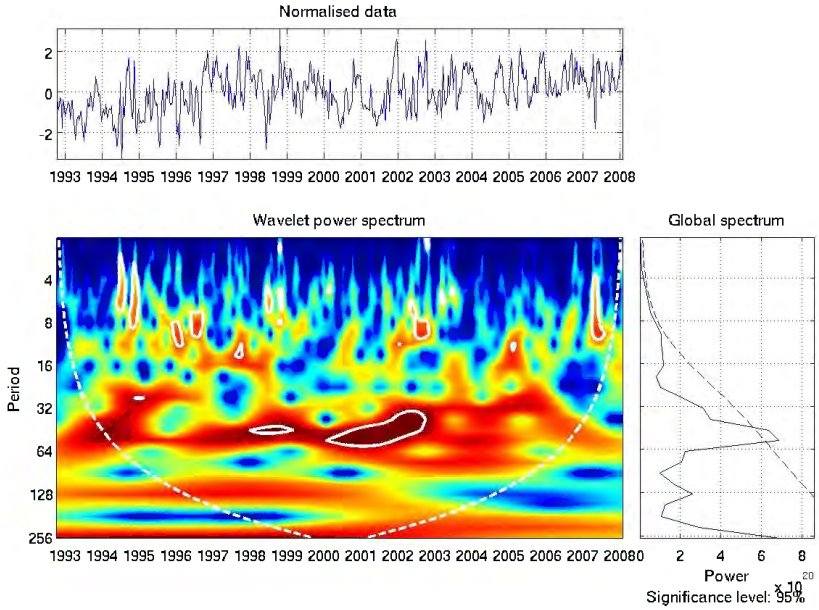

Figure 26: Same as for Figure 22 but for the SBdy.

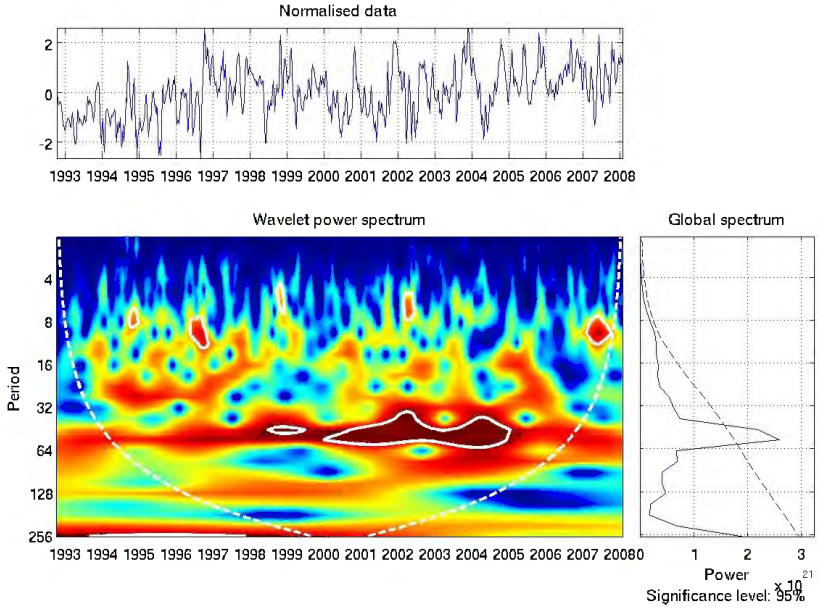

Figure 27: Same as for Figure 22 but for the SBZ.

APPENDIX F

Acronyms

AA: Antarctica
AABW: Antarctic Bottom Water
AAIW: Antarctic Intermediate Water
AARI: Arctic and Antarctic Russian Institute
AASW: Antarctic Surface Water
ACC: Antarctic Circumpolar Current
ADT: Absolute Dynamic Topography
AGEM: Altimetry Gravest Empirical Mode
AKE: Anomaly of Kinetic Energy
AOML: Atlantic Oceanographic and Meteorological Laboratory
APF: Antarctic Polar Front
APZ: Antarctic Polar Frontal Zone
ASTTEX: Agulhas-South Atlantic Thermohaline Transport Experiment
AWI: Alfred Wegner Institute
BONUS: Biogeochemistry of the southern Ocean: interactions between NUtrients, dynamics, and ecosystem Structure
CDW: Circumpolar Deep Water
CLS: Collecte Localisation Satellites
CMDT: Combined Mean Dynamic Topography
COI: Cone of Influence
CT: Cumulative Transport
CTD: Conductivity-Temperature-Depth
CWT: Continuous Wavelet Transform
DH: Dynamic Height
EKE: Eddy Kinetic Energy
ERS: European Remote Sensing satellite
GDAC: Global Data Assembly Centre
GEM: Gravest Empirical Mode
GH: GoodHope
GRACE: Gravity Recovery and Climate Experiment
HC: Heat Content
HCA: Heat Content Anomaly
IFREMER: Institut Français de Recherche pour l'Exploitation de la Mer
CLIVAR: Climate Variability and Predictability
IMAU: Institute for Marine and Atmospheric research Utrecht
ISOS: International Southern Ocean Study
KNMI: Koninklijk Nederlands Meteorologisch Instituut
LADCP: Lowered Acoustic Doppler Current Profiler

LCDW: Lower Circumpolar Deep Water
LPO: Laboratoire de Physique des Océans
MADT: Maps of Absolute Dynamic Topography
MKE: Mean Kinetic Energy
MOC: Meridional Overturning Circulation
MSLA: Maps of Sea Level Anomaly
MSLP: Mean Sea Level Pressure
NADW: North Atlantic Deep Water
NCAR: National Center for Atmospheric Research
NCEP: National Centers for Environmental Prediction
NOAA: National Oceanographic and Atmospheric Administration
NRF: National Research Foundation
PIES: Pressure Inverted Echo Sounders
RMS: Root Mean Square
RMSD: Root Mean Square Difference
SACCF: Southern Antarctic Circumpolar Current Front
SACCZ: Southern Antarctic Circumpolar Current Zone
SAF: Subantarctic Front
SAM: Southern Annular Mode
SAMW: Subantarctic Mode Water
SANAP: South African National Antarctic Program
SASW: Subantarctic Surface Water
SAZ: Subantarctic Zone
SBdy: Southern Boundary of the ACC
SBZ: Southern Boundary Zone
SC: Salt Content
SCA: Salt Content Anomaly
SOI: Southern Oscillation Index
SSH: Sea-Surface-Height
SST: Sea-Surface-Temperature
STC: Subtropical Convergence
STD: Standard Deviation
STF: Subtropical Front
STIAS: Stellenbosch Institute for Advanced Study
STSW: Subtropical Surface Water
SURVOSTRAL: Surveillance de l'Océan Austral
Sv: Sverdrup
T-S: Temperature-Salinity
THC: Thermohaline Circulation
TKE: Total Kinetic Energy
TP: Topex-Poseidon

Tr: Transport
UBO: Université de Bretagne Occidentale
UCDW: Upper Circumpolar Deep Water
WECCON: Weddell Sea Convection Control
WOCE: World Ocean Circulation Experiment
WSBW: Weddell Sea Bottom Water
WSDW: Weddell Sea Deep Water
WSW: West-South-West
XBT: Expendable Bathythermograph

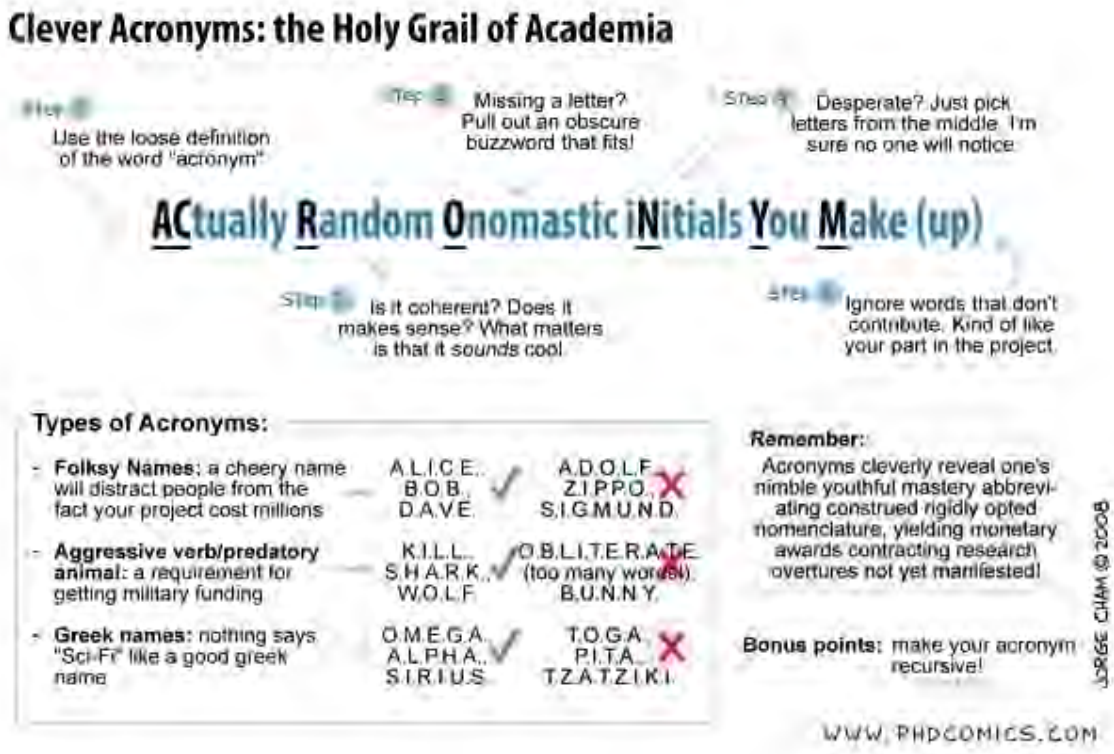
Clever Acronyms: the Holy Grail of Academia
Step 1
Use the loose definition of the word "acronym"
Step 2
Missing a letter? Pull out an obscure buzzword that fits!
Step 3
Desperate? Just pick letters from the middle. I'm sure no one will notice
ACtually Random Onomastic iNitials You Make (up)
Step 4
Is it coherent? Does it makes sense? What matters is that it sounds cool.
Step 5
Ignore words that don't contribute. Kind of like your part in the project.
Types of Acronyms:
- Folksy Names: a cheery name will distract people from the fact your project cost millions
A.L.I.C.E.
B.O.B.
D.A.V.E.
A.D.O.L.F.
Z.I.P.P.O.
S.I.G.M.U.N.D.
- Aggressive verb/predatory animal: a requirement for getting military funding
K.I.L.L.
S.H.A.R.K.
W.O.L.F.
O.B.L.I.T.E.R.A.T.E. (too many words!)
B.U.N.N.Y.
- Greek names: nothing says "Sci-Fi" like a good greek name
O.M.E.G.A.
A.L.P.H.A.
S.I.R.I.U.S.
T.O.G.A.
P.I.T.A.
T.Z.A.T.Z.I.K.I.
Remember:
Acronyms cleverly reveal one's nimble youthful mastery abbreviating construed rigidly opted nomenclature, yielding monetary awards contracting research overtures not yet manifested!
Bonus points: make your acronym recursive!
JORGE CHAM © 2008
WWW.PHDCOMICS.COM